Gas sensing with carbon nanotube networks

Morgan, Christopher

Gas sensing with carbon nanotube networks

Christopher Morgan

Molecular and Materials Physics Group
Department of Physics
Queen Mary, University of London

Submitted in partial fulfilment of the requirements for the degree of
Doctor of Philosophy

Declaration

I declare that the work presented in this thesis is my own and has not been submitted at another institution other than Queen Mary, University of London.

Christopher Morgan

Acknowledgments

This thesis would not have been possible without the help and support which I have received over the past three years both in and off campus. Firstly, I big thanks goes to my supervisor Mark Baxendale. I feel lucky to have worked with such a great scientist.

Thanks to the Quantum Detection Group at the National Physical Laboratory for their support not least Patrick Joseph-Franks and Lizzie Brown. A large debt of gratitude must be paid to Dr. Ken Scott for invaluable laboratory assistance, Geoff Gannaway for all the excellent mechanical work and George Nevill for an (almost) limitless supply of precious metals and well crafted evaporation boats, which I could never replicate. Thanks and cheers goes to my fellow lab and office mates without whom life at Queen Mary would have been immeasurably less pleasurable.

I would like to thank my parents, Carl and Jackie and my brother Stephen for all their support and encouragement throughout my life. Finally, a big thanks must go to my dearest girlfriend Amber for sharing the past three years trials and tribulations.

Abstract

Carbon nanotubes are an exciting new material with exemplary mechanical and electronic properties. Carbon nanotubes can be either metallic or semiconducting; either type has properties which rival conventional materials. The one-dimensional electronic nature of these materials leads to extreme sensitivity to the local energy landscape, a desirable property for a sensing element.

Production of carbon nanotubes currently has no method of growing nanotubes with a specific electronic property, any differentiation occurs through processing a heterogenous ensemble. Recently, networks of carbon nanotubes have shown attractive properties for electronic applications. The self-selecting current path has properties averaged from the ensemble of nanotubes providing repeatability in addition to flexibility and transparency.

This thesis is a study of the transport properties of thin and thick networks of single-walled carbon nanotubes and their electrical response to oxygen adsorption in both a simple resistive geometry and as the gate layer in a nanotube-metal-oxide-silicon capacitor. The thickness of network was found to determine the electrical characteristics of the network ensemble, thin networks displaying semiconducting transport characteristics, thick networks becoming more metallic. The response of the nanotube networks to oxygen exposure was found to be dependent on UV treatment. UV-desorbed networks exhibited an increased conductance upon oxygen-exposure, adsorbed networks exhibited a decrease in conductance upon further oxygen-exposure. Thinner, more semiconducting nanotube networks exhibited a greater change in conductance upon oxygen exposure. The nanotube-metal-oxide-semiconductor capacitor also showed a greater change in flat-band capacitance for thin nanotube networks. The capacitance of the nanotube device at the nanotube network flat-band voltage is shown to be influenced by both oxygen and nitrogen gases. The origin of the behaviour of the flat-band voltage is attempted to be understood and future work is suggested.

Contents

List of Figures

List of Abbreviations

CNT	Carbon-nanotube
SWNT	Single-wall carbon nanotube
SWNTn	Single-wall carbon nanotube network
MWNT	Multi-wall carbon nanotube
CV	Capacitance-voltage
CVD	Chemical vapour deposition
HiPco	High pressure carbon monoxide decomposition
TEP	Thermo-electric power
SDS	Sodium dodecyl sulfate
DIW	Deionised water
SWNT-MOS	Single wall carbon nanotube metal-oxide-semiconductor
HF	High frequency
LF	Low frequency
DIP	Dual in-line package
s-SWNT	Semiconducting SWNT
m-SWNT	Metallic SWNT
SCU	Semiconductor characterisation Unit
FFT	Fast fourier transform
DSG	Digital signal generator
RE	Reference electrode
WE	Working electrode
CE	Counter electrode

SigCU	Signal conditioning unit
RT	Room temperature
DOS	Density of states
vHs	van Hove singularity
VRH	Variable-range hopping
FIT	Fluctuation induced tunnelling

List of Symbols

Symbol	*Meaning*	*Unit*
q	Electronic charge	C
T	Temperature	K
ΔH_{ads}	Heat of adsorption	eV
E_{ads}	Adsorption energy	eV
E_{des}	Desorption energy	eV
Θ	Fractional surface coverage	
N_{A}	Avogadro's number	
M	Atomic number	
R	Universal gas constant	
τ_0	Period of single atom vibration	s
σ	Surface coverage	m^2
μ	Carrier mobility	$\text{cm}^2/\text{V}\cdot\text{s}$
V_{FB}	Flat-band voltage	V
V_{TH}	Threshold voltage	V
V_{G}	Gate voltage	V
Q_{si}	Space-charge density in semiconductor	C/cm^2

z	Displacement perpendicular to surface	m
ϕ_{M}	Metal work function	eV
ϕ_{S}	Semiconductor work function	eV
ϕ_{MS}	Metal and semiconductor work function difference	eV
ϕ_{f}	Energetic difference between conduction band edge and Fermi energy	eV
V_{S}	Surface potential	V
Q_{IT}	Total areal charge density residing at traps located at the oxide/semiconductor interface	$\mathrm{C/cm^2}$
Q_{OT}	Oxide-trapped charge	$\mathrm{C/cm^2}$
Q_{IT}	Total areal charge density residing in traps located at the oxide/semiconductor interface	$\mathrm{C/cm^2}$
X_{C}	Capacitive reactance	Ω
N_{AA}	Total concentration of acceptor impurities	$\mathrm{cm^{-3}}$
ΔQ_{n}	Change in electrical charge due to electrons	C
ΔQ_{p}	Change in electrical charge due to holes	C
N_{A}	Concentration of ionised acceptor impurities	$\mathrm{cm^{-3}}$
n_{i}	Intrinsic carrier concentration	$\mathrm{cm^{-3}}$
χ_{si}	Electron affinity of silicon	eV
E_{g}	Energy difference between the conduction band and valence band edges	eV
V_t	Thermal voltage	V
V_{bi}	Built-in voltage	V
f_{AC}	Small signal frequency	Hz
L_{C}	FET channel length	m

W	FET channel width	m
G	Conductance	S
$C(x,t)$	One dimensional concentration	kg/m
D	Molecular diffusion coefficient	m^2/t
E_{ads}	Adsorption energy	eV
σ	Standard deviation	
γ	Diffusion index	
n_{s}	Number of electrons	
N	Number of adsorbed species	
s	Total amount of substance	kg
$\mathbf{c}_{\text{h}}$	Chiral vector	m
$\mathbf{a}$	Graphene lattice unit vector	m
a	Graphene lattice constant	Å
d	Diameter of nanotube	Å
E_{2D}	2D energy dispersion relation for π-bands in a graphene sheet	eV
E_{ii}^{S}, E_{ii}^{M}	Energy separation between vHs of semiconducting/metallic SWNT	eV
k_{B}	Boltzmann constant	m^2 kg s^{-2} K^{-1}
E_{F}	Fermi level energy	eV
$g(E_{\text{F}})$	Density of states at the Fermi level	
n_{h}	Number of available states for hopping	
r	Distance from localised state	

g_{m}	Transconductance	S

Chapter 1

Introduction and Background

1.1 Motivation and Objective

Carbon nanotubes possess many properties which are desirable characteristics of a sensing medium; these include small size, high strength, high electrical and thermal conductivity and high specific surface area.

The sensing response of carbon nanotubes has been demonstrated independently in the literature in a resistive, capacitative and field-effect-transistor geometry. The possibility exists for a sensor to combine all three sensing geometries in one device.

Metal-oxide-semiconductor (MOS) capacitors are an important sensor technology. The advantages of the MOS structure include high sensitivity and selectivity, fast response time, low cost and integrated small size. The most important advantage of MOS sensors is that they can be fabricated using modified micro-electronic technology. Sensitivity to gaseous species is determined by chemical reaction of the analyte at the catalytic metallic surface. Diffusion of the reaction product through the metal catalyst provides the sensing signal. The range of species to which the MOS sensor is sensitive depends on the catalytic action of the metal gate electrode. Currently the most common MOS sensor uses a Pd gate to catalytically decompose hydrogen allowing diffusion through the metal gate. The limited range of sensitivity is the greatest disadvantage of MOS sensors.

The objective of this thesis is to explore the suitability of single-walled nanotube networks as a gate material in a metal-oxide-semiconductor based sensor and to evaluate whether such a device geometry is suitable for operation as a MOS capacitor, field-effect transistor and resistive based sensor simultaneously. The dependence of the device

properties on nanotube network thickness will be determined. The role of Fermi level pinning in top-contacted and bottom-contacted device geometries will be evaluated. To our knowledge this area has not been explored before. In order for the implications of the investigation to be as far reaching as possible an archetypal system consisting of a network of single-walled carbon nanotubes interacting with oxygen will be considered. Single-walled carbon nanotubes provide one-wall over which the adsorption event and electrical conductance occurs. Oxygen is employed as an archetypal analyte due to the existing body of work which considers the interaction of oxygen with carbon nanotubes and the necessity of considering oxygen adsorption on the operation of sensors operating in ambient conditions.

1.2 Summary

In the remainder of Chapter 1 the essential background of the thesis is covered. An overview of the physical properties of carbon nanotubes is given in Section 1.3. Section 1.4 considers the dispersal and electronic transport of carbon nanotubes, nanotube / metal contact, nanotube networks and nanotube based field-effect transistors. In Section 1.5 the sensitivity of carbon nanotubes is discussed and a review of previous work concerning nanotube sensors is given with specific focus on nanotube gas sensors. It is demonstrated that nanotubes have been used to detect a variety of analytes with some ambiguity as to the origin of the observed signal. The basic principles of adsorption on surfaces are considered in Section 1.6. The physical principles of traditional MOS capacitors are discussed in Section 1.7. The predominant established micro-sensing techniques are critically described in Section 1.8.

In Chapter 2 the experimental techniques required for the measurements presented in thesis are given, the nanotube material is characterised and the quality and physical properties discussed. Explanation is given of preparation and fabrication of the devices and the methodology for performing the measurements is detailed.

The transport characteristics of thin and thick nanotube networks are presented in Chapter 3. The temperature dependence of conductance is found to differ in functional form between the thin and thick nanotube networks. Thin networks display semiconducting transport characteristics whilst thicker networks display a metallic component in the transport behaviour. UV-desorbed networks exhibit an increased connectivity upon oxygen exposure whilst the transport characteristics remain

determined by the probability of charge carrier hopping between localised states.

The conductance response of thin and thick nanotube networks to oxygen adsorption is investigated in Chapter 4. Laboratory-air exposed nanotube networks exhibit a decrease in conductance when exposed to oxygen. Vacuum pressure fails to recover the original conductance. Strong absorption of UV-radiation by delocalised π-electrons provides an efficient way to desorb surface impurities in vacuum. Desorbed networks exhibit an increased conductance on exposure to oxygen due to p-doping of the carbon nanotubes. The kinetics of oxygen adsorption are investigated and oxygen diffusion through the nanotube network considered. The role of contaminants on the sensing response of the SWNT network in the laboratory-air-exposed state is discussed.

In Chapter 5 carbon nanotubes are employed as the gate layer in a nanotube-metal-oxide-silicon capacitor. The conductance and capacitance of both thin and thick nanotube networks display an increase upon oxygen exposure from a UV-desorbed state. The flat-band voltage of the nanotube-metal-oxide-silicon capacitor is dependent on the difference in work-function between the silicon and nanotube. When thick nanotube networks were used as the gate material of the capacitor a positive shift of flat-band voltage occurred. Nanotube-metal-oxide capacitors with a thin nanotube network gate displayed an additional flat-band voltage, due to a large degree of adsorption occurring at the silicon / nanotube interface. The difference in flat-band voltage between oxygen adsorbed nanotube and UV-desorbed nanotube is large. The possible reasons for the observed results are discussed and future experiments are described.

Chapter 6 summarises the results and conclusions presented in this thesis and the future direction for the work is described.

1.3 Carbon nanotube properties

1.3.1 Historical overview

Carbon nanotubes are unique one dimensional π-conjugated nanoscale materials. Since discovery, carbon nanotube based research has been intense partly due to the theoretical interest in 1D-materials and also through the extraordinary mechanical, structural and electronic properties of nanotubes themselves, Table 1.1.

Carbon nanotubes (CNT) are ideally suited to the electrical sensing of gases and

biological species due to their large surface area, excellent electrical transport and current carrying properties and facile charge transfer characteristics. In addition, carbon nanotubes perform well as ionisation based gas sensors due to the large field concentration induced by the high aspect ratio.

The carbon atom has six electrons which occupy $1s^2$, $2s^2$ and $2p^2$ atomic orbitals. The core $1s^2$ electrons are strongly bound whilst the remaining four valence electrons are weakly bound and able to quantum mechanically 'mix' through orbital hybridisation. The type of hybridisation determines the defining properties of carbon allotropes, Table 1.2. Until 1985 the only known crystalline forms of carbon were graphite and diamond. Diamond is characterised by four sp^3 hybridised orbitals leading to a tetrahedral structure. Graphite is characterised by three sp^2 hybridised orbitals which leads to a planar trigonal structure. The fourth valence electron of carbon atoms in graphite form a p_z orbital which contribute to a delocalised π electronic system.

A new crystalline form of carbon was discovered in 1985 by Kroto *et al.* [6]; this allotrope, which has stability due to its football-like structure, is termed a fullerene of which C_{60} (or Buckminsterfullerene) is the most widely known example. However, it was not until 1990 that large quantities of purified fullerenes were available due to advances in chemical separation and production via the arc discharge technique [7]. Fullerenes were found in the soot generated from an electrical arc between two carbon electrodes in an inert atmosphere of helium. In this process one of the electrodes is consumed whilst a deposit may be formed on the other electrode. One year later Iijima observed carbon nanotubes [8] (1991) whilst analysing such an electrode deposit from an arc chamber by transmission electron microscopy (TEM), Figure 1.1.

Property	**Comparison**
Carrier mobility: 79000 cm^2/Vs (at RT) [1]	> Hole mobility in Si
Maximum electrical current density: $> 10^9$ A/cm^2 [2]	100 times greater than copper wires
Thermal conductivity: 6600 W m^{-1} $K^{-}1$ [3]	> Diamond
Tensile strength: 150 GPa [4]	100 times the strength of steel
Youngs modulus: $\sim$ 1 TPa [5]	> Diamond

Table 1.1 Remarkable properties of carbon nanotubes.

Dimension	**0-D**	**1-D**	**2-D**	**3-D**
Allotrope	C_{60}	Carbon nanotube	Graphite	Diamond
Hybridisation	sp^2	sp^2	sp^2 (sp)	sp^3
Density (g/cm^3)	1.72	1.2 2.0	2.26	3.515
Bond length (Å)	1.4	1.44	1.42	1.54
Electronic	Semiconductor	Metal or	Semi-metal	Insulator
properties	E_g =1.9 eV	semiconductor		E_g =5.47 eV

Table 1.2 Characteristic properties of carbon allotropes [9].

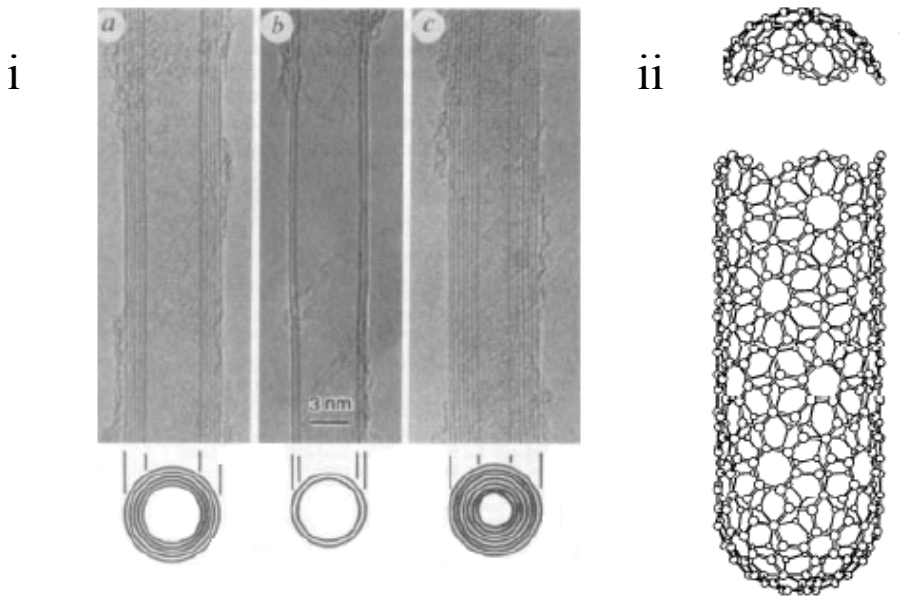

Figure 1.1 i)TEM images of MWNT as discovered by Iijima. The cross section of each tube is illustrated. Adapted from [8] ii) Chiral fibre with hemispherical caps, adapted from [10].

Rather than being cylindrical graphitic tubes, which were previously known, these tubes were perfectly graphitised with closed caps containing pentagonal rings, like the fullerenes, and importantly, helicoidal with differing degrees of helicity [8]. Quantised values of circumferential electron wavevector determine the electronic properties of such tubes, and as shall be shown, result in both semiconducting and metallic behaviour, depending geometrical considerations. The diameter of the nanotubes were similar to that of fullerenes but with micrometer lengths. The carbon nanotubes discovered by Iijima consisted of many walls, termed multiwalled carbon nanotubes (MWNT)[1].

[1]The first known application of MWNTs occurred not post 1991 but some 400 years prior, MWNTs have been discovered in the blades of Damascus swords [11].

The observation of distinct helicities or chiralities, dependent on how the atoms are arranged around the tube, led to theoretical predictions about the electronic properties of such tubes with respect to specific chiralities [10] which shall be discussed in detail in Section 1.3.3. In 1993, Iijima was successful in isolating single-walled carbon nanotubes (SWNT) [12] with the eventual isolation of large numbers being achieved by Thess in 1996 [13] using laser vaporisation techniques. This resulted in the commercial availability of carbon nanotubes and an increase in both commercial and academic research interests.

Near perfect electron transmission of carbon nanotubes has been demonstrated with electron interference effects [14]. Field effect transistors based on individual SWNT exhibit properties greater than any known semiconductor [1]. The study of the interaction of carbon nanotubes with gaseous species began in 2000 with the publication of work highlighting the sensitivity of the resistance and thermoelectric power of SWNTs to gaseous species [15, 16]. Since then work has focused on exploiting the high surface-to-volume ratio and fast electron-transfer kinetics of CNT through a variety of sensing geometries.

The lack of controllable synthesis for specific band-gap or band-gap range of carbon nanotubes provides single nanotube devices with a range of transport properties. Recent interest has turned to aligned arrays of nanotubes [17] and random networks [18] as means to obtain controllable device performance.

1.3.2 Structure

A carbon nanotube can be thought of as a rolled up layer of graphene. The carbon atoms will therefore be arranged in a hexagonal structure and the lattice may be described by two lattice vectors

$$\mathbf{a}_1 = (\frac{\sqrt{3}}{2}a, \frac{a}{2}) \ , \ \mathbf{a}_2 = (\frac{\sqrt{3}}{2}a, -\frac{a}{2}). \tag{1.1}$$

where $a = |\mathbf{a}_1| = |\mathbf{a}_2| = 1.42 \times \sqrt{3} = 2.46$ Å is the lattice constant of the graphene sheet as a result of the C-C bond length of 1.42 Å in graphene. These vectors span a 2D Bravais lattice, with a basis of two atoms the lattice of graphene is obtained, as shown in Figure 1.2.

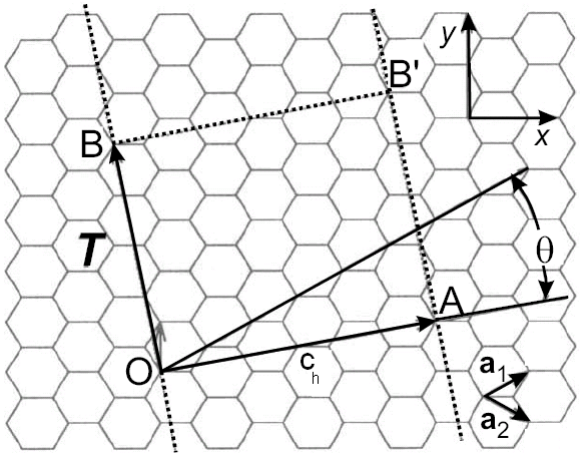

Figure 1.2 Unrolled hexagonal network of nanotube. If site O is connected to A and B connected B' a tube of chiral vector $\mathbf{c}_\mathrm{h}$ = (4,2) is constructed. θ describes the chiral angle of the tube whilst the translational vector $\mathbf{T}$ is perpendicular to to the tube axis. Reproduced from [9].

There is an infinite number of nanotube geometries, however they can all be described with reference to the chiral vector $\mathbf{c}_\mathrm{h} = n\mathbf{a}_1 + m\mathbf{a}_2$ therefore we can denote a given tube by the indices (n, m). The chiral vector is also the circumference of the nanotube, and the translation vector, $\mathbf{T}$, is parallel to the tube axis. The rectangle formed by these two vectors defines the unit cell of the nanotube. Alternatively nanotubes may be characterised by the diameter, d, and the angle, θ, between $\mathbf{c}_\mathrm{h}$ and $\mathbf{a}_1$. Most nanotubes have axial chiral symmetry however there are two special symmetry directions which have non-chiral symmetry. These tubes are termed 'zig-zag' with indices $(n, 0)$ and thus a chiral vector angle of $\theta = 0°$ and 'armchair' with indices (n, n) and chiral vector angle of $\theta = 30°$ all other chiralities of nanotube are described by θ in between that of the armchair and zig-zag nanotube. Figure 1.3 gives a schematic diagram for a metallic 'armchair' nanotube and a semiconducting 'zig-zag' carbon nanotube. The geometrical structure of a single-walled nanotube can now be readily defined leading to a unique way of identifying tube types for SWNT. However for MWNT each layer will have its own particular chirality defined by (n, m).

1.3.3 Electronic properties

As stated previously, a nanotube can be considered to be a rolled sheet of graphene with closed caps. It is therefore pertinent to begin the treatment of the electronic band structure of carbon nanotubes by modifying the band structure of graphene by adding

in discrete values for the circumferential wavevector, which will appear mathematically as periodic boundary conditions. The band structure of graphene was calculated by Wallace [19] in 1947 by using a tight binding approximation, considering the π and π^*-bands only. In graphene the valence orbital is a $2p_z$ or π-orbital, due to reasons of symmetry this π-orbital cannot interact with the σ orbital (composed of 2s and $2p_{x,y}$) and therefore simplifies the dispersion relation. The two-dimensional energy dispersion relation for the π-bands only in a graphene sheet may be expressed as [20]

$$E_{2D}(k_x, k_y) = \pm\gamma_0 \left[1 + 4\cos\left(\frac{\sqrt{3}k_x a}{2}\right)\cos\left(\frac{k_y a}{2}\right) + 4\cos^2\left(\frac{k_y a}{2}\right)\right]^{1/2} \tag{1.2}$$

where γ_0 is the nearest-neighbour transfer integral.

The conduction and valence bands are degenerate at six points, known as **K** points. Saito *et al.* introduced periodic boundary conditions for the nanotubes in a circumferential direction [20] as the electrons are only free to move in the axial direction. This leads to energy quantisation of $\mathbf{k}\cdot\mathbf{c}_h = 2\pi q$ $(q = 0, 1, 2...)$ and thus discrete values of allowed wavevector, visualised as a series of parallel equidistant lines in reciprocal space, Figure 1.3. The number of these one dimensional modes can be shown [20] to correspond to the number of hexagons in the 1D unit cell mapped out by vectors $\mathbf{c}_h$ and **T**. The number of circumferential k modes corresponds to a 1D conduction channel along the nanotube axis. From this formalism it is easy to see that as we increase the diameter of the nanotube, and therefore increase the size of the 1D unit cell the number of 1D modes or sub-bands will increase.

The quantisation of allowed **k** vector, determined by the chiral vector, determines whether a carbon nanotube is metallic or semiconducting. If the lines of allowed **k** pass through one of the gapless **K** points then the tube will be metallic. If none of the allowed lines of **k** or subbands pass through the zero gap Fermi point (**K** point) then the tube will be semiconducting, Figure 1.3.

The 1D nature of carbon nanotubes has implications for the electronic density of states (DOS). Figure 1.4 gives the energy dependence of the electronic DOS for a metallic and semiconducting nanotube, as calculated by Saito *et al.* [20]. Note the van Hove singularities (vHs) in Figure 1.4, these singularities occur at the band edges. The DOS for a 1D material varies as $\frac{dE}{dk}^{-1}$, at band edges $\frac{dE}{dk} = 0$ and a singularity is encountered. The occurrence of vHs in SWNT was confirmed experimentally by Wildöer [23] through locally probing the DOS through scanning tunnelling spectroscopy (STS). From these

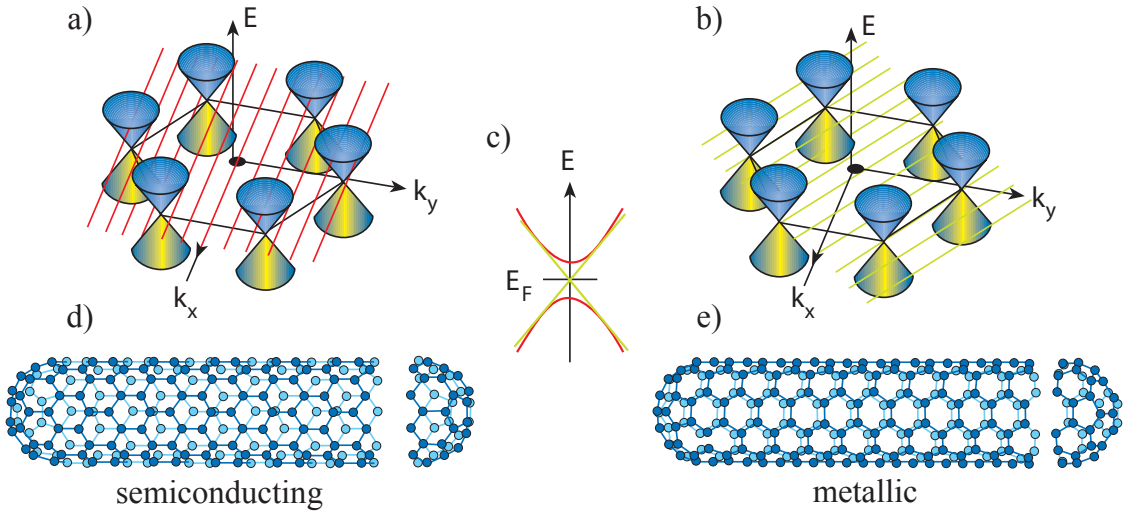

Figure 1.3 Nanotube band structure. a) Schematic diagram showing semiconducting nanotube band structure. b) Schematic diagram of metallic nanotube band structure. Allowed electron states are determined by the intersection of allowed wave vector (red / green lines) and graphene band structure. c) Schematic diagram showing metallic and semiconducting dispersion relation, first (sub)bands shown. d) Schematic diagram showing semiconducting 'zig-zag' nanotube structure. e) Schematic diagram showing metallic 'armchair' nanotube structure. Adapted from [21].

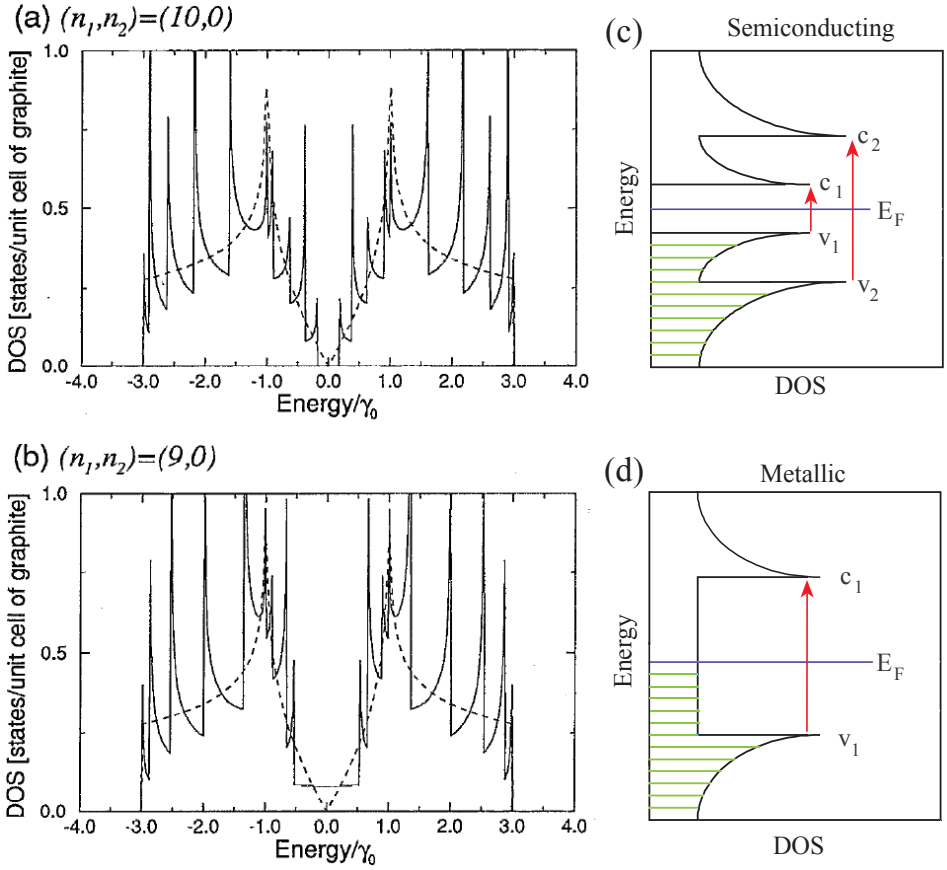

Figure 1.4 a) & b) Electronic density of states for two 'zig-zag' carbon nanotubes [20]. $(n_1, n_2) = (10, 0)$ displays a zero density of states at the Fermi level and is therefore semiconducting. $(n_1, n_2) = (9, 0)$ displays a non-zero density of states at the Fermi level and is therefore metallic. c) & d) Interband vHs transitions of metallic, E_{ii}^{M}, and semiconducting, E_{ii}^{S}, carbon nanotubes. Distinct features in Raman spectra for specific values of (n, m) couple to these transitions when the laser excitation energy is in resonance with the interband transition, adapted from [22].

experiments it was possible to discern the band gap due to the first pair of vHs for semiconducting, E_{11}^{S} and metallic, E_{11}^{M}, carbon nanotubes. The band structure of CNTs is also addressable optically. Resonant Raman spectroscopy on individual CNTs [24] gives the resonant vHs transition energy and specific (n, m) indices maybe assigned. In addition, spectrofluorimetric measurements on SWNTs have been mapped to specific chiralities [25], facilitating the bulk determination of the composition of SWNT samples through simple spectrofluorimetric means.

1.4 Nanotube devices

1.4.1 Dispersion of nanotubes

A dispersion of carbon nanotubes in a solvent forms a colloidal system[2]. Organic solvents form a thermodynamically unstable colloid with nanotubes, the length of stability depending on organic solvent used. Aggregation of colloidal particles eventually forms due to van der Waals attraction between carbon nanotubes overcoming forces from the solvent.

Surface active agents such as surfactant, polymers or other colloidal particles can modify the interface of particle-suspending medium increasing the metastability of the colloidal suspension. Amphiphilic molecules such as sodium dodecyl sulfate (SDS), Figure 1.5, facilitate extremely stable (years) aqueous solutions of SWNTs [26]. Bundles of nanotubes are broken up through the dual action of micellar formation and 'thinning' of nanotube bundles through the impartation of mechanical energy through ultrasonication. Once a micelle forms around a SWNT the tube is in a pure hydrocarbon environment. Colloidal stability results form electrostatic and/or steric repulsion. The presence of individual nanotubes deposited from a SDS/nanotube colloidal solution has been verified through TEM [27] measurements and fluorescence across the band gap of semiconducting nanotubes [28].

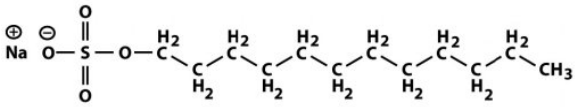

Figure 1.5 A molecule of anionic surfactant sodium dodecyl sulfate (SDS), $C_{12}H_{25}SO_4Na$, 12-carbon hydrophobic tail and a polar sulfate group.

[2]A dispersed phase evenly distributed through a dispersion medium.

However, experiments have confirmed that SDS perturbs the electronic properties of carbon nanotubes resulting in interfacial effects such as an increase in resistance and degradation of transistor properties such as on-current [29] as well as doping like effects manifest in asymmetry of $G(V)$ traces [30]. Interestingly, side-wall protonation of carbon nanotubes controlled through acidity of solution was detectable through the destruction of photoluminescence spectral peaks of nanotubes. These peaks originating from semiconductor transitions in the nanotubes could be restored by increasing the pH to neutrality or through UV-radiation [28].

Complete removal of SDS from SWNT [29] can be achieved with immersion in deionised water (DIW) for 30 minutes, confirmed through removal of sulphur $1s$ peaks in XPS spectra. In addition, the removal of SDS through DIW immersion increased the conductance, on-current and stability of SWNT-FET devices [29]. Photoemission studies suggest that the use of Na-containing surfactant introduces residual Na which is only removed after high temperature ($\sim$ 1300 K) annealing in vacuum [31].

1.4.2 Transport

Carbon nanotubes are ballistic conductors at room temperature [30]. An electronic mean free path of the order of tens of microns provides a CNT conductance which is independent of length, over lengths less than the mean free path. As discussed in Section 1.3.3 a nanotube has circumferentially quantised wavevector giving a 1D-electronic character. The conductance of a 1D-channel is given by the Landauer formula:

$$G = \left(\frac{2q^2}{h}\right) MT \tag{1.3}$$

where q is the charge of charge carriers, M is the number of modes and T the average transmission probability per mode [32]. There are two conduction modes in carbon nanotubes giving a maximum conductance for a single CNT of $4q^2/h$. Conductance near the maximum theoretical value have been recorded for both semiconducting [33] and metallic [34] CNT.

1.4.3 Nanotube networks

A thin film of SWNT created from a single production source will consist of metallic and semiconducting nanotubes of different diameter with a heterogenous mix of band-gaps. Fuhrer *et al.* [35] have shown that the intersection of two s-SWNTs or m-SWNTs form

a good electrical contact with conductance ~ 0.1 e^2/h whereas the intersection of a metallic and a s-SWNT forms a Schottky barrier with a barrier height approximately equal to 1/2 the band gap of the SWNT. A highly interconnected thin film is expected to be electrically continuous with properties that depend on the interconnections and the inherent properties of CNTs. The presence of impurities in the network may effect both the nanotube interconnections and the properties of individual tubes themselves. Doping of the nanotubes within the network can significantly alter the conductance of the network [36–39] through a modulation of the charge carrier density and/or nanotube interconnection barrier. The conductivity of carbon nanotube networks has been shown by Hecht *et al.* [40] to have a power law dependence on CNT length and an inverse power law dependence on the CNT diameter, thus highlighting the critical role of carbon nanotube interconnections.

The conductivity of CNT networks is dependent on the concentration of conducting channels within the system. Percolation theory describes the variation of conductivity with the concentration of equivalent conducting channels (p) [41] as

$$\sigma \propto (p - p_{\mathrm{c}})^{\eta} \tag{1.4}$$

where p_{c} is the percolation threshold and η is the critical exponent which depends only on the dimensionality of the network. Theoretical calculations provide the critical exponent for 2D and 3D systems as 1.3 and 1.94 respectively [41]. A system where equivalent conductors form a network with a thickness less than the average conductor length would be expected to show 2D behaviour, whilst a system where the thickness is greater than the average length would be expected to show 3D behaviour. Experimental determination of the critical exponent for thin ($10 - 100$ nm) nanotube systems where the thickness is less than the average CNT length provides critical exponents both below [42] and above [43] the theoretical 2D value, whilst thicker CNT systems provide critical exponents below the 3D theoretical value [44, 45]. The variation between the experimental and theoretical value of η for carbon nanotube systems should not be interpreted as a reduction/increase in the dimensionality of the network but is more likely to be a result of the heterogeneity of electronic structure and bundle/nanotube size within a nanotube sample and the resulting effect on the formation of percolating metallic current paths. Bekyarova *et al.* [42] experimentally determined the critical thickness for percolation to be $t_{\mathrm{c}} = 3$ nm, close to the average diameter of a nanotube bundle, indicating that a single bundle/nanotube deposition layer is enough to provide

a percolating network.

The thickness of CNT networks has been shown to determine the transport characteristics, thicker films approaching more metallic type conduction through a weaker temperature dependence and non-zero conductance in the zero-temperature limit [46,47]. This behaviour is likely caused by the increasing fraction of low resistance intertube junctions and metallic current pathways as the thickness is increased. A model in which metallic regions interrupted by thin barriers through which charge carriers must tunnel has been successful in describing the conducting behaviour of nanotube networks [46,48,49]

$$\rho = \frac{R_{\mathrm{b}} + R_{\mathrm{m}}}{a} \tag{1.5}$$

where R_{b} is the mean resistance arising from tunnelling through barriers, R_{m} is the mean resistance arising from metallic conduction and a is the mean number of metallic SWNTs per unit cross sectional area. The thermally assisted conduction process is derived from Sheng's model of fluctuation induced tunnelling (FIT) [50] and takes the following form for thermally assisted conduction arising from thin barriers in CNT networks [46]

$$\frac{R_{\mathrm{B}}}{a} = B \exp\left(\frac{T_{\mathrm{b}}}{T + T_{\mathrm{s}}}\right) \tag{1.6}$$

where B is a temperature independent constant and $k_{\mathrm{B}}T_{\mathrm{b}}$ indicates the order of magnitude of the typical barrier energies and the magnitude of $T_{\mathrm{s}}/T_{\mathrm{b}}$ indicates the extent of quantum tunnelling resistivity. The metallic conductivity is described by [46]

$$\frac{R_{\mathrm{m}}}{a} = A \exp\left(\frac{-T_{\mathrm{m}}}{T}\right) \tag{1.7}$$

where A is a temperature independent constant and phonons of energy $k_{\mathrm{B}}T_{\mathrm{m}}$ that have wave vectors $2k_{\mathrm{F}}$ spanning the Fermi surface are required to backscatter the charge carriers [51]. The thickness of the nanotube network determines to what extent metallic nanotubes dominate the transport characteristics of the network. As film thickness increases there is a greater quantity of good quality percolating metallic paths and the contribution of the metallic component of Equation 1.5 increases, occasionally a positive $\mathrm{d}R/\mathrm{d}T$ occurring in a broad temperature region [47,52] is observed. Thin films have reported a complete absence of the metallic conduction as described in Equation 1.5 with the conduction described through the entire temperature range by tunnelling through thin barriers (~ 7 meV) between conductive islands [42]. The electrical barriers

postulated to interrupt conductive islands in Equation 1.5 could arise from intertube junctions as a result of differing electrical structure of the tubes as discussed or could possibly be due to localisation near defects or at tube junctions.

Variable range hopping in which tunnelling between localised states is assisted by absorption of phonons has been observed in a number of CNT systems [37, 46, 52–55], described by [56]

$$G = G_0 \exp\left[-\left(\frac{T_0}{T}\right)^{\gamma}\right] \tag{1.8}$$

$$T_0 = \frac{\beta}{k_{\mathrm{B}} g(E_{\mathrm{F}}) \alpha^3} \tag{1.9}$$

where $\gamma = 1/(d+1)$ with d indicating the dimensionality of hopping, α is the localisation length of electronic wavefunction, β is a numerical constant and $G_0 \sim T^{-0.35}$ [56].

In very thin CNT films where the number of percolating metallic paths is reduced the localisation of charge carriers dominates conduction. As the temperature tends towards zero so does the conductance. Localised states are found in the band gap of disordered semiconductors. Conduction occurs by hopping (phonon assisted tunnelling) between electronic localised states. As the temperature decreases the number of states within an accessible energy decreases and the mean hopping range increases. An indication of the origin of the localised states can be determined from the localisation length α and the dimensionality d.

Well connected nanotube networks would be expected to have a higher dimensionality than sparsely connected networks. Experimentally the dimensionality of nanotube networks has been increased by the removal of amorphous carbon and metallic impurities by acid treatment [38] and decreased through the reduction of nanotube filler concentration [55]. The dimensionality of nanotube networks is also dependent on the charge carrier density, Vavro *et al.* observed a reduction in the VRH dimensionality of nanotube networks with reduced p-doping [37], indicating the dependence of network transport characteristics on tube-tube coupling. The value of T_0 is dependent on the localisation length α and the density of states at the Fermi energy $g(E_{\mathrm{F}})$. The value of T_0 is inversely dependent on the cube of the localisation length α and is therefore very sensitive to changes in this length, T_0 is also inversely dependent on the density of states at the Fermi energy $g(E_{\mathrm{F}})$. It has been suggested that as the thickness of nanotube networks is reduced the overlap of electronic wavefunctions decreases and the

localisation length is reduced [46]. However, as the fraction of metal/semiconducting nanotubes is changed the density of states at the Fermi energy is also modulated. Benoit *et al.* [55] observed that by scaling $g(E_F)$ (the density of states of a thick SWNT network) with respect to the loading fraction of carbon nanotubes within a polymer matrix then equivalent localisation lengths ($\alpha \sim 8$ nm) were obtained indicating that localisation occurs not through bundle-bundle hopping (as this would be expected to scale with the loading fraction) but either through on bundle/tube localisation or localisation occurring at the bundle/tube interconnects. A similar localisation length ($\alpha = 17$ nm) was calculated by Yosida *et al.* [164] through low-field transverse magneto-resistance measurements and the origin of the localisation by consideration of the length scale is attributed to hopping between the nanotubes within bundles or between bundles themselves at the nanotube/bundle junctions. Localisation lengths as high as 700 nm have been observed by Fuhrer *et al.* [52] for 3D-VRH, which is similar to theoretical calculations which find the mean free path of a $(5, 5)$ CNT to be 1.6 μm at 250 K, whilst experimental mean free paths of 1.6 μm [57] and 0.8 μm [58] have been recorded at room temperature within single SWNT. The mean free path must be greater than the localisation length in order to maintain wavefunction coherence. Such a large localisation length and the fact that the localised states must extend across many tube crossings in order to provide 3D-VRH implies a well connected nanotube network and also that bundle junctions are not the source of localisation. Fuhrer *et al.* postulates that the wavefunction decays along the nanotube themselves and that the 3D radius of localisation can be interpreted as a 1D localisation length.

The quality of bundle/nanotube junctions in nanotube networks drastically affect the transport properties and also of great importance are the quality of nanotubes within the network. Kaiser *et al.* [59] observed an increase in the T_0 parameter through the ion irradiation of thin SWNT networks with a 3D-VRH functional form. Ion irradiation created defects in the nanotubes however the dimensionality of VRH remained the same. The increase in T_0 was attributed to a decrease in the localisation length as a result of increased disorder in the network. As stated previously T_0 is proportional to $g(E_F)^{-1}$ and $\alpha^{-1/3}$ and therefore highly sensitive to changes in the localisation length α.

Conduction in nanotube networks features functional forms which are similar to conducting polymers [60] indicting that some features of SWNT network conduction are a feature of fibrillar 1D systems. However, observation of extremely long localisation lengths [52] indicates that properties of the individual components of the system are

available to the macroscopic CNT network. Field-effect mobilities about an order of magnitude larger than that of materials typically used in thin-film transistors have been reported [18].

1.4.4 Nanotube / metal contact

Metal contacted nanotubes show excellent transport properties approaching the theoretical limit [14]. Early doped semiconducting SWNT transport experiments exhibited very low conductances, partially due to an un-optimised metal/semiconductor interface. A difference in work-function at a metal/semiconductor interface leads to an exchange of charge and a resulting dipole which produces a Schottky barrier. In traditional contacts between metals and bulk semiconductors a planar dipole sheet forms at the interface inducing long range Fermi level pinning. Charge transfer between a metal contact and end-bonded CNT forms a dipole ring. This has profound effects on the resultant band-bending at the interface [61]. The electrostatic potential can be considered constant far from a dipole sheet, far from a dipole ring the potential decays as the third power of distance. Any potential shift at the metal-carbon nanotube interface will decay rapidly, therefore the Schottky barrier is only a few nanometres wide and carriers may efficiently tunnel through the barrier in addition to being thermionically emitted, Figure 1.6. The tunnel barrier may be thinned electrostatically, increasing the tunnel current. Scanning gate microscopy has confirmed the increased field dependence at certain metal/semiconducting SWNT (s-SWNT) interfaces [62].

As a consequence of the reduced spatial extent of induced band bending the metal workfunction plays a crucial role in charge carrier injection into CNT. Low work-function metals frequently make non-Ohmic contacts with p-type nanotubes leading to CNT-FETs whose operation is dominated by gate induced modulation of the Schottky barrier [63, 64]. High work function metals, such as Pd, frequently make Ohmic contacts to CNT [65], with conductances close to the ballistic transport limit of $4q^2/h$ [33]. Scanning probe techniques have been employed to directly measure the contact resistance of a Cr/Au contacted s-SWNT [65] showing that Schottky barriers are not formed at the contacts and that the transmissivity approaches theoretical limits.

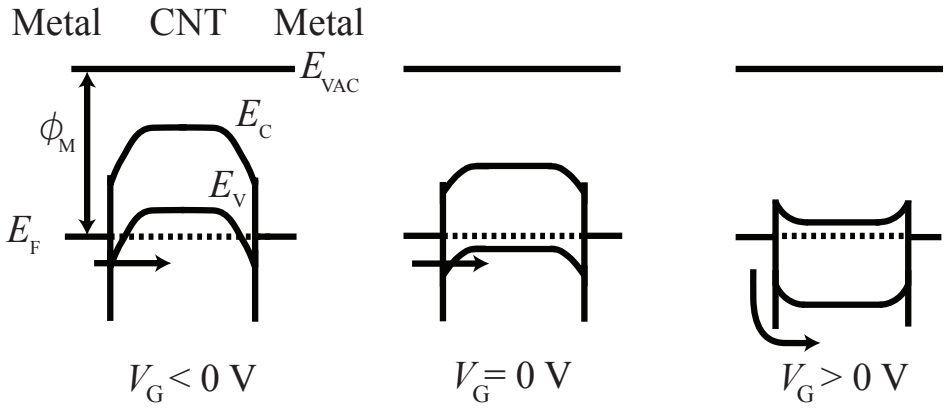

Figure 1.6 Schematic band diagrams showing hole injection from a metal into the valence band of a *p*-doped SWNT at various gate voltages. Negative gate voltages induce upward band bending, shifting the Fermi level into the valence band. The Schottky barrier at the metal/nanotube interface is thinned increasing the tunnelling probability. Positive gate voltages induce a downward bending of the valence band and an effectively higher barrier must be overcome by the holes injected from the left metal contact.

1.4.5 Field Effect Transistors

The first CNT-FETs were fabricated in 1998 [66, 67]. The exceptional electronic properties of CNT such as ballisticity [33] and high mobilities [1] combined with the excellent coupling to the gate electrode as a result of the dimensions of the nanotube make CNTs a very attractive electronic material.

The conductance of a CNT-FET depends on the Fermi level energy in the bulk and the Fermi level energy at the contacts, Figure 1.6. As mentioned previously, the position of the Fermi level at the contacts is determined by charge transfer at the interface causing Fermi level pinning and a resulting Schottky barrier. The position of the Fermi level in the bulk of the CNT is determined by the gate voltage, V_G. Positive gate voltages electrostatically decrease the energy of conduction band states reducing the barrier for electron transport. Negative gate voltages increase the energy of valence band states reducing the barrier for hole transport. The efficiency of this process is determined by the capacitance between the nanotube and gate. This capacitance has two contributions, C_E, the electrostatic capacitance which is determined by the geometry between nanotube and gate and the properties of the insulating dielectric, and a quantum capacitance C_Q which depends on the density of states in the channel [32]. Conventional Schottky barrier transistors have a temperature dependance due to thermionic emission over the barrier. This property is manifest in the inverse sub-threshold slope [68]

$$S = \left(\frac{\mathrm{d} \log I}{\mathrm{d}V_{\mathrm{G}}} \right)^{-1} \tag{1.10}$$

The temperature dependence of S in a conventional MOSFET is $S \sim k_{\mathrm{B}}T/q$, approximately 60 meV/dec at room temperature. In a CNT Schottky barrier FET, S was found to be independent of temperature [63, 64] due to tunnelling through the Schottky barrier. As discussed previously the height of the Schottky barrier is controllable by the metal work-function. However, Schottky barriers can be thin enough to allow ambipolar CNT-FET operation [69,70]. The width of the Schottky barrier may be thinned electrostatically. Double-gated CNT have been demonstrated [71] in which gates near the contact selectively thinned the Schottky barrier whilst an independent gate modulated the bulk. In this configuration values of S approaching 60 meV have been reported [71].

Another measure of CNT-FET performance is the transconductance

$$g_{\mathrm{m}} = \frac{\mathrm{d}I}{\mathrm{d}V_{\mathrm{G}}} \tag{1.11}$$

$$g_{\mathrm{m}} = \mu \left(\frac{C_{\mathrm{G}}}{L_{\mathrm{G}}} \right) \left(\frac{V_{\mathrm{DS}}}{L_{\mathrm{G}}} \right) \tag{1.12}$$

where μ is the carrier mobility, C_{G} is the gate capacitance and L_{G} is the gate length and V_{DS} is the source drain voltage. The highest reported transconductance in a back gated nanotube transistor is ~ 30 μA/V, achieved through the use of a a high-k dielectric material [72].

Until CNT synthesis methods are of sufficient sophistication to grow specific chiralities of nanotube, eliminating the heterogenous spread of SWNT band-gap, a promising route for reproducible electronics are aligned arrays [17] and random networks of CNT [18]. The metallic nanotube content within the network critically determines the transistor performance [73]. Various techniques to decrease the metallic fraction, such as growth methods which preferentially produce semiconducting nanotubes [74], elimination of metallic tubes thermally [75] and chemically [76] hold promise to improve CNT network FET performance. In 2007 Bae *et al.* reported SWNT network FET devices with a current on/off ratio of $\sim 10^4$ [77] achieved with novel growth techniques [74].

1.5 Nanotube sensors and their sensitivity

A carbon nanotube FET may exhibit an electrical response to a species through the following mechanisms:

1. change in metal work-function at metal/CNT interface
2. capacitative gating of nanotube
3. charge transfer between nanotube and analyte

The response of a semiconducting SWNT-FET to gaseous species was first reported by Kong *et al.* in 2000 [16]. It was found that exposure of a SWNT-FET to NO_2 increased the threshold voltage whilst exposure to NH_3 decreased the threshold voltage. The SWNT-FET in its un-adsorbed state behaved as a *p*-doped semiconductor, the un-adsorbed threshold voltage could be returned after exposure to a flow of argon for 12 hours. The origin of the chemical gating effect for each molecule was investigated through first-principles calculations, NO_2 was found to have a binding affinity with SWNT with an associated charge transfer. Calculations found no binding affinity for NH_3, the chemical gating effect was attributed to interactions with SiO_2 or adsorbed O_2 on the SWNT surface. In later work Kong passivated part of a SWNT [78], demonstrating the ability to create a rectifying *p*-*n* junction through partial doping. The question of where the dominant sensing response occurs has been investigated with passivated contacts [79, 80]. A chemical gating effect induced by oxidising or reducing molecules perturbed the SWNT band structure, inducing changes in conductance, whilst any effect from the contacts was eliminated. In addition Liu *et al.* [80] showed that bulk passivated devices exhibited a local change in the band structure at the contacts which increased or decreased the inverse sub-threshold slope, S, depending on whether contact transparency was decreased or increased respectively.

The inherent *p*-type effects displayed by devices in ambient conditions have been attributed to oxygen doping [15,69]. Differentiation between the observed *p*-type doping induced by oxygen exposure of SWNT-FET devices constructed from a single nanotube and potassium *n*-type doping [81] has been addressed by Heinze *et al.* [70]. Heinze found that oxygen adsorption at the metal/CNT interface increases the work function and reduced the Schottky barrier for hole transmission, the transparency of the contacts is improved for hole conduction, therefore no shift in threshold voltage. Charge transfer

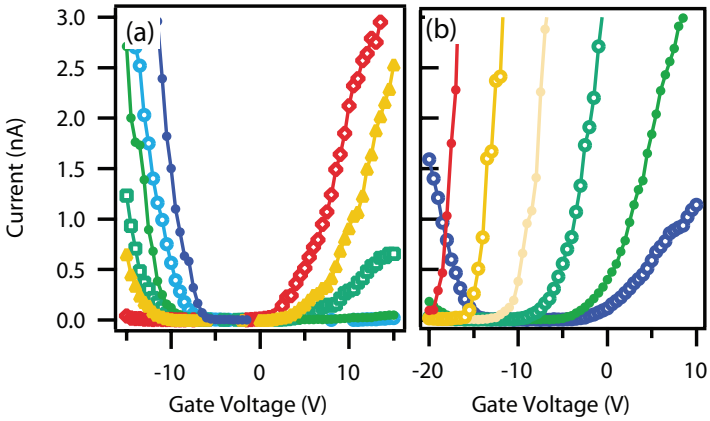

Figure 1.7 The experimentally measured effect of a) oxygen adsorption from an annealed state (red line) with increasing pressures of oxygen (orange, light green, dark green and light blue) and ambient conditions (blue); b) potassium doping on SWNT-FETs, curves right to left correspond to increasing deposited amounts of potassium [70].

between nanotube and analyte, such as in the case of potassium doping lead to a shift in the threshold voltage, V_{TH}. Using the above qualitative theorems to construct quantitative models Heinze *et al.* theoretically reproduced the transfer characteristics, given experimentally in Figure 1.7.

However, there is significant debate as to the precise influence of oxygen on the electronic properties of CNTs. In addition to the work reported above in which oxygen is found to modify the Schottky barrier, numerous works reporting *p*-type doping of the SWNT bulk by oxygen adsorption are found [15, 82, 83]. Kang *et al.* reports *p*-doping and associated threshold voltage shifts upon oxygen molecule adsorption on a long SWNT [83], providing evidence for doping within the frame-work described by Heinze. There is also strong theoretical evidence for charge transfer induced by O_2 physisorption on SWNT [83–86], with a charge of $0.1e$ transferred from the nanotube to the O_2 molecule suggested [84, 86]. Networks and bundles of SWNT have shown reversible doping effects of oxygen atmospheres through thermoelectric power (TEP) measurements [15, 82], however the TEP has also found to be enhanced by Schottky barriers [87] by providing an electron-hole asymmetry.

Oxygen physisorbs onto the basal planes of graphite and then migrates to defect sites where it is possible for O_2 to dissociate and chemisorb without any energy barrier [88]. Defects on CNT consist of topological defects, defects caused through rehybridisation and defects caused by incomplete bonding. The presence of defects increase CNT

resistivity [89] whilst providing tangled and non-uniform morphologies. Nanotube defects also provide sensitivity to some species, for example pristine SWNT display no sensitivity to ammonia whilst HNO_3-treated nanotubes with a high defect density are sensitive to ammonia [90]. Defects on SWNT have been shown to provide a route for chemisorption of oxygen [91–93]. Whilst Chan *et al.* suggests that singlet O_2 may be chemisorbed at room temperature on a pristine SWNT [92]. The electronic effect of chemisorbed oxygen is debated. Valentini *et al.* proposes that chemisorption of oxygen changes the conductivity of MWNTs from *p*-type to *n*-type through electron donation by the oxygen molecule [93]. Theoretical studies by Grujicic *et al.* indicate that oxygen chemisorption occurs at defect sites with the result that the electrical effect of the defect is practically annulled [91]. Nanotube defects with chemisorbed oxygen increase the SWNT workfunction, the C-O bond produces a surface dipole with a significant transfer of electron density from the carbon to the oxygen [94] which suggests a *p*-type doping mechanism [95].

The presence of residual impurities could also play a role in nanotube sensitivity [31, 96]. The presence of residual metal catalyst in SWNT networks could affect the CNT sensitivity, the activation energy for oxidation is reduced by the presence of residual metal catalyst [96]. Photoemission studies performed by Goldoni *et al.* [31] on SWNT networks confirmed the presence of residual Na, present as a result of dispersion in surfactant. The photoemission spectra of the Na containing network confirmed an electronic response to oxygen - the O1s core level spectra was detected. Upon temperature annealing at 1270 K for 2 hours Na was removed and any response to oxygen (pressure 10^{-6} mbar) was eliminated. Goldoni attributed the response to oxygen of the Na containing SWNT network to charge transfer between a Na-O complex and the nanotube [31]. The temperature at which the Goldoni samples are annealed is close to the graphitisation temperature of graphite (2070 K [97]) whilst MWNT of diameter 10 nm have been reported to sublime at 2500 K [98], the increased strain present in SWNT is likely to reduce this temperature. Therefore it is possible that the high temperature annealing performed by Goldoni *et al.* removes Na and graphitises the SWNT. The removal of defects from CNT samples through high temperature annealing at ~ 1500 K has been reported by reference to HR-TEM images [99] and Raman spectra [100], current induced graphitisation of nanotubes has also been reported [101]. Goldoni presents clear evidence for the effect of residual Na on the electronic properties of the nanotubes but there is no discussion of the defect density present within the sample [31]. Indeed

theoretical calculations predict no charge transfer for physisorbed oxygen on pristine SWNT [102]. Ulbricht [103] finds experimentally that O_2 weakly physisorbs on SWNT. In addition experimental data presented by Robinson *et al.* indicates that the degree of oxidation of the SWNT determine the response to analytes, oxidation occurring on $\sim 2\%$ of the SWNT provides $\sim 1000\%$ increase in the amount of charge transfer [104]. Similar studies by Valentini [105] indicate that the response of SWNT resistive sensors to NO_2 is mediated by the presence of defects - defective tubes providing a greater ΔG. The reported p-type behaviour of SWNT is possibly a result of deeply adsorbed minority oxygen species occurring at defect sites.

A consideration of device operation in the ambient atmosphere must also include the effect of water vapour. Water is physisorbed on CNT [106] and can form a complete hydrogen bonded monolayer [107]. Watts *et al.* observed an increase in resistance of a p-doped nanotube network upon exposure to humid air [95]. The magnitude of resistance increase was dependent on the number of chemisorbed oxygen species on the CNT surface as a result of a reduced effective electronegativity of the bonded oxygen due to hydrogen bonds [95]. Theoretical calculations demonstrate that water is a weak n-type dopant on SWNT [106, 107], Pati *et al.* predict $0.03e^-$ transferred from single H_2O to a CNT [106]. Nanotubes with low heat treatment and confirmed p-type behaviour show an increase in R at low water vapour concentrations whilst at higher concentrations R decreases [107]. Zahab *et al.* attributed the dependence of sign of ΔR on water vapour concentration to a compensation effect due to n-type water doping of p-type semiconducting SWNT network [108]. Maniwa *et al.* [109] observed the temperature dependence of SWNT networks change upon exposure to water vapour saturated air at room temperature from a purely semiconducting dependence ($\mathrm{d}R/\mathrm{d}T > 0$) to include a metallic region ($\mathrm{d}R/\mathrm{d}T < 0$) with a crossover temperature $T^* = 200 - 250$ K. However, SWNT networks annealed at high temperature (500 K) show an increased resistance upon water vapour exposure with no observable reduction in the resistance [110], although it cannot be ascertained as to whether this is due to an insufficient water vapour concentration or to the initial state of the SWNT network (previous reports of a compensating effect were concerning SWNT networks with p-type behaviour or oxygen exposed and therefore p-doped to some extent).

Hysteresis in SWNT-FET has been attributed to charge trapping caused by the presence of water vapour [107, 111, 112]. Detailed studies investigating the effect of water vapour concentration on the characteristics of SWNT-FET have shown that at

low humidities the threshold voltage (V_{TH}) moves to more negative voltages as expected from a charge trapping mechanism. In addition the conductance also decreases with humidity attributed to compensation of hole charge carriers by electrons donated by H_2O molecules. As the humidity increases the conductance increases due to an excess of electrons.

Carbon nanotubes exhibit sensitivity to a wide range of molecules. The sensitivity of conductiometric SWNT sensors have been increased by coating with a polymer amine, increasing the number of binding sites and reducing the binding energy with the effect of producing reversible adsorption and sensitivity at the parts-per-trillion level [113]. Selectivity may be controlled by coating with chemoselective layers [113, 114]. The response of single-strand DNA coated SWNT-FET devices may be tuned to various analytes through the DNA nucleotide sequence, although the mechanism remains unclear [115].

Most CNT sensors are irreversible [16, 79, 116–118]. Reversibility of SWNT gas sensors may be manually achieved through UV irradiation [118], thermal annealing [16], application of an electric field [116] or hydrolysis [117]. Occasionally CNT sensors show reversible characteristics [115, 119, 120] due to highly graphitised structure and low levels of impurities. Adsorbate induced perturbations of the dielectric properties of SWNT have been exploited in a number of sensing geometries [114, 121]. Capacitors detect polarisation of the surface adsorbates. Faster response times are achieved in chemicapacitors rather than chemiresistors [114]. The sensing response of defective SWNT networks was analysed in terms of capacitance and conductance. It was observed that defects increase the response of both capacitance and conductance and that the conductance of the device saturates whilst the capacitance appears to carry on increasing as a function of partial pressure of analyte [104]. This was interpreted as charge transfer occurring at defect sites which also serves as nucleation sites for additional condensation of the analyte. The finite density of defect sites leads to a saturation in conductance, whilst the capacitance continues to increase as more condensation occurs and electric field induced polarisation of the analyte molecules contributes to additional capacitance.

Chemicapacitative SWNT sensors already rival the sensitivity and response time of commercial products [122] and at low vapour concentrations $\Delta G/\Delta C$ was shown to be a constant for specific analytes [122] which could be used to identify chemical species.

1.6 Adsorption

1.6.1 Mechanism

There are two types of adsorption that can occur on a surface, physisorption and chemisorption. Physisorbed species interact weakly via the van der Waals force with the adsorbent, the adsorption energy, E_{ads}, defined as the average binding energy per mole between adsorbate and surface atoms, is typically small $E_{\text{ads}} = 2$ kcal/mole. Chemisorbed species possess a surface chemical bond with the surface atoms providing a strong interaction, typically $E_{\text{ads}} > 15$ kcal/mole.

In 1932 Lennard-Jones [123] described qualitatively the adsorbate/substrate complex in terms of a one dimensional potential energy surface, $V(z)$, shown for a molecule and its atomic constituents in Figure 1.8. At large values of z the potential of the atomic constituents must be above that of the molecule, the difference between the two potentials is the dissociation energy of the free molecule, E_{diss}. At low temperature a molecule arriving at the surface finds an energetic minimum at z_{phys} and binds in a physisorbed state due to the van der Waals interaction. Depending on the potential energy surface the molecule could stay at z_{phys} or approach a chemisorbed state at z_{chem} as a molecule or dissociated molecule. Figure 1.8 illustrates three possible adsorption scenarios:

(a) potential energy curve of molecule and constituents cross at minimum energy for dissociative chemisorption. Dissociative chemisorption can only be reached from physisorbed state by provision of activation energy. In absence of activation energy molecular physisorption occurs.

(b) Potential energy of molecule is lower than that of constituents for all z. Molecular chemisorption via physisorption occurs.

(c) Dissociated chemisorption state has the lowest energy and can be reached directly, no activation energy.

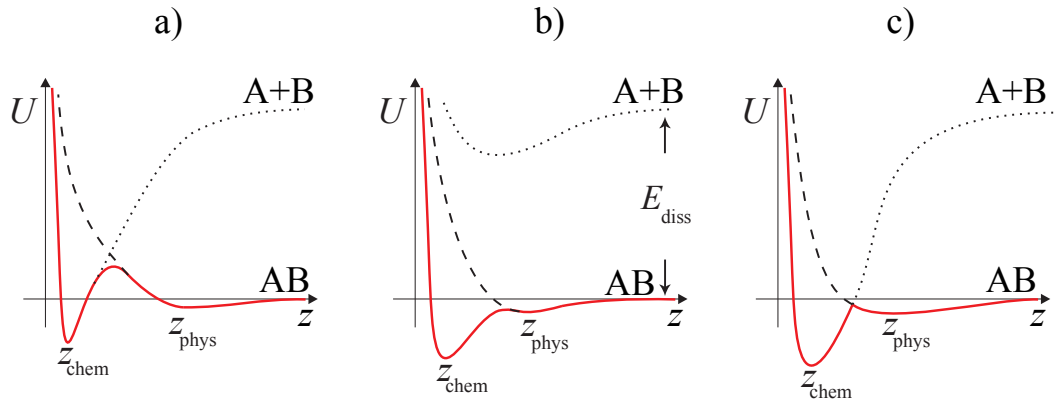

Figure 1.8 The potential energy, U, of an adsorbate/substrate complex as the adsorbate approaches the surface $z = 0$ from $z = \infty$. Three equilibrium configurations are shown: a) molecular physisorption; b) molecular chemisorption; c) dissociative chemisorption. Adapted from [123].

1.6.2 Adsorption kinetics

In this section a brief overview of diffusion phenomena and adsorption kinetics for a non-interacting and interacting monolayer will be given.

The rate of adsorption may be limited by the following factors: 1) the rate of mass transfer of gas to the adsorbed surface (external diffusion); 2) the rate of mass transfer within the pores of adsorbent (internal diffusion); 3) the rate of transfer of heat from adsorbate to adsorbent; 4) the surface migration rate, the rate of activated migration to energetically favourable site; 5) the rate of the surface process requiring an activation energy; 6) charge-transfer phenomena.

Surface diffusion

In a normal diffusion process through an isotropic material the diffusion front is Gaussian in profile. Specifically the change in concentration with time in one dimension is of the form

$$\frac{dC}{dt} = D^2 \frac{d^2C}{dx^2} \tag{1.13}$$

where C is concentration, D is the molecular diffusion coefficient, t is time and x is displacement. Equation 1.13 has a solution

$$C(x,t) = \frac{s}{2\sqrt{\pi Dt}} \exp\left(-x^2/4Dt\right) \tag{1.14}$$

where $s = \int_{-\inf}^{+\inf} Cdx$ the total amount of substance. The concentration (or intensity gradient) should decay proportional to $t^{-1/2}$. Another important characteristic of diffusion phenomena is the variance which indicates the width of the distribution. The variance of Equation 1.14 is defined as

$$\sigma^2 = 2Dt \tag{1.15}$$

where σ is the standard deviation of the mass distribution. Therefore if the diffusion coefficient is constant the variance of the mass distribution grows linearly with time. Generally the variance of the mass distribution can be written as

$$\sigma^2 = 2Dt^{\gamma} \tag{1.16}$$

where γ is an index which describes the diffusive regime, $\gamma = 1$ describes normal diffusion, $1 < \gamma < 2$ describes super-diffusion, $\gamma < 1$ describes sub-diffusion and $\gamma = 2$ describes ballistic diffusion [124, 125].

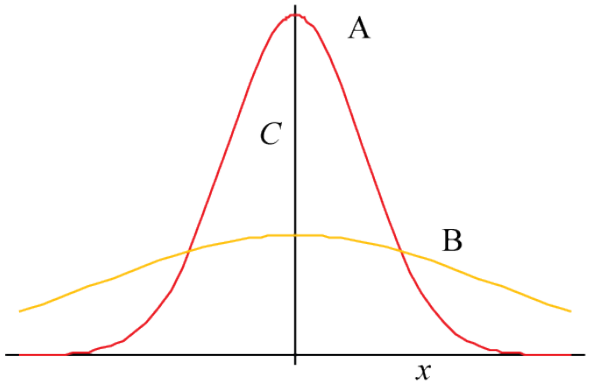

Figure 1.9 Diffusion in an isotropic media. Applied to our system curve A can be considered the initial concentration versus x profile of the nanotube network at $t = 1/64$. Curve B is at some time later ($t = 1/8$) and shows the concentration profile has extended over x.

In the case of SWNT network oxygen adsorption, the diffusion of oxygen molecules through the network can be considered proportional to an increase in surface coverage of oxygen on the nanotube network, Θ, thereby increasing $G - G_0$ through increased charge-transfer. The variation in conductance, $G(t) - G(t = 0)$, can be considered to be proportional to the standard deviation of the distribution of oxygen molecules. Therefore, for normal diffusion of oxygen through the system a log-log plot of $G - G_0$ vs. t would have a linear relationship with a gradient of $\frac{1}{2}$.

Kinetics of monolayer coverage

In addition to diffusion phenomena the kinetics of adsorption is dependent on the nature of interaction of adsorbate with the adsorbing surface. As mentioned previously, Section 1.6.1, this interaction can be strong, as in the case of chemisorption, or weak, as in the case of physisorption. The mathematical description of these two types of interaction is derived from two basic isotherms, the differentiating factor being the heat of adsorption $\Delta H_{\text{ads}} = E_{\text{ads}} - E_{\text{des}}$ with surface coverage. Physisorbed molecules, characterised by the Langmuir isotherm, are assumed to have a constant ΔH_{ads} with fractional surface coverage Θ. The Langmuir isotherm was derived by assuming that the adsorption is terminated upon completion of a monomolecular adsorbed gas layer, that the surface is homogenous, and the species are non-interacting i.e. ΔH_{ads} remains constant with surface coverage. The Langmuir isotherm can be expressed as [126]

$$\frac{\Theta}{1-\Theta} = AP \exp\left(\frac{\Delta H_{\text{ads}}}{RT}\right) \tag{1.17}$$

where $A = N_{\text{A}}(2\pi MRT)^{-1/2}\tau_0\sigma_0^{-1}$, N_{A} is Avogadro's number, M is the atomic number, R the universal gas constant, τ_0 the period of single atom vibration and σ_0 the surface coverage. In most chemisorption processes ΔH_{ads} is considered to decrease with coverage due to the repulsive interaction between adsorbate molecules when they are in close proximity to each other. Chemisorption behaviour can be modelled by modifying the Langmuir equation given above to include a linear variation of ΔH_{ads} with Θ, expressed as

$$\Delta H_{\text{ads}} = \Delta H_{\text{ads}_0}(\Theta = 0)(1 - a\Theta) \tag{1.18}$$

where ΔH_{ads_0} is the adsorption energy at zero coverage and a is a proportionality constant. The Temkin isotherm is one such isotherm which describes a linear variation of ΔH_{ads} with Θ, and can be expressed as [126]

$$\Theta \sim \frac{RT}{\Delta H_{\text{ads}}(\Theta = 0)a} \ln A_0 P \tag{1.19}$$

where $A_0 = A \exp[\Delta H_{\text{ads}}(\Theta = 0)/RT]$.

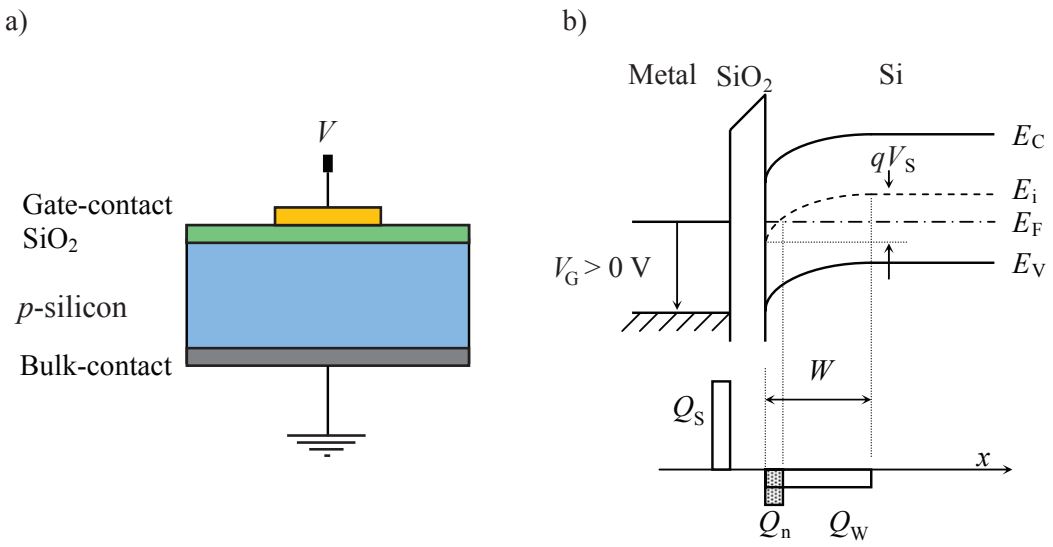

Figure 1.10 a) Schematic of simple MOS capacitor. b) Energy band diagram of p-Si MOS capacitor under reverse bias; where Q_S is the induced surface charge, Q_n is the inversion layer charge, Q_W is the space-charge, W is the width of the space-charge layer, V_G is the gate voltage, V_S is the surface charge voltage and E_C, E_i, E_F and E_V are the conduction band energy, intrinsic Fermi level energy and valence band energy, respectively.

1.7 Principles of MOS capacitors

The MOS structure is essentially a capacitor consisting of a semiconductor (e.g. silicon) onto which an insulator (e.g. SiO_2) is grown by thermal oxidation before a metal film is deposited, Figure 1.10. The semiconductor and the metal film form two plates of a parallel plate capacitor, separated by the oxide dielectric.

Application of a potential V_G (gate voltage) between the semiconductor and the metal film creates an electric field in the capacitor structure which extends through the insulator and into the semiconductor region. The magnitude of this field is proportional to the induced surface charge (Q_S) and is rapidly screened in the metal due to the high charge density but decreases more gradually in the semiconductor due to the lower free carrier density.

Any process that alters either the charge on the gate or its potential will alter the capacitance of the device, providing a method of detection. To investigate which terms could be perturbed by gaseous exposure, the gate capacitance, C_G, of a MOS device will be defined for three operating regimes: forward bias (majority carriers accumulate in semiconductor surface region), reverse bias (negative charge appears in semiconductor

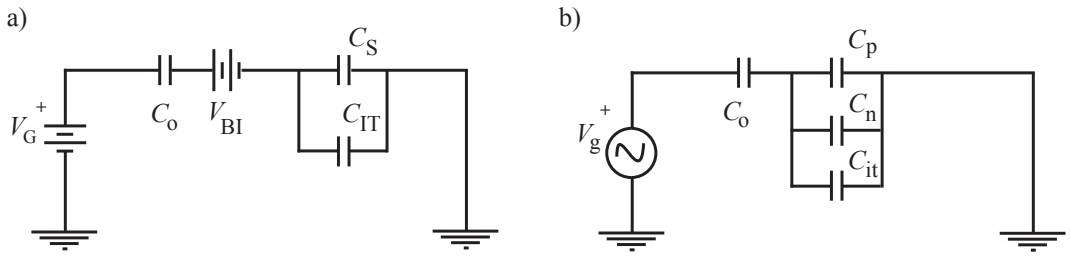

Figure 1.11 Circuit diagrams of a) d.c. equivalent circuit model b) small-signal equivalent model. Where C_o is the oxide capacitance, V_{BI} is the built in voltage in the semiconductor, C_S is the d.c. capacitance of the semiconductor, C_{IT} is the d.c. capacitance of charge stored in interface traps, C_p and C_n are the differential capacitance of holes/electrons in semiconductor, C_{it} is the differential capacitance of charge stored in interface traps.

surface region, majority carriers depleted, Figure 1.10 b)) and strong reverse bias (high negative charge is induced in semiconductor surface region, carriers inverted), Figure 1.12. The gate voltage, V_G, can be defined for all regimes as [127]:

$$V_G = V_{FB} + V_S - \frac{\epsilon_S E_S}{C_o} \tag{1.20}$$

where V_{FB} is the flat-band voltage, V_S is the surface potential, ϵ_S is the dielectric constant of silicon, E_S is the electric field in silicon and C_o is the oxide capacitance.

Under forward bias the MOS device has a large concentration of majority carriers in the silicon below the gate. The gate capacitance, C_G, can be considered to originate from a parallel plate capacitor with an oxide layer as the dielectric, a constant capacitance is thus obtained:

$$C_G = \frac{C_o C_S}{(C_o + C_S)} \tag{1.21}$$

where C_S is the capacitance of the semiconductor comprised of the capacitance due to electrons, C_n, and the capacitance due to holes, C_p, Figure 1.11.

Under reverse bias, energy-band schematic given in Figure 1.10 b), the gated Si surface of the MOS device is depleted of majority carriers. The gate capacitance can be simply determined by assuming that all carriers are depleted in the space-charge layer under the gated oxide. Specific values of the depletion width x_d, V_S and E_S are obtained for the depletion condition:

$$x_d = \left(\frac{2\epsilon_s V_S}{qN_{\rm AA}}\right) \tag{1.22}$$

$$V_{\rm S} = \frac{qN_{\rm AA}x_{\rm d}^2}{2\epsilon_{\rm S}} \tag{1.23}$$

$$E_{\rm S} = \frac{2V_{\rm S}}{x_{\rm d}} = \left(\frac{2qN_{\rm AA}V_{\rm S}}{\epsilon_{\rm S}}\right)^{1/2} \tag{1.24}$$

where $N_{\rm AA}$ is the concentration of ionised p-type acceptor dopant impurities. Incorporating Equations 1.22 - 1.24 into Equation 1.20 gives:

$$V_{\rm G} = V_{\rm FB} + V_{\rm S} + \frac{(2\epsilon_{\rm S}qN_{\rm AA}V_{\rm S})^{1/2}}{C_{\rm o}} \tag{1.25}$$

the dependence of $V_{\rm S}$ on $V_{\rm G}$ can be found by rearranging eq. 1.25 to give:

$$V_{\rm S} = [(V_{\rm G} - V_{\rm FB}) + V_{\rm AA}]^{1/2} - {V_{\rm AA}}^{1/2} \tag{1.26}$$

where $V_{\rm AA} = \epsilon_{\rm S}qN_{\rm AA}/2{C_{\rm o}}^2$. $C_{\rm n} = 0$ due to the depletion condition, $C_{\rm it} = 0$ as $Q_{\rm it} = 0$ and $C_{\rm p} \neq 0$ as the hole concentration, $P(x)$, rises to $N_{\rm AA}$ at the edge of the depletion layer, $x = x_{\rm d}$. Therefore, $C_{\rm p}$ is given by the parallel-plate capacitance of the depletion layer $\epsilon_{\rm s}/x_{\rm d}$. The capacitance of the semiconductor can therefore be written as :

$$C_{\rm S} = C_{\rm n} + C_{\rm p} \simeq C_{\rm p} \simeq C_{\rm d} = \epsilon_{\rm S}/x_{\rm d} = \left(\frac{\epsilon_{\rm S}qN_{\rm AA}}{2V_{\rm S}}\right) \tag{1.27}$$

$$= C_{\rm o}\left[V_{\rm AA}(V_{\rm G} - V_{\rm FB}) + \frac{V_{\rm AA}^2}{(V_{\rm G} - V_{\rm FB})}\right] \tag{1.28}$$

The semiconductor capacitance is in series with the oxide capacitance, giving the gate capacitance as:

$$C_{\rm G}(V_{\rm G}) = \frac{C_{\rm o}C_{\rm S}}{(C_{\rm o} + C_{\rm S})} = \frac{C_{\rm o}}{1 + \left[\frac{V_{\rm G} - V_{\rm FB}}{V_{\rm AA}}\right]} \tag{1.29}$$

therefore perturbation of $V_{\rm FB}$ at a fixed $V_{\rm G}$ would give rise to a detectable shift of $C_{\rm G}$. Perturbation of $V_{\rm FB}$ is discussed later in this Section.

Under increasing reverse bias carrier concentrations in the gated silicon surface are inverted. The presence of minority carriers provides a frequency dependence, requiring a high frequency (HF) and low frequency (LF) description of $C_{\rm G}$. In the high frequency case the signal frequency exceeds that required for efficient generation-recombination

trapping, resulting in no change in the charge caused by minority carriers, $\Delta Q_{\rm n} = 0$, and therefore $C_{\rm n} = 0$. As the applied d.c. bias voltage is increased $\Delta Q_{\rm n}$ is positive whilst $\Delta Q_{\rm p} \simeq 0$ therefore $\Delta x_{\rm d} \simeq 0$ and as before $C_{\rm S} = C_{\rm n} + C_{\rm p} \simeq C_{\rm p} \simeq C_{\rm d} = \epsilon_{\rm S}/x_{\rm d} = (\epsilon_{\rm S} q N_{\rm AA} 2V_{\rm S})$. Under inversion the threshold condition applies, $V_{\rm S} = 2V_{\rm F}$ where $V_{\rm F}$ is the Fermi potential. The semiconductor capacitance is now:

$$C_{\rm S} = \left(\frac{\epsilon_{\rm S} q N_{\rm AA}}{4V_{\rm F}}\right)^{1/2} \tag{1.30}$$

which is dependent on temperature but independent of exposure to gases or vapours.

The low frequency behaviour of $C_{\rm G}$ in increasing inversion is that of an increasing $C_{\rm S}(V_{\rm G})$, rising to $C_{\rm G} \approx C_{\rm o}$. This is due to the increasing minority carrier density and also the high rate of generation and recombination of minority carriers in response to the low signal frequency. The depletion approximation is no longer valid as $dQ_{\rm N} \neq 0$, $C_{\rm n} \neq 0$. Retaining the carrier concentration in the space charge layer leads to the following definition of the surface concentration of electrons, $N_{\rm S}$:

$$N_{\rm S} = N_{\rm B} \exp[qV_{\rm S}/kT] = N_{\rm AA} \exp[q(V_{\rm S} - 2V_{\rm F})/kT] \tag{1.31}$$

$$\simeq \frac{{C_{\rm o}}^2 (V_{\rm G} - V_{\rm FB})^2}{2\epsilon_{\rm S} kT} \tag{1.32}$$

where $N_{\rm B}$ is the concentration of electrons in the bulk semiconductor. The electric field in the semiconductor can be written as:

$$E_{\rm S} \simeq \left(\frac{2kTN_{\rm AA}}{\epsilon_{\rm S}} \exp[q(V_{\rm S} - 2V_{\rm F})/kT]\right)^{1/2} \tag{1.33}$$

$$\simeq C_{\rm o}(V_{\rm G} - V_{\rm FB})/\epsilon_{\rm S} \tag{1.34}$$

which gives the following $C_{\rm n}$:

$$C_{\rm n} = \mid q(N_{\rm S} - N_{\rm B})/E_{\rm S} \mid \approx \mid qN_{\rm S}/E_{\rm S} \mid = [q(V_{\rm G} - V_{\rm FB})/2kT]C_{\rm o} \tag{1.35}$$

which can be perturbed by gaseous vapour through modification of $V_{\rm FB}$ as shown below. As $C_{\rm n}$ increases the capacitance $C_{\rm G}$ will approach $C_{\rm o}$ as $C_{\rm G} = C_{\rm o}C_{\rm n}/(C_{\rm o} + C_{\rm n})$.

The flat-band term can be expanded to give

$$V_{\rm FB} = \phi_{\rm MS} - \frac{(Q_{\rm IT} + Q_{\rm OT})}{C_{\rm o}} \tag{1.36}$$

where $\phi_{\rm MS}$ is the difference in work function between metal and semiconductor, $Q_{\rm IT}$ is the total areal charge density residing in traps located at the oxide/semiconductor

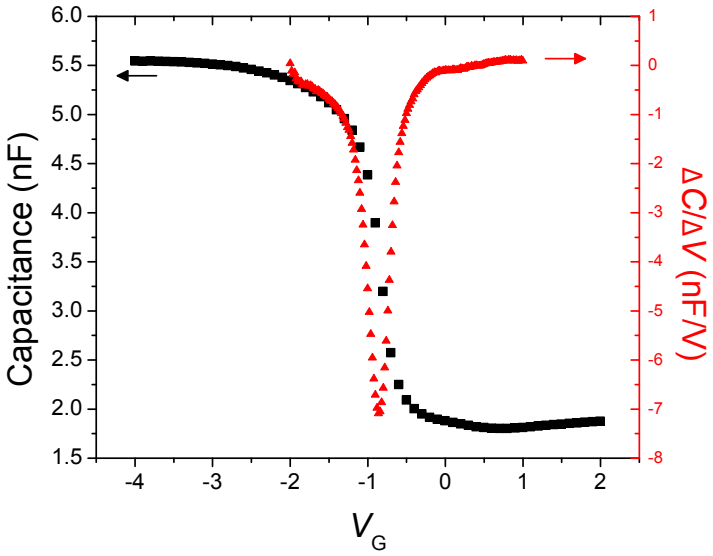

Figure 1.12 MOS capacitance voltage curve of a p-Si device at high small signal frequency, $f_{\mathrm{AC}} = 100$ kHz. The mathematical derivative $\mathrm{d}C/\mathrm{d}V_{\mathrm{G}}$ has a minima peak at V_{FB}. The behaviour can be explained by starting at the left-hand side, $V << 0$, holes are accumulated. As the negative voltage decreases a depletion layer forms acting as a dielectric in series with the gate oxide. As the voltage becomes very positive negative charges are attracted to the semiconductor surface, the carriers are inverted.

interface and Q_{OT} is the oxide-trapped charge. The flat-band voltage is easily detectable through the minima of $\mathrm{d}C/\mathrm{d}V_{\mathrm{G}}$ [128, 129], Figure 1.12.

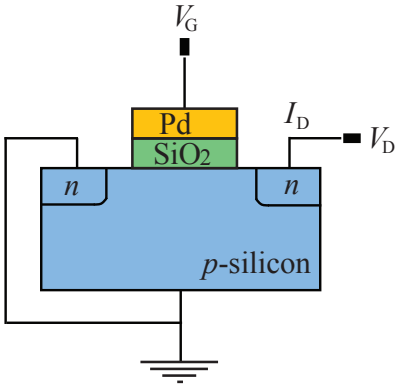

Figure 1.13 Schematic diagram of a MOSFET hydrogen sensor.

1.8 Micro-sensing methodologies

Gas micro-sensors are miniature transducers that detect gas molecules and produce an electrical signal the magnitude of which varies in proportion to the concentration of the gas. Carbon nanotube based sensors have been discussed in Section 1.5. A description of the most common non-nanotube gas micro-sensors follows.

Metal-Oxide-Semiconductor (MOS) sensors

Metal-Oxide-Semiconductor (MOS) sensors fall into two main categories - metal-oxide-semiconductor field effect transistors (MOSFET) and metal-oxide-semiconductor capacitors.

As stated previously the flat-band voltage of a MOS-capacitor, Figure 1.13, is given by

$$V_{FB} = \phi_{MS} - \frac{(Q_{IT} + Q_{OT})}{C_o} \qquad ((1.36))$$

the term ϕ_{MS} can be altered through the presence of gaseous species and the formation of a dipole layer, the modified metal-semiconductor workfunction is then

$$\phi_{MS} = \phi_{MS_0} + q\Delta V \qquad (1.37)$$

where ϕ_{MS_0} is the unmodified metal semiconductor work-function difference and ΔV is the potential produced by the formation of a dipole layer. Perturbation of ϕ_{MS} through adsorbed species at the insulator/gate interface was first observed by Lundström in 1975 [130], in which a MOSFET with palladium gate was used to sense hydrogen. The

critical component being the catalytic action of the palladium electrode in decomposing molecular hydrogen to atomic hydrogen, thus facilitating diffusion through the metal gate and the formation of a dipole layer. Since then the response of MOS capacitors with many different types of gate metal and analyte gas have been investigated.

As in MOS-capacitor sensors the sensing signal in MOSFET sensors is caused by a perturbation of gate voltage due to a rise in surface potential caused by the adsorbed dipole layer. In MOSFET sensors this causes a shift in the $I-V$ characteristics, shifting the threshold voltage. The shift in threshold voltage can be defined

$$V_{\mathrm{T}} = V_{\mathrm{T0}} - \Delta V \tag{1.38}$$

where V_{T0} is the initial threshold voltage and ΔV is the potential produced by the formation of the dipole layer.

In addition to hydrogen, sensitivity has to ammonia and hydrocarbons has been reported for the gate metals Pd, Pt and Ir [131]. This type of sensor exhibits good selectivity, showing cross-sensitivity to only a few other compounds. A limitation of MOS sensors is caused by baseline drift due to the movement of sodium ions within the silicon oxide under the influence of an electric field. This effect can be reduced by using Si_3N_4 or SiN_4 as the gate insulator. Another limitation of MOS based sensors is that the response can be diminished after storage in air for a long time.

Semiconducting metal-oxide sensors

The chemical interaction of gas molecules with semiconducting metal oxide surfaces leads to changes in electrical conductivity. The sensing material is deposited as a polycrystalline film on a substrate with interdigitated electrodes for heating.

The conductivity of metal-oxides arises from either oxygen vacancies acting as electron donors (n-type) or excess oxygen atoms acting as electron acceptors (p-type). SnO_2 (n-type) is the most frequently used semiconducting material for gas sensing. Chemisorbed oxygen creates extrinsic surface acceptor states that immobilise conduction band electrons from the near-surface region of an n-type semiconductor. Under ambient conditions the near surface region is depleted of electrons providing a lower conductance than regions without chemisorbed oxygen, Figure 1.14. As long as neighbouring grains are in electrical contact then the same applies for the overall conductance of the entire material. For p-type semiconductors the chemisorption of oxygen leads to an

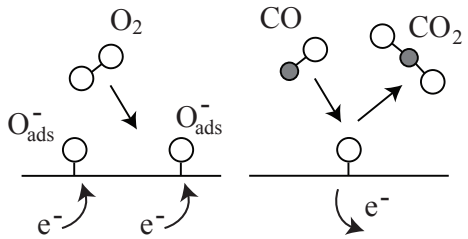

Figure 1.14 Simple schematic representing the origin of sensing signal of n-type semiconducting metal-oxide. LHS: Chemisorption of oxygen from gas phase leads to immobilisation of conduction electrons in the near surface-region. RHS: Reducing gases abstract surface bound oxygen, thereby releasing electrons back into the crystal.

accumulation surface layer and higher conductance. Foreign gas molecules with either reducing or oxidising properties will affect the density of charge carriers in the near surface region of each grain. The conductance varies in proportion to the concentration of adsorbed gas giving a very simple circuit design with fast response time. The situation is made more complex by the role of humidity or partial deactivation of the sensor surface by irreversible adsorption of gas molecules. The life time of metal-oxide sensors is very good and the fabrication cost of the sensors low.

Selectivity of semiconducting metal-oxide sensors is a problem since sensitivity is displayed to a wide range of oxidising and reducing gases. Doping with metallic clusters may enhance certain chemical reactions. A degree of selectivity can also be achieved by consideration of the size dependence of gas molecule on diffusion through the metal-oxide.

Generally the temperature-dependence of sensitivity is marked by a maximum at a few hundred degrees above room temperature due to the kinetics of both the reaction of analyte gas with surface adsorbed oxygen and the replacement of the latter from the gas phase. Semiconductor metal-oxide sensors therefore consume a large amount of power. Furthermore these sensors suffer from poisoning and require re-calibration regularly.

Conducting polymer based sensors

Electrochemically deposited conducting polymer sensors change their conductance in the presence of gases and vapours. The first use of electrochemically deposited polymer films for conductance based gas sensing occurred in 1983 where an irreversible response to ammonia was demonstrated [132]. Later work demonstrated a reversible conductance

response to organic vapours at room temperature [133].

Typically conducting polymers used in gas sensing applications require conjugation of a monomer such as pyrrole, aniline and thiophene. The change in conductance may arise from any process which changes the carrier mobility or density. Possible mechanisms for changes in conductance are sorption based polymer chain swelling which perturbs inter-chain transport, disruption of conjugation which thus affecting mobility or doping effects which affect both mobility and carrier density.

Many different polymers are available and are therefore sensitive to a broad range of gases and have a room temperature (low power) operation. By varying the counter-ion present in polymer sensors the the sensitivity and diversity of response may be influenced [134].

The main limitation of conductive polymer based sensors is the small magnitude of sensing response which is significantly affected by humidity and temperature.

Electrochemical sensors

An electrochemical sensing cell consists of an electrolyte sandwiched between a sensing electrode and a counter electrode, forming a complete circuit through the electrolyte.

Electrochemical sensors can be classified into two categories: potentiometric sensors and amperometric sensors. Amperometric electrochemical sensors produce a signal when the analyte gas diffuses through a porous membrane to the sensing electrode where it is oxidised or reduced. When the anode and cathode are in electrical contact electrolytic ionic conduction occurs and a current flows. Potentiometric sensors consist of two half cells where one half only involves the sensing species of interest. If the reference half cell contains a known mixture of the analyte gas information then the concentration may be deduced.

Advantages include room temperature operation with little power consumption. However, the electrolyte concentration may vary and the sensitivity of potentiometric sensors is poor [135].

Surface acoustic wave (SAW) sensors

Surface acoustic wave sensors are highly sensitive to surface perturbations. Surface acoustic waves are generated by piezoelectric substrates. As the acoustic wave propagates through or on the surface of the material, any changes to the characteristics

of the propagation path affect the frequency and amplitude of the wave. The electric field necessary to displace the piezoelectric substrate is provided by an input interdigitated transducer. The acoustic wave is converted into an electrical signal by an output interdigitated transducer.

An advantage of SAW sensors is that they are compatible with microelectronic fabrication. However, they are limited by baseline noise and instability at elevated temperatures [136].

Thermal conductivity sensors

Thermal conductivity sensors compare the thermal conductivity between a sample gas and a stationary or flowing reference gas. The thermal conductivity is obtained by measuring the temperature of heated elements in both the sample and reference cell. The measurement is non-specific so the each application must be calibrated with reference to a known concentration of appropriate reference gas. The response time is slow and the transduction is non-specific. However the sensor is effective over a broad concentration range.

Fiber optic sensors

Fibre optic sensors consist of optical fibres coated with a sensitive layer. The adsorption of analyte changes the optical properties of the sensitive layer. Possible properties which may be perturbed by adsorption are optical phase as used in interferometric sensors, scattering of light, refractive index changes, optical adsorption and fluorescence quenching. Selectivity is introduced through the sensitive material. For example a ruthenium complex has been successfully used for detecting the fluorescence of oxygen in a LED based fibre-optic sensor [137].

Fiber optic sensors are unaffected by electric and magnetic interference. In addition fibre optic sensors do not consume any analyte or are easily poisoned. Disadvantages of fibre optic sensors include interference with ambient light.

1.8.1 Comparison with nanotube sensors

The properties of the microelectronic sensors considered in this Section and nanotube sensors considered in Section 1.5 are summarised in Table 1.3. Carbon nanotube based sensors possess many of the advantages of traditional micro-electronic sensors in addition

to properties due to the unique structure of carbon nanotubes. The conducting channel is close to the analyte as all atoms are surface atoms in a single wall carbon nanotube. This provides excellent electrostatic coupling between the analyte and nanotube. The conduction channels of a typical FET are located under the surface which add to background noise. Having one conduction channel therefore increases the sensitivity. The small size of carbon nanotubes leads to high spatial resolutions and provides the option for having many sensors on one device.

Currently sensors constructed from individual nanotubes are limited by expensive fabrication costs due to the small device size and the high material costs due to the inability to grow a defined electronic type of nanotube. Many existing sensors have low cost and are suitable for their desired application despite the disadvantages. Once the production costs of SWNT are lowered then carbon nanotubes will rival these sensors also.

The implementation of carbon nanotubes as the gate material in a MOS sensor would provide additional information about the analyte through the shift in the flat-band voltage. The sensor would also be able to be operated as a FET based sensor and resistive sensor in the same geometry. The response of a sensor to oxygen is important as most sensors are intended to be operated in air.

Sensor	Measurement	Advantages	Disadvantages
MOS capacitor / MOSFET	Flat-band voltage / threshold voltage	High selectivity and sensitivity, easily integrated with silicon technology.	Base-line drift. Response diminished in air. Limited range of analytes.
Metal-oxide	Conductance	Fast response time and simple circuit design. Low cost.	Poor selectivity. Poor efficiency due to large power consumption. Easily poisoned.
Conducting polymer	Conductance	Low power operation. Tunable sensitivity.	Small sensing signal. Signal greatly affected by humidity and temperature.
Electro-chemica	Potentiometric or amperometric	Room temperature operation. Low power consumption.	Poor sensitivity. Electrolyte concentration may vary.
SAW	Acoustic	Compatible with microelectronic fabrication.	Large degree of baseline noise. Instability at elevated temperatures.
Thermal conducting	Calorimetric	Sensitive to broad concentration range.	Slow response time. No selectivity.
Fibre optic	Optical	Unaffected by electrical and magnetic interference.	Interference with ambient light.
Nanotube resistor	Conductance	High sensitivity due to band structure of semiconducting CNT and large surface area. One conduction channel. Fast response time. Selectivity can be given through nanotube coatings. Low power. Very small size.	High processing costs. Device fabrication limited by uncontrollable production of metallic or semiconducting SWNT. Without coating reversibility is limited.
Nanotube FET	Threshold voltage	As nanotube resistor. Controllable doping through gate modulation of Fermi level.	As nanotube resistor.

Table 1.3 Summary of micro-electronic sensor properties.

Chapter 2

Experimental Techniques

2.1 Sample preparation and characterisation

2.1.1 Solution preparation

SWNTs produced via the high-pressure carbon monoxide (HiPco) method were purchased from Carbon Nanotechnologies Incorporated. Raman and UV-vis spectrographic analysis provided information on the quality and approximate diameter distribution of SWNTs, Section 2.1.3.

To overcome the strong van der Waal interaction between nanotubes an anionic surfactant was used to prepare an aqueous SWNT dispersion. The dispersion of SWNTs in SDS/water solution has been studied by other groups [138], giving an initial parameter space for our study. SWNTs obtained from Carbon Nanotechnologies Inc. were used without further modification. An aqueous solution containing 0.44 wt% SWNT with 1 wt% SDS (Sigma-Aldrich, Product No. L6026) was prepared. The SWNT/SDS solution was subject to mild probe sonication of power 100 W and frequency 20 kHz for 1 hour 30 mins. Centrifugation at 3000 U/min for 2 hours separated higher density contaminants from dispersed SWNTs, the SWNT supernatant was extracted. The solution was then diluted by a factor of 100 before deposition.

2.1.2 Deposition

Networks of SWNTs were airbrushed (Everythingairbrush[1], Model AB-135A) onto the device substrate through an o-ring sealed mechanical compression mask of aperture 4

[1] http://www.everythingairbrush.com/

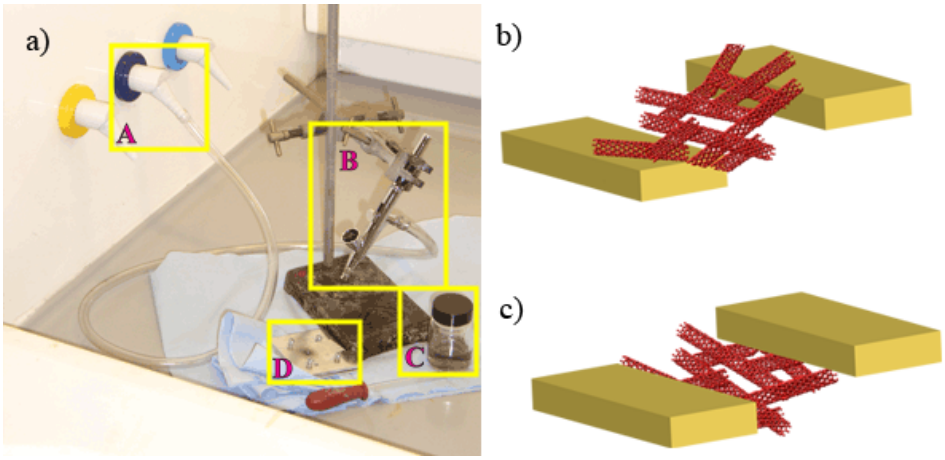

Figure 2.1 a) Experimental set-up for sensing experiments. A - filtered compressed air outlet. B - airbrush. C - SWNT-SDS solution. D - compression mask. b) Schematic diagram of bottom contacted SWNT network. c) Schematic diagram of top contacted SWNT network.

mm ×4 mm, setup shown in Figure 2.1 a). Substrates either had metallic contacts deposited prior to network deposition, giving a bottom-contacted SWNT network, Figure 2.1 b), or post network deposition resulting in top-contacted SWNT network, Figure 2.1 c). The airbrush was pressurised with filtered compressed air and held approximately 5 cm above the substrate. Single sweep brush strokes were applied, following each brush stroke the samples were allowed to dry (determined through a decrease in intensity of reflected light from solution droplets). Post deposition all samples were soaked in de-ionised water for 20 minutes to remove excess SDS. The topography of a sample obtained with an atomic-force microscope (AFM) mid-way through deposition exhibits smallest topographic height $\sim$ 2 nm with majority of structures $>$ 2 nm indicative of SWNT bundles, Figure 2.2.

2.1.3 Sample characterisation

Raman spectroscopy

As a result of the strong coupling between electrons and phonons in the 1D CNT system Raman scattering provides information on the vibrational modes of SWNTs and the electronic band structure. The 1D nature and associated band structure of SWNTs provide a resonant behaviour to the characteristic Raman scattering when incident photons drive optical transitions between van Hove singularities, as first reported by Rao *et al.* [139]. The energy spacing between van Hove singularity pairs, between which

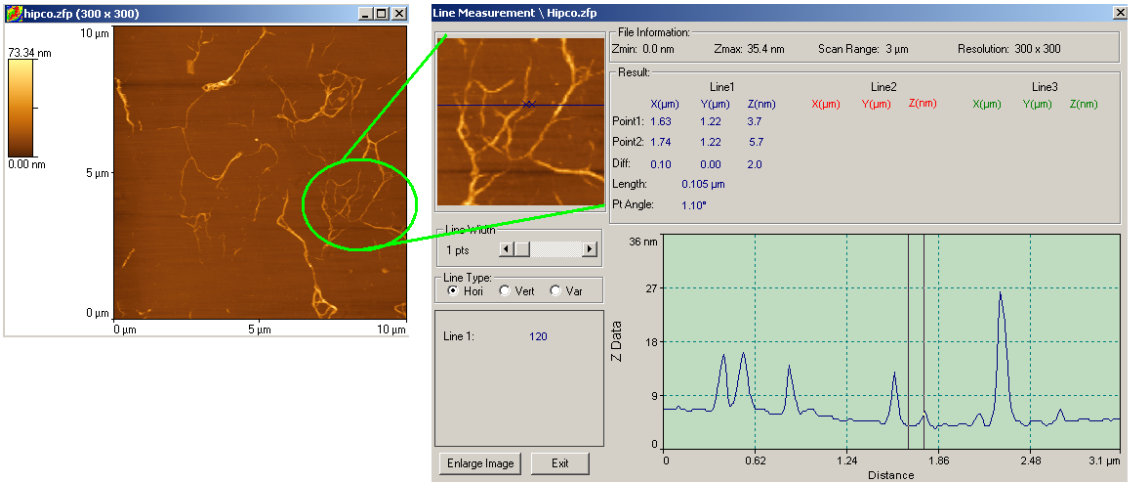

Figure 2.2 Non-contact mode, tilt adjusted, AFM image of non-percolating network airbrushed onto quartz substrate. Smallest feature size ~ 2 nm, with majority of structures $\gg 2$ nm indicative of SWNT bundles.

the optical transition occurs, scales inversely with the nanotube diameter. A Raman signal is predominantly observed from a proportion of the (n, m) nanotubes within a sample which are in resonance with the excitation energy.

The high degree of symmetry in carbon nanotubes leads to only a few Raman active modes. As a consequence the variation of Raman signal intensity with the Raman shift frequency ν displays three significant regions:

1. In the frequency range 100 cm^{-1} $< \nu <$ 350 cm^{-1} a Raman signal is provided by the radial breathing mode (RBM). The RBM mode is defined by the radial in-phase motion of carbon atoms. The RBM frequency ν_{RBM} is inversely dependent on the diameter of the carbon nanotube and is weakly dependent on the chirality [140].

2. At $\nu \sim 1350$ cm^{-1} a Raman signal termed the D-band can be observed. D-band features in carbon nanotubes are observed as a result of a reduction in symmetry of the carbon lattice due to the presence of defects or impurities [141].

3. In the frequency range 1550 cm^{-1} $< \nu <$ 1650 cm^{-1} the G-band Raman signal is commonly found. The origin of the G-band is related to the tangential C-C stretching modes of graphite. Semiconducting nanotubes produce a two-peak G-band structure (G^+ and G^-) with a Lorentzian line shape [142]. The presence of electronic states at the Fermi level in metallic CNTs causes the G-band peak to be broadened to a Breit-Wigner-Fano (BWF) line shape [143]. The vibrational modes in the G-band are insensitive to changes in the nanotube diameter [139].

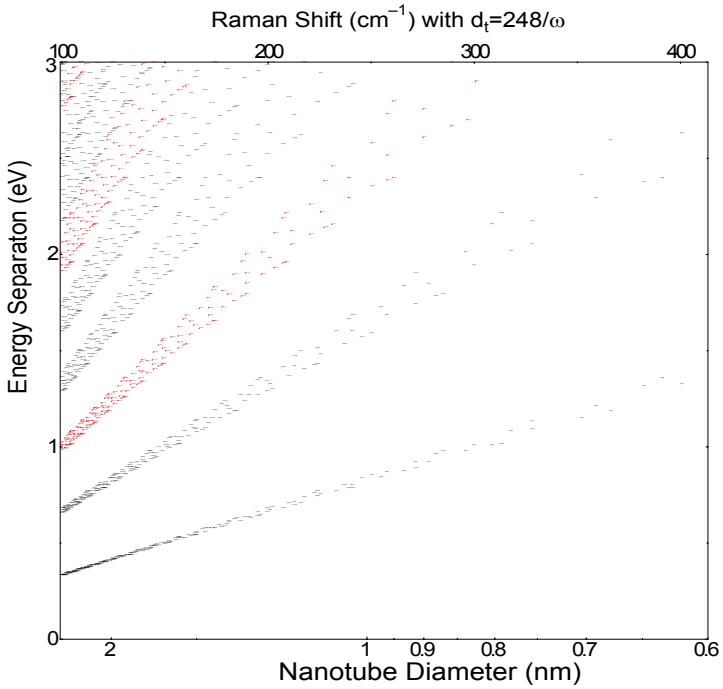

Figure 2.3 The vHs energy separation in the density of states of SWNT [145]. Calculated using the tight binding approach with the parameters carbon-carbon interaction energy $\gamma_0 = 2.9$ eV and carbon-carbon bond length $a_{C-C} = 0.144$ nm.

The interpretation of Raman signals is aided by the organisation of electronic transitions within nanotubes of different chiralities as a function of their diameter. This has been achieved theoretically using the tight-binding approximation by Kataura *et al.* [142] where electronic transitions E_{ii} are predicted based upon the chirality vector. A diagram showing the position of (n, m) indices on E_{ii} vs. d_t axes is known as the Kataura plot and is commonly used for determining (n, m) indices from the experimentally determined RBM ($\nu_{RBM} \propto 1/d_t$), Figure 2.3. However, it has been shown that an experimentally derived organisation of electronic transitions as a function of diameter [144] deviate from the theoretically deduced Kataura plot at small CNT diameters. This is predominately a result of the actual nanotube structure being more complicated than that which the tight-binding approximation considers, for example trigonal warping effects [9] contribute increasingly to the electronic band structure as the diameter decreases, are not considered by the tight-binding approximation.

Instrumentation

Resonance Raman spectra were recorded on two systems:

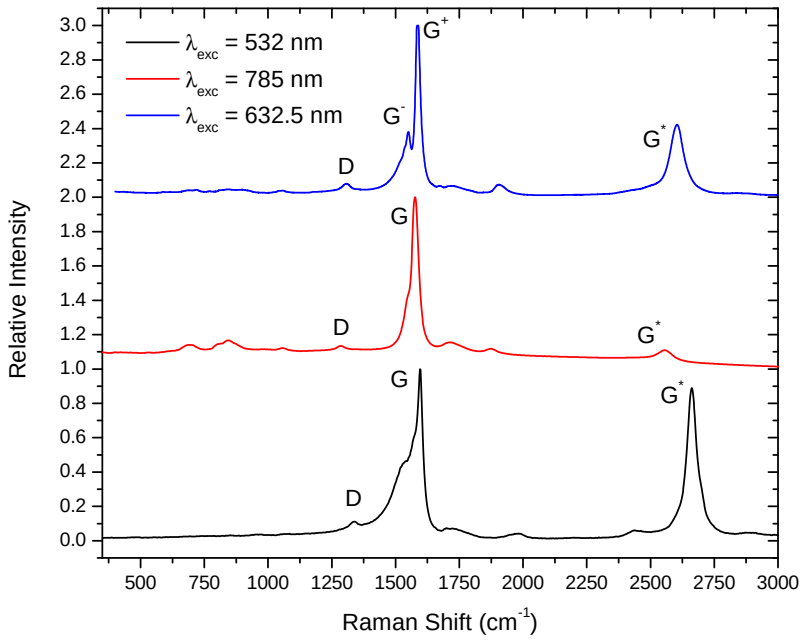

Figure 2.4 Raman spectra for HiPco SWNTs using various excitation wavelengths.

1. Renishaw Raman System Model 3000. He/Ne laser with emission wavelength $\lambda_{\text{exc}} = 632.8$ nm (1.96 eV). The laser spot has a diameter of 1 μm at the sample, with a power density $\sim 10^5$ W/cm^2. Operates in the back scattering geometry and detects anti-Stokes Raman shifts in the range -30 cm$^{-1} < \nu < -800$ cm^{-1} and Stokes Raman shifts in the range 400 cm$^{-1} < \nu < 3000$ cm^{-1}.

2. Nicolet 910 FTIR spectroscopy. Laser emission wavelengths of $\lambda_{\text{exc}} = 532$ nm (2.33 eV) and $\lambda_{\text{exc}} = 785$ nm (1.58 eV). Detects Stokes Raman shifts in the range $0 < \nu < 3000$ cm^{-1}.

Raman spectra were recorded in ambient conditions. Thanks to Zahra Alemipour for some additional Raman data.

Quality of graphitisation

The Raman spectra of the SWNT HiPco sample for $\lambda_{\text{exc}} = 532$ nm, $\lambda_{\text{exc}} = 632.5$ nm and $\lambda_{\text{exc}} = 785$ nm in the spectral range 650 cm$^{-1} < \nu < 3000$ cm^{-1} is given in Figure 2.4.

The quality of a nanotube sample can be evaluated by analysis of the peak intensity ratio of the G-band to the D-band. The G/D ratio was calculated at each of the

λ_{exc}(nm)	I_D	$\nu[I_D]$ (cm^{-1})	I_G	$\nu[I_G]$ (cm^{-1})	I_G/I_D	$\overline{I_G/I_D}$
532	0.112	1337	1	1596	8.9	9.7
632.5	0.079	1308	1	(G^+)1588	12.7	
785	0.135	1287	1	1576	7.4	

Table 2.1 Relative intensities (I_D and I_G) and Raman shift wavenumbers ($\nu[I_D]$ and $\nu[I_G]$) of the D-band and G-band maxima of HiPco SWNTs at various excitation wavelengths (λ_{exc}).

SWNT production method	G/D	Purification method	G_{pure}/D_{pure}
Methane CVD [146]	3.5	Hydrofluoric acid oxidation	13.5
Arc-discharge, relative purity of 60% was determined through near-infrared spectroscopy [147]	~ 8	-	-
Oxygen assisted CVD [148]	16	-	-
Arc-discharge, initial purity of 60% estimated by transmission and scanning electron microscopies [149]	13	Thermal oxidation and hydrochloric acid treatment	35

Table 2.2 Comparison of SWNT production methods and associated peak intensity ratio of G-band to D-band.

excitation wavelengths and the average taken, Table 2.1. This characteristic value of the quality of HiPco SWNTs presented in this thesis can be compared with values reported in the literature, Table 2.2. The value of G/D ratio observed for the SWNTs used within this thesis correspond well to the values of G/D ratio reported for SWNTs with a relative 60% purity. Values from the literature reported in Table 2.2 suggest that an improvement of sample quality could be obtained with an oxidative treatment thereby decreasing the carbonaceous impurity content. The graphitisation of CNT samples could be improved through high temperature annealing ($T \sim 1500$ K) which has been reported to increase graphitisation by reference to HR-TEM images [99] and Raman spectra [100], current induced graphitisation of CNT [101] could also increase sample quality.

RBM analysis

The RBM Raman signals at the excitation wavelengths $\lambda_{exc} = 532$ nm, $\lambda_{exc} = 632.5$ nm and $\lambda_{exc} = 785$ nm are given in Figure 2.5. The vHs energy separations E_{ii} for a given (n, m) SWNT as a function of diameter is given in Figure 2.3. The vHs energy separation was calculated using the tight binding approximation with the carbon-carbon

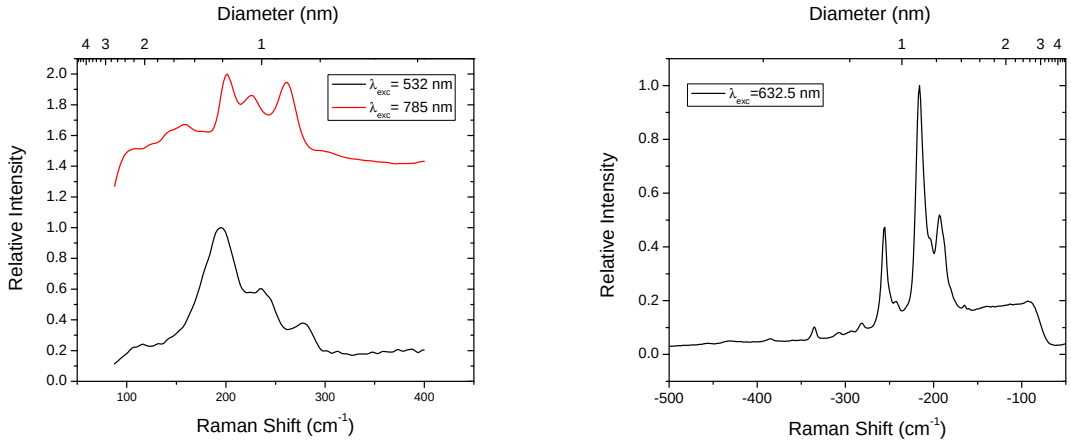

Figure 2.5 Raman spectra for HiPco SWNTs using various excitation wavelengths.

				$\nu(\mathrm{cm}^{-1})$				
(n,m)	d(nm)	Type	θ	Exp.	$248/d_t$	E_{exc}(eV)	E_{ii}(eV)	ΔE (meV)
(8,6)	1.0	Semi	25.2	261.3	255.7	1.58	1.66	0.08
(9,7)	1.1	Semi	25.9	226.5	224.8	1.58	1.47	-0.11
(13,10)	1.6	Metal	25.7	159.1	156.4	1.58	1.53	-0.05
(9,6)	1.0	Metal	23.4	236	238.9	2.33	2.22	-0.11
(15,3)	1.3	Metal	8.9	193.3	187.0	1.96	1.98	0.02
(10,7)	1.2	Metal	24.2	216	211.1	1.96	2.01	0.05
(8,3)	0.8	Semi	15.3	335.2	317.2	1.96	2.13	0.17

Table 2.3 Assigned (n, m) and comparison of experimentally observed and predicted Raman shifts and excitation energies. Theoretical values calculated with $\gamma_0 = 2.9$ eV [145].

interaction energy $\gamma_0 = 2.9$ eV and carbon-carbon bond length $a_{\mathrm{C-C}} = 0.144$ nm [145]. The dependence of the RBM frequency on the SWNT diameter for isolated SWNT on SiO_2 substrate has been shown to follow the relationship [24]

$$\nu_{\mathrm{RBM}} = 248/d_t \tag{2.1}$$

SWNTs are considered to have E_{ii} within a resonant window $E_{\mathrm{exc}} \pm 0.1$ eV [24]. The (n, m) indices and CNT diameter determined by correlation of the Kataura plot with the experimentally found ν_{RBM} and incident laser energy E_{exc} for the the HiPco sample used in this thesis are given in Table 2.3.

The diameter distribution of HiPco tubes given in Table 2.3 is broad 0.8 nm $< d_t <$ 1.6 nm as has been previously reported [150]. In the small sample space of 7 measurements 4/7 SWNT were metallic the remainder were semiconducting SWNT

0.76 eV $\leq E_{11} \leq$ 1.08 eV.

UV-vis spectroscopy

Purely resistive top contacted devices were deposited on microscope glass slides, enabling SWNT network thickness to be determined through UV-visible transmittance spectrophotometry, in Chapter 3 UV-vis measurements were performed with a Hitachi U-3000 spectrophotometer, in Chapter 4 and 5 UV-vis measurements were performed with a Perkin Elmer Lambda 950 spectrophotometer. Non-transparent silicon based devices, or bottom contacted glass substrate devices, were airbrushed in tandem with a microscope glass slide facilitating UV-visible transmittance spectrophotometry. Absorption features corresponding to chirality dependent interband transitions arising from van Hove singularities are apparent in typical UV-visible spectra as shown in Figure 2.6. The appearance of broad features are demonstrative of quenching associated with nanotube bundles, with the induced inhomogeneity introducing a red shift of absorption peaks [151]. Semiconducting SWNTs produced via the HiPco method are expected to have the E_{11} transition in the wavelength range 800 nm to 1600 nm, whilst the E_{22} transition is expected in the range 550 nm to 900 nm. Metallic SWNTs are expected to have a van Hove transition in the range 400 nm to 600 nm [28]. The two-terminal resistance of the nanotube/metal contact was measured and correlated with the absorbance of the network at $\lambda = 500$ nm.

Beer's law states that the absorbance, A, of a material is directly proportional to the path-length of light through the material, l, the extinction coefficient, ϵ, and the material density, d

$$A = \epsilon d l \tag{2.2}$$

Previous studies by Zhao *et al.* [152] and Bahr *et al.* [153], have confirmed the validity of Beer's law for SWNT solutions, providing SWNT extinction coefficients in the range 2.86×10^4 cm^{2}g^{-1} [153] $< \epsilon_{500\ \mathrm{nm}} < 3.5 \times 10^4$ cm^{2}g^{-1} [152] at $\lambda = 500$ nm. The variation of ϵ in the above studies can be attributed to the fraction of individual SWNT versus SWNT bundles present in the measurement sample as a result of differing filtration methods and differing organic solvent used to form the dispersions (dimethylformamide was chosen by Zhao *et al.*, 1,2-dichlorobenzene was chosen by Bahr *et al.*). Nanotube bundles may scatter incident light and thus be the cause of interference in absorption

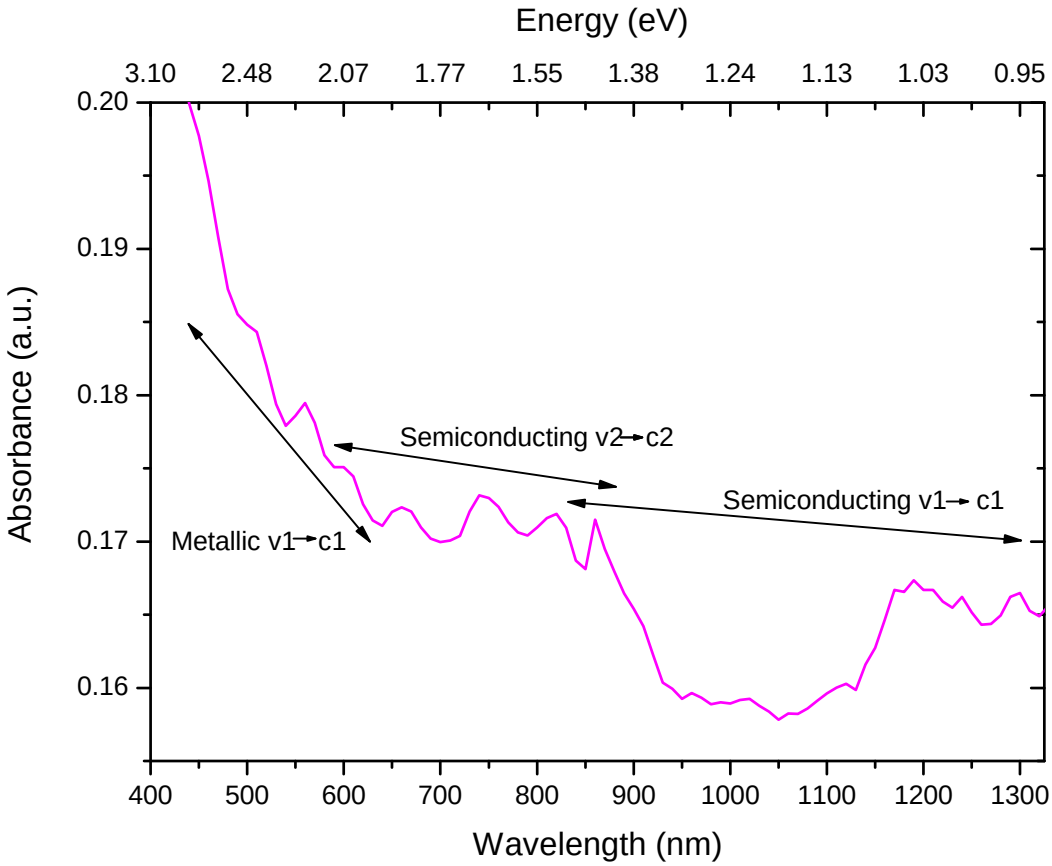

Figure 2.6 UV-visible absorption spectra of SWNT network on microscope glass substrate, $\Delta\lambda = 10$ nm. Absorption regions related to metallic or semiconducting nanotube band structure are present and can be ascribed to transitions from valence to conduction band van Hove singularities, labelled as $v_n \rightarrow c_n$, where n is an index of the van Hove singularities position increasing from $E = 0$. Peak broadening and red shifting of peaks is expected due to bundle quenching and substrate interactions.

measurements [154]. The UV-vis absorption spectrum of bundled SWNT has been shown to be red-shifted and broadened [155], the origin of the spectral red-shift possibly resulting from a decrease in the band-gap of SWNT tubes as a consequence of bundle formation [151].

The determination of SWNT network thickness through SWNT absorbance measurements and Beer's law has also been investigated by Bekyarova *et al.* [42] and confirmed through AFM measurements. The density of deposited nanotubes was obtained by Bekyarova *et al.* through a density gradient method, in which SWNTs are immersed in liquids of various densities, yielding a SWNT density in the range $1.57\ \mathrm{g \cdot cm^{-3}} < d < 1.59\ \mathrm{g \cdot cm^{-3}}$ [42]. The values of ϵ and d reported in the literature will be employed in calculating the upper and lower limits of SWNT network thickness through Beer's law.

Determination of error in calculated SWNT network thickness

The error in the absorbance measurements performed in this thesis are detailed in Table 2.4 and comprise error in the baseline flatness and photometric accuracy.

Chapter	UV-vis instrument	ΔA (A)
3	Hitachi U-3000	0.002
4 & 5	Perkin Elmer Lmbda 950	0.001

Table 2.4 Accuracy of absorbance measurements.

The error in determining the SWNT network thickness is found by propagating the errors in the absorbance, extinction coefficient and material density through a rearranged Equation 2.2, $l = A/(\epsilon d)$. The variation in the values of ϵ and d obtained from the literature give the error in $l = 11\%$, the final error in the thickness of SWNT networks given in this thesis include the relative error in the absorbance.

Summary of characterisation

HiPco SWNT presented in this thesis have a G/D ratio of $I_{\mathrm{G}}/I_{\mathrm{D}} = 9.7$ calculated from the average G/D ratio at $\lambda_{\mathrm{exc}} = 532$ nm, $\lambda_{\mathrm{exc}} = 632.5$ nm and $\lambda_{\mathrm{exc}} = 785$ nm. The G/D ratio of HiPco SWNTs used within this thesis correspond well to values of G/D ratio reported for SWNTs with a relative 60% purity, Table 2.2.

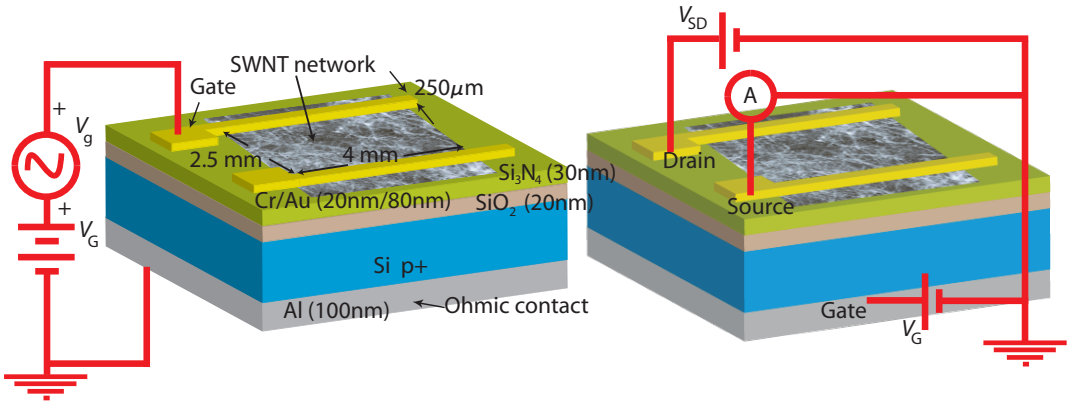

Figure 2.7 LHS: SWNT-MOS device structure of top contacted simple electrode p-doped (boron) silicon with 20 nm SiO_2 and 30 nm Si_3N_4, with 100 nm Al Ohmic contact. SWNT network deposited through mechanical compression mask to localise nanotube area. RHS: The same device structure operated as a SWNT-FET, channel length $L_C = 2.5$ mm, channel width $W = 4$ mm.

The diameter distribution of the HiPco tubes given in Table 2.3 is broad 0.8 nm $< d_t <$ 1.6 nm as has been previously reported [150]. In the small sample space of 7 measurements 4/7 SWNT were metallic and the remainder were semiconducting SWNT with E_{11} energies in the range 0.76 eV $\leq E_{11} \leq$ 1.08 eV.

UV-vis spectra of SWNT networks presented in this thesis demonstrate absorption maxima corresponding to the electronic configuration of the nanotube. The thickness of SWNT networks are calculated from the absorbance intensity at $\lambda = 500$ nm and Beer's Law. The thickness of the SWNT networks are given in the relevant Chapters.

2.1.4 Device fabrication

Device substrate

Non-field effect SWNT networks have a microscope glass slide substrate. The device structure of the field-effect capacitor device is shown schematically in Figure 2.7. Field-effect capacitor device substrates comprise a bulk p-type silicon, one face of which has 100 nm aluminium layer, the other face consists of a 20 nm native oxide with a further 30 nm Si_3N_4. Boron-doped silicon wafers were supplied by Si-Mat [2], the surface resistivity is in the range 20 $\Omega \cdot$cm $\leq \rho \leq$ 30 Ω·cm, which corresponds, by use of Irvin's plot [156], to $N_A \sim 1 \times 10^{15}$cm^{-3}. Both faces of as supplied wafers had 20nm SiO_2

[2] http://www.si-mat.com/

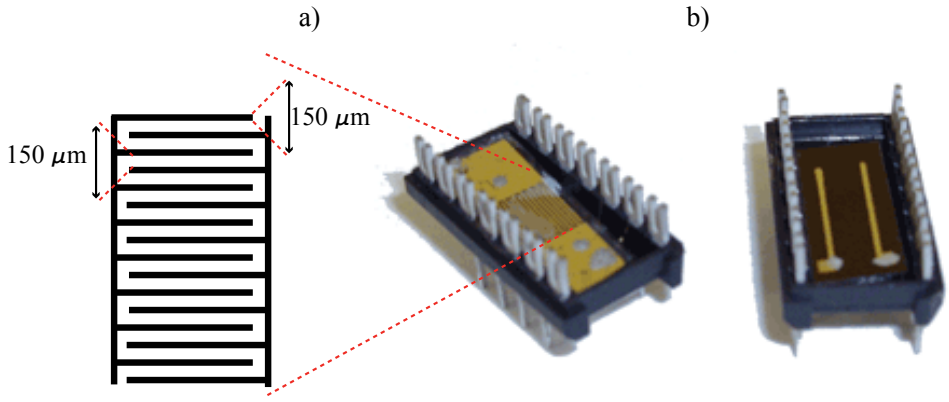

Figure 2.8 Two SWNT network samples mounted in DIL header, demonstrating two types of electrode configuration employed within this thesis. The electrodes consist of a) thermally evaporated Au/Cr interdigitated electrodes on microscope glass slide substrate, b) thermally evaporated Au/Cr strip electrodes on doped Si substrate.

thermally grown layer followed by a CVD grown 30nm Si_3N_4 layer. On one face of the silicon the SiO_2 and Si_3N_4 layer was removed by hydrofluoric acid (HF) treatment, see Appendix A item 2 for details. A 100 nm thick aluminium layer was deposited onto the exposed silicon face of the wafer by thermal evaporation. To improve the Ohmic contact of the Si-Al interface the wafer was then annealed at 623 K for 5 minutes in laboratory atmospheric conditions.

Both of the substrate types (glass slide substrate and doped silicon based) are cleaned through sequential sonication for 5 minutes in acetone and methanol before network deposition/ metal evaporation.

Nanotube network contact deposition

Metal electrodes of Cr (20 nm) and Au (80 nm) were thermally deposited pre/post network-deposition, depending on device configuration. The electrode geometry was defined with a shadow mask and consisted of either:

1. an interdigitated Cr/Au array of 8 sets of fingers with finger width 150 μm and inter-finger separation of 150 μm, Figure 2.8 a). The interdigitated evaporation mask was supplied by Photofabrication Limited[3].

or

[3]http://www.photofab.co.uk/

2. two strips of Cr/Au, length 1 cm and width 250 μm, Figure 2.8 b). The strip electrode mask was fabricated through the chemical etching of a molybdenum sheet, see Appendix A.

the thickness of deposited metal was determined by a quartz crystal oscillator. SWNT network devices were mounted on a commercially available 14-pin DIL header (Farnell, product code: 176-761), Figure 2.8. Electrical contact between the sample and DIL header was provided through gold wire (25 μm diameter) adhered with conductive colloidal silver paint. All samples in as-produced state are air exposed and therefore p-doped to some extent by atmospheric oxygen [15, 157].

2.2 Transport characteristics of nanotube networks

Thin and thick networks were deposited on microscope glass slides and the UV-visible transmission spectra recorded. Temperature dependent conductance measurements were performed using a continuous-flow He cryostat (Oxford Instruments) in two-contact mode. $I - V$ characteristics were recorded using a Keithley 4200-Semiconductor Characterisation Unit (SCU) data acquisition system in the temperature range 4 K $< T <$ 300 K.

Carbon nanotubes exhibit strong optical absorption $\sim$ 270 nm due to π-electron plasmon excitation [142]. Adsorbates were removed from the nanotube / nanotube-metal interface through exposure to UV radiation [118] while situated in the cryostat in partial vacuum ($\sim$ 20 mbar) and helium atmosphere for approximately 14 hours, inducing a decrease in the sample conductance. UV-exposure desorbs physisorbed and chemisorbed species through the dissipation of energy from photoexcited plasmons which break the molecule-nanotube interaction [118]. The UV source consisted of a fluorescent lamp of intensity 1600 μW/cm^2 with a wavelength vs. intensity central peak at $\sim$ 360 nm and a full-width-half-maximum of 40 nm, Figure 2.9. The temperature dependence of conductance was then measured after UV-desorption, thus providing temperature dependence data for a SWNT network in an absorbed and desorbed state.

2.2.1 Determination of errors

Possible sources of error are temperature T, current I and voltage V. The temperature was recorded to an accuracy of $\pm$0.01 K.

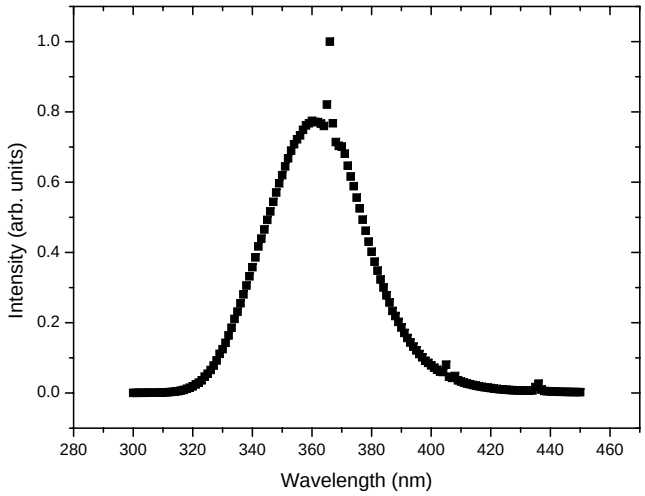

Figure 2.9 Spectra of UV lamp source for in situ desorption within cryostat. There is a sharp peak at 365 nm indicating a mercury emission, the wide lobes are thus obtained from a phosphor coating.

Electrical measurements were performed with a Keithley 4200 Semiconductor Characterisation Unit (SCU), the accuracy provided by the Keithley 4200-SCU in sourcing voltage and measuring current vary depending on the range of voltage or current required, Table 2.5.

The zero-bias differential conductance, $G = \mathrm{d}I/\mathrm{d}V$, is calculated through

$$\frac{\mathrm{d}I}{\mathrm{d}V} = 1/2\left(\frac{I_{\mathrm{i+1}} - I_{\mathrm{i}}}{V_{\mathrm{i+1}} - V_{\mathrm{i}}} + \frac{I_{\mathrm{i}} - I_{\mathrm{i-1}}}{V_{\mathrm{i}} - V_{\mathrm{i-1}}}\right)$$

The error in each variable was treated as originating from the same source (dependent

Variable	Range	Resolution	Accuracy
I (measure)	$0 < I \leq 100$ nA	100 fA	0.05 % + 30 pA
I (measure)	100 nA $< I \leq 1$ μA	1 pA	0.05 % + 100 pA
I (measure)	$1 < I \leq 10$ μA	10 pA	0.05 % + 600 pA
I (measure)	$10 < I \leq 100$ μA	100 pA	0.033 % + 3 nA
I (measure)	100 μA $< I \leq$ 1mA	1 nA	0.035 % + 30 nA
I (measure)	1 mA $< I \leq 10$ mA	10 nA	0.037 % + 300 nA
V (source)	$0 < V \leq 200$ mV	5 μV	0.02 % + 150 μV

Table 2.5 The accuracy of the Keithley 4200-SCU. The accuracy of sourceing/measuring current/voltage is dependent on the measurement range, the relative accuracy decreases with measurement range.

error) and propagated through the calculation of G.

$$\Delta\left(\frac{\mathrm{d}I}{\mathrm{d}V}\right) = \frac{I_{\mathrm{i+1}} - I_{\mathrm{i}}}{V_{\mathrm{i+1}} - V_{\mathrm{i}}}\left(\frac{\Delta I_{\mathrm{i+1}} + \Delta I_{\mathrm{i}}}{I_{\mathrm{i+1}} - I_{\mathrm{i}}} + \frac{\Delta V_{\mathrm{i+1}} + \Delta V_{\mathrm{i}}}{V_{\mathrm{i+1}} - V_{\mathrm{i}}}\right) + \frac{I_{\mathrm{i}} - I_{\mathrm{i-1}}}{V_{\mathrm{i}} - V_{\mathrm{i-1}}}\left(\frac{\Delta I_{\mathrm{i}} + \Delta I_{\mathrm{i-1}}}{I_{\mathrm{i}} - I_{\mathrm{i-1}}} + \frac{\Delta V_{\mathrm{i}} + \Delta V_{\mathrm{i-1}}}{V_{\mathrm{i}} - V_{\mathrm{i-1}}}\right) \quad (2.3)$$

The calculated ranges of error in the zero-bias differential conductance, G, for each device are given in Tables 2.6, 2.7 and 2.8.

Temperature	Current	Error in G (%)
4 K $\leq T \leq$ 20 K	$0 < I \leq 100$ nA	$0.44 \leq \Delta G\% \leq 3.86$
30 K $\leq T \leq$ 80 K	100 nA $< I \leq 1$ μA	$0.39 \leq \Delta G\% \leq 0.48$
90 K $\leq T \leq$ 300 K	$1 < I \leq 10$ μA	$0.39 \leq \Delta G\% \leq 0.47$

Table 2.6 Thin UV-desorbed SWNT network error in zero-bias differential conductance, G, with respect to the appropriate current range accuracy.

Temperature	Current	Error in G (%)
$T = 4$ K	$0 < I \leq 100$ nA	$\Delta G = 0.46\%$
5 K $\leq T \leq$ 11 K	100 nA $< I \leq 1$ μA	$0.41 \leq \Delta G\% \leq 0.56$
20 K $\leq T \leq$ 80 K	$1 < I \leq 10$ μA	$0.38 \leq \Delta G\% \leq 0.46$
100 K $\leq T \leq$ 300 K	$10 < I \leq 100$ μA	$0.37 \leq \Delta G\% \leq 0.41$

Table 2.7 Thin O_2-adsorbed SWNT network error in zero-bias differential conductance, G, with respect to the appropriate current range accuracy.

Temperature	Current	Error in G (%)
4 K $\leq T \leq$ 300 K	1 mA $< I \leq 10$ mA	$0.43 \leq \Delta G\% \leq 0.8$

Table 2.8 Thick O_2-adsorbed SWNT network error in zero-bias differential conductance, G, with respect to the appropriate current range accuracy.

Due to the large variation of error in G in the current range $0 < I \leq 100$ nA any measurements taken in this range will use the specific error at that temperature. Measurements taken in all other current ranges will use the upper value for the error within that range. Appendix B gives error calculations for the thin SWNT network in UV-desorbed state as an example.

A bias dependent conductance $G(V)$ was calculated from $I-V$ data. The largest error in $G(V)$ occurred at the smallest variable range, see Table 2.5. The error was found to be

$$\frac{\Delta V}{V} \approx 0.2\% \qquad \frac{\Delta I}{I} \approx 0.2\%$$

The above values were then used to calculate the error in G

$$G = \frac{I}{V} \Longrightarrow \frac{\Delta G}{G} \approx \frac{\Delta I}{I} + \frac{\Delta V}{V} \approx 0.4\%$$

This relative error was then used to calculate the error in G at all other V.

2.3 Sensing experiments

2.3.1 Experimental

The experimental setup utilised for gas sensitivity experiments is given in Figure 2.10. The sample under test was mounted in a vacuum-tight sample box equipped with 12 mW UV LED, with a typical wavelength $\lambda_{\text{typical}} = 400$ nm (RS Components, product code: 454-4396) situated 2 cm above sample and with an intensity of 0.03 mW/cm^2. The sample chamber is connected to an oil-free turbomolecular vacuum pump (Leybold, model: Dry-M-Basic) via two valves. One valve had an attachment for a bladder to facilitate back filling of gases into the sample chamber, providing exposure of the device to the analyte gas at atmospheric pressure. The second valve was used to isolate the turbomolecular vacuum pump. Gases described in this thesis were obtained from BOC and are of the following purity, methane 99.998%, nitrogen 99.998%, oxygen 99.5%.

2.3.2 Sensing via conductance

The conductance of the samples was monitored by periodically sampling ($\Delta t = 1$ s) the current whilst applying a fixed bias of ≤ 10 mV, using the Keithley 4200-SCU data acquisition system. Samples were initially placed under vacuum of $\sim 1 \times 10^{-6}$ mbar (achieved via a fore-pump pressure of $\sim 1 \times 10^{-3}$ mbar) and exposed to UV LED illumination, as detailed in Section 2.3.1, for 12 hours whilst measuring the conductance with time as described. This serves to desorb surface and inter-bundle adsorbates (surface dopants) from the nanotubes, evidenced in a conductance decrease. Once

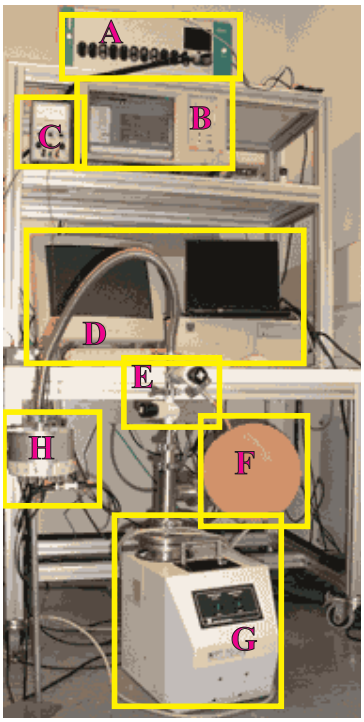

Figure 2.10 Experimental set-up for sensing experiments. A - Autolab Potentiostat PGSTAT12. B - Keithley 4200-SCU data acquisition system. C - power supply. D - PC. E - gas in valve and isolate pump valve. F - test gas bladder. G - Leybold Dry-M-Basic oil free pump. H - sample chamber.

the SWNT networks conductance is stable exposure to various analytes may be accomplished at 1 atmosphere pressure. Following exposure to analytes from a desorbed state, the samples can then be re-exposed to analytes from an adsorbed state. This is achieved via cycling vacuum ($\sim 1 \times 10^{-5}$ mbar achieved by turbomolecular pump[4] via a dual diaphragm fore-pump pressure of $\sim 1 \times 10^{-3}$ mbar) and analyte exposure whilst recording I vs. t as described.

Determination of errors

Electrical measurements were performed with a Keithley 4200-SCU, the accuracy provided by the Keithley 4200-SCU in sourcing voltage and measuring current vary depending on the range of voltage or current required. The errors in V and I were treated as originating from the same source (dependent error) and propagated through the calculation of G. The current range, voltage range and associated accuracy for each of the networks in Chapter 4 are given in Table 2.9 with the average error in G. The error in G of thick-mat and thin-mat could be reduced by increasing the applied bias to 10 mV.

Network	I range	I accuracy	V range	V accuracy	Avg. ΔG %
thin-id	$0 < I \leq 100$ nA	0.05 % + 30 pA	$0 < V \leq 200$ mV	0.02 % + 150 μV	1.5
thick-id	100 μA $< I \leq 1$ mA	0.035 % + 30 nA	$0 < V \leq 200$ mV	0.02 % + 150 μV	1.5
thin-mat	$0 < I \leq 100$ nA	0.05% + 30 pA	$0 < V \leq 200$ mV	0.02 % + 150 μV	7 (des.) 3.7 (ads.)
thick-mat	100 μA $< I \leq 1$ mA	0.035 % + 30 nA	$0 < V \leq 200$ mV	0.02 % + 150 μV	15

Table 2.9 The average error for UV-desorption and O_2-adsorption experiments in Chapter 4. The error is the same in desorption and adsorption unless stated. The thick-mat SWNT network has an applied bias of 1 mV, resulting in large error in G, all other networks have an applied bias of 10 mV.

2.3.3 Sensing via field effect

The capacitance variation of the SWNT-MOS device with applied voltage (d.c. and small-signal voltage, see Section 1.7 for detail) were investigated in both the UV-desorbed and oxygen-adsorbed state, following UV-desorption and oxygen-adsorption as detailed in Section 2.3.2.

SWNT-MOS capacitance-voltage measurements were obtained in the range -4 V $< V_{\mathrm{G}} < 2$ V, with a small-signal voltage $V_{\mathrm{g}} = V_0 \sin(2\pi f_{\mathrm{AC}} t)$, where f_{AC} is the frequency

[4]This is less than the the pressure quoted for desorption under UV due to shortened vacuum time.

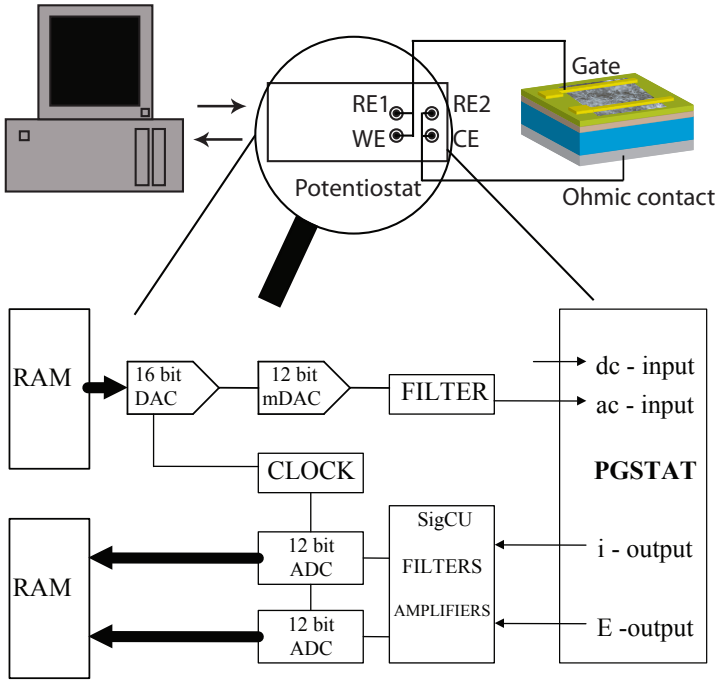

Figure 2.11 Schematic diagram showing the data acquisition set-up during C-V experiments. The steps described in Section 2.3.1 are employed for housing the sample and controlling sample pressure.

of small-signal voltage change, $V_0 = 0.01$ V and 10 Hz $< f_{\mathrm{AC}} <$ 1 MHz. The d.c. and a.c. signals will be controlled and the impedance change acquired through an Autolab[5] Potentiostat Model: PGSTAT12 with FRA module.

The Autolab potentiostat with FRA expansion module (henceforth refereed to as the potentiostat) was controlled through the I/O bus on a Windows 2000 PC, recorded data was saved to the PC hard disk. A schematic showing the data acquisition system with detail of the internal operation of the potentiostat is given in Figure 2.11. The potentiostat was set-up for a two-terminal C-V measurement by attaching reference electrode 1 (RE1) to the working electrode (WE) which was then attached to the gate terminal of the MOS capacitor, Figure 2.11. The second reference electrode (RE2) was attached to the counter electrode (CE) which were then connected to the Ohmic contact of the MOS capacitor. The potentiostat consisted of a digital signal generator (DSG), a signal conditioning unit (SigCU), and a fast analog-to-digital converter with two channels (ADC). The DSG consisted of a large digital memory, which is loaded with the digital representation of the applied signal and a fast settling 16-bit digital-to-analog converter. A multiplying digital-to-analog converter controlled the signal amplitude.

[5]Autolab manufactured by Eco Chemie, http://www.ecochemie.nl

The time-dependent potential and current signals from the potentiostat were filtered and amplified by the SigCU and digitised by means of the ADC. The acquired signals were stored in the digital memory on the ADC board. The analysis of the time-domain measurements were performed by means of the fast fourier transform (FFT) method. Both the potential signal $e(t)$ and current signal $i(t)$ were transformed to $E(f)$, $I(f)$ and their complex conjugated $E^{\circ}(f)$ and $I^{\circ}(f)$. The cell impedance, Z, is calculated from the equation:

$$Z = \frac{E(\mathrm{f})E^{\circ}(f)}{I(f)I^{\circ}(f)} \tag{2.4}$$

The capacitance of the device was then calculated by the control software running on the Windows PC.

The gate contact of SWNT-MOS capacitors may be utilised as the source and drain electrodes for a SWNT-FET as shown in Figure 2.7. The FET measurements were performed and recorded on a Keithley 4200-SCU. Measurements comprised either a source-drain voltage scan at fixed gate bias recording the source drain current or gate-voltage scan at fixed source drain voltage recording the source-drain current. Measurements were performed in the UV-desorbed and oxygen adsorbed states as described previously.

Determination of errors

The conductance of the devices under test in Chapter 5 upon UV-desorption/O_2-adsorption were performed with the Keithley 4200-SCU. The transient response of the devices presented in Chapter 5 were measured with an applied bias of $V = 10$ mV. The accuracy provided by the Keithley 4200-SCU in sourcing voltage in the range $0 < V \leq 200$ mV is stated as 0.02 % + 100 μV. The accuracy provided by the Keithley 4200-SCU in measuring current in the range $0 < I \leq 100$ nA is stated as 0.05 % + 30 pA. The average error in the conductance of the thick SWNT networks with an applied bias of $V = 10$ mV was found to be $\Delta G_{\mathrm{thick}} = 1.1\%$ for all devices presented in Chapter 5.

Capacitance-voltage measurements were performed with the Autolab PGSTAT12 with FRA module. The error in sourcing voltage is $\Delta V = 0.2\%$. The error in the capacitance measurements critically depends on the ratio between measured values of voltage and current and the output of the potentiostat, known as the resolution.

Depending on the impedance of the device under test the potentiostat adjusts the internal signal amplification to maximise the resolution. The impedance of the SWNT-MOS devices in the frequency range 10 Hz $\leq f_{\mathrm{AC}} \leq$ 1 MHz vary from 10 Ω to 10 MΩ, through discussion with Autolab technicians a suitable value of the error in capacitance was agreed to be 1%. The mathematical derivative, $\mathrm{d}C/\mathrm{d}V$, of the capacitance voltage scans are calculated in order to extract the flat-band voltage, as described in Chapter 1.7. Treating the error in C and V as dependent and propagating the errors through the calculation of $\mathrm{d}C/\mathrm{d}V$ results in errors $> 90\%$. The mathematical derivative of C-V measurements is therefore unsuitable for obtaining information about the absolute values of $\mathrm{d}C/\mathrm{d}V$, Chapter 5 will only consider the voltages at which minima in the $\mathrm{d}C/\mathrm{d}V$ vs. V (i.e. the flat-band voltage) occur.

SWNT-FET electrical measurements were performed with a Keithley 4200-SCU, the accuracy provided by the Keithley 4200-SCU in sourcing voltage and measuring current vary depending on the range of voltage or current required. The errors in V and I were treated as originating from the same source (dependent error) and propagated through the calculation of G. The current range, voltage range and associated accuracy for each of the networks in Chapter 4 are given in Table 2.10. The calculation of transconductance $g_{\mathrm{m}} = \mathrm{d}I_{\mathrm{D}}/\mathrm{d}V_{\mathrm{G}}$ increased the relative error especially in the low current regions. The error in g_{m} was calculated through Equation 2.3. The average error in g_{m} through -4 V $< V_{\mathrm{G}} < 4$ V was 40% whilst at -1 V where the transconductance was compared between devices the error was $\sim 20\%$.

Network	I_{SD} range	I accuracy	V_{G} & V_{SD} range	V_{G} & V_{SD} accuracy
U1A & U2A	100 nA $< I \leq 1$ μA	0.05 % + 100 pA	$0 < V \leq 200$ mV	0.02 % + 150 μV
U1A & U2A	100 nA $< I \leq 1$ μA	0.05 % + 100 pA	200 mV $< V \leq 2$ V	0.02 % + 300 μV
U1A & U2A	100 nA $< I \leq 1$ μA	0.05 % + 100 pA	2 V $< V \leq 20$ V	0.02% + 1.5 mV

Table 2.10 The error in I_{SD}, V_{G} and V_{SD} for devices U1A and U2A during FET measurements.

Chapter 3

Network Transport Characteristics

Networks of single-wall carbon nanotubes (SWNT) form a unique porous material comprising 1D objects. The system is inhomogeneous due to the mixture of semiconducting and metallic nanotubes within the network and the variance in inter-tube coupling. Localised electron states play an important role in electron conduction in disordered networks, however the extent to which localisation effects dominate has been shown to depend on the thickness of the SWNT network, thicker films approaching increased metallic behaviour, through a heterogenous model [46]. In this study the temperature dependence of conduction for thin and thick SWNT networks with top-contacted interdigitated electrodes is presented. Temperature dependent $I-V$ characteristics were recorded using a Keithley 4200-SCU data acquisition system in the temperature range 4 K $\leq T \leq$ 300 K. The thin SWNT network was exposed to UV radiation whilst situated in the cryostat in partial vacuum ($\sim$ 20 mbar) and helium atmosphere for approximately 14 hours, resulting in a decrease in the sample conductance. The UV source consisted of a broad range fluorescent lamp of full-width-half maximum wavelength range 340 nm $< \lambda <$ 380 nm and intensity 1600 μW/cm^2. The temperature dependence of conductance was then measured after UV-desorption, thus providing temperature dependence data for a SWNT network in an adsorbed and desorbed state.

3.1 Device characteristics

SWNTs produced via the high-pressure carbon monoxide (HiPco) method were processed into solution and deposited on glass slides as described in detail in Section 2.1.

Network	Abs. (A)($\lambda = 500$ nm)	Thickness (nm)	R (Ω)
thin-id	0.048 ± 0.002	1000 ± 200	5150 ± 8
thick-id	0.061 ± 0.002	1300 ± 200	11.60 ± 0.02

Table 3.1 Two-terminal resistance and absorption at 500 nm of thin and thick SWNT networks deposited onto microscope glass slides from SDS-SWNT solution through air-brush technique and subsequent rinsing in DI water.

Two percolating SWNT networks of controlled thickness were produced by air-brushing SWNT-SDS solution onto microscope glass slides. Samples were then rinsed in deionised water to remove residual SDS. The thickness of the formed nanotube network is characterised through optical absorption in the UV-visible range, recorded on a Hitachi U-3000 spectrophotometer as detailed in Section 2.1.2. The networks absorption at 500 nm and corresponding thickness calculated through Beer's law (see Section 2.1.3 for detail) and two-terminal resistance are given in Table 3.1 and Figure 3.1.

A Cr/Au interdigitated array was directly evaporated onto each network through an interdigitated shadow mask. The resulting structure has an interdigitated separation of ~ 150 μm. Contact was made to the interdigitated samples in a two-probe configuration with gold wire and colloidal silver paint. The networks are labelled as thin-id and thick-id corresponding to the thin and thick SWNT networks with interdigitated electrodes respectively. All samples in as produced state were air exposed and therefore p-doped to some extent by atmospheric oxygen [15, 157].

3.2 Conductance versus temperature

dc electrical conductance was measured in the temperature range 4 K $< T <$ 300 K for both thin-id and thick-id SWNT samples in a fully adsorbed laboratory-air-exposed state, confirmed through stability of I vs. V. The thin-id SWNT network was exposed to UV illumination in partial He atmosphere for 14 hours, as detailed previously in Section 2.2. The temperature dependence of conductance was then measured after UV-desorption.

Both the thin-id and thick-id SWNT networks exhibited increasing nonlinear $I - V$ characteristics as the temperature was decreased, Figure 3.2. For all SWNT networks the zero-bias differential conductance, G, was found to increase with increasing temperature, Figure 3.3. Positive $\mathrm{d}G/\mathrm{d}T$ behaviour is indicative of a semiconductor-type conduction

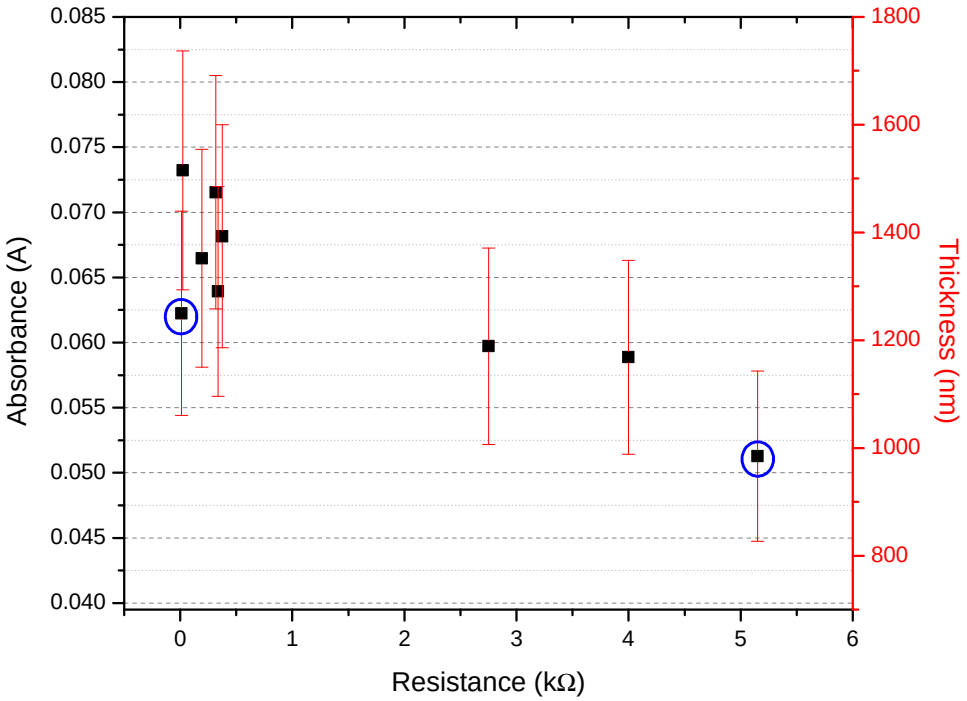

Figure 3.1 Resistance versus absorption at 500 nm and Beer's Law derived thickness of as prepared SWNT networks. Error bars represent error in Beer's law derived SWNT network thickness, as described in Chapter 2.1.3. Highlighted data points correspond to thin-id (low absorbance) and thick-id (high absorbance) SWNT networks referred to in this Chapter.

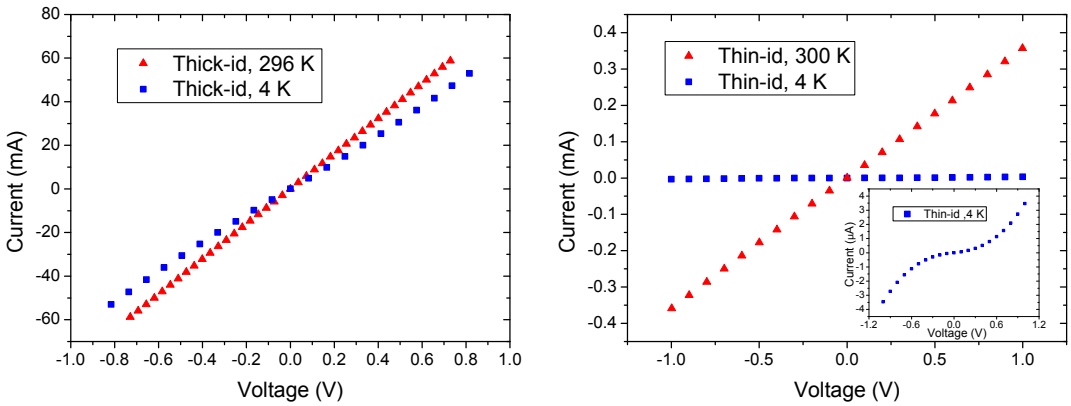

Figure 3.2 $I - V$ characteristic at room temperature ($\sim$ 300 K) and 4 K for thick-id and thin-id SWNT networks. Error bars are obscured by data points.

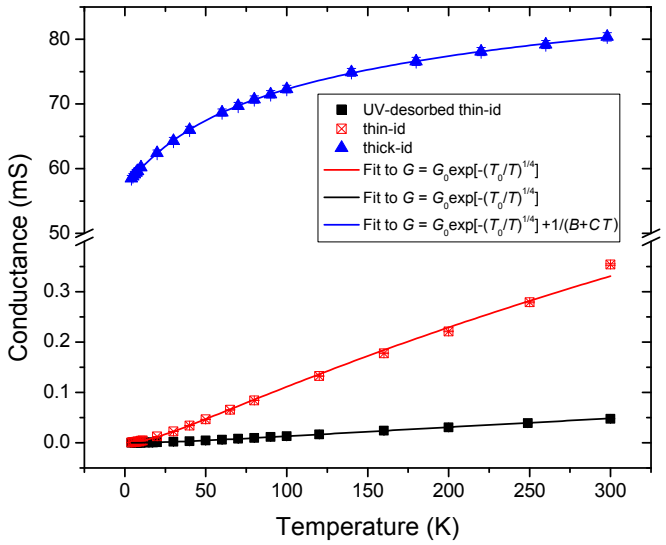

Figure 3.3 Zero-bias differential conductance vs. temperature for thin-id and thick-id SWNT networks, error bars obscured by data points. Error weighted fitting of UV-desorbed (—) and laboratory-air exposed (—) thin-id sample to Equation 3.2 is given. Error weighted fitting of laboratory-air exposed (—) thick-id sample to Equation 3.4 is given. Exposure of the thin-id sample to laboratory-air increases the room temperature conductance by 640% relative to the UV-desorbed state.

mechanism. The thin-id network in both the UV-desorbed and laboratory-air exposed state have zero conduction in the zero-temperature limit indicating a thermally activated conduction mechanism. The thick-id network has a comparatively reduced $\mathrm{d}G/\mathrm{d}T$ trend and finite conductance in the zero-temperature limit, possibly indicating more metallic character as reported by Skakalova *et al.* [46]. The critical thickness for percolation to occur in a SWNT network was calculated by Bekyarova *et al.* to be $t_c = 3$ nm [42]. Below the critical thickness Bekyarova *et al.* reported that SEM images detailed the formation of clusters of interconnected nanotubes that remain isolated from each other and therefore do not form a conducting channel, whilst above the percolation threshold a dense network of interconnected conducting channels is formed. The thickness of thin-id and thick-id networks exceeds t_c by more than a factor of 300 indicating that the networks are highly interconnected.

Considering the UV-desorbed state as the reference state, exposure to laboratory-air increases the room temperature conductance of the thin-id network by 640%. Close

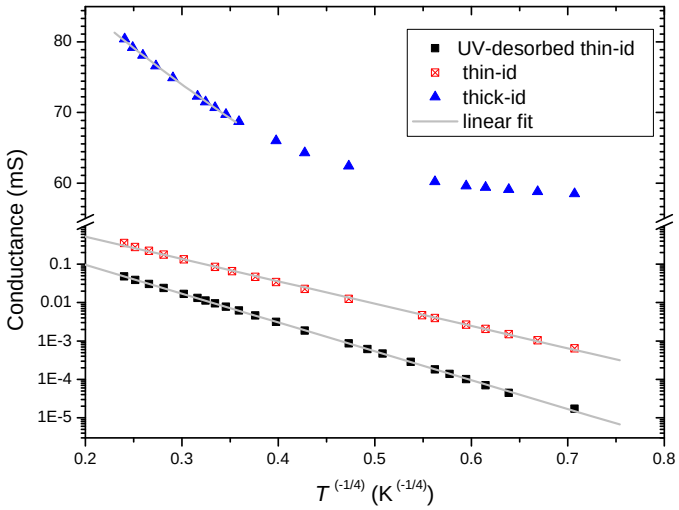

Figure 3.4 Conductance (G) vs $1/T^{1/4}$ for thick-id network and thin-id SWNT network in UV-desorbed and lab.-air-exposed state. Solid line indicates a linear fit of the data.

to room temperature all three samples follow a 3D variable-range hopping (3D-VRH) conduction model, Figure 3.4 :

$$G = G_0 \exp\left[-\left(\frac{T_0}{T}\right)^{1/4}\right] \tag{3.1}$$

$$T_0 = \frac{\beta}{k_B g(E_F)\alpha^3} \tag{3.2}$$

where $g(E_F)$ is the density of states at the Fermi level, α is the localisation length (related to the spatial extent of the electron wave function), β is a numerical constant and $G_0 \sim T^{-0.35}$ [56]. The thin-id network in both the laboratory-air-exposed and UV-desorbed state follow a 3D-VRH functional form throughout the entire temperature range 4 K $< T <$ 300 K, Figure 3.3. Fitting parameters to Equation 3.2 are given in Table 3.2. The thick-id network has a linear dependence of G on $T^{-1/4}$ in the temperature range 60 K $< T <$ 300 K, Figure 3.4, consistent with a 3D-VRH functional form. The variation of conductance with temperature for the thick-id network can be described throughout the entire temperature range 4 K $< T <$ 300 K by a model that includes a metallic component in series with that of the disorder induced 3D-VRH component

Network	Treatment	Model	G_0 (S)	T_0 (K)	Metallic parameters	
thick-id	lab.-air-exp.	Eq. 3.3	0.091 ± 0.003	700 ± 100	$A = 0.0544 \pm 0.0008$	$T\mathrm{m} = 0.14 \pm 0.04$
thick-id	lab.-air-exp.	Eq. 3.4	0.1183 ± 0.0004	7.3 ± 0.2	$B = 27 \pm 0.2$	$C = 4.9 \pm 0.1$
thin-id	UV-des.	Eq. 3.2	0.0031 ± 0.0001	90000 ± 600	-	-
thin-id	lab.-air-exp.	Eq. 3.2	0.0104 ± 0.0006	43000 ± 2000	-	-

Table 3.2 Fitting results for thin-id network to Equation 3.2 and thick-id network to Equation 3.3 throughout the entire temperature range 4 K $< T <$ 300 K, Figure 3.3. Error values correspond to the standard errors of parameters obtained from a error weighted fit to the data.

Origin	T_m	$k_\mathrm{B}T_\mathrm{m}$ (meV)
this thesis	0.14 ± 0.04	0.0121 ± 0.003
Skakalova *et al.* [46]	1830	160
Shiraishi and Ata [48]	420	36

Table 3.3 Comparison of experimentally found zone boundary-phonon energies.

$$G = G_0 \exp\left[-\left(\frac{T_0}{T}\right)^{1/4}\right] + A\exp\left(\frac{T_\mathrm{m}}{T}\right) \tag{3.3}$$

where A is a temperature independent constant and T_m a characteristic temperature. The exponential metallic component arises from scattering in quasi-1D materials where a phonon of energy $k_\mathrm{B}T_\mathrm{m}$ and wave vector $2k_\mathrm{F}$ is required to back-scatter the charge carrier [51]. As the temperature is reduced the probability of obtaining a high energy phonon required to back-scatter the charge carrier decreases exponentially. This form of metallic scattering has been noted in 1D conductive polymers [158] and SWNT networks [46,48]. The fitting parameters of the thick-id network to Equation 3.3 are given in Table 3.2. The metallic component in the thick-id network has a phonon energy $k_\mathrm{B}T_\mathrm{m} = 0.0121 \pm 0.003$ meV which is many orders of magnitude less than the expected theoretical energy for zone-boundary phonons $124 - 186$ eV [159] and less than the thermal energy $k_\mathrm{B}T$. Comparison between the thick-id zone-boundary phonon and those reported for SWNT networks in the literature is given in Table 3.3. The extremely low back-scattering phonon energy given by the fit indicates that the metallic resistivity is not limited by zone-boundary phonon back-scattering.

The temperature dependence of the thick-id network may be described by inclusion of an isotropic low energy acoustic phonon scattering which varies the conductance as $G \sim 1/T$ where the modes responsible for back-scattering are thermally populated to

low temperatures [160]. Resulting in the following expression

$$G = G_0 \exp\left[-\left(\frac{T_0}{T}\right)^{1/4}\right] + \frac{1}{B + CT} \tag{3.4}$$

where B and C are temperature independent constants. The fitting parameters of the thick-id network to Equation 3.4 are given in Table 3.2 and the trend is given in Figure 3.3. Carrier scattering from defects or impurities has been shown experimentally to reduce the mean free path in SWNT [58] which could provide an explanation for the absence of high-energy zone-boundary back-scattering.

Series models of conduction for thick SWNT networks commonly consist of fluctuation-induced tunnelling (FIT) of charge carriers through barriers separating metallic regions described by either a quasi-1D zone-boundary phonon scattering component or linear metallic component, as described in Section 1.4.3. The temperature dependence of conductance of the thick-id network did not follow the FIT + metallic functional form indicating that the conduction is limited by barriers between conducting regions which are too thick for fluctuation induced tunnelling to occur. The observation of a VRH functional form in the temperature dependence of conductance indicates that in the barrier regions electron states are localised, requiring thermal activation to propagate.

The form of VRH in both the thin-id and thick-id network is three dimensional. Physically this means that the number of available states for hopping n_h is related to the distance r from the localised state via $n_\mathrm{h} \propto r^3$ indicating a well connected network (if states were localised on a single nanotube then $n_\mathrm{h} \propto r$). 3D-VRH has been observed in many SWNT network systems in the literature [37, 38, 46, 55]. Control of the dimensionality has been achieved through doping of the networks [37], strongly doped networks exhibiting higher dimensional behaviour presumably indicating a doping mediated control of the connectivity. The dimensionality has also been demonstrated to be affected by sample structure [38], harsh acid treatments providing a breaking up of bundles which add to the number of fibrillar components and increase the network connectivity, thereby altering the dimensionality from 2D to 3D; a concomitant increase in T_0 was observed from 500 K to 5000 K indicating a decrease in the product $g(E_\mathrm{F}) \cdot \alpha^3$ as a result of increased disorder and/or increased charge carrier localisation.

Comparison between the fitting parameters for thin-id and thick-id in the laboratory-air exposed state reveal $T_0(\mathrm{thin}) \sim 60 \times T_0(\mathrm{thick})$ and $G_0(\mathrm{thick}) \sim 9 \times$

G_0(thin).

Physically G_0 describes the geometry of the samples, increasing both with cross-sectional area (and therefore the number of contributing conducting filamentary branches in the network) and in the case of a series combination of metallic and localised conduction (Equation 3.3) G_0 also varies with the fraction of total length described by VRH or metallic conduction. The observation of larger G_0 in thick-id is expected.

The parameter T_0 is inversely proportional to the density of states at the Fermi level, $g(E_\mathrm{F})$, and is extremely sensitive to the localisation length, α, as $T_0 \propto g(E_\mathrm{F})^{-1}\alpha^{-1/3}$. In a thick nanotube network, such as thick-id, all-metallic pathways are expected to dominate the conduction due to high connectivity and therefore large degree of freedom for the current pathway. The density of states at the Fermi level would be expected to be greater in a network with an increased proportion of metallic pathways, giving a smaller T_0. Depending on the location of carrier localisation a decreased network thickness may reduce the degree of wavefunction overlap. Kaiser *et al.* [161] attributed an increase in T_0 as network thickness decreased to a reduced localisation length by consideration of the increased sensitivity of T_0 to α. However, Benoit *et al.* [55] observed an increase in T_0 when the density of nanotubes in a polymer matrix is varied which was attributed to a reduction in the localised carrier density by reference to a compressed SWNT mat. By fractionally varying $g(E_\mathrm{F})$ in proportion to the nanotube filling fraction a constant α was obtained [55] suggesting that localisation occurs at regions unaffected by the nanotube density, i.e. localisation occurs in the transverse direction within bundles or bundle interfaces. Without sufficient studies on how the nanoscale morphology varies with network thickness it is not certain whether the increased T_0 in thin-id network is a result of a reduction in $g(E_\mathrm{F})$ or $g(E_\mathrm{F})$ and α.

The exposure of UV-desorbed SWNT network thin-id to laboratory-air increases G_0 by 235% and decreases T_0 by 52%. The increase of G_0 after laboratory-air exposure of thin-id is due to an increased connectivity of the network as a result of the oxygen doping of semiconducting SWNT [15,157], shifting the Fermi energy into a transport band of a percentage of SWNT and increasing $g(E_\mathrm{F})$. The increase in $g(E_\mathrm{F})$ causes a decrease in T_0 upon laboratory-air exposure of thin-id as $T_0 \propto g(E_\mathrm{F})^{-1}$. Similar effects have been observed by Skakalova *et al.* [36] who observed an increased conductance and increased far-IR absorbance as charge carrier density in nanotube networks was increased by donor doping. The shifting of $g(E_\mathrm{F})$ through adsorption of dopants thereby increasing the number of contributing fibrillar conduction paths may also change the localisation

length through geometrical means. As discussed above Benoit [55] determined that the localisation length of SWNT networks of various densities was constant. Investigation of the variation of α with network geometry is required. Oxygen adsorption may increase the localisation length. Increasing the disorder of SWNT through ion-irradiation has been shown to increase the localisation of the electronic wavefunctions [162]. The mean free path of charge carriers in SWNT has been shown to be reduced by increased disorder [58]. Dangling bonds at defect sites can be satisfied through oxygen adsorption [88], this may decrease the electronic 'disorder' of the nanotube and therefore reduce the localisation of wavefunctions, increasing α, thereby decreasing T_0. The possibility exists that the above mechanism occurs through oxygen adsorption on nanotubes through laboratory-air exposure. The presence of Na impurity as a result of SDS exposure may provide a path for oxygen adsorption and associated charge transfer [31], it is therefore desirable that the transport characteristics be investigated for SWNT networks with varying degrees of residual Na. Fe catalyst impurities within the SWNT network may also perturb the inherent electronic properties of SWNT, it has been noted that the presence of residual catalyst particles decreases the activation energy for oxidation [96].

The effect of water vapour contained within laboratory-air must also be considered in the response of thin-id and thick-id networks. As discussed in Section 1.5, water molecules on CNT act as a charge trap [107, 111] and n-type dopant [106–109]. Theoretical calculations predict $0.03e^-$ transferred from single H_2O molecule to a CNT [106], reducing the conductance of p-type SWNT devices under low humidity [107, 108]. Compensation of p-type SWNT devices by electrons donated from H_2O molecules has been observed to increase the conductance under very humid conditions [107–109] (humidity $>$ 65% [107]), changing the temperature dependence from semiconducting to metallic [109]. However, under laboratory conditions humidity $<<$ 65%, water molecules are expected to provide weak electron donation, slightly compensating the p-type doping effect of oxygen adsorption. Watts *et al.* suggests that water-vapour may reduce the conductance of SWNT by affecting the charge-transfer caused by chemisorbed oxygen [95], as discussed in Section 1.5 and Chapter 4.

Due to differences in production, purification and processing a large degree of heterogeneity exists between the reported electrical characteristics of SWNT networks, as discussed in Section 1.4.3. SWNT networks whose temperature dependence is described by VRH exhibit a range of dimensionality and values of T_0, a sample of the reported results in the literature is given in Table 3.4. The localisation length α

Author *et al.*	Sample description	d	T_0 (K)	α (nm)	Notes
Shiraishi [48]	HiPco SWNT purity = 95%. Avg. sample thickness 150 nm.	1D	34	10000	Calculated using 1D-VRH formula $T_0 = 8e^2/(k_B\kappa\alpha)$ with C_{60} relative dielectric const. κ.
Vavro [37]	Purified HiPco SWNT, H_2SO_4 doped.	1D	60	350	α calculated using VRH formula, Eqn. 1.9, $d = 1$ and $g(E_F) = 2.187$ eV^{-1}nm^{-1} [9].
Kymakis [149]	Carbolex SWNT, purity = 60%. Sample thickness 200 nm.	3D	15	-	Purification of SWNT by hydrothermal method [163] increased purity to 90% and $T_0 = 12$ K.
Fuhrer [52]	SWNT produced by arc discharge, purified in HNO_3. Sample size 3 mm x 1 mm x 0.05 mm.	3D	250	700	α calculated from $R(kT, 0) = R/2(0, 3/8eEa)$ where E is electric field and a the Bohr radius of an electronic state.
Benoit [55]	Pressed pellet formed from arc discharge SWNT, typical purity between 70% and 90%.	3D	-	8	No value given for $g(E_F)$ or T_0 from which α is calculated.
Liu [38]	Arc discharge SWNT purified by nitric acid bath for 2 hours.	3D	5000	-	As prepared sample described by 2D-VRH with $T_0 \sim 525$ K.
Yosida [164]	Arc discharge SWNT, purity 60%	3D	10600	-	T_0 value recorded above 20 K $< T <$ 300 K.

Table 3.4 Sample of reported values of T_0 extracted from the temperature dependence of SWNT networks as available in the literature.

may be calculated from T_0 requiring calculation or estimation of $g(E_F)$. Theoretical calculations predict that metallic SWNT have a density of states at the Fermi level of $g(E_F)_{th.} = 2.187$ eV^{-1}nm^{-1} [9]. Ideally the localisation length would be calculated from an average density of states of the SWNT network. An estimation of an average $g(E_F)$ is obtainable from the literature. Fuhrer *et al.* observes 3D-VRH with $T_0 = 250$ K for a SWNT network of thickness 50 μm [52]; temperature and electric field dependence of R determine the Bohr radius of localised states $a = 700$ nm through the relation

$$R(k_B, 0) = \frac{R}{2}(0, \frac{3}{8}qEa) \tag{3.5}$$

Approximating the localised Bohr radius as calculated by Fuhrer *et al.* [52] to the localisation length provides (Equation 3.2) a density of states at the Fermi level of $g(E_F)_{net.} = 2.2\times10^{-6}$ eV^{-1}nm^{-1} for the ensemble of air exposed SWNT. As expected $g(E_F)_{net.} < g(E_F)_{th.}$ due to a small fraction of total network contributing to the

Network	Treatment	$T = 4$ K		$T = 10$ K	
		$G(0,T)$ (nS)	l/d	$G(0,T)$(nS)	l/d
thin-id	lab.-air-exp.	580 ± 20 (3%)	$6.4 \pm 0.2\times10^{-4}$ (3%)	3710 ± 10 (0.3%)	$6.04 \pm 0.05\times10^{-4}$ (0.8%)
thin-id	UV-des.	15.2 ± 0.5 (3%)	$7.0 \pm 0.2\times10^{-4}$ (3 %)	169.4 ± 0.6 (0.4%)	$6.59 \pm 0.05\times10^{-4}$ (0.8 %)

Table 3.5 Extracted parameters relating non-Ohmic VRH conductance, Equation 3.6, and Figure 3.5.

conductance. Under the assumption that the effective thickness of thick-id (1.3 μm) is comparable to the measured thickness of the network presented by Fuhrer *et al.* [52] (50 μm) the localisation length of electronic states in thick-id may be calculated using $g(E_{\mathrm{F}})_{\mathrm{net.}}$, $\alpha_{\mathrm{thick-id}} = 2.3$ μm. Calculating α for thick-id with $g(E_{\mathrm{F}})_{\mathrm{th.}}$ provides $\alpha_{\mathrm{thick-id}} = 23$ nm. Localisation lengths calculated from the density of states at the Fermi energy for a single metallic SWNT and the density of states at the Fermi energy for the network ensemble provide minimum and maximum estimates respectively. The localisation length presented by Fuhrer *et al.* $\alpha = 700$ nm [52] was noted to be less than 1.6 μm, the theoretical mean free path of a (5,5) nanotube at 250 K [165]. Experimentally mean free paths of 1.6 μm [57] and 0.8 μm [58] have been recorded at room temperature within single SWNT, with an increasing defect density noted to reduce the mean free path. The mean free path must be greater than the localisation length in order to maintain wavefunction coherence, thus it seems likely that the upper limit of estimated localisation length is excessive.

At low temperature $I - V$ curves of both thin-id and thick-id networks became non-linear, Figure 3.2. Thin-id SWNT network in both the lab.-air-exposed and UV-desorbed state displayed non-linearities at 100 K with large non-linearities observable at 60 K. Thick-id SWNT network became non-linear at 20 K. A possible origin of this non-linear behaviour is electric field E enhanced hopping probability providing non-Ohmic VRH. The non-Ohmic VRH conductance can be expressed as [56]

$$G(E,T) = G(0,T)\exp\left(\frac{eVl}{dk_{\mathrm{B}}T}\right) \tag{3.6}$$

where d, E and V are voltage probe separation, electronic field and measured voltage between probes, l is the length parameter related to the maximum hop length between the hopping sites. Figure 3.5 shows the conductance data as a function of applied voltage for the thin-id network in both the lab.-air-exposed and UV-desorbed states for $T = 4$ K and 10 K. There is good agreement between the data and fitting

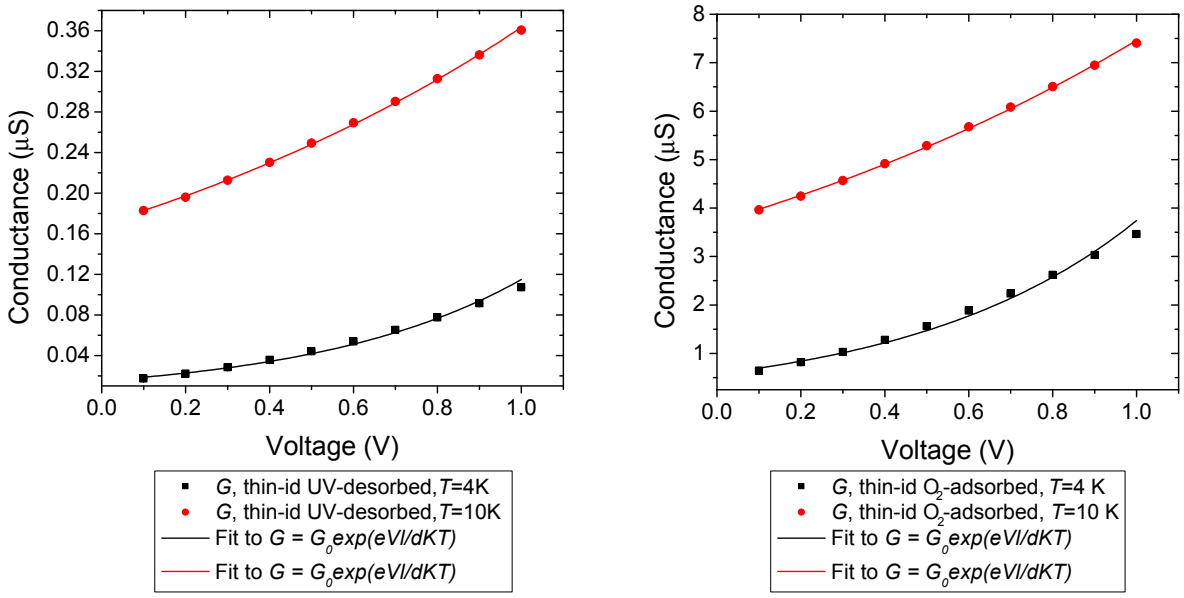

Figure 3.5 Error weighted fitting results for field dependent variable range hopping conduction, Equation 3.6, at $T = 4$ K and 10 K in UV-desorbed and O_2-adsorbed states. Error bars obscured by data points.

curves in both lab.-air-exposed and UV-desorbed states. The voltage probe distance is unknown due to the filamentary nature of the SWNT network and interdigitated metallic contacts, therefore the parameter l/d is extracted from Figure 3.5 and given in Table 3.5. At both the temperatures shown the non-linearity in $G(V)$ decreases from the UV-desorbed to laboratory-air exposed state implying a small but significant reduction in the maximum hop length dependent parameter, l/d. At $T = 4$ K there is a $(9 \pm 4)\%$ decrease from the UV-desorbed to laboratory-air exposed state. At $T = 10$ K there is a $(8 \pm 1)\%$ decrease from the UV-desorbed to laboratory-air exposed state. A change in effective voltage probe distance is possible considering the proposed change in geometry of the conducting fibrillar network, as indicated through an increase in the geometrical pre-factors extracted from the temperature dependence of conductance in the UV-desorbed and laboratory-air exposed states. The assumption that d is changing and α is constant upon laboratory air exposure implies that $g(E_F)$ of thin-id is doubling upon O_2 adsorption, $g(E_F) \propto 1/T_0$. Experimentally the density of states of semiconducting SWNT have been shown to increase upon exposure to pure O_2 by scanning tunnelling microscopy [15]. Theoretical studies performed by Jhi *et al.* [84] calculated the DOS of a semiconducting SWNT in which one O_2 molecule was adsorbed per atom thick cross-sectional slice. The DOS at the Fermi energy was shown

to approximately double in comparison with the DOS of the SWNT in addition to introducing a greater DOS at $\mid E \mid > E_{\mathrm{F}}$ with a shape determined by the oxygen molecular states.

However, the exponential variation of conductance with applied voltage may also be described by the non-Ohmic fluctuation-induced tunnelling model [166]

$$G = G_0 \exp(V/V_0) \tag{3.7}$$

where G_0 is the temperature dependent zero-field conductance. The V_0 parameter depends strongly on the conductance limiting barrier energy, decreasing with increasing temperature. Exposure to laboratory-air from a UV-desorbed state introduces an increase in V_0 indicating an increase in tunnelling probability through the barrier. The observation of non-linearity at 100 K is in correspondence with the reported energy barrier approximation in SWNT mats [158] in which the temperature dependency of the zero-bias conductance followed the FIT functional form.

Further investigation into the field-dependent conductivity is required in order to accurately determine the conduction mechanism under high applied electric field. Precise control of the E field is required in order to determine the energies involved in hopping/tunnelling.

3.3 Conclusion

The dependence on temperature of electrical conductance of thin (labelled thin-id) and thick (labelled thick-id) networks of SWNTs has been investigated. Thin-id network was shown to follow Mott's 3D-VRH conductance model in both the laboratory-air-exposed and UV-desorbed state. Thick-id network was shown to follow a model that includes a metallic component in series with a disorder induced 3D-VRH component. The VRH parameter T_0 was shown to be dependent on SWNT network thickness. Thinner networks incorporate a higher proportion of semiconducting SWNTs in the current path, reducing the averaged density of states at the Fermi energy of the nanotube ensemble. Exposure to UV radiation has the effect of desorbing adsorbates from a proportion of nanotubes (long time constants are associated with the desorption process - see Chapter 4.2), reducing the connectivity of the network and therefore G_0. The dominating effect of laboratory-air-exposure was considered to be oxygen doping which increased the connectivity of the SWNT network and therefore G_0, indicating that the proportion

of nanotubes with a Fermi energy located in a transport band had increased.

The value of T_0 was found to decrease on exposure to laboratory-air from a UV-desorbed state as a result of an increase in $g(E_{\mathrm{F}})$. T_0 is also strongly dependent on the localisation length the dependence of which, if any, on network thickness and adsorption state cannot be quantified with the current experimental data. Further studies on the low-temperature magnetic field dependence of conductivity would provide the localisation length of the networks. Field dependent conductance measurements identified an exponential dependence of conductance on applied voltage, indicating a field mediated increase in the hopping or tunnelling probability. The likely presence of SDS and associated Na ion may provide a point of reaction for oxygen and be accompanied by an associated charge-transfer. An investigation is required into the effect of differing amounts of residual SDS on the temperature dependence of conductance.

Chapter 4

Sensing via Conductance

The two-terminal conductance of a SWNT network is sensitive to oxygen-adsorption. The adsorption behaviour is found to be dependent on the SWNT network adsorption state. Networks exposed to atmospheric conditions exhibit a conductance decrease upon oxygen-adsorption, whilst UV-desorbed networks exhibit a conductance increase upon oxygen-adsorption. The network adsorption kinetics are given by $G(t) - G(t = 0)$ versus time and provides information about the interaction between oxygen and the SWNT network.

4.1 SWNT network conductance response

Thin-id and thick-id SWNT networks presented in Chapter 3 were exposed to UV illumination, $\lambda = 400$ nm, intensity $= 0.03$ mW/cm^2, for 2.5 hours whilst under vacuum of pressure $\sim 1 \times 10^{-5}$ mbar, desorbing adsorbates and decreasing the conductance, Figure 4.1. The conductance of thin-id and thick-id networks after 2.5 hours UV-desorption decreased by $45 \pm 2\%$ and $3 \pm 3\%$ respectively, approaching baseline conductance.

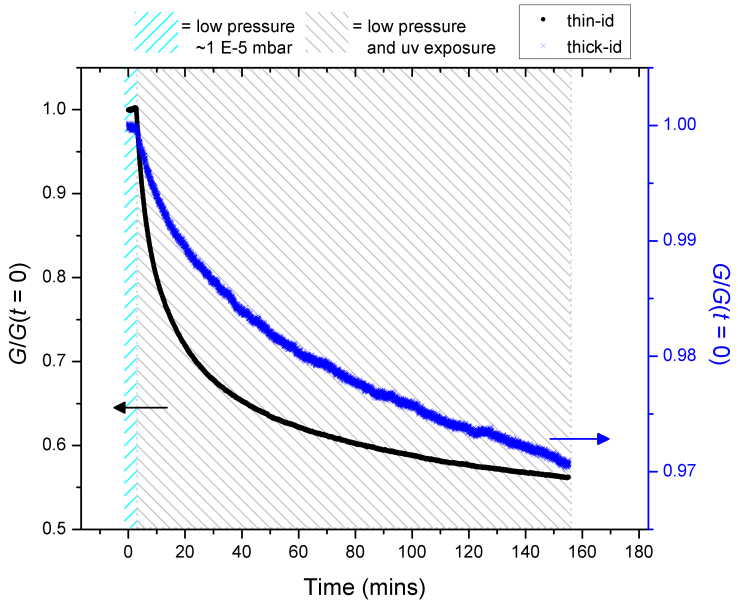

Figure 4.1 Exposure of thin-id and thick-id SWNT networks to UV radiation. Error in $G \pm 1.5\%$ for thin-id and thick-id SWNT networks, error bars not shown.

Carbon nanotubes exhibit strong optical absorption at ~ 270 nm due to π-electron plasmon excitation [142]. Molecular photodesorption of adsorbates occurs through the dissipation of photoexcited plasmon energy disrupting the molecule-nanotube binding. The desorption of oxygen in vacuum decreases the number of hole charge carriers in the network, reducing the density of states at the Fermi level [15, 86]. The decrease of conductance with UV-desorption is a result of removal of oxygen dopants from the SWNT network. Chen *et al.* observed a three order of magnitude decrease in conductance of an air-exposed individual SWNT (grown by CVD direct on substrate) under UV-desorption in vacuum ($\lambda = 254$ nm, intensity $= 2$ mW/cm^2) to occur over 250 seconds [118]. The faster conductance decrease under UV-desorption demonstrated by Chen *et al.* in comparison to Figure 4.1 is a result of both the efficient photodesorption of SWNT occurring at $\lambda \sim 270$ nm and the increased intensity of irradiation. Semiconducting nanotubes exhibit a large response to molecular doping/de-doping [15, 16]. The change in conductance for thin-id and thick-id networks between air-exposed and UV-desorbed state was less than that reported by Chen *et al.* due to the mix of metallic and semiconducting nanotubes in thin-id and thick-id networks.

Upon stabilisation of the SWNT networks conductance (determined through stability

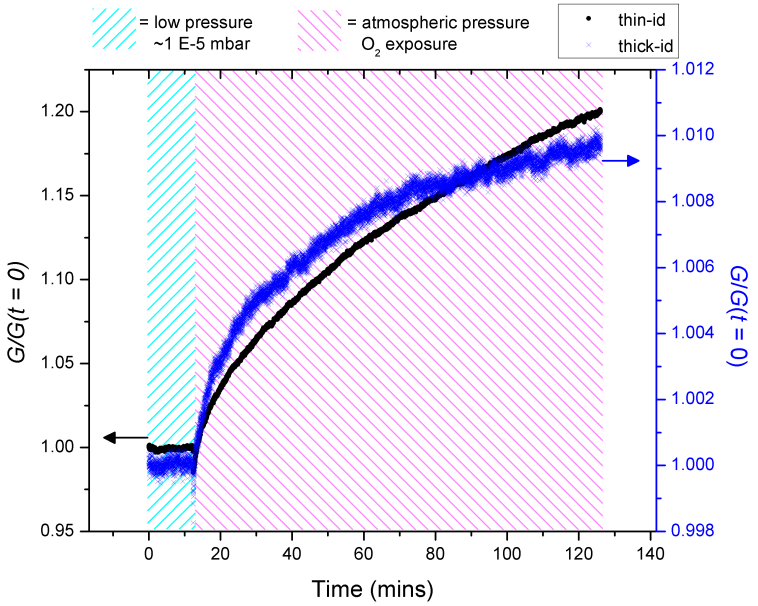

Figure 4.2 Response of thin-id and thick-id networks to O_2 from a UV-desorbed state. Conductance increase is greater for the thin-id SWNT network than for the thick-id SWNT network. $V = 10$mV for both SWNT networks. Error in $G \pm 1.5\%$ for thin-id and thick-id SWNT networks, error bars not shown.

of the I - V trace) the sample chamber was exposed to atmospheric pressure molecular oxygen providing a conductance increase due to O_2 adsorption, Figure 4.2.

Oxygen exposure increases the number of hole charge carriers - increasing the density of states at the Fermi level and increasing the conductance, Figure 4.2. This is confirmed by the observed increase in the VRH geometrical prefactor G_0, reported in Chapter 3, indicating an increase in the number of contributing filamentary conduction paths. An increase in $g(E_F)\alpha^3$ was also reported in Chapter 3, most likely due to an increase in $g(E_F)$ although perturbation of α cannot be eliminated at present. The increase of conductance with oxygen adsorption approaches a steady state after 2 hours exposure. The conductance of thin-id increases by $20 \pm 2\%$ the conductance of thick-id increases by $1 \pm 2\%$.

SWNT networks formed from predominantly metallic and individual tubes provide a conductance response to an analyte which scales with sensor base conductance [117]. The UV-desorbed thick-id network exhibits a smaller response to oxygen due to a reduced connection to surface sites (as a result of a 30% increase in effective thickness and possibly increased bundling in thick-id) and an increased metallic character as reported in Chapter 3.

Device	$\Delta G/G_0$ (%) over 2 hours	$\Delta G/G_0$ (%) over 500 seconds
Thin-id (UV-desorbed)	$+20 \pm 2$	$+4 \pm 2$
Kuo [167], untreated	-	+1
Kuo [167], treated	-	+3
Collins [15], baked in air	-	+15

Table 4.1 Comparison of changes in conductance of nanotube networks to 1 atm. oxygen exposure from from vacuum. The percentage change of thick-id was within the bounds of error for the measurement.

Although the response of SWNT networks to oxygen exposure is dependent on the network thickness, comparison may be made with similar networks reported in the literature, Table 4.1. Kuo *et al.* directly compared the response of as produced SWNT to 1 atm. oxygen exposure from vacuum pressure 1×10^{-4} mbar to a SWNT sample in which surface impurities were removed with a flash-lamp triggered exothermal reaction [167]. Removal of surface impurities increased the base conductance as a result of improving the junctions between SWNTs. In addition the removal of surface impurities increased the magnitude and speed of the conductance increase upon O_2 adsorption indicating that surface impurities inhibit the interaction of oxygen with SWNT. Collins *et al.* reported SWNT networks which had been annealed in air ($\sim$ 700°C) to remove amorphous carbon displayed a $10 - 15\%$ increase in conductance occurring over seconds upon oxygen adsorption [15]. As can be seen in Table 4.1 the response of the UV-desorbed thin-id network is similar to the networks reported by Kuo and Collins. In Section 2.1.3 the purity of the SWNT HiPco material from which thin-id and thick-id were formed was found to have an approximate relative purity of 60%. Removal of carbonaceous impurities through heating in air or an exothermal reaction would possibly eliminate the need for UV-desorption by reducing the bonding sites for chemisorbed oxygen. The response time may be increased through the removal of carbonaceous impurities which hinder the interaction of oxygen with nanotubes.

Laboratory-air exposed thin-id and thick-id SWNT networks were cycled between a vacuum pressure $\sim 1\times10^{-5}$ mbar and atmospheric pressure molecular oxygen, Figure 4.3. Conductance of both thin-id and thick-id networks decreased upon molecular oxygen exposure. Vacuum pressure failed to recover the conductance completely, resulting in an overall decrease in conductance. As noted for the increase in conductance upon O_2 exposure from a UV-desorbed state, Figure 4.2, conductance response (ΔG)

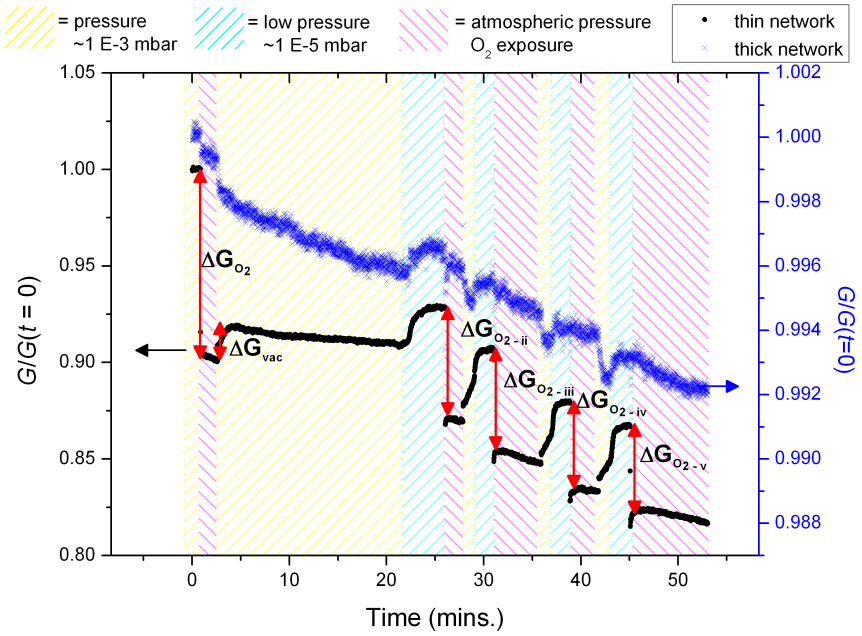

Figure 4.3 Response of thin-id and thick-id SWNT networks to O_2 / vacuum ($\sim 1 \times 10^{-5}$ mbar via $\sim 1 \times 10^{-3}$ mbar) cycling from a laboratory-air-exposed state. $V = 10$mV for both SWNT networks. Error in $G \pm 1.5\%$ for thin-id and thick-id SWNT networks, error bars not shown.

	ΔG_{O_2-i}	ΔG_{O_2-ii}	ΔG_{O_2-iii}	ΔG_{O_2-iv}	ΔG_{O_2-v}
$\Delta G/G_0\%$	9 ± 2	6 ± 2	6 ± 2	6 ± 2	6 ± 2

Table 4.2 Percentage change of conductance of thin-id SWNT network upon O_2 exposure from vacuum pressure $\sim 1 \times 10^{-5}$ mbar.

is reduced in the thicker network. The average change in conductance for thin-id upon exposure to oxygen from a vacuum pressure $\sim 1 \times 10^{-5}$ mbar is given in Table 4.2.

As shown in Figure 4.1 UV-desorption is required to remove chemisorbed O_2 species. Under the applied vacuum pressure $\sim 1{\times}10^{-5}$ mbar chemisorbed oxygen is not desorbed. Collins *et al.* suggest chemisorbed oxygen is only removed after heating to $110° - 150°$C after several hours [15]. The observed decrease in conductance for cycling between vacuum and oxygen exposure could be caused by scattering from defects or non-thermal phonons generated by gaseous collisions with the tube walls as suggested by Sumanasekera *et al.* [82]. However this mechanism does not satisfactorily explain the irreversibility in the change in conductance when cycling between oxygen exposure and vacuum pressure, Figure 4.3.

The oxygen used for exposure to the SWNT networks is supplied at high purity (Chapter 2), however the filled bladder method used in introducing oxygen to the sample chamber may also introduce water vapour. The effect of water vapour on nanotube networks has been discussed in Section 1.5. At low humidities ($<< 65\%$) water adsorption decreases the conductance of CNTs [95, 107, 108]. Water has been proposed to be a mild electron donor when adsorbed on SWNT [107] and compensation of *p*-type SWNTs has been observed [108]. Watts *et al.* proposes that hydrogen bonded water decreases the electronegativity of chemisorbed oxygen species reducing the density of hole carriers [95]. In both proposed mechanisms the incomplete desorption of water in vacuum and the presence of chemisorbed oxygen on the SWNT network would lead to a non-recoverable baseline conductance. Indeed this has been reported by Watts *et al.* who observes MWNT mats with a large degree of carboxylic defects to exhibit a decrease in conductivity upon exposure to laboratory-air from vacuum with a non-recoverable baseline conductance upon re-application of vacuum pressure. The above mechanism could be responsible for the conductance decrease in thin-id and thick-id devices observed in Figure 4.3.

The purity of the SWNT networks plays an important role in sensor response time, reversibility and magnitude of conductance change. The possibility should be considered that the origin of charge-transfer from the nanotube network upon oxygen exposure may not be a result of direct oxygen adsorption on the SWNTs. The presence of Na impurities within the SWNT network may play a role in the change in conductance. Oxygen is highly reactive with Na leading to the possibility of charge-transfer through a Na-O complex. Photoemission studies by Goldoni [31] indicate that the removal of residual Na occurs only after annealing in high vacuum at 1270 K for 2 hours. The Na containing SWNT network responded electrically to oxygen adsorption. After removal of Na from SWNT network Goldoni [31] observed no electrical response of the network to oxygen. In addition, trace amounts of catalyst impurities may decrease the activation energy for oxidation [96] thus perturbing the conductance response of the SWNT network to oxygen adsorption.

Defects have been demonstrated to mediate SWNT sensor response to a range of analytes [104,105]. Oxidation occurring at 2% of the carbon atoms increased the amount of charge transfer by 1000% [104]. The SWNT starting material had comparable G/D Raman intensity ratios to a material of purity 60% as shown in Section 2.1.3. Sonication could have further increased the defect density. The conductance increase upon O_2

adsorption from a UV-desorbed state is comparable with the literature [15,167], although as shown in Figure 4.2 the magnitude of ΔG on oxygen adsorption is highly dependent on the thickness of SWNT network. Chemisorbed oxygen could provide a mechanism for a decrease in conductance upon further exposure to oxygen due to water adsorption as proposed by Watts *et al.* [95] and discussed previously.

The highest energy adsorption site determines the sensor response and reversibility. Reversibility and sensitivity of SWNT network resistive sensors have been increased by coating the SWNT network with a polymer amine which decreases the binding energy and provides additional sites for adsorption [113]. Exploitation of the polymer amine technique provides reversible sensitivity at the parts-per-trillion level to thionyl chloride, a strong electron acceptor [113]. In addition to purification of SWNT networks the coating of thin-id and thick-id networks is a possible method for improving the sensor response and reversibility.

Figure 4.4 shows the exposure of two UV-desorbed samples under vacuum ($\sim 1 \times 10^{-5}$ mbar) to methane. The sample thickness is within the range spanned by the thin-id and thick-id samples presented earlier in this Chapter. Methane adsorption decreases the sample conductance. Methane is an electron-donating-gas; charge transfer shifts the Fermi level towards the conduction band. The decrease in conductance could indicate a compensation effect implying that the SWNT network was p-type prior to methane exposure. Therefore charge-transfer from the adsorption of methane would reduce the density of charge carriers in the network, reducing conductance.

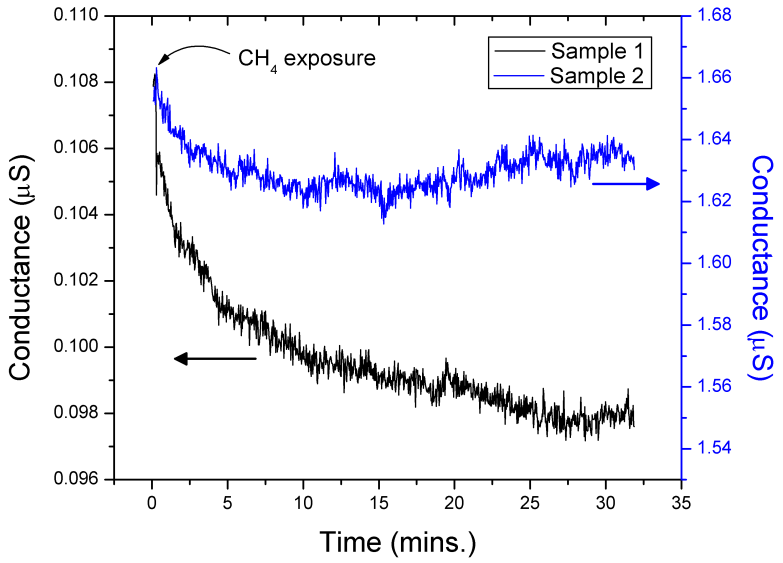

Figure 4.4 Preliminary data showing SWNT network exposure from vacuum ($\sim 1 \times 10^{-5}$ mbar) to CH_4 from a UV-desorbed state. $V = 10$mV for both SWNT networks. The thickness of samples 1 and 2 is within the range spanned by thin-id and thick-id samples presented earlier in this Chapter.

4.2 Oxygen-adsorption kinetics

Samples of increasing thickness were deposited on quartz substrates with two single stripe metal contacts as described in Section 2.1. The thickness was determined with a UV-visible spectrophotometer and two-terminal resistance versus transmittance at 500 nm recorded, Figure 4.5. Samples A and F, henceforth referred to as thin-mat and thick-mat, were exposed to atmospheric pressure molecular oxygen after UV-desorption for ~ 40 hours in vacuum of pressure $\sim 1 \times 10^{-5}$ mbar, Figure 4.6. The conductance of both networks increased with time upon exposure to molecular oxygen, Figure 4.7.
The observed time dependence $G(t) - G(t = 0)$ can be well described by a diffusive adsorption process. As outlined previously in Section 1.6.2 the diffusion front in an isotropic material has a Gaussian profile

$$C(x,t) = \frac{s}{2\sqrt{\pi D t}} \exp\left(-x^2/4Dt\right) \qquad ((1.13))$$

where $s = \int_{-\inf}^{+\inf} C dx$ the total amount of substance and D is the molecular diffusion coefficient. As the concentration of oxygen molecules spreads out through the network a proportional amount of charge transfer occurs.

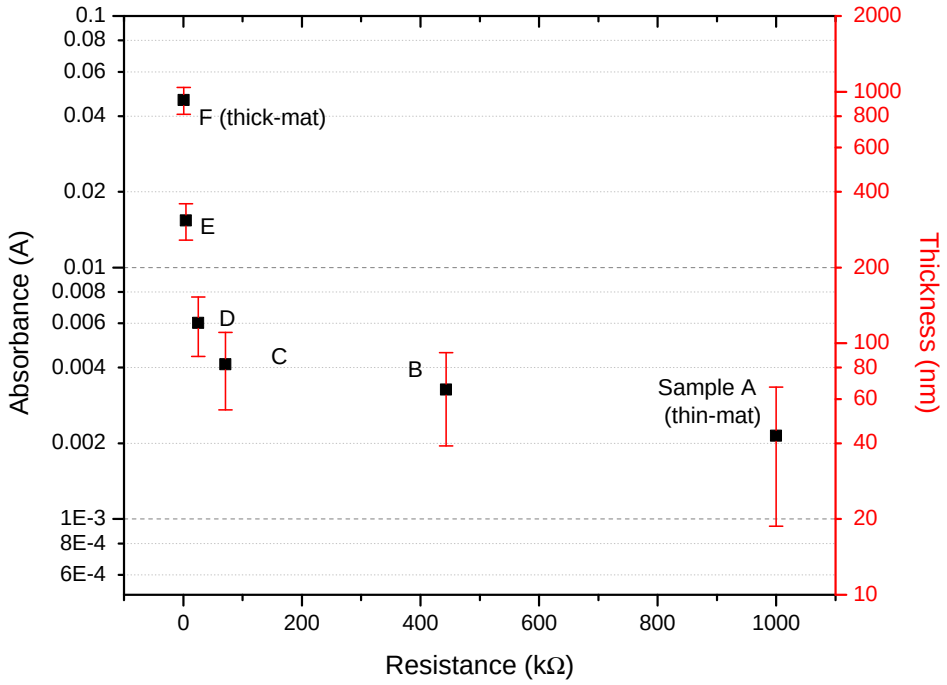

Figure 4.5 Resistance versus absorbance at $\lambda = 500$ nm and thickness of SWNT network on glass microscope slide. Error bars represent error in Beer's law derived SWNT network thickness, see Chapter 2.1.2. The error in the absorbance measurements are $\Delta A \pm 0.001$ A.

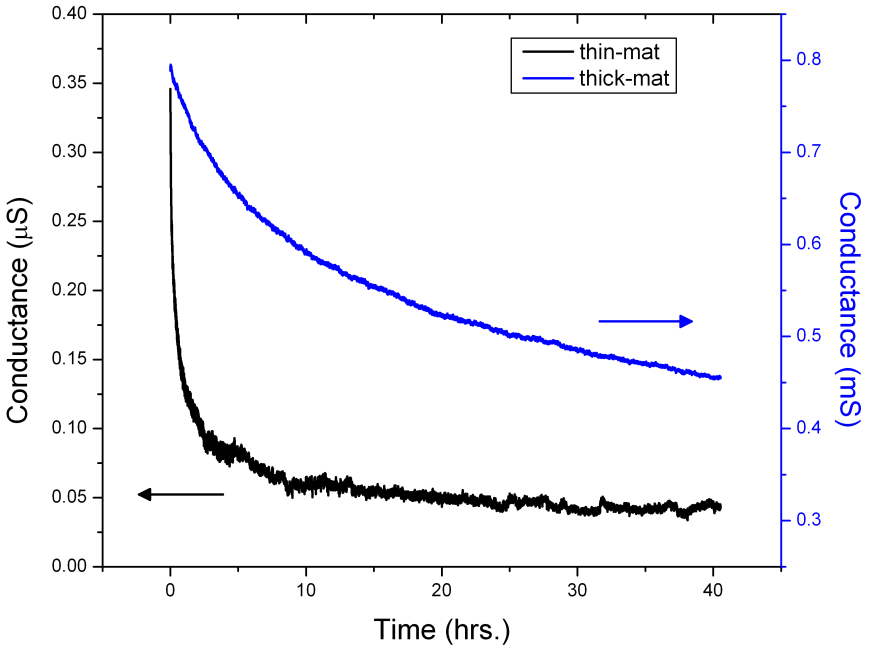

Figure 4.6 Thin-mat and thick-mat SWNT networks exposed to UV radiation for 40 hours. $V_{\text{thin-mat}} = 10$ mV, $V_{\text{thick-mat}} = 1$ mV. Error in $G_{\text{thin-mat}} = 7\%$, error in $G_{\text{thick-mat}} = 15\%$, error bars not shown. Sample thickness determines the rate of desorption.

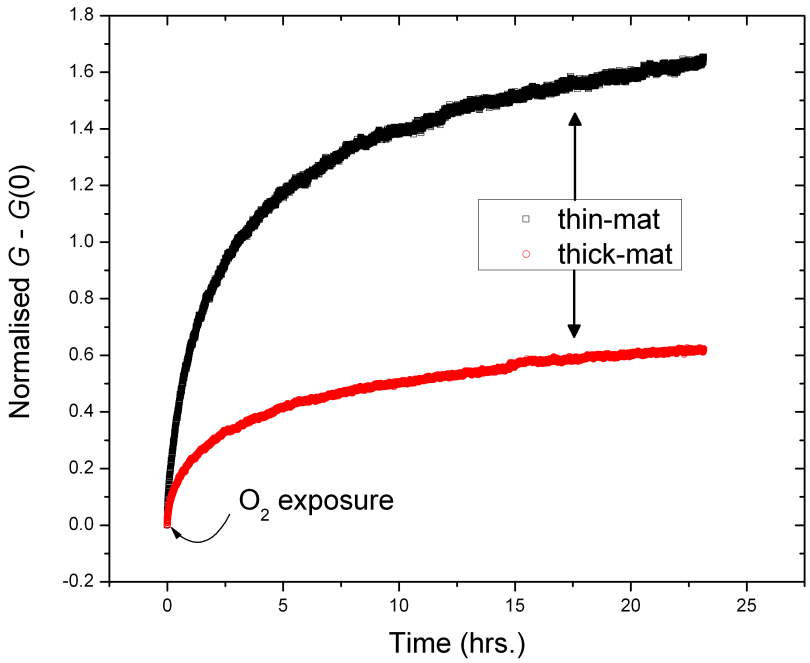

Figure 4.7 Normalised $G(t) - G(t = 0)$ versus t for thin-mat and thick-mat SWNT networks exposed to molecular oxygen at $t = 0$ over a period of 23 hours. $V_{\text{thin-mat}} = 10$ mV, $V_{\text{thick-mat}} = 1$ mV. Error in $G_{\text{thin-mat}} = 3.7\%$, error in $G_{\text{thick-mat}} = 15\%$, error bars not shown.

Sample	d_1	Range of t (secs.)	d_2	Range of t (secs.)
thin-mat	0.66 ± 0.02	$0 < t < 174$	0.582 ± 0.001	$174 < t < 4900$
thick-mat	0.58 ± 0.02	$0 < t < 433$	0.451 ± 0.001	$433 < t < 5800$

Table 4.3 Fitting parameters for linear fit to Figure 4.8.

The variation in conductance, $G(t) - G(t = 0)$, can be considered to be proportional to the standard deviation of the spatial distribution of oxygen molecules. The adsorption kinetics of thin-mat and thick-mat SWNT networks exhibit two separate linear regimes when plot on log-log axes, Figure 4.8, indicating a power-law relationship of the form

$$G(t) - G_0 = a \cdot t^d \tag{4.1}$$

where d is the diffusion parameter and a is a constant. Parameters of Equation 4.1 are extracted from Figure 4.8 and given in Table 4.3. The variance of a normal diffusive process was defined previously, Section 1.6.2, as

$$\sigma^2 = 2Dt^\gamma \tag{(1.16)}$$

where σ is the standard deviation of mass distribution and γ is an index which describes the diffusive regime ($\gamma = 1$ describes normal diffusion, $1 < \gamma < 2$ describes super-diffusion, $\gamma < 1$ describes sub-diffusion and $\gamma = 2$ describes ballistic diffusion [124, 125]). Therefore, for a normal diffusive process $\sigma = 2Dt^{1/2}$ giving $d = 0.5$ in Equation 4.1. Both thin-mat and thick-mat samples have $d_1 > 0.5$, see Table 4.3, characteristic of super-diffusion [125] where $< x^2(t) >$ evolves non-linearly with time. Super-diffusive behaviour or enhanced diffusion is observed in porous systems, fractal geometries and Levy flights. The thickness of the samples determines the duration of the initial diffusive regime. A crossover occurs to a lower gradient, d_2, for both thin-mat and thick-mat samples. This second regime, characterised by d_2, was observed over a much longer time period, $\Delta t > 79$ minutes.

The thick SWNT network diffusion parameter $d_2 = 0.451$ is characteristic of sub-diffusive behaviour. Abnormal diffusion of this type ($\gamma < 1$) is more common and can be attributed to a trapping induced broad distribution of particle release time [124].

Possible trapping sites within the nanotube network are SWNT defects [168], semiconducting SWNT junctions [169] and nanotube bundle groves and interstitial sites [103]. Also, adsorption onto m-SWNT or bundles with m-SWNT at the surface

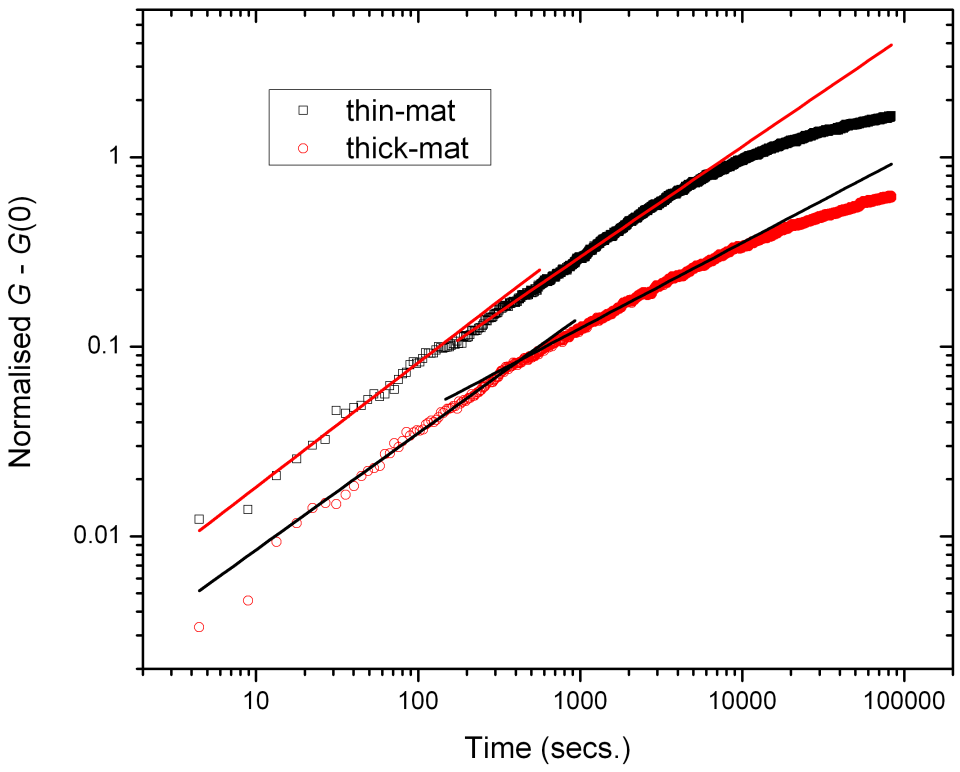

Figure 4.8 Normalised $G(t) - G(t = 0)$ versus t for thin-mat and thick-mat SWNT networks plot on double-log scales. $V_{\mathrm{thin-mat}} = 10$ mV, $V_{\mathrm{thick-mat}} = 1$ mV. Error in $G_{\mathrm{thin-mat}} = 3.7\%$, error in $G_{\mathrm{thick-mat}} = 15\%$, error bars not shown. Both samples exhibit regions of linearity. The thin-mat SWNT network has a gradient of 0.655 followed by a transition at $t = 174$ secs. ($\sim$ 3 mins.) to a gradient of 0.582. The thick-mat SWNT network has a gradient of 0.582 followed by a transition at $t = 433$ secs. ($\sim$ 7 mins.) to a gradient of 0.451. Both samples depart from a linear relationship at later t.

may act as trapping sites in terms of doping efficiency (smaller conductance increase expected from oxygen-adsorption on m-SWNT, see Section 1.5). The lower value of d for the thick network could therefore be explained by an increase in the metallic component within the filamentary conduction path, as described in Chapter 3. However, both samples undergo a transition to a regime with a lower value of d and it is therefore reasonable to assume that the adsorption kinetics of both samples become influenced by trapping mechanisms at $t = t(d_2)$. Zahab *et al.* observed gaussian diffusion to occur for water adsorption on a SWNT mat of thickness 200 μm in which the SWNT material was purified by means of acid treatment and annealing under nitrogen atmosphere at 1200°C [108]. Two regimes of characteristic diffusion parameter were found by Zahab to occur - a fast regime during the first 15 minutes with diffusion parameter $d = 0.7$ and a slower regime with characteristic diffusion parameter $d = 0.35$ occurring from 15 minutes to 14 hours. The difference in diffusion parameters and length of time over which they occur between the results reported in this Chapter and those reported by Zahab *et al.* reflects the variation in processing of the SWNT material, thickness of the SWNT mat and also the electronic and steric differences between water and O_2. Possibly the very long time over which Zahab *et al.* observes diffusion to be characterised by sub-diffusive behaviour is a result of hydrogen bonding between water molecules inhibiting molecular diffusion.

The adsorption kinetics for both samples depart from Gaussian diffusion at $t \sim 5000$ seconds ($t \sim 1.4$ hours). Considering the variation in conductance with time is proportional to the fractional surface coverage of the SWNT network, $(G(t) - G_0) \propto \Theta$, the thin-mat and thick-mat SWNT networks can be described in this later regime by an Elovich-type adsorption equation

$$\frac{\mathrm{d}\Theta}{\mathrm{d}t} = a^{-b\Theta} \tag{4.2}$$

where a and b are coefficients and Θ is the fractional surface coverage. The Elovich isotherm describes activated adsorption dynamics such as that for a charge-transfer limited adsorption process due to the build up of a space-charge layer on a semiconducting surface. Equation 4.2 describes a linear variation of Θ and therefore $G - G_0$ with $\log(t)$. The adsorption kinetics data for thin-mat and thick-mat samples versus time on linear-log axes, Figure 4.9, clearly show a linear regime, fit by the Elovich type equation

$$G(t) - G_0 = \xi \log(at) \tag{4.3}$$

where a is a constant and ξ is the gradient of the linear fit of $G(t) - G(t = 0)$ versus $\log(t)$. The extracted parameters are given in Table 4.4. The kinetics of adsorption of the thin-mat SWNT network appear to crossover to a lower value of ξ, whilst the thick-mat SWNT network maintains the same Elovich adsorption parameters. This is possibly indicative of a thickness dependent transition in the Elovich adsorption kinetics.

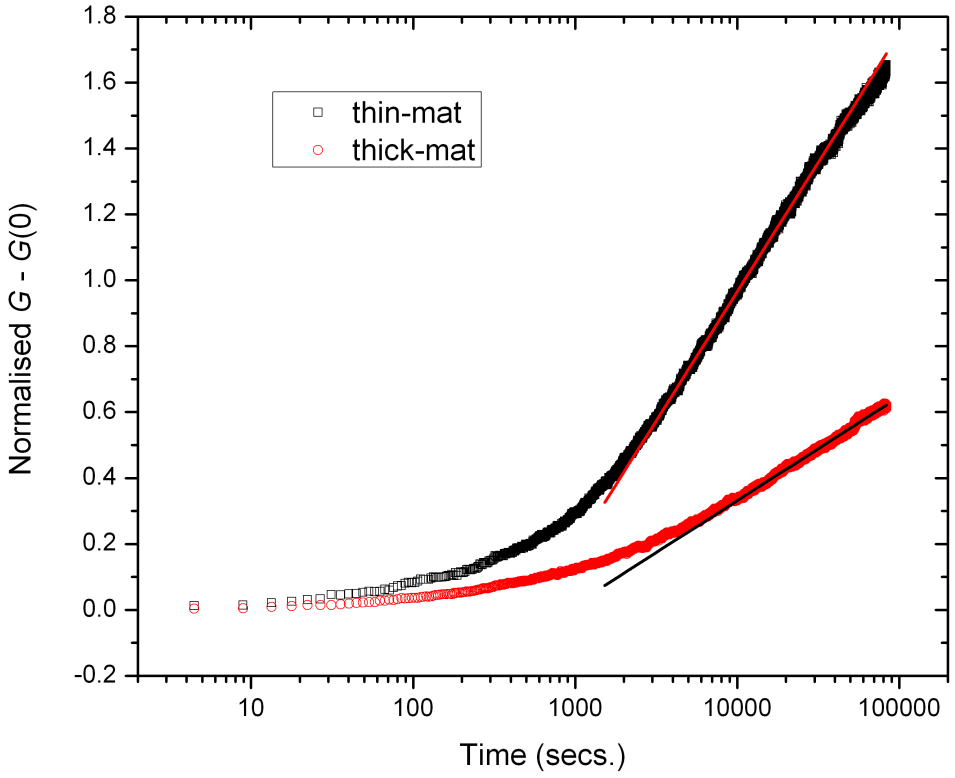

Figure 4.9 Normalised $G(t) - G(t = 0)$ versus t for thin-mat and thick-mat SWNT networks plot on linear-$(G(t) - G(t = 0))$ log-time axes. $V_{\text{thin-mat}} = 10$ mV, $V_{\text{thick-mat}} = 1$ mV. Error in $G_{\text{thin-mat}} = 3.7\%$, error in $G_{\text{thick-mat}} = 15\%$, error bars not shown. Both samples exhibit significant regions of linearity. The thin-mat SWNT network appears to undergo a transition to a reduced gradient after $t = 42786$ seconds ($\sim$ 12 hours). The thick-mat SWNT network displays linear behaviour in $(G(t) - G(t = 0))$ vs. log t from $t = 11277$ seconds ($\sim$ 3 hours).

The Elovich isotherm describes any adsorption mechanism that requires an activation

Sample	ξ	Range of t (secs.)	Duration (hours)
thin-mat	0.34 ± 0.02	$4900 < t < 42785$	10.9
thick-mat	0.14 ± 0.01	$11277 < t < 83340$	20.0

Table 4.4 Fitting parameters for linear fit to Figure 4.9.

energy ΔE and for which the activation energy increases with surface coverage, Θ, i.e. $\Delta E \propto \Theta$, yielding a general Elovich rate equation of the form

$$\frac{\mathrm{d}\Theta}{\mathrm{d}t} \propto A \exp^{-b\Theta/RT} \tag{4.4}$$

where A and b are constants and R is the universal gas constant. The Elovich-like adsorption demonstrated by the adsorption kinetics of thin-mat and thick-mat SWNT networks, Figure 4.9, is a result of charge-transfer limited adsorption. The SWNT network donates electrons to adsorbed molecular oxygen, $O_2 + ae^- \rightarrow O_2^-$, where $a \leq 1$ due to possible fractional charge-transfer through physisorption [84, 85] in addition to chemisorption [91]. The possibility exists for charge-transfer between the nanotube network and oxygen through electron donation from localised donor states occurring at semiconductor-semiconductor SWNT interfaces [169], Figure 4.10. This process is limited by a potential barrier, V_s, formed from the dipole layer created by the redistribution of charge between the O_2 molecule and the nanotube network.

The potential barrier, V_s, increases with Θ and the arrival rate, $\mathrm{d}n_\mathrm{s}/\mathrm{d}t$, of electrons at the surface, $z = 0$, over V_s is given by [126]

$$\frac{\mathrm{d}n_\mathrm{s}}{\mathrm{d}t} = N \left(\frac{k_\mathrm{B}T}{2\pi m_\mathrm{e}} \right)^{1/2} \exp^{-eV_\mathrm{s}/k_\mathrm{B}T} \tag{4.5}$$

where n_s is the number of electrons, N is the number of adsorbed species and m_e is the mass of an electron. The rate of $\frac{\mathrm{d}n_\mathrm{s}}{\mathrm{d}t}$ is dependent on the specific electronic configuration of the adsorbing gas and adsorbate, therefore the possibility exists to determine the type of gas through the adsorption kinetics.

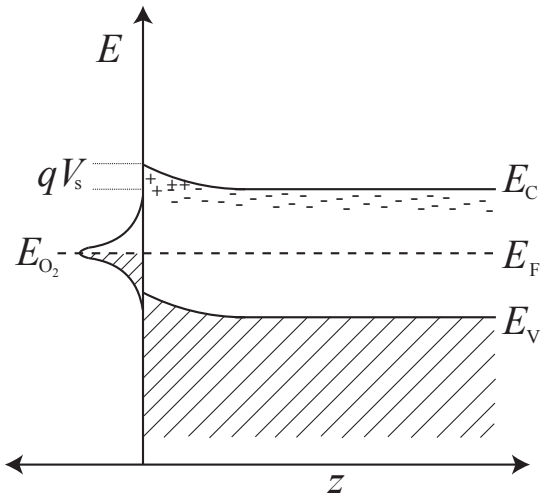

Figure 4.10 Charge-transfer over potential barrier V_s. In addition to thermionic excitation over the barrier electrons may hop through localised donor states [169]. As adsorption and associated charge-transfer proceeds, a dipole layer is formed consisting of negatively charged O_2 molecules and positively charged space-charge region. This is a self-limiting process as the arrival rate of electrons at the surface is exponentially dependent on the barrier height which increases with the number of electrons at the surface.

4.3 Reproducibility of measurements

As demonstrated the conductance of UV-desorbed (O2-adsorbed) SWNT networks increases (decreases) upon oxygen-adsorption (UV-desorption). There is a long time constant to both UV-desorption and oxygen-adsorption processes, Figure 6.1 and Figure 6.2. The magnitude of conductance variation depends on the time of the preceding UV-desorption or oxygen-adsorption conditioning step. Repeatability of device performance depends on the time given for the adsorption/desorption process.

The behaviour reported in this Chapter has been observed on a number of different samples. All samples displayed the reported dependence on adsorption/desorption state with regard to direction of change in conductance and magnitude of change in conductance.

4.4 Conclusion

The response of SWNT network based resistive sensors have been shown to depend on the adsorption state of the network.

The conductance of the UV-desorbed networks increases upon oxygen adsorption. Oxygen adsorption increases the number of hole carriers in the network. The connectivity of the network is increased through oxygen exposure, confirmed through the observed increase in the VRH geometrical pre-factor G_0 upon oxygen exposure, presented in Chapter 3. Vacuum pressure of $\sim 1{\times}10^{-4}$ mbar is unable to remove oxygen species possibly indicating chemisorption of oxygen within the network. Further exposure of the SWNT networks to oxygen from an oxygen-adsorbed state results in a decrease in the sample conductance. A possible mechanism for the decrease in conductance with further oxygen-adsorption is due to water-vapour adsorption on the SWNT networks.

The kinetics of oxygen-adsorption on thin-mat and thick-mat SWNT networks were investigated. Initially the adsorption kinetics of both the thin-mat and thick-mat networks can be described by diffusion phenomena. The thickness of the network has a moderate effect on the duration of diffusion limited adsorption. The thin-mat SWNT network is described by $G(t) - G(0) = at^d$ for $t \leq 82$ minutes, the thick-mat SWNT network is described by $G(t) - G(0) = at^d$ for $t \leq 97$ minutes. During this diffusive regime of adsorption kinetics both thin-mat and thick-mat networks experience a lowering in characteristic parameter d. The point at which this occurs is significantly dependent on the network thickness, with the change in d occurring for thin-mat and thick-mat samples at $t_{\text{thin}} \sim 3$ minutes and $t_{\text{thick}} = 7$ minutes. The decrease in d is indicative of a broad distribution of particle release time, possibly due to trapping of oxygen at sites with poor charge transfer efficiency. The lower value of d in the thicker nanotube network could be due to an increased number of traps or a reduction in the doping efficiency as a result of a greater metallic component in the network.

For the remainder of the adsorption kinetics experiment adsorption becomes rate limited by an increasing energetic barrier due to a dipolar layer formed between the adsorbed molecules and SWNT network. This is modelled using an Elovich adsorption isotherm and is suggestive of significant charge transfer between the network and adsorbate.

Chapter 5

Sensing via Field Effect

SWNT-MOS structures comprising SWNT networks on Cr/Au electrodes were fabricated as described in Section 2.1. Results presented in this chapter comprise devices differentiated by contact geometry and film thickness.

5.1 Response of metal oxide capacitor

In this section the response of a MOS capacitor to molecular oxygen will be investigated. The MOS capacitor is of the specifications given in Section 2.1 but with a metallic gate only. The MOS capacitor gate consists of thermally evaporated Cr (20 nm) followed by Au (80 nm). The device was exposed to UV radiation under vacuum ($\sim 1 \times 10^{-6}$ mbar) for multiple hours followed by oxygen exposure as described in Section 2.3. The results in the frequency range 1 kHz $\leq f_{\mathrm{AC}} \leq$ 1 MHz are given in Figure 5.1.
The accumulation depletion and inversion regimes of MOS capacitor operation can be seen clearly in Figure 5.1. The $\mathrm{d}C/\mathrm{d}V_{\mathrm{G}}(V_{\mathrm{G}})$ trace shows the flat-band condition between the Cr/Au metal contact and Si band structure as a minimum. There is no significant change in $C(V_{\mathrm{G}})$ and there is no shift of flat-band voltage in $\mathrm{d}C/\mathrm{d}V_{\mathrm{G}}(V_{\mathrm{G}})$ upon oxygen exposure.

5.2 Nanotube-metal oxide capacitor

Thin and thick SWNT-MOS capacitor devices were fabricated in both top-contacted and bottom-contacted configurations. The thickness of the SWNT networks was estimated by performing UV-visible spectrophotometry ($\Delta\lambda$ = 10 nm) of samples deposited

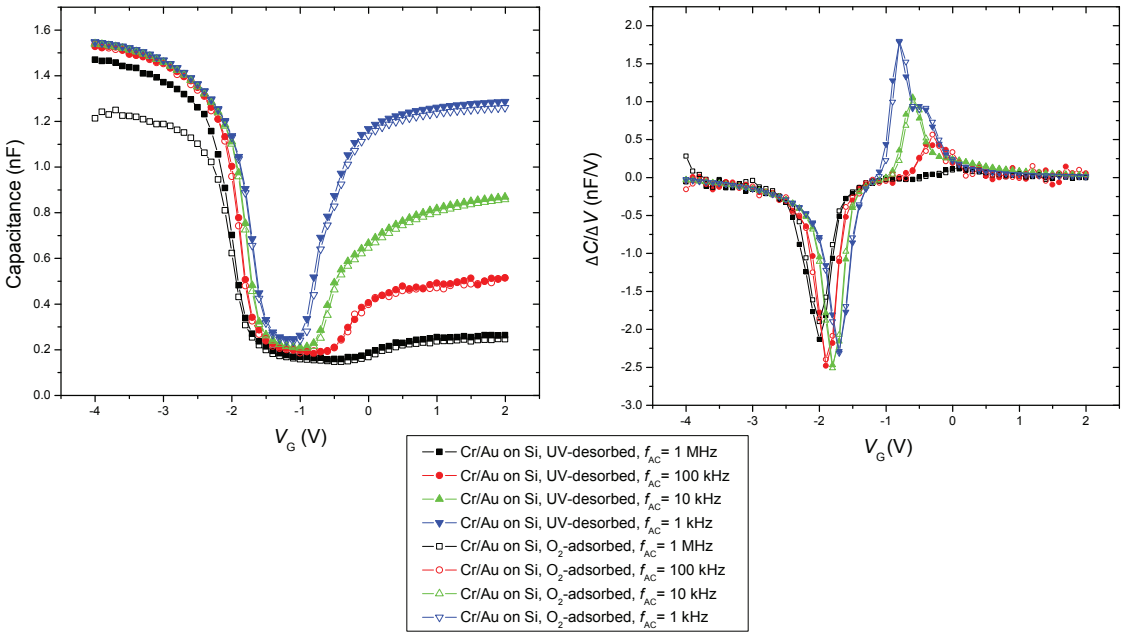

Figure 5.1 The left-hand graph shows the capacitance response of a UV-desorbed MOS structure to atmospheric pressure oxygen exposure. $C(V_G)$ measured in range -4 V $\leq V_G \leq 4$ V at 1 kHz $\leq f_{AC} \leq 1$ MHz. The right hand graph gives the derivative $dC/dV_G(V_G)$.

		Label	Abs. (A), $\lambda = 500$ nm	Thickness (nm)	R (k Ω)
Thick	Top-contacted	O1A	0.108 ± 0.001	2200 ± 300	14.21 ± 0.02
	Bottom-contacted	U1A	0.052 ± 0.001	1100 ± 200	44.62 ± 0.08
Thin	Top-contacted	O2A	0.002 ± 0.001	40 ± 30	394 ± 1
	Bottom-contacted	U2A	0.010 ± 0.001	200 ± 40	1274 ± 3

Table 5.1 Resistance and absorption data at $\lambda = 500$ nm for thick and thin SWNT networks in top-contacted and bottom-contacted configurations.

conjointly with the SWNT-MOS capacitor devices and then applying Beer's Law, Section 2.1.3. The two-terminal resistance was measured under vacuum ($\sim 1 \times 10^{-6}$ mbar) subsequent to UV-desorption for 12 hours as described. The resistance and absorption at 500 nm form characteristic data for each device, Table 5.1.

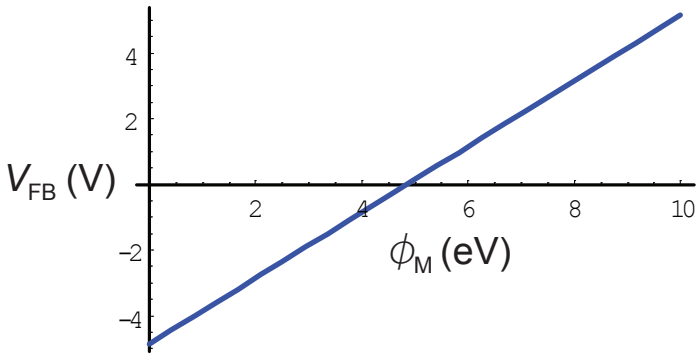

Figure 5.2 Simple relation between V_{FB} and ϕ_{M}, as described in Equation 5.1, where n_i, χ_{si} and $E_{\mathrm{g}}/2q$ are 10^{10} cm^{-3}, 4.05 eV and 0.56 eV/C respectively.

5.2.1 Ideal MOS behaviour

The expression for flat-band voltage V_{FB} of the MOS structure was shown previously

$$V_{\mathrm{FB}} = \phi_{\mathrm{MS}} - \frac{(Q_{\mathrm{IT}} + Q_{\mathrm{OT}})}{C_{\mathrm{o}}} \qquad ((1.36))$$

Considering an ideal, trap-free interface and oxide ($Q_{\mathrm{IT}} + Q_{\mathrm{OT}} = 0$) then V_{FB} is simply described by:

$$V_{\mathrm{FB}} = \phi_{\mathrm{MS}} = \phi_{\mathrm{M}} - \chi_{\mathrm{si}} - \frac{E_{\mathrm{g}}}{2q} - V_{\mathrm{t}} \cdot ln \cdot \frac{N_{\mathrm{A}}}{n_{\mathrm{i}}} \qquad (5.1)$$

where χ_{si} is the electron affinity of the semiconductor, E_{g} is the difference between the conduction band minimum energy and valence band maximum energy of the silicon and the last product describes the built-in voltage of the silicon, V_{bi}, where $V_{\mathrm{t}} = kT/q$ is the thermal voltage, N_{A} is the concentration of ionised acceptor dopant impurities and n_{i} is the concentration of intrinsic carriers. The value of N_{A} was estimated through correlation with the stated surface resistivity of the Si wafer [1] (20 $\Omega \cdot$cm $\leq \rho \leq$ 30 $\Omega \cdot$cm) on Irvin's plot [156] giving $\mathrm{N_A} \sim 1 \times 10^{15}\mathrm{cm}^{-3}$. Typical values of n_{i}, χ_{si} and $E_{\mathrm{g}}/2q$ are 10^{10} cm^{-3}, 4.05 eV and 0.56 eV/C respectively for silicon [127]. A plot of V_{FB} versus ϕ_{M} using the appropriate values is given in Figure 5.2.

The metal contacts consist of thermally evaporated Cr (20 nm) followed by Au (80 nm) either top-contacting or bottom-contacting the SWNT network. The predominant thermally evaporated metal at the Si_3N_4 surface would therefore be expected to be Cr, $\phi_{\mathrm{Cr}} = 4.5$ eV [170] and therefore we would expect $V_{\mathrm{FB_{Cr}}} \sim -0.35$ V. The workfunction of

[1] $Si/SiO_2/Si_3N_4$ wafer supplied by Si-Mat, http://www.si-mat.com/.

SWNT have been reported to be, 4.8 eV $\leq \phi_{\mathrm{SWNT}} \leq$ 5 eV, as determined experimentally through photoelectron emission [171, 172] and theoretically through first principles calculations [173]. This would result in an expected flat-band voltage for SWNTs of $-0.05 \leq V_{\mathrm{FB_{SWNT}}} \leq 0.15$. As the effect of the interface and oxide traps has been neglected, the relative positions rather than the exact values of the flat-band voltages would be expected to be reproduced experimentally.

5.2.2 Thick network results

Device testing (explained in detail in Section 2.3.3) followed the following procedure:

1. Desorption of adsorbates with UV radiation ($\geq$ 12 hours exposure) and low pressure (1×10^{-5} mbar), G vs. t recorded using the Keithley 4200-SCU.

2. Exposure to atmospheric pressure molecular oxygen, G vs. t recorded using the Keithley 4200-SCU.

3. Capacitance-voltage measurements recorded at $f_{\mathrm{AC}} = 1$ MHz, 100 kHz, 10 kHz, 1 kHz, 100 Hz and 10 Hz using the Autolab PGSTAT12 with FRA module.

Transient conductance response to molecular oxygen exposure

Stability of devices O1A (top-contacted) and U1A (bottom-contacted) upon exposure to molecular oxygen was determined by monitoring the two-terminal conductance vs. time, Figure 5.3. The exposure of the SWNT networks to O_2 induced an increase in the sample conductance.

Capacitive response to molecular oxygen exposure

The differential capacitance of devices O1A and U1A were recorded at 1 MHz, 100 kHz, 10 kHz, 1 kHz, 100 Hz and 10 Hz in the UV-desorbed state. The devices were then exposed to molecular oxygen at atmospheric pressure. Upon stabilisation of the transient conductance response C-V scans at the frequencies outlined above were repeated, Figure 5.4 and Figure 5.5.

The capacitance of device O1A and U1A increase with decreasing f_{AC}, as expected from the frequency dependence of capacitive reactance, $X_{\mathrm{C}} \propto 1/f_{\mathrm{AC}}$. The effect of molecular oxygen is found to differ between the top-contacted (O1A) and

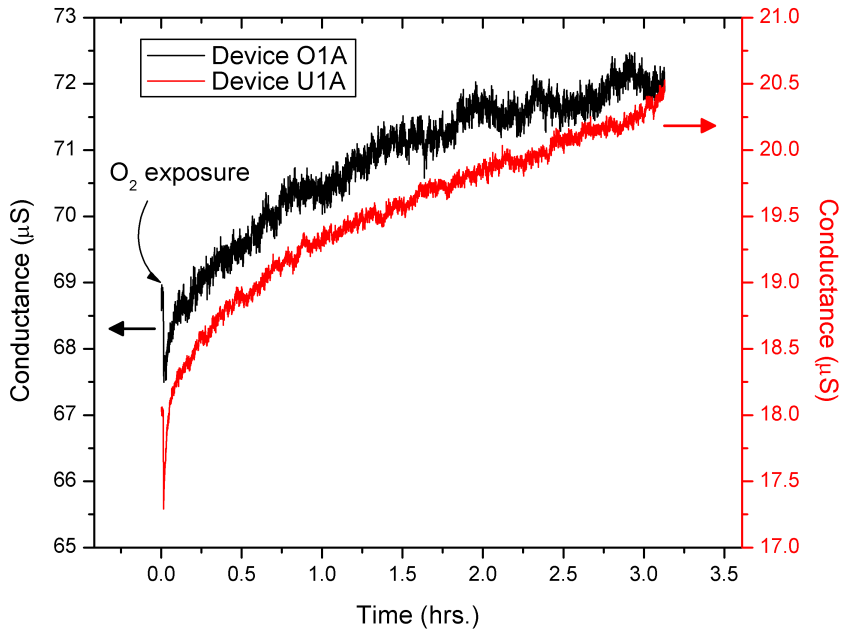

Figure 5.3 Conductance of devices U1A and O1A over 3 hour period following oxygen exposure. Error in $G = \pm 1.1\%$, error bars not shown. Device O1A exhibits $\sim 4 \pm 2\%$ increase in conductance after 3 hours. Device U1A exhibits $\sim 13 \pm 2\%$ increase in conductance after 3 hours.

bottom-contacted (U1A) thick SWNT-MOS capacitors, device O1A displays an increase in $C(V_G)$ upon exposure to molecular oxygen for all values of V_G, whilst U1A exhibits increased $C(V_G)$ only in the depletion region of device operation.

The derivative dC/dV_G variation with V_G is instructive of the flat-band voltage V_{FB}. Due to a large degree of noise in $dC/dV_G(V_G)$ at $f_{AC} = 1$ MHz and 100 kHz in both devices, it was necessary to apply FFT low pass filtration at these frequencies.

Figure 5.6 and Figure 5.7 give the $dC/dV_G(V_G)$ curves for device O1A in both the molecular oxygen-adsorbed and UV-desorbed states. In the frequency range 1 kHz $\leq f_{AC} \leq 1$ MHz device O1A has one minima of $dC/dV_G(V_G)$ at V_{Peak1}, which is dependent on both frequency, UV-desorption and oxygen adsorption. In the frequency range 10 Hz$\leq f_{AC} \leq 100$ Hz device O1A has a more complicated spectrum, most probably due to activation of trapping centres in the doped silicon-oxide interface [127]. For the purpose of this analysis the minima with the greatest magnitude will be considered. The induced voltage shifts associated with the flat-band minima in $dC/dV_G(V_G)$ are summarised in Table 5.2, exposure to molecular oxygen introduces a positive ΔV_{FB}. Device O1A

f_{AC}	Device state	V_{Peak1}	ΔV_{Peak1}
1 MHz	UV-desorbed	-1.121 ± 0.002	0.140 ± 0.004
	O_2-adsorbed	-0.981 ± 0.002	
100 kHz	UV-desorbed	-0.961 ± 0.002	0.080 ± 0.004
	O_2-adsorbed	-0.881 ± 0.002	
10 kHz	UV-desorbed	-0.861 ± 0.002	0.020 ± 0.003
	O_2-adsorbed	-0.841 ± 0.002	
1 kHz	UV-desorbed	-0.841 ± 0.002	0.020 ± 0.003
	O_2-adsorbed	-0.821 ± 0.002	
100 Hz	UV-desorbed	-0.821 ± 0.002	0.040 ± 0.003
	O_2-adsorbed	-0.781 ± 0.002	
10 Hz	UV-desorbed	-0.881 ± 0.002	0.060 ± 0.003
	O_2-adsorbed	-0.821 ± 0.002	

Table 5.2 Summarised flat-band voltage shifts for device O1A between UV-desorbed network state and O_2-adsorbed network state. Error values are rounded to one significant figure. There is a finite shift of V_{Peak1} upon exposure to O_2 at every value of applied AC frequency, $V_{Peak1} = V_{FB_{SWNT}}$.

consists of a top-contacted thick nanotube film. There is a strong possibility that neither the Cr or Au are in contact with the Si_3N_4 surface, therefore the silicon electronic energy bands can only align with the SWNT network as V_G is increased, providing one flat-band voltage. This point is further emphasised through the increase in capacitance of O1A in the accumulation region and to a lesser extent in the depletion region, Figure 5.4. It was shown in Section 1.7 that the capacitance in the accumulation region can be considered to arise from a parallel plate capacitor formed by the gate contact material and accumulation layer, with the oxide forming a dielectric spacer. Therefore, any increase in capacitance in the accumulation region of $C(V)$ (and also to a lesser extent in the depletion region as $C_G = C_o C_S/(C_o + C_S)$) is caused by an increased capacitance in the gate material, in this case the SWNT network only. The reason this is not observed in a device with Au/Cr and SWNT network at the surface can be seen from the relation between V_{FB} with ϕ_M. The material with the lowest energy ϕ_M approaches the flat-band condition with Si at lower values of V_G; therefore the accumulation region capacitance is dominated by Cr, which is insensitive to O_2 exposure. V_{Peak1} observed for device O1A, Figure 5.6 and Figure 5.7, is therefore ascribed to the flat-band voltage of the SWNT network, $V_{Peak1} = V_{FB_{SWNT}}$.

Figure 5.8 and Figure 5.9 give the $dC/dV_G(V_G)$ curves for device U1A in both the molecular oxygen-adsorbed and UV-desorbed states. Induced voltage shifts are summarised in Table 5.3. Device U1A displays two significant minima in $dC/dV_G(V_G)$

f_{AC}	Device state	V_{Peak1}	ΔV_{Peak1}	V_{Peak2}	ΔV_{Peak2}
1 MHz	UV-desorbed	-1.700 ± 0.003	-0.020 ± 0.007	-1.140 ± 0.002	0.180 ± 0.004
	O_2-adsorbed	-1.720 ± 0.003		-0.961 ± 0.002	
100 kHz	UV-desorbed	-1.620 ± 0.003	0.018 ± 0.006	-0.921 ± 0.002	0.080 ± 0.004
	O_2-adsorbed	-1.602 ± 0.003		-0.841 ± 0.002	
10 kHz	UV-desorbed	-1.500 ± 0.003	0.000 ± 0.006	-0.841 ± 0.002	0.100 ± 0.003
	O_2-adsorbed	-1.500 ± 0.003		-0.741 ± 0.001	
1 kHz	UV-desorbed	-1.400 ± 0.003	0.000 ± 0.006	-0.761 ± 0.002	0.060 ± 0.003
	O_2-adsorbed	-1.400 ± 0.003		-0.701 ± 0.001	
100 Hz	UV-desorbed	-1.380 ± 0.003	0.000 ± 0.006	-0.761 ± 0.002	0.060 ± 0.003
	O_2-adsorbed	-1.380 ± 0.003		-0.701 ± 0.001	
10 Hz	UV-desorbed	-1.400 ± 0.003	0.000 ± 0.006	-0.821 ± 0.002	0.060 ± 0.003
	O_2-adsorbed	-1.400 ± 0.003		-0.761 ± 0.002	

Table 5.3 Summarised flat-band voltage shifts for device U1A between UV-desorbed network state and O_2 adsorbed network state. Error are values rounded to one significant figure. Exclusive of results taken at 1 MHz and 100 kHz there is zero shift upon exposure to O_2 for V_{Peak1}, assigned to the flat-band voltage of Au/Cr. For peaks 2 and 3 there is a strong shift of the peak upon exposure to oxygen.

in the frequency range $1\text{ MHz} < f_{AC} < 10\text{ Hz}$. At $f_{AC} = 100$ Hz a third minima appears, the magnitude is small and will be excluded from further analysis.

The minimum occurring at the more negative voltage, V_{Peak1}, shows no significant response to molecular oxygen exposure. $\Delta V_{Peak1} = 0$ for frequencies 10 Hz, 100 Hz, 1 kHz and 10 kHz, however at frequencies 100 kHz and 1 MHz there are shifts of ± 0.02 V. The $dC/dV_G(V_G)$ traces at 100 kHz and 1 MHz were processed through FFT filtration at a frequency of 4 Hz, and therefore error could be introduced through this process. V_{Peak1} is attributed to $V_{FB_{Cr/Au}}$ due to the lack of reactivity with molecular oxygen and the expected dependence of V_{FB} on ϕ_M, Figure 5.2.

The second minimum, V_{Peak2}, occurring at a more positive voltage displays a trend similar to that of device O1A - a positive voltage shift upon oxygen exposure for all frequencies, and is attributed to $V_{FB_{SWNT}}$. The low frequency ($10 < f_{AC} < 100$ Hz) traces of device U1A become complex as V_G is increased.

Table 5.4 contrasts the response of thick SWNT networks in top-contacted and bottom-contacted configurations, given graphically in Figure 5.10. No response is expected from the Au/Cr metallic contacts, the small $\Delta V_{FB_{Au/Cr}}$ observed for device U1A is attributed to an artifact of the FFT filtration. The magnitude of $\Delta V_{FB_{SWNT}}$ generally increases with frequency, a possible origin could be the deactivation of low

	O1A		U1A	
f_{AC}	$\Delta V_{FB_{Cr/Au}}$	$\Delta V_{FB_{SWNT}}$	$\Delta V_{FB_{Cr/Au}}$	$\Delta V_{FB_{SWNT}}$
1 MHz	NA	0.140 ± 0.004	-0.02 ± 0.007	0.180 ± 0.004
100 kHz	NA	0.080 ± 0.004	0.018 ± 0.006	0.080 ± 0.004
10 kHz	NA	0.020 ± 0.003	0.000 ± 0.006	0.100 ± 0.003
1 kHz	NA	0.020 ± 0.003	0.000 ± 0.006	0.060 ± 0.003
100 Hz	NA	0.040 ± 0.003	0.000 ± 0.006	0.060 ± 0.003
10 Hz	NA	0.060 ± 0.003	0.000 ± 0.006	0.060 ± 0.003

Table 5.4 Comparison of induced flat-band voltage shifts in thick SWNT network devices O1A and U1A upon oxygen adsorption from a UV-desorbed state. A single flat-band voltage was discernable for sample O1A, with a value dependent on atmospheric conditions. Sample U1A displayed two flat-band voltages, one of which was dependent on atmospheric conditions.

frequency traps at high small signal frequencies as described in Section 1.7.

The positive ΔV observed in $V_{FB_{SWNT}}$ for O1A and U1A must satisfy $V_{FB_{SWNT}} = \phi_{SWNT} - \phi_S$ and can therefore be attributed to an increase in ϕ_{SWNT}. This change in work-function occurs through an increase of the surface dipole, D, contribution to ϕ through $\phi = D - E_F$. Resonance between energy levels in the SWNT network and oxygen facilitate a charge transfer either by physisorption [84] or chemisorption [91] reflecting the large electronegativity of oxygen. The induced shift in work-function is described by the Helmholtz equation:

$$\Delta\phi = -4\pi q \int \mathrm{d}\bar{\mathrm{r}} z \delta n(\bar{r}) \tag{5.2}$$

where $\delta n(\bar{r})$ is the change in charge density which accompanies adsorption.

Traditional MOS capacitors with a palladium gate are typically used as hydrogen sensors [174,175] as described in Chapter 4. Hydrogen diffuses through the Pd metal gate and forms a surface dipole layer at the metal-oxide interface modifying the workfunction of Pd which modifies the field in the silicon. Flat-band voltage shifts of 1 V were observed in $C - V$ curves of Pd-MOS capacitor with 50 nm SiO_2 layer and 10 nm Pd film in response to 4% H_2 at 20°C with a response and recovery time of 10 seconds and 1 minute respectively [174]. Recently 7 nm thin oxide layer was grown on a Pd-MOS sensor through dry plasma oxidation of highly clean n-type silicon which was demonstrated to improve both the sensitivity and response time to hydrogen adsorption [175]. Similar improvements could be achieved in the SWNT-MOS capacitor through thinning of the oxide layer or using a high dielectric constant insulator.

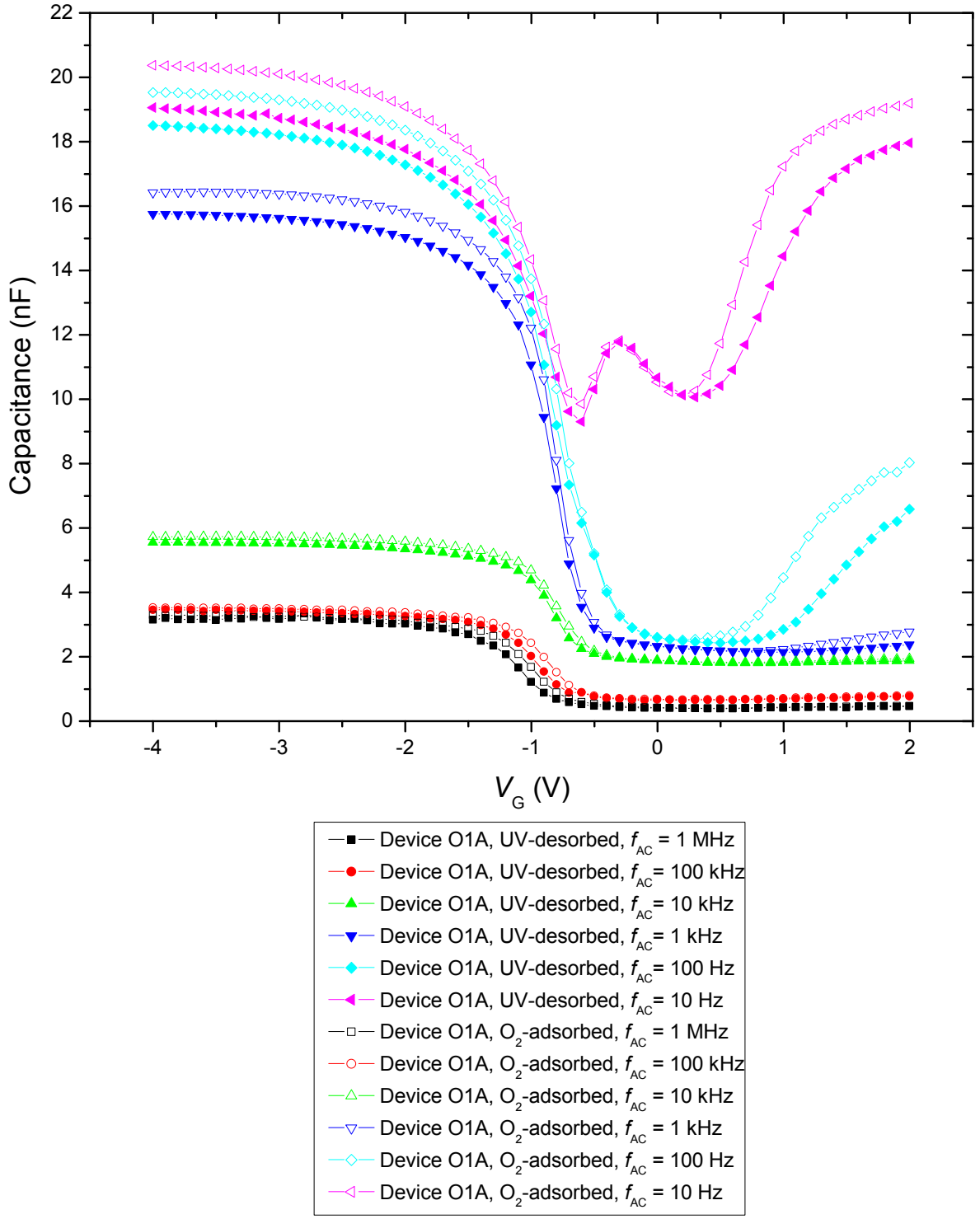

Figure 5.4 Capacitance-voltage scan for device O1A (top-contacted). Unfilled data points denote the molecular-oxygen-adsorbed state. The capacitance of the device increases upon oxygen exposure throughout the entire range of DC bias, V_G.

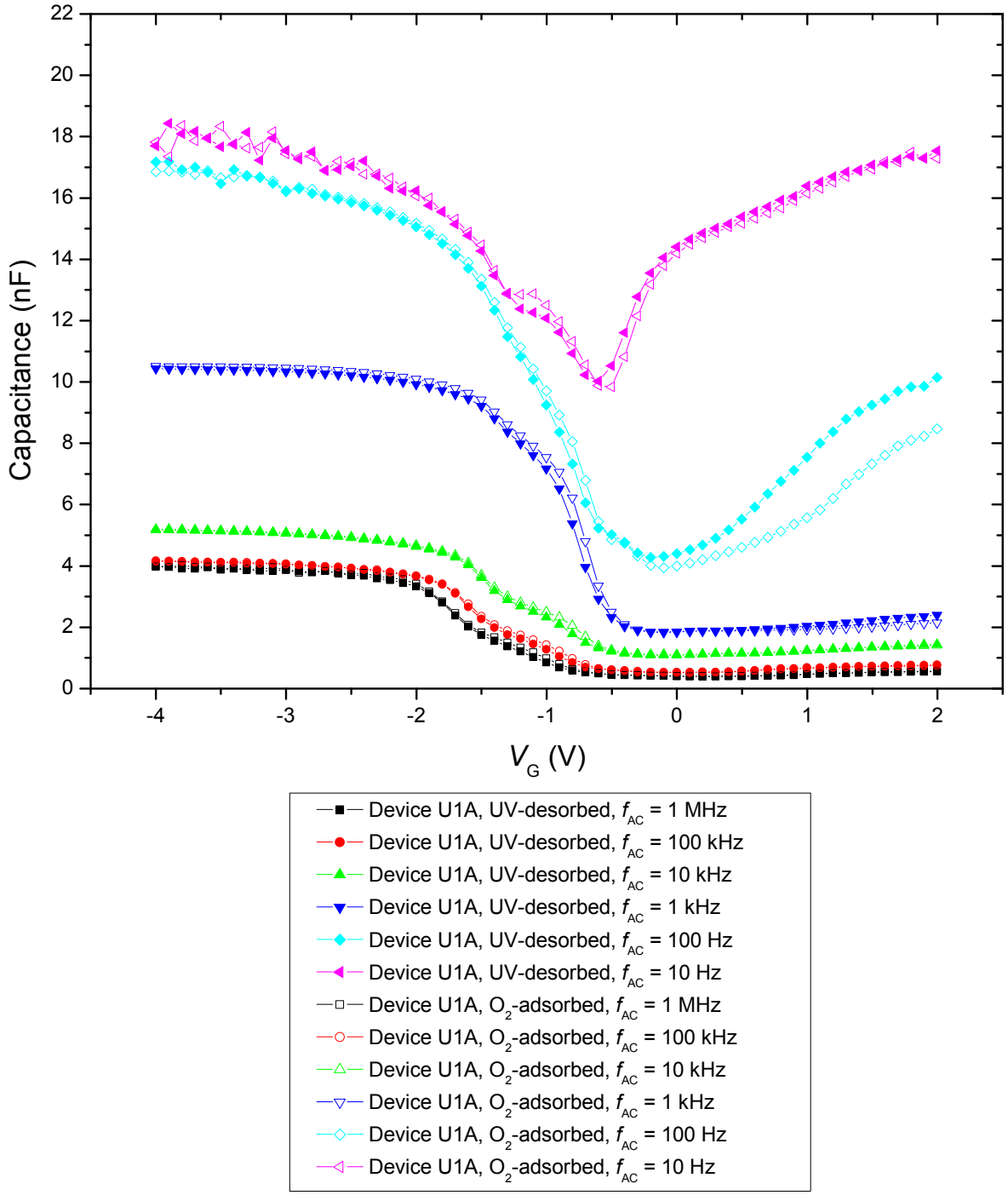

Figure 5.5 Capacitance-voltage scan for device U1A (bottom-contacted). Unfilled data points denote the molecular-oxygen adsorbed state. The capacitance of the device in response to molecular oxygen-adsorption increases as we approach flat-band conditions and the depletion region.

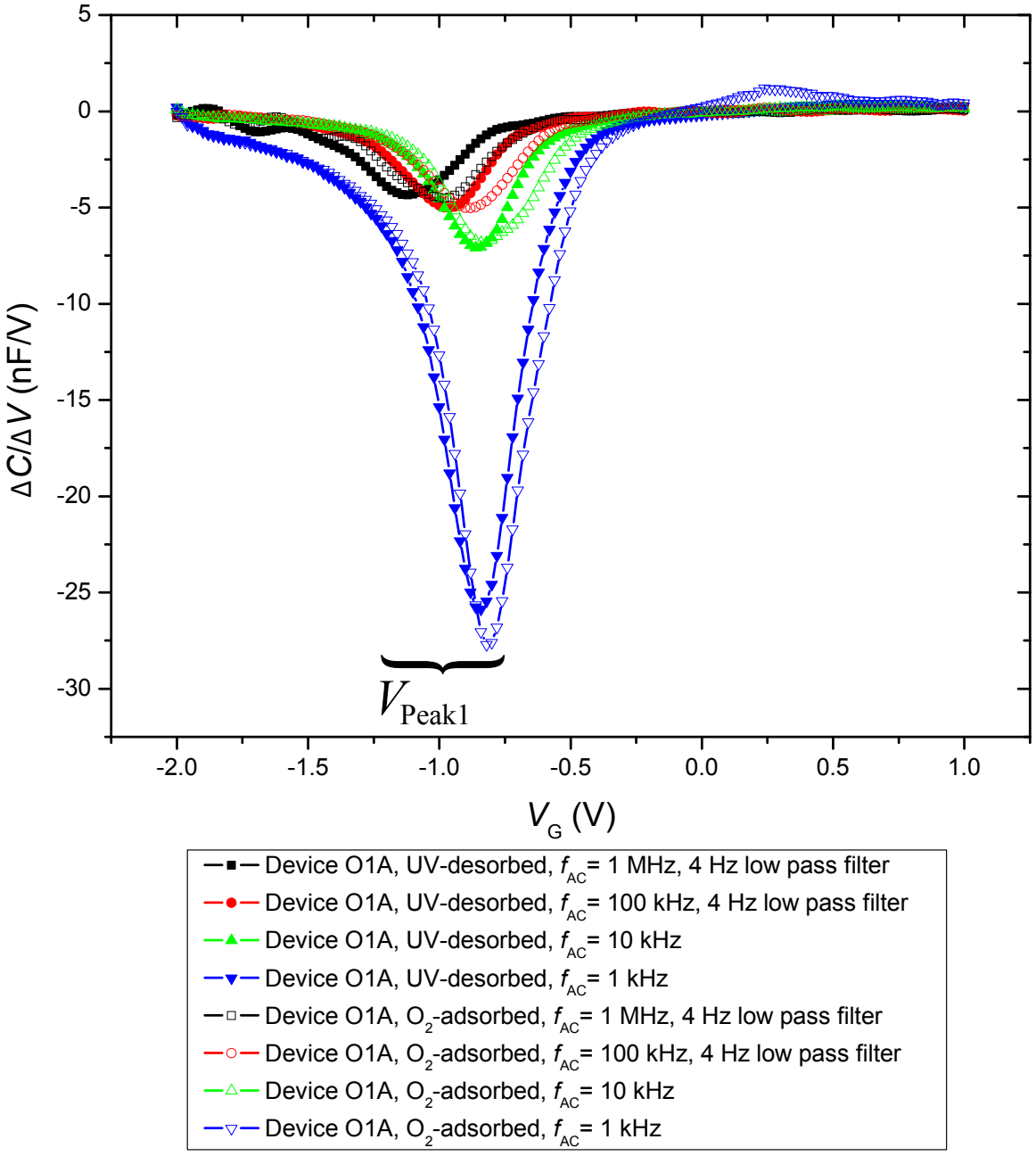

Figure 5.6 The variation of $\mathrm{d}C/\mathrm{d}V_\mathrm{G}$ with V_G for device O1A, 1 kHz $\leq f_\mathrm{AC} \leq$ 1 MHz. Minima in $\mathrm{d}C/\mathrm{d}V_\mathrm{G}(V_\mathrm{G})$ signifies the flat-band voltage V_FB. Due to high frequency noise in $\mathrm{d}C/\mathrm{d}V_\mathrm{G}(V_\mathrm{G})$ at f_AC = 1 MHz and 100 kHz low pass FFT filtration was implemented at a cutoff frequency of 4 Hz. One frequency dependent minima is observed, V_Peak1, with a value dependent on UV-desorption and O_2-adsorption, $V_\mathrm{Peak1} = V_{\mathrm{FB}_\mathrm{SWNT}}$.

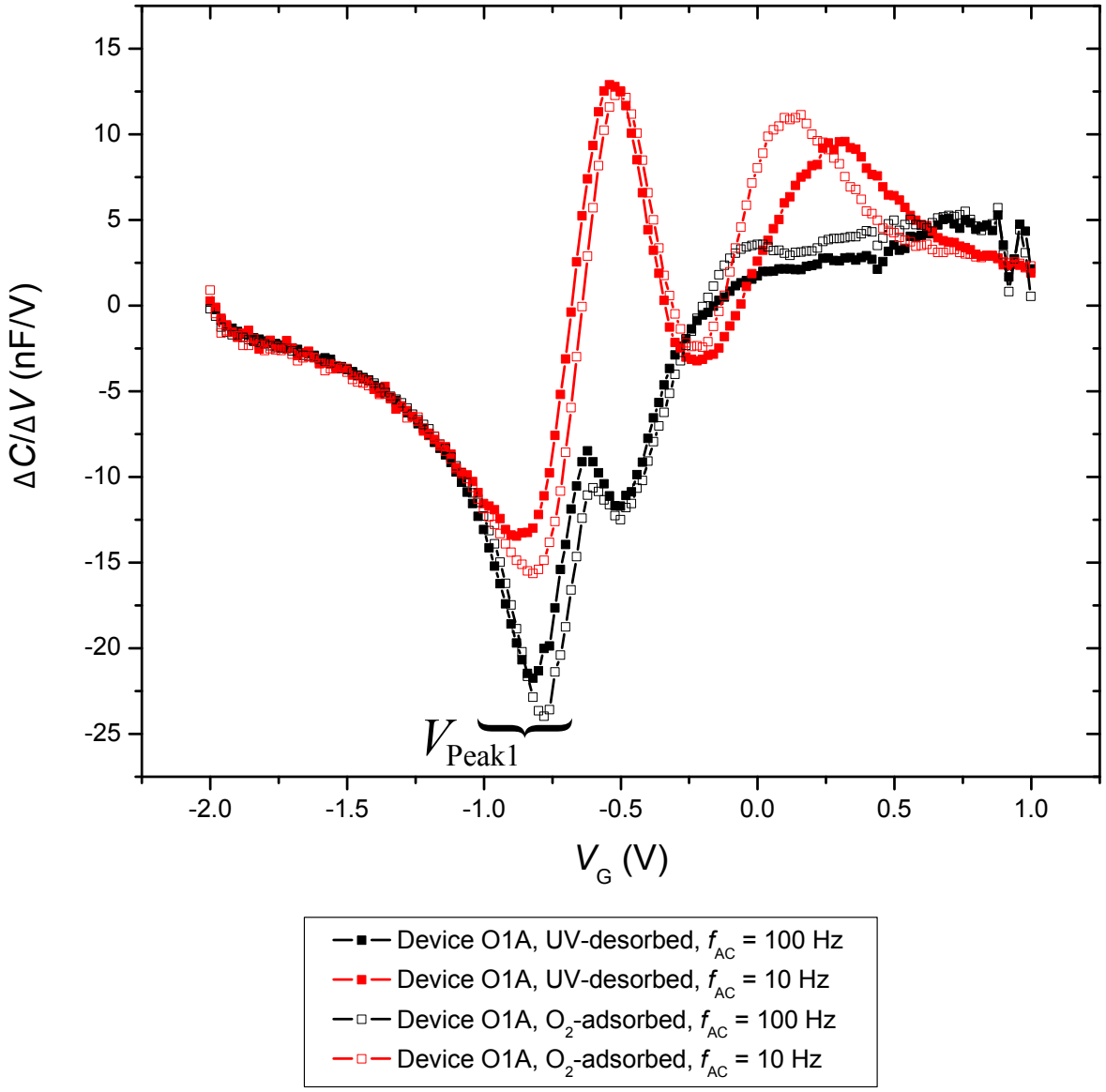

Figure 5.7 The variation of $\mathrm{d}C/\mathrm{d}V_G$ with V_G for device O1A, $f_\mathrm{AC} = 100$ Hz and 10 Hz. Minima in $\mathrm{d}C/\mathrm{d}V_\mathrm{G}(V_\mathrm{G})$ signifies the flat-band voltage V_FB. Two minima are observed for both frequencies, however analysis is restricted to the minima occurring at the lower gate voltage. V_Peak1 is dependent on the UV/O_2 exposure, $V_\mathrm{Peak1} = V_{\mathrm{FB}_\mathrm{SWNT}}$.

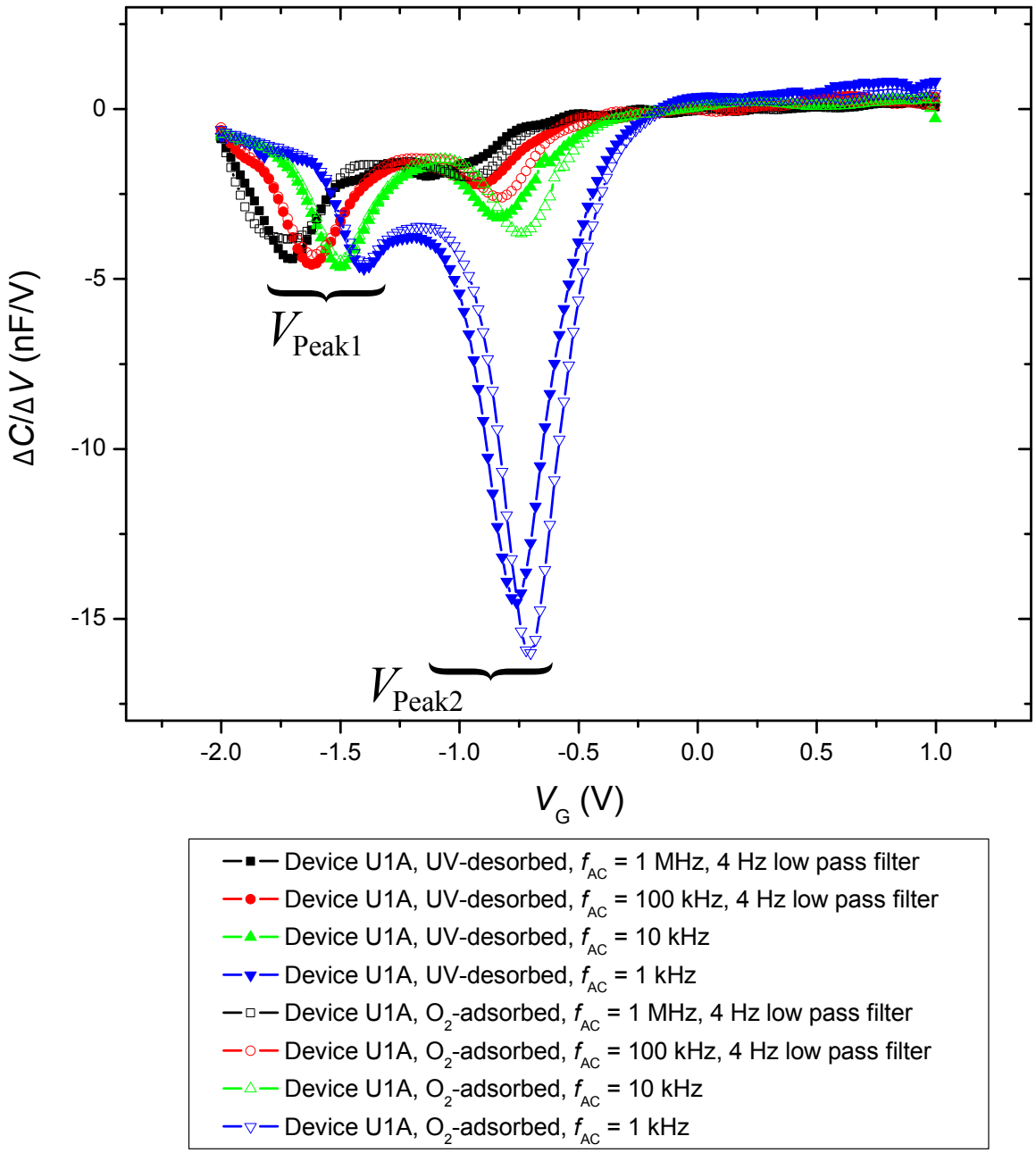

Figure 5.8 The variation of $\mathrm{d}C/\mathrm{d}V_G$ with V_G for device U1A, 1 kHz $\leq f_\mathrm{AC} \leq$ 1 MHz. Minima in $\mathrm{d}C/\mathrm{d}V_\mathrm{G}(V_\mathrm{G})$ signifies the flat-band voltage V_FB. Due to high frequency noise in $\mathrm{d}C/\mathrm{d}V_\mathrm{G}(V_\mathrm{G})$ at $f_\mathrm{AC} = 1$ MHz and 100 kHz low pass FFT filtration was implemented at a cutoff frequency of 4 Hz. Two frequency dependent minima are observed. V_Peak1 is independent of UV/O_2 exposure, $V_\mathrm{Peak1} = V_{\mathrm{FB}_\mathrm{Cr/Au}}$. V_Peak2 is dependent on UV-desorption and O_2-adsorption, $V_\mathrm{Peak2} = V_{\mathrm{FB}_\mathrm{SWNT}}$.

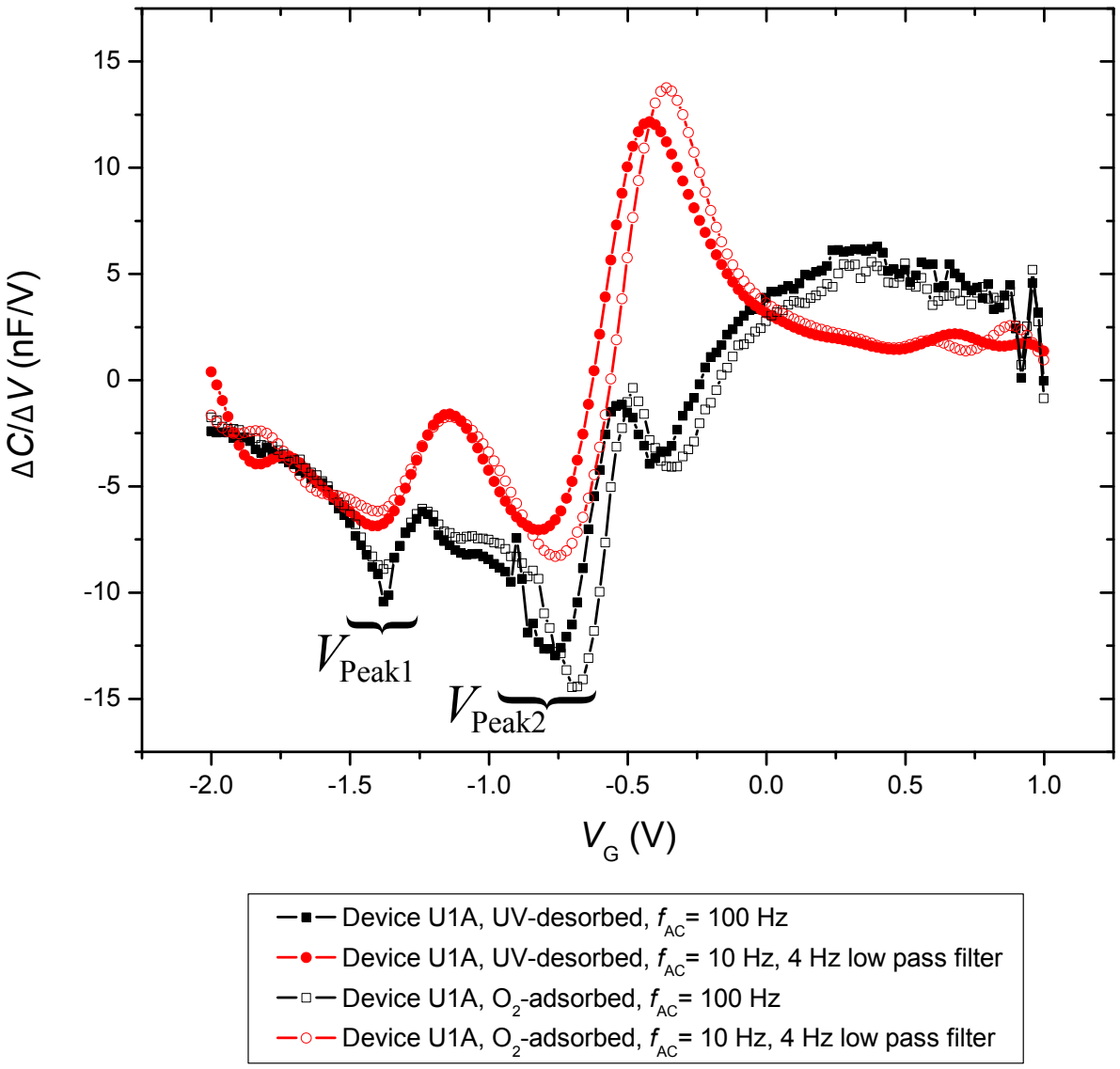

Figure 5.9 The variation of $\mathrm{d}C/\mathrm{d}V_G$ with V_G for device U1A, $f_\mathrm{AC} = 100$ Hz and 10 Hz. Minima in $\mathrm{d}C/\mathrm{d}V_\mathrm{G}(V_\mathrm{G})$ signifies the flat-band voltage V_FB. V_Peak1 is independent of UV-desorption and O_2-adsorption, $V_\mathrm{Peak1} = V_{\mathrm{FB}_\mathrm{Cr/Au}}$. V_Peak2 is dependent on UV-desorption and O_2-adsorption, $V_\mathrm{Peak2} = V_{\mathrm{FB}_\mathrm{SWNT}}$.

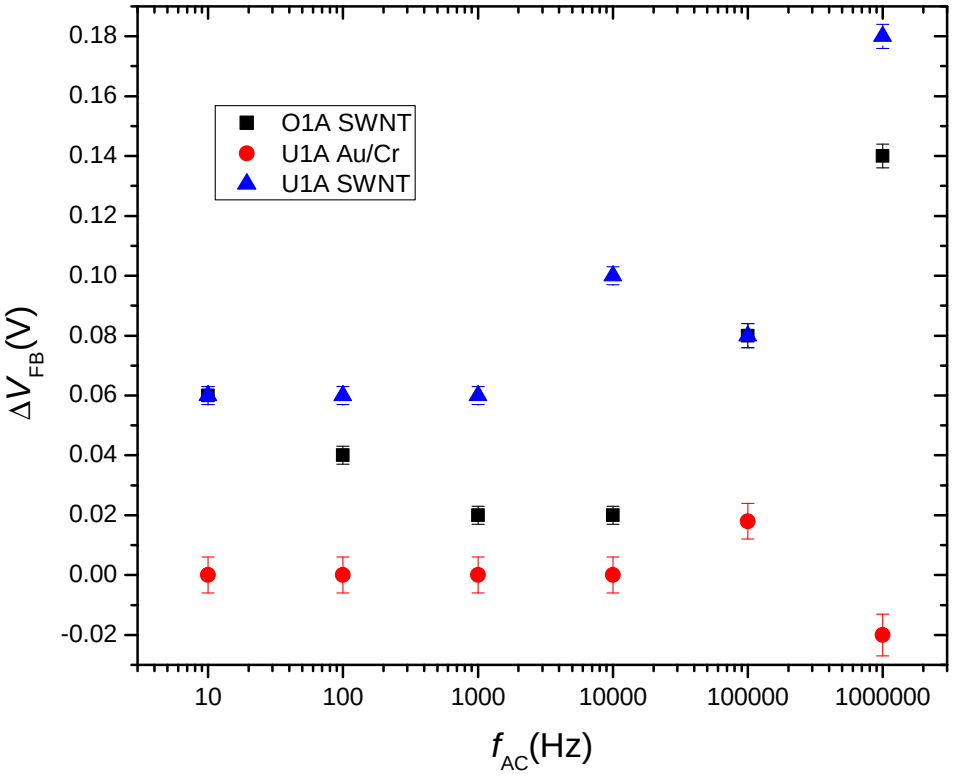

Figure 5.10 Comparison of V_{FB} for device O1A (top-contacted) and U1A (bottom-contacted). Plot on the diagram are $\Delta V_{\mathrm{FB_{SWNT}}}$ for devices O1A and U1A and $\Delta V_{\mathrm{FB_{Cr/Au}}}$ for device U1A. Device O1A has no detectable $\Delta V_{\mathrm{FB_{Cr/Au}}}$ due to a combination of contact geometry and SWNT network thickness.

5.2.3 Thin network results

Device testing (explained in detail in Section 2.3.3) followed the following procedure:

1. Desorption with UV radiation ($\geq$ 12 hours exposure) and low pressure (1×10^{-5} mbar), G vs. t recorded.

2. Exposure to atmospheric pressure molecular oxygen, G vs. t recorded.

3. Capacitance-voltage scans at $f_{AC} = 1$ MHz, 100 kHz, 10 kHz, 1 kHz, 100 Hz and 10 Hz.

Transient conductance response to molecular oxygen exposure

Stability of devices O2A (top-contacted) and U2A (bottom-contacted) upon exposure to molecular oxygen determined through monitoring the two-terminal conductance with time, G vs. t, Figure 5.11.

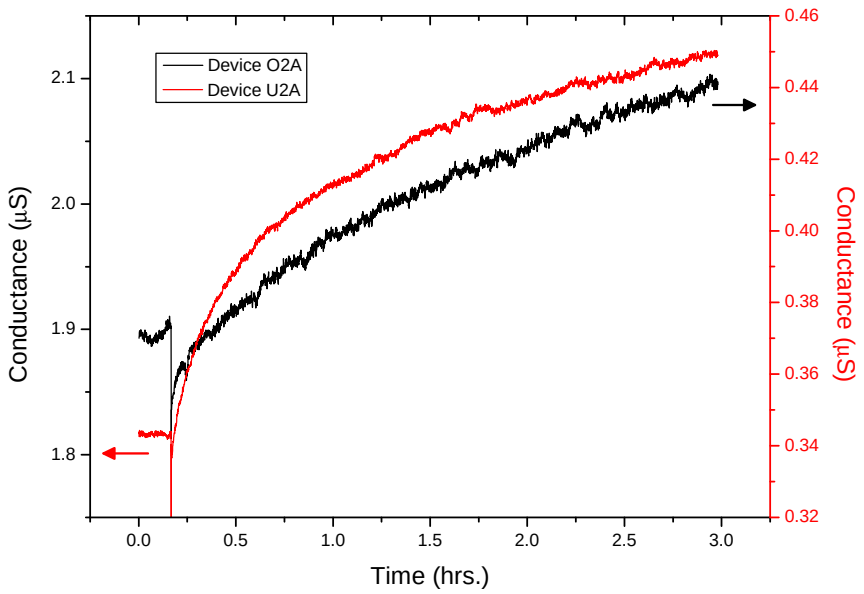

Figure 5.11 Conductance of devices O2A and U2A over 3 hour time period after oxygen exposure. Error in $G = \pm 1.1\%$, error bars not shown. Device O2A exhibits $\sim 10 \pm 2\%$ increase in conductance, device U2A exhibits $\sim 30 \pm 3\%$ increase in conductance over 3 hours.

Capacitive response to molecular oxygen exposure

The differential capacitance of thin SWNT-MOS devices O2A (top-contacted) and U2A (bottom-contacted) were recorded at $f_{\mathrm{AC}} = 1$ MHz, 100 kHz, 10 kHz, 1 kHz, 100 Hz and 10 Hz in the UV-desorbed state. Subsequent to UV-desorption both devices were exposed to molecular oxygen at atmospheric pressure. Upon stabilisation of the transient conductance response C-V scans at the afore mentioned frequencies were repeated, Figure 5.12 and 5.13. The capacitance of devices O2A and U2A increase with decreasing f_{AC} except at $f_{\mathrm{AC}} = 1$ MHz. At high frequencies ($f_{\mathrm{AC}} > 100$ Hz) the effect of molecular oxygen is to increase the capacitance of the device in the depletion regime only, as expected from MOS theory, Section 1.7. At low frequencies, $f_{\mathrm{AC}} = 100$ Hz and 10 Hz, the C-V variation is affected by the activation of low frequency charge traps.

The $\mathrm{d}C/\mathrm{d}V_{\mathrm{G}}(V_{\mathrm{G}})$ traces for device O2A are given in Figures 5.14, 5.15 and 5.16. FFT filtration at 4 Hz was employed at high (1 MHz and 100 kHz) and low (100 Hz and 10 Hz) frequencies due to noise. Device O2A displayed two minima in $\mathrm{d}C/\mathrm{d}V_{\mathrm{G}}(V_{\mathrm{G}})$ at $f_{\mathrm{AC}} > 100$ Hz subsequent to UV-desorption. Upon exposure to molecular oxygen a third minima in $\mathrm{d}C/\mathrm{d}V_{\mathrm{G}}(V_{\mathrm{G}})$ was introduced, signifying another flat-band voltage. This behaviour was noted at all frequencies tested greater than 100 Hz and is particularly well defined at $f_{\mathrm{AC}} = 10$ kHz, 1 kHz, due to clear signal in these measurements (no filtration required). $\mathrm{d}C/\mathrm{d}V_{\mathrm{G}}(V_{\mathrm{G}})$ for device U2A given in Figures 5.17, 5.18 and 5.19. FFT filtration at 4 Hz was employed for device U2A at 100 kHz $\leq f_{\mathrm{AC}} \leq 1$ MHz in both the O_2-adsorbed and UV-desorbed state and at $f_{\mathrm{AC}} = 100$ Hz in the O_2 exposed state. Device U2A displayed two minima in $\mathrm{d}C/\mathrm{d}V_{\mathrm{G}}(V_{\mathrm{G}})$ at $f_{\mathrm{AC}} > 100$ Hz subsequent to UV-desorption. Upon exposure to molecular oxygen similar behaviour for device O2A was noted, namely the occurrence of a third minima in $\mathrm{d}C/\mathrm{d}V_{\mathrm{G}}(V_{\mathrm{G}})$, however this was at best poorly defined ($f_{\mathrm{AC}} \geq 100$ kHz). The C-V curves of devices O2A and U2A at $f_{\mathrm{AC}} = 100$ Hz and 10 Hz have complex variations in $\mathrm{d}C/\mathrm{d}V_{\mathrm{G}}(V_{\mathrm{G}})$ due to the activation of low frequency charge trapping, only well defined minima in $\mathrm{d}C/\mathrm{d}V_{\mathrm{G}}(V_{\mathrm{G}})$ will be considered.

In the UV-desorbed sate device O2A displays two distinct minima in $\mathrm{d}C/\mathrm{d}V_{\mathrm{G}}(V_{\mathrm{G}})$, in the oxygen-adsorbed state three distinct minima are observable. The shifts in voltage of each minima in $\mathrm{d}C/\mathrm{d}V_{\mathrm{G}}(V_{\mathrm{G}})$ are given in Table 5.5. V_{Peak1} displays zero shift of V_{FB} from a UV-desorbed state to an O_2-adsorbed state, except at $f_{\mathrm{AC}} = 100$ kHz where there is a slight shift of V_{Peak1}, $\Delta V_{\mathrm{Peak1}} = -0.02$ V. $\mathrm{d}C/\mathrm{d}V_{\mathrm{G}}(V_{\mathrm{G}})$ at $f_{\mathrm{AC}} = 100$ kHz was

f_{AC}	Dev. State	V_{Peak1}	ΔV_{Peak1}	V_{Peak2}	V_{Peak3}	ΔV_{Peak3}	$\Delta V_{Peak2-Peak3}$
1 MHz	UV-des.	-2.041 ± 0.004	0.000 ± 0.008		-1.241 ± 0.002	-0.020 ± 0.005	-0.280 ± 0.006
	O_2-ads.	-2.041 ± 0.004		-1.521 ± 0.003	-1.261 ± 0.003		
100 kHz	UV-des.	-1.901 ± 0.003	-0.020 ± 0.008		-0.961 ± 0.002	-0.160 ± 0.004	-0.440 ± 0.005
	O_2-ads.	-1.921 ± 0.004		-1.401 ± 0.003	-1.121 ± 0.002		
10 kHz	UV-des.	-1.781 ± 0.004	0.000 ± 0.007		-0.821 ± 0.002	-0.040 ± 0.003	-0.480 ± 0.004
	O_2-ads.	-1.781 ± 0.004		-1.301 ± 0.003	-0.861 ± 0.002		
1 kHz	UV-des.	-1.681 ± 0.003	0.000 ± 0.007		-0.741 ± 0.001	0.020 ± 0.003	-0.460 ± 0.004
	O_2-ads.	-1.681 ± 0.003		-1.201 ± 0.002	-0.721 ± 0.001		
100 Hz	UV-des.						
	O_2-ads.						
10 Hz	UV-des.	-1.761 ± 0.004	0.040 ± 0.007		-0.841 ± 0.002	0.040 ± 0.003	-0.220 ± 0.004
	O_2-ads.	-1.721 ± 0.003		-1.061 ± 0.002	-0.801 ± 0.002		

Table 5.5 Flat-band voltages, V_{FB}, of device O2A in the oxygen-adsorbed and UV-desorbed states.

filtered with an FFT algorithm, possibly introducing error in the position of minima. Also, the minimum is determined through finding the minimum value of $dC/dV_G(V_G)$, therefore the large step size of V_G could introduce error in determining V_{FB}. Due to the behaviour of the ideal SWNT-MOS device, calculated in Section 5.2.1, and the correspondence of peak position with the MOS capacitor (no SWNT network present) given earlier in Figure 5.1, the minima occurring at the more negative voltage, V_{Peak1}, is attributed to the Cr layer of the Cr/Au contact, $V_{Peak1} = V_{FB_{Cr/Au}}$. The change in $dC/dV_G(V_G)$ minima occurring at the least negative voltage, V_{Peak3}, is low ~ 0.02 V and changes sign, possibly indicating that this is a noise-induced process. The large shift in ΔV_{Peak3} at $f_{AC} = 100$ kHz upon oxygen exposure can be attributed to the complex change in spectra, which appears to be a convolution of two peaks, clearly shown in Figure 5.21. Despite the insensitivity of V_{Peak3} to UV/O_2 exposure V_{Peak3} is attributed to the SWNT network due to the predicted relationship between ϕ and V_{FB}; the position of this peak is similar to that observed for the thick SWNT-MOS devices however the magnitude of the peak is reduced reflecting the network thinness, $V_{Peak3} = V_{FB_{SWNT}}$. The minima occurring in the O_2 adsorbed state between $V_{FB_{Cr/Au}}$ and $V_{FB_{SWNT}}$ network is attributed to the effect of O_2-adsorption on the thin SWNT network, $V_{Peak2} = V_{FB_{SWNT_{O_2}}}$. An increased level of noise, due lower conductivity in the thin SWNT-MOS devices, results in poorly defined minima in $dC/dV_G(V_G)$ at $f_{AC} = 100$ Hz, preventing extraction of V_{FB}. The induced changes in flat-band voltage upon oxygen-adsorption of a UV-desorbed network are summarised in Table 5.7.

The extracted flat-band voltages from $dC/dV_G(V_G)$ for SWNT-MOS device U2A are given in Table 5.6. At $f_{AC} = 100$ Hz and 10 Hz it was not possible to clearly determine any flat-band minima. This could be due to a combination of the reduced

f_{AC}	Dev. State	V_{Peak1}	ΔV_{Peak1}	V_{Peak2}	V_{Peak3}	ΔV_{Peak3}	$\Delta V_{Peak2-Peak3}$
1 MHz	UV-des.	-1.941 ± 0.004	0.000 ± 0.008		-1.121 ± 0.002	0.000 ± 0.004	-0.180 ± 0.005
	O_2-ads.	-1.941 ± 0.004		-1.301 ± 0.003	-1.121 ± 0.002		
100 kHz	UV-des.	-1.821 ± 0.004	0 ± 0.007		-0.921 ± 0.002	-0.060 ± 0.004	-0.200 ± 0.004
	O_2-ads.	-1.821 ± 0.004		-1.121 ± 0.002	-0.981 ± 0.002		
10 kHz	UV-des.	-1.721 ± 0.003	0.02 ± 0.007		-0.781 ± 0.002		-0.080 ± 0.003
	O_2-ads.	-1.701 ± 0.003		-0.861 ± 0.002			
1 kHz	UV-des.	-1.641 ± 0.003	0.02 ± 0.007		-0.701 ± 0.001		-0.020 ± 0.003
	O_2-ads.	-1.6208 ± 0.003		-0.721 ± 0.001			
100 Hz	UV-des.						
	O_2-ads.						
10 Hz	UV-des.						
	O_2-ads.						

Table 5.6 Flat-band voltage shifts induced in sample U2A. Some flat-band voltages are missing due to poor resolution in minima of $dC/dV_G(V_G)$.

conductivity of the SWNT network in device U2A and the activation of low frequency charge traps in the silicon. In the UV-desorbed state device U2A has two distinct minima in $dC/dV_G(V_G)$ at $f_{AC} > 100$ Hz, these are labelled V_{Peak1} and V_{Peak3}. V_{Peak1} displays zero shift from a UV-desorbed state to an O_2-adsorbed state, except at $f_{AC} = 10$ kHz and 1 kHz where there is a slight shift of V_{Peak1}, $\Delta V_{Peak1} = 0.02$ V. The minimum is determined through finding the minimum value of $dC/dV_G(V_G)$, therefore the large step size of V_G could introduce error in determining V_{FB}. However, good correspondence with other devices presented and the expected relation between ϕ and V_{FB} lead to ascribing $V_{Peak1} = V_{FB_{Cr/Au}}$. In the UV-desorbed state V_{Peak3} is labelled at each f_{AC} for device U2A. Upon exposure to O_2 V_{Peak3} is visible at $f_{AC} = 1$ MHz and 100 kHz however at $f_{AC} = 10$ kHz and 1 kHz the third flat-band voltage introduced by the adsorption of O_2 onto the SWNT network has merged with V_{Peak3}. For frequencies $f_{AC} = 10$ kHz and 1 kHz in the oxygen-adsorbed state the merged minima comprising the SWNT network flat band voltage and the oxygen-adsorbed SWNT network flat-band voltage is labelled as V_{Peak2}, Figure 5.18. For frequencies $f_{AC} = 1$ MHz and 100 kHz in the oxygen adsorbed state a third flat-band voltage, V_{Peak2} is clearly resolved from V_{Peak1} and V_{Peak3}. V_{Peak3} is attributed to the SWNT network, $V_{Peak3} = V_{FB_{SWNT}}$ and V_{Peak2} is attributed to the oxygen adsorbed SWNT network, $V_{Peak2} = V_{FB_{SWNT_{O2}}}$ at all frequencies.

Both the thin devices appear to show the presence of a third minima in the $dC/dV_G(V_G)$ trace, clearly resolved for device O2A and convoluted for U2A, summarised in Table 5.7. The reason for a clearly resolved third flat-band voltage in device O2A could be due to the robust electrical contact formed through top-contacted electrodes. Enhanced Fermi level pinning of SWNT to the metal electrode would be

	O2A			U2A		
f_{AC}	$\Delta V_{FB_{Cr/Au}}$	$\Delta V_{FB_{SWNT}}$	$\Delta V_{FB_{SWNT_{O2}}}$	$\Delta V_{FB_{Cr/Au}}$	$\Delta V_{FB_{SWNT}}$	$V_{FB_{SWNT_{O2}}}$
1 MHz	0.000 ± 0.008	-0.020 ± 0.005	-0.280 ± 0.006	0.000 ± 0.008	0.000 ± 0.004	-0.180 ± 0.005
100 kHz	-0.020 ± 0.008	-0.160 ± 0.004	-0.440 ± 0.005	0.000 ± 0.007	-0.060 ± 0.004	-0.200 ± 0.004
10 kHz	0.000 ± 0.007	-0.040 ± 0.003	-0.480 ± 0.004	0.020 ± 0.007	NA	-0.080 ± 0.003
1 kHz	0.000 ± 0.007	0.020 ± 0.003	-0.460 ± 0.004	0.020 ± 0.007	NA	-0.020 ± 0.003
100 Hz	NA	NA	NA	NA	NA	NA
10 Hz	0.040 ± 0.007	0.040 ± 0.003	-0.220 ± 0.004	NA	NA	NA

Table 5.7 Comparison of flat-band voltage shifts in thin SWNT network devices O2A and U2A upon oxygen-adsorption from a UV-desorbed state.

expected in top contacted devices. The spatial extent of Fermi level pinning has been shown to be very short ranged (~ 2 nm) in SWNTs [61].

The third flat-band voltage in $\mathrm{d}C/\mathrm{d}V_G(V_G)$ is a result of the thinner SWNT network. The temperature and field dependence of conductivity, $G(E,T)$, of thin and thick SWNT networks is described by Mott's 3D variable range hopping model, as shown in Chapter 3; the thick network was found to have an additional phonon activated metallic component providing a thickness-dependent transport characteristic.

The effect of film thickness on the electrical properties of SWNT network is further highlighted when the devices presented in this Chapter are operated as FETs, see Figure 2.7 for schematic diagram. The conduction channel is formed by the SWNT network, channel length $L_C = 2.5$ mm, channel width $W = 4$ mm. The gate contact is formed by the Ohmically contacted back plane of silicon. Transfer characteristics of bottom-contacted thin and thick devices, U1A and U2A, were recorded within the gate voltage range $-4\ \mathrm{V} < V_G < 4\ \mathrm{V}$ with a source-drain voltage of $V_D = 0.1$ V for device U1A and $V_D = 0.5$ V for device U2A. Figure 5.22 shows the transfer curves and transconductance ($\mathrm{d}I_D/\mathrm{d}V_G$) in the UV-desorbed and oxygen-adsorbed state, following the same procedure of desorption/adsorption as detailed previously.

Upon oxygen-adsorption devices U1A and U2A display an increase in drain current. The polarity of the gate field dependence of both bottom-contacted devices indicate that the SWNT network behaves as a p-type thin film semiconductor in both O_2-adsorbed and UV-desorbed states. The rate limiting process of conduction was found to be 3D-VRH in the UV-desorbed and O_2 adsorbed state, the effect of Schottky barriers at the nanotube-metal contact or at s-SWNT-m-SWNT junctions can be eliminated, although ideally Schottky barrier tunnelling would be investigated through $G(E,T,V_G)$. The origin of p-type behaviour is likely due to p-doping by deeply adsorbed oxygen within

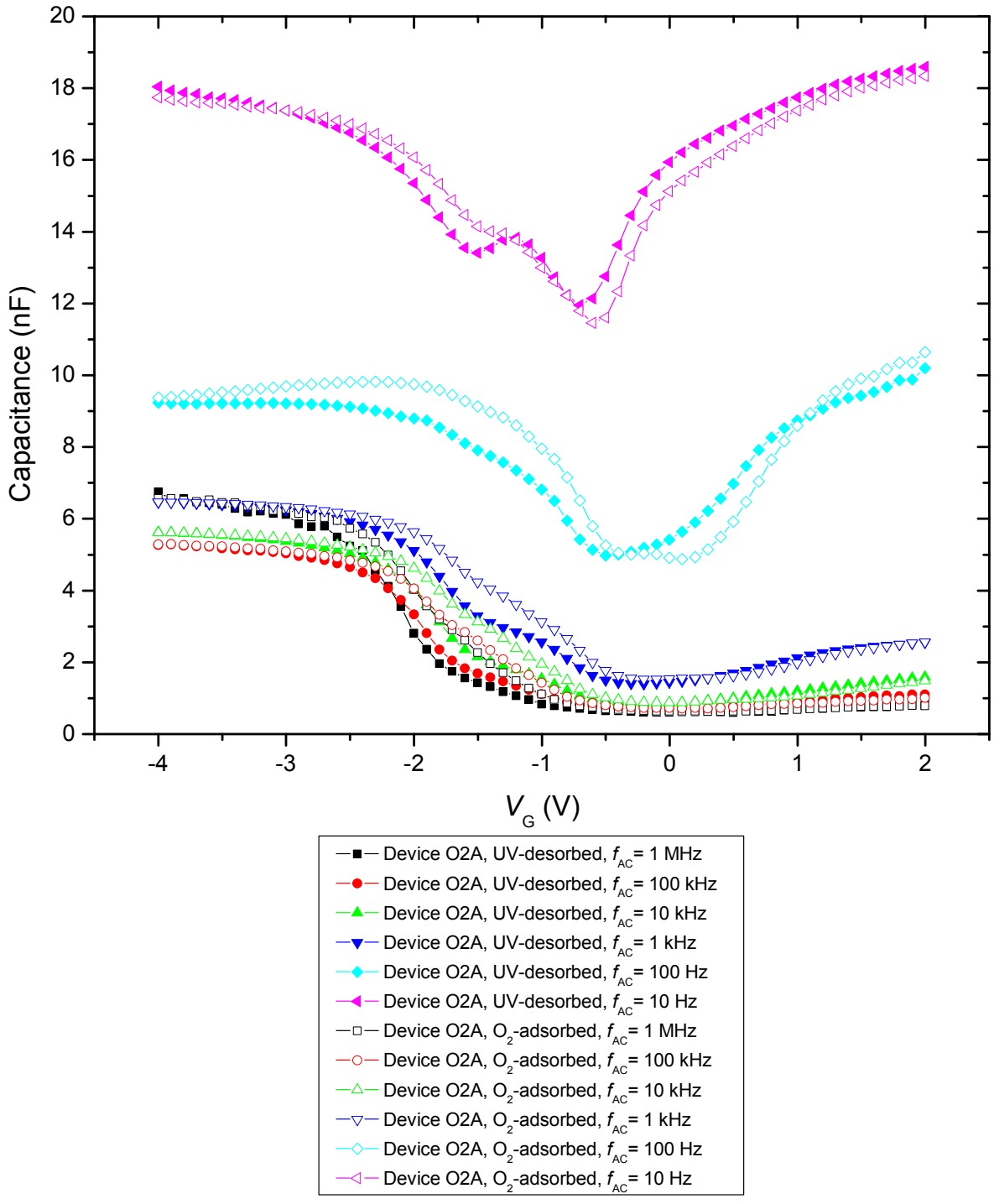

Figure 5.12 Capacitance-voltage scan for device O2A (top-contacted). Unfilled data points denote molecular oxygen-adsorbed state.

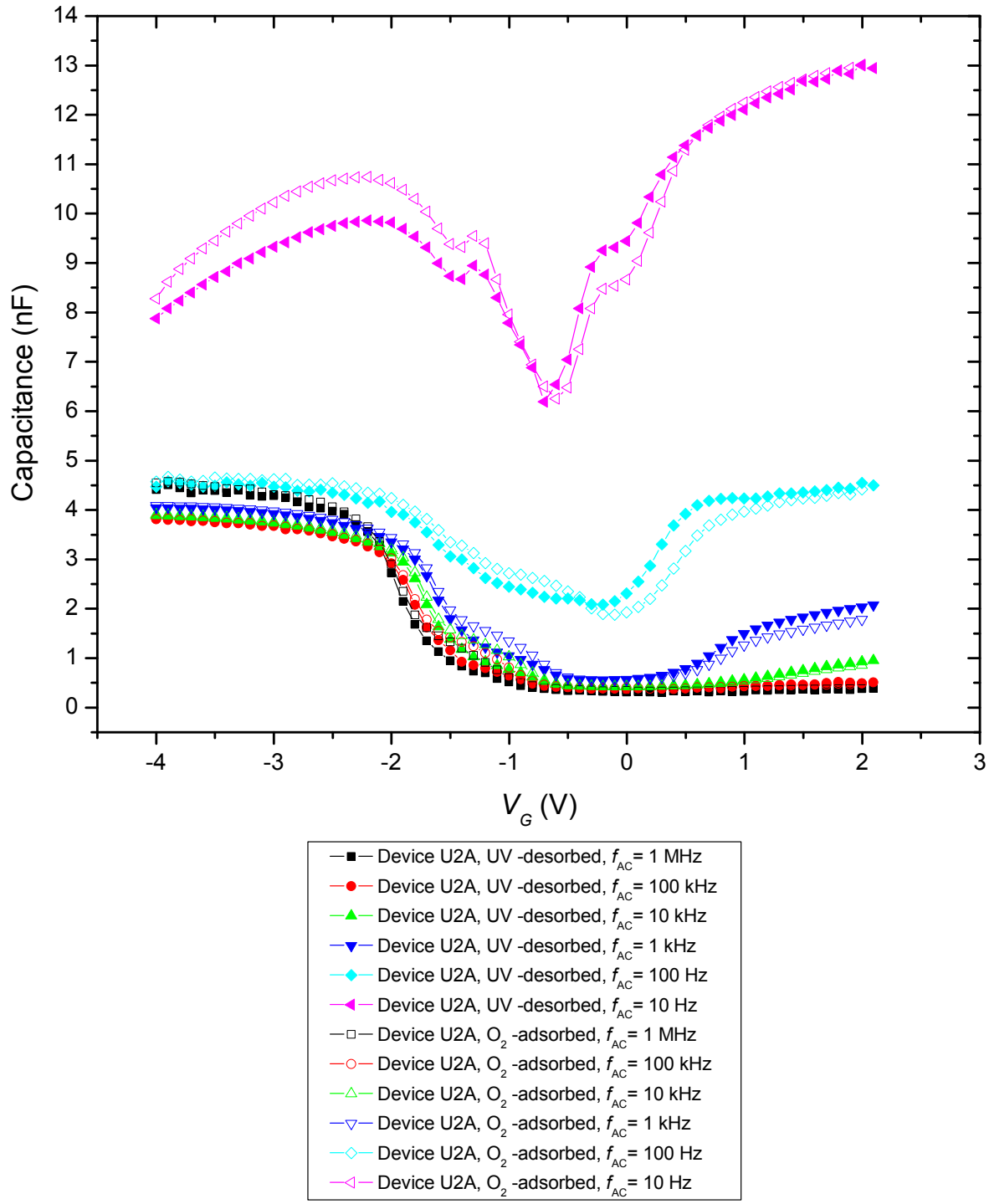

Figure 5.13 Capacitance-voltage scan for device U2A (bottom-contacted). Unfilled data points denote molecular oxygen-adsorbed state.

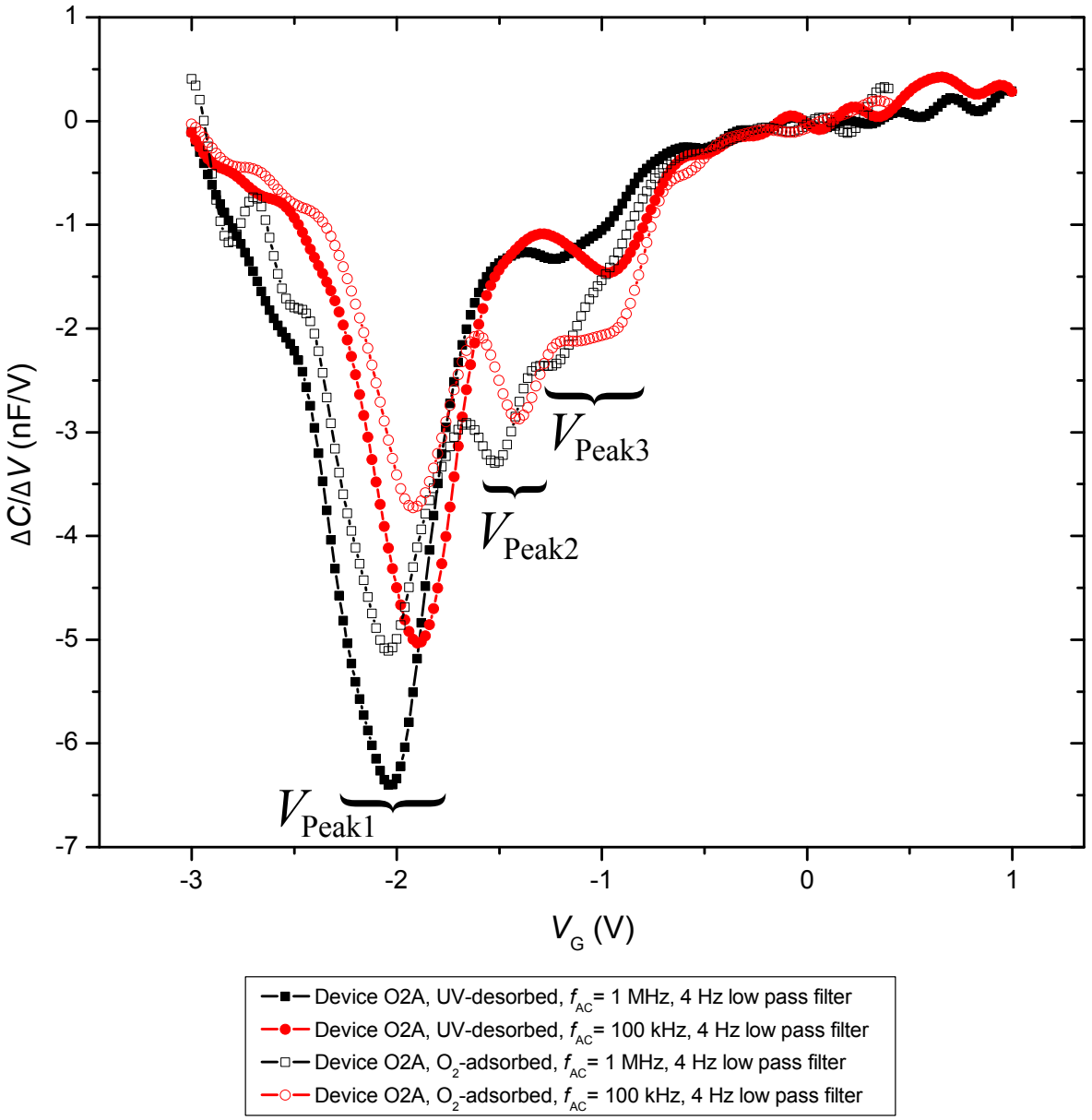

Figure 5.14 $\mathrm{d}C/\mathrm{d}V_\mathrm{G}(V_\mathrm{G})$ for device O2A, $f_\mathrm{AC} = 1$ MHz and 100 kHz. Minima $\mathrm{d}C/\mathrm{d}V_\mathrm{G}(V_\mathrm{G})$ signifies the flat-band voltage V_FB. Three minima/maximma areg observed. V_Peak1 is independent of UV-desorption and O_2-adsorption, V_Peak2 and V_Peak3 are dependent on UV-desorption and O_2-adsorption.

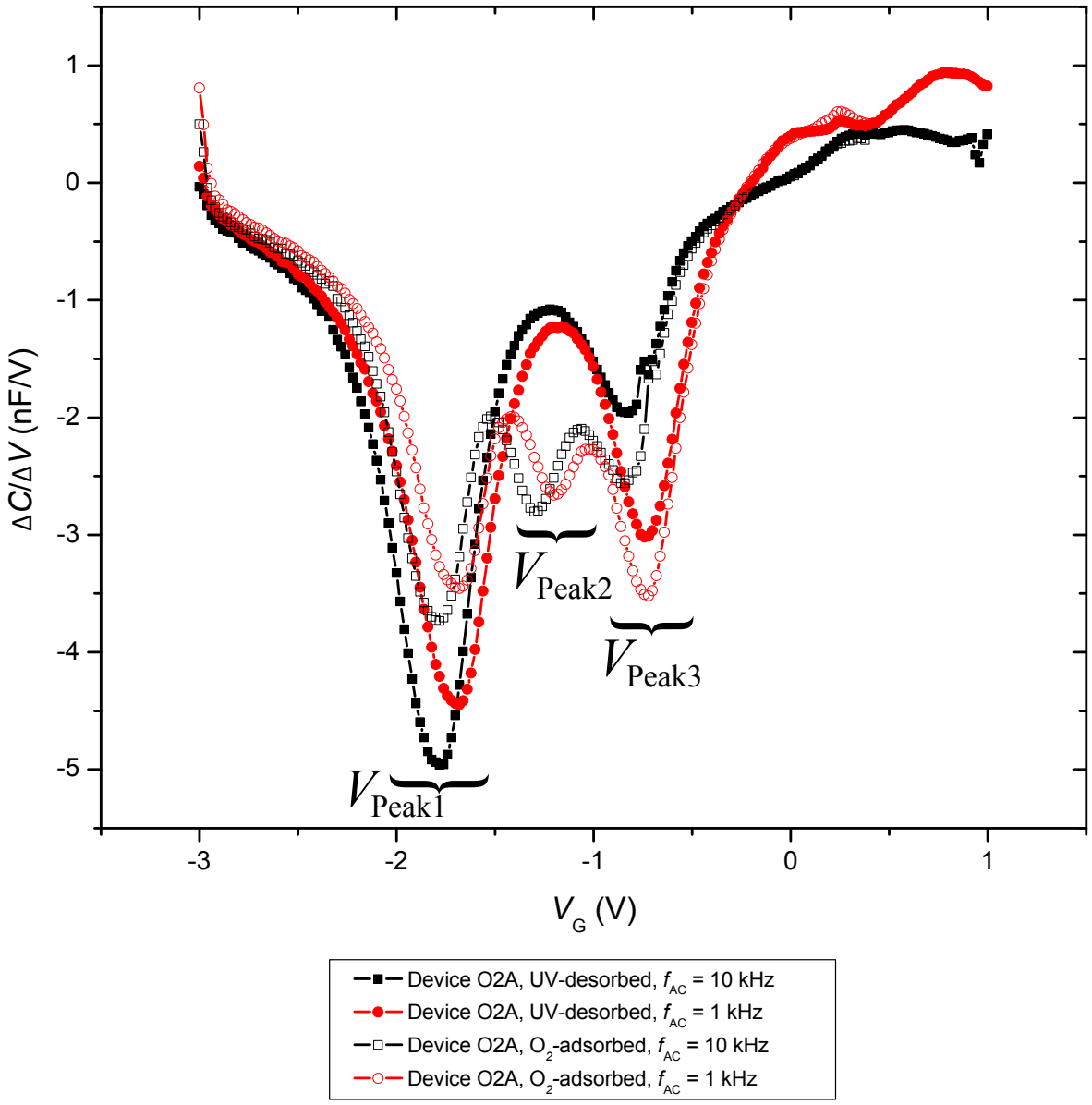

Figure 5.15 $\mathrm{d}C/\mathrm{d}V_\mathrm{G}(V_\mathrm{G})$ for device O2A, $f_\mathrm{AC} = 10$ kHz and 1 kHz. Minima $\mathrm{d}C/\mathrm{d}V_\mathrm{G}(V_\mathrm{G})$ signifies the flat-band voltage V_FB. Three minima/maximma are observed. V_Peak1 is independent of UV-desorption and O_2-adsorption, V_Peak2 and V_Peak3 are dependent on UV-desorption and O_2-adsorption.

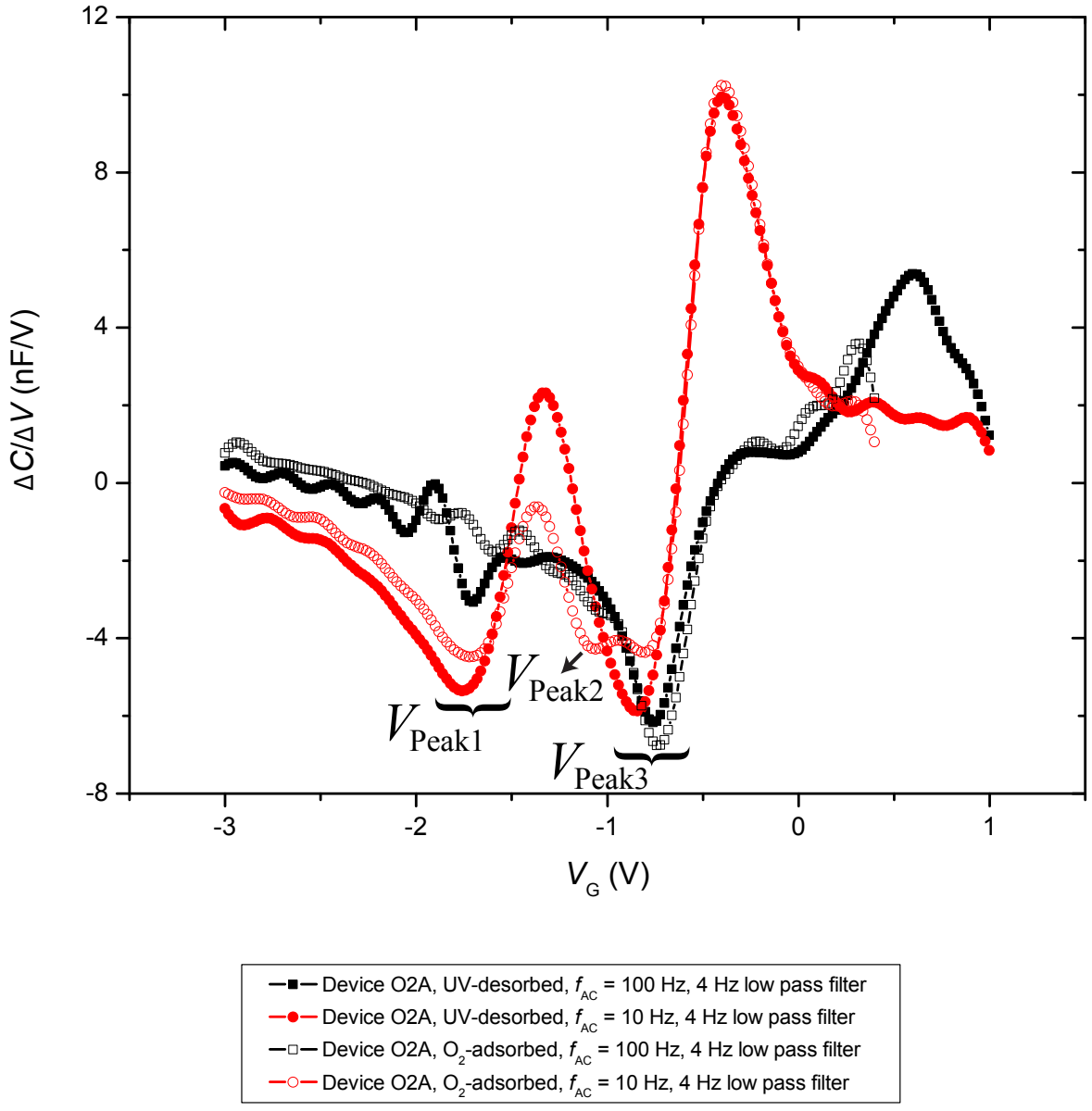

Figure 5.16 $\mathrm{d}C/\mathrm{d}V_\mathrm{G}(V_\mathrm{G})$ for device O2A, $f_\mathrm{AC} = 100$ Hz and 10 Hz. Minima $\mathrm{d}C/\mathrm{d}V_\mathrm{G}(V_\mathrm{G})$ signifies the flat-band voltage V_FB. Three minima/maximma are observed. V_Peak1 is independent of UV-desorption and O_2-adsorption, V_Peak2 and V_Peak3 are dependent on UV-desorption and O_2-adsorption.

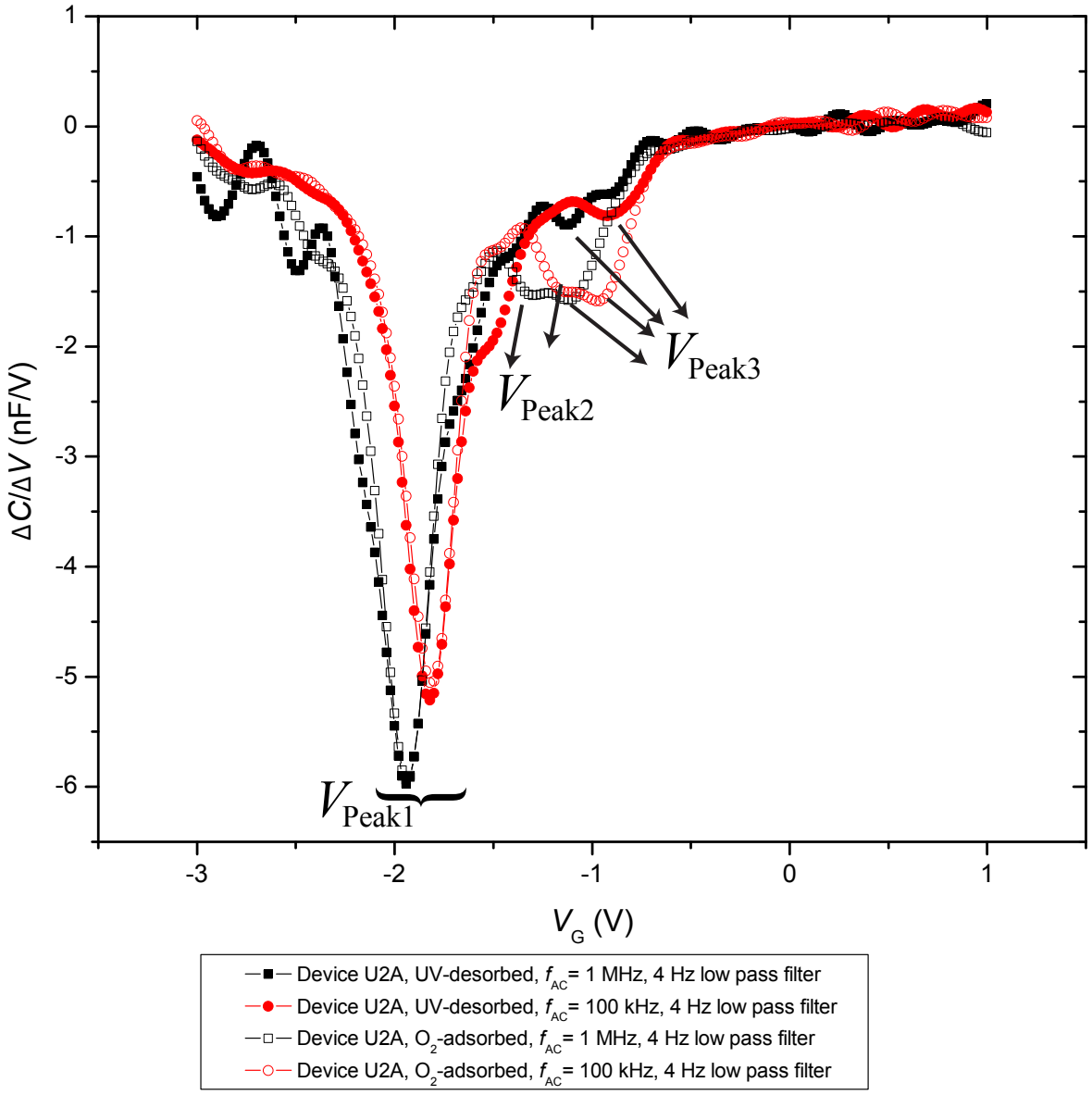

Figure 5.17 $\mathrm{d}C/\mathrm{d}V_\mathrm{G}(V_\mathrm{G})$ for device U2A, $f_\mathrm{AC} = 1$ MHz and 100 kHz. Minima $\mathrm{d}C/\mathrm{d}V_\mathrm{G}(V_\mathrm{G})$ signifies the flat-band voltage V_FB. V_Peak1 is independent of UV-desorption and O_2-adsorption. A response to O_2 is observed in the range $-1.5\ \mathrm{V} < V_\mathrm{G} < -1\ \mathrm{V}$.

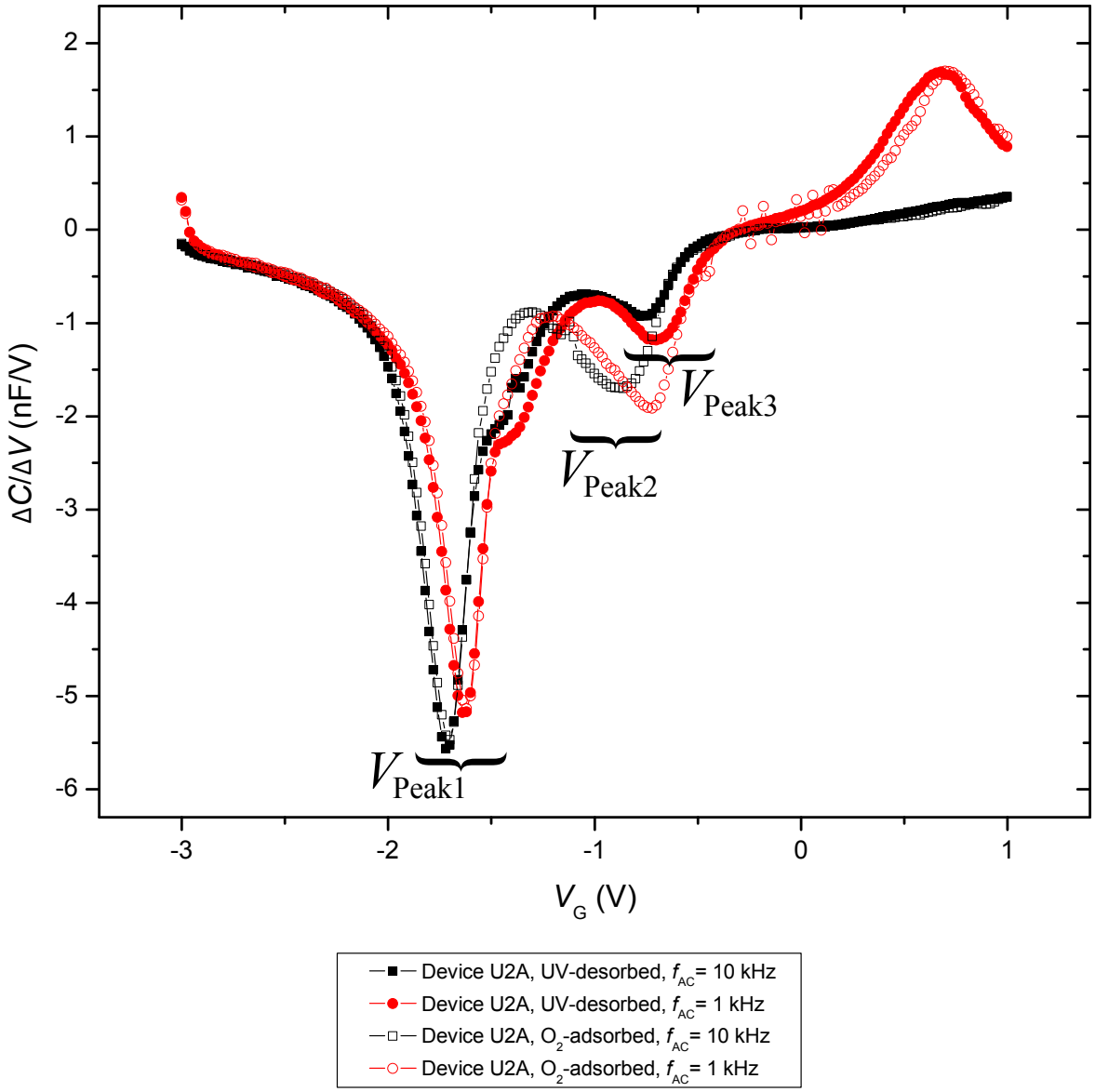

Figure 5.18 $\mathrm{d}C/\mathrm{d}V_\mathrm{G}$ variation with V_G for device U2A, $f_\mathrm{AC} = 10$ kHz and 1 kHz. Minima $\mathrm{d}C/\mathrm{d}V_\mathrm{G}(V_\mathrm{G})$ signifies the flat-band voltage V_FB. The peak (V_Peak1) at more negative values of V_G is independent of UV-desorption and O_2-adsorption. A response to O_2 is observed in the range -1.5 V $< V_\mathrm{G} < -1$ V.

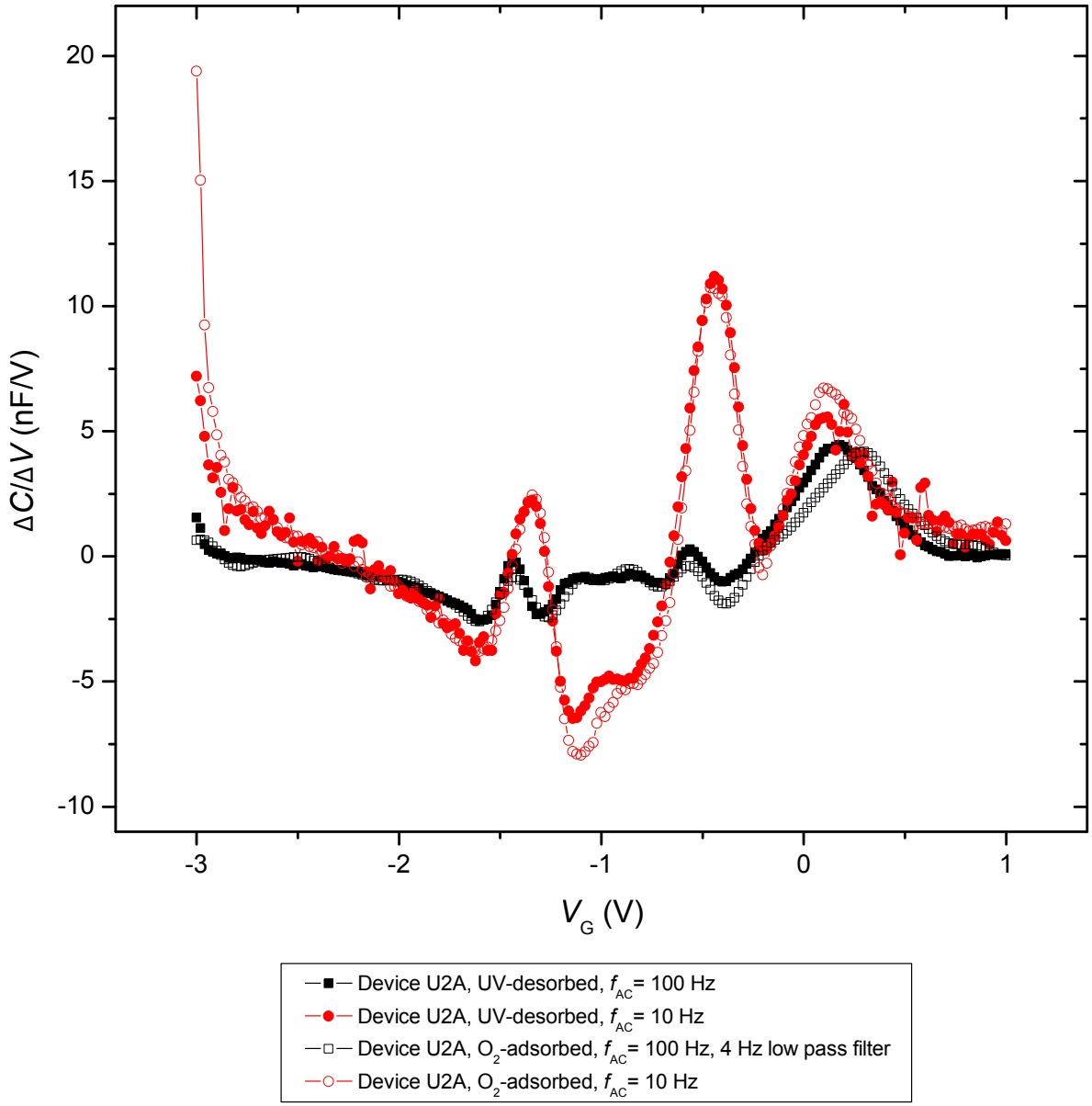

Figure 5.19 $\mathrm{d}C/\mathrm{d}V_\mathrm{G}$ variation with V_G for device U2A, $f_\mathrm{AC} = 100$ Hz and 10 Hz. Due to high level of noise no detailed analysis of minima position was attempted.

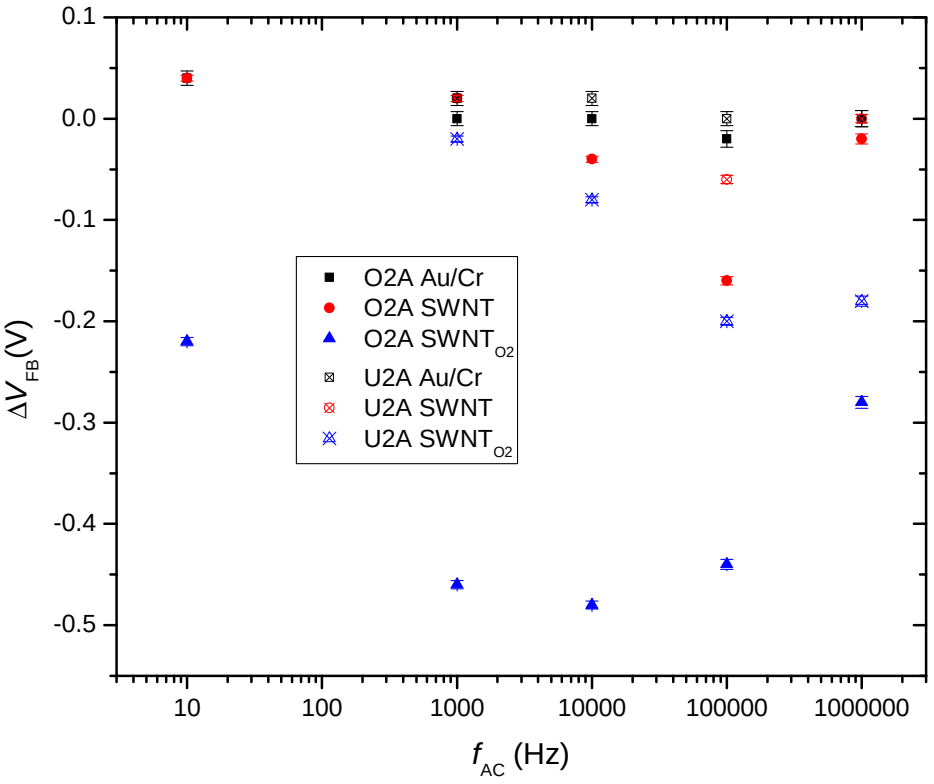

Figure 5.20 Comparison of V_{FB} for devices O2A and U2A. Both devices have three ΔV_{FB} which can be assigned to Au/Cr, SWNT network and an analyte-induced shift labelled $\mathrm{SWNT_{O2}}$. The error bars are partially obscured by the data points.

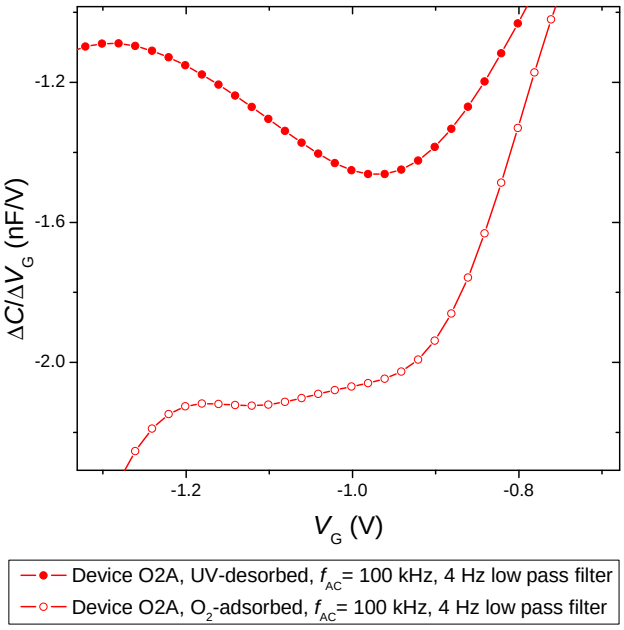

Figure 5.21 Device O2A $\mathrm{d}C/\mathrm{d}V_\mathrm{G}(V_\mathrm{G})$ in reduced range of V_G. Exposure to molecular oxygen introduces a complex change in $\mathrm{d}C/\mathrm{d}V_\mathrm{G}(V_\mathrm{G})$ spectra.

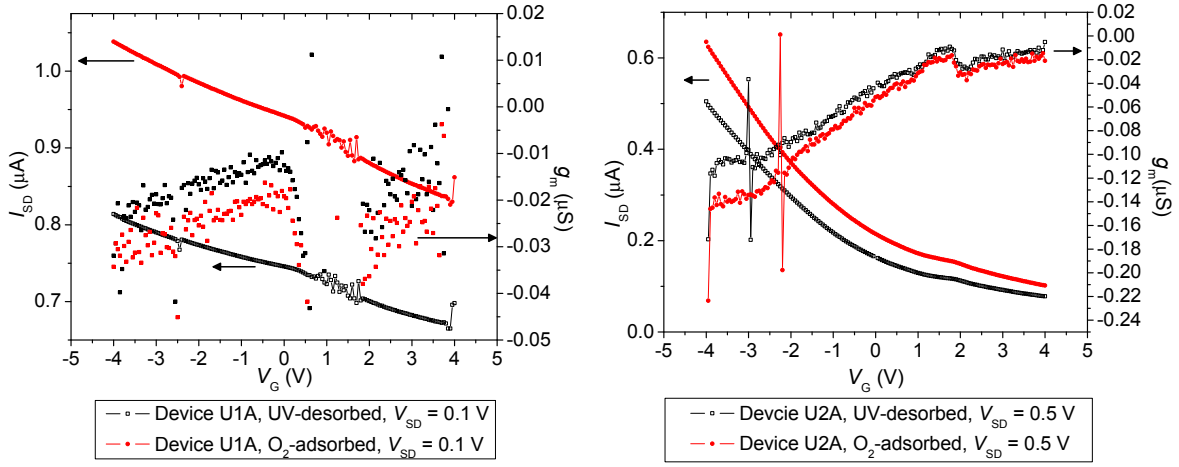

Figure 5.22 Transfer characteristics and transconductance ($\mathrm{d}I_\mathrm{D}/\mathrm{d}V_\mathrm{G}$) of thick (U1A) and thin (U2A) bottom-contacted devices operated in FET mode. The carrier channel consists of a SWNT network with an Ohmically contacted Si gate. $V_\mathrm{SD} = 0.1$ V device U1A, $V_\mathrm{SD} = 0.5$ V device O2A. Device U2A exhibits a greater change in transconductance. The error in g_m was calculated through Equation 2.3. The average error in g_m through -4 V $< V_\mathrm{G} <$ 4 V was 40% whilst at -1 V the error in $g_\mathrm{m} =\sim 20\%$.

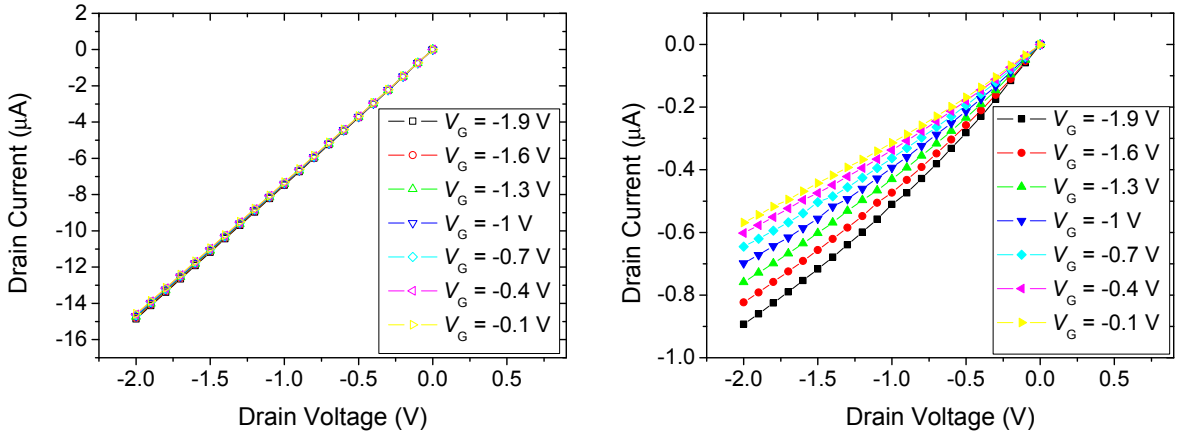

Figure 5.23 Drain current vs. drain voltage of device U1A and U2A operated as FETs with gate voltages ranging between -1.9 V to -0.1 V in 0.3 V steps. Device U2A exhibits a much greater modulation of current density with gate voltage.

the SWNT network.

	$\mid g_{m_{UV}} \mid, V_G = -1$	$\mid S_{UV} \mid$	$\mid S_{O_2} \mid$
U1A (thick network)	0.015 ± 0.003 μS	NA	NA
U2A (thin network)	0.068 ± 0.01 μS	7.6 V/dec	8.4 V/dec

Table 5.8 Extracted parameters from the transfer curves of devices U1A and U2A. No inverse sub-threshold slope, S, was determinable for device U1A due to no obvious threshold voltage V_{TH}.

The magnitude of transconductance is greater in device U2A than device U1A, Table 5.8, highlighting the increased semiconducting nature of the thin device. The thin network U2A includes more s-SWNT or larger band gap s-SWNT in the network due to reduced connectivity of the network. The enhanced field effect present in device U2A is also highlighted when the drain current versus drain voltage is examined with gate voltages ranging between -1.9 V to -0.1 V in 0.3 V steps, given in Figure 5.23, highlighting the *p*-type nature of conduction in the device. The presence of such a large off-state current in the thicker device indicates a large number of metallic or small band gap s-SWNT present in the network and that conduction occurs significantly above the percolation threshold. Zhang *et al.* [29] performed a comparison of the electrical characteristics of single SWNT transistors deposited from SDS solution and washed by a range of rinse times in DIW and ethanol. The transconductance, on current and stability of single SWNT transistors was found to be improved by an increased wash time [29].

The thick network could have a greater amount of residual SDS remaining in the network which would contribute to a reduced transconductance. Snow *et al* [176] demonstrated a SWNT network on a polymeric substrate of transconductance 0.5 mS/mm for a channel length of 7 μm, significantly larger than the best transconductance presented in this Chapter of $\sim$ 0.02 μS/mm. Optimisation of the SWNT network thickness, greater control of the nanotube bundling and the use of an interdigitated array to maximise device width over minimum device area would lead to significantly greater values of transconductance.

There is no observable current saturation within -4 V $\leq V_{\rm G} \leq$ 4 V and it is interesting to note that Snow *et al.* [18] observed current saturation at $V_{\rm G} = -4$ V with a thin film device with channel length 1/100th the channel length of the devices reported here. A greater channel length, $L_{\rm C}$, increases the number of interfacial traps, $N_{\rm IT}$, between the carbon nanotubes and gate insulator [73] leading to a greater interfacial trap capacitive component $C_{\rm IT} = {\rm d}(qN_{\rm IT})/{\rm d}\phi_{\rm S}$ where $\phi_{\rm S}$ is the SWNT surface potential due to the gate voltage. This extra capacitance would shift the gate voltage through [73]:

$$V_{\rm G} = \left(\frac{1}{\alpha_{\rm G}} + \frac{C_{\rm IT} + C_{\rm Q}}{C_{\rm o}}\right)\phi_{\rm S} - \frac{q(p-n)}{C_{\rm o}} + V_{\rm FB} \tag{5.3}$$

where $\alpha_{\rm G} = C_{\rm o}/(C_{\rm o} + C_{\rm S} + C_{\rm D})$ is the gate control factor, $C_{\rm o}$ is the gate oxide capacitance, $C_{\rm Q}$ is the quantum capacitance and $C_{\rm S}$ and $C_{\rm D}$ are the capacitances of the source and drain electrodes respectively. The increased number of SWNT/nitride interface traps obtained with an increased channel length would therefore shift the saturation voltage of the SWNT-FET device to a lower voltage, effectively stretching out the transfer curve of the FET. In the above formulism the inverse sub-threshold slope (see Section 1.4.5) can be defined as $S = m(A \cdot kT/q)$, where A is constant and $m = 1 + C_{\rm IT}/C_{\rm ox}$. The exponential sub-threshold region (-2 V $< V_{\rm G} <$ 0 V) of the transfer curve of device U2A in the UV-desorbed and O_2 adsorbed state displays an increase S by $\sim$ 10 % upon O_2 adsorption, Table 5.8. This increase in S is caused by an increase in the capacitance of the nanotube/nitride interface traps upon oxygen-adsorption. Defects on SWNTs at the gate oxide interface are probable locations for interface traps. Adsorption of oxygen at these defect sites [91] would lead to a capacitance increase and could explain the third flat-band voltage observed in the thin devices.

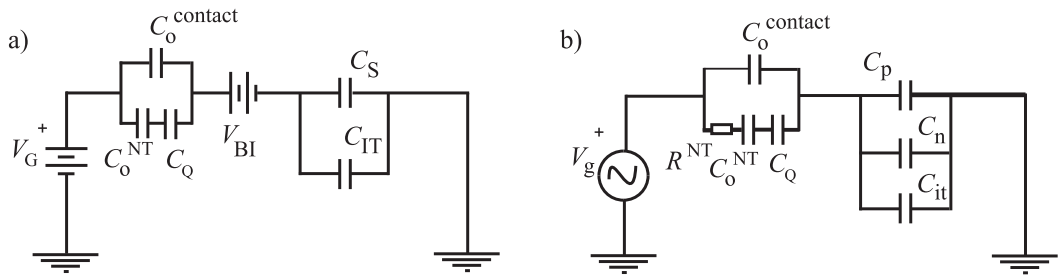

Figure 5.24 Circuit diagrams of a) d.c. equivalent circuit model b) small-signal equivalent model. Where $C_o{}^{contact}$ is the oxide capacitance with respect to the metal contact, $C_o{}^{NT}$ is the oxide capacitance with respect to the nanotube network, R^{NT} is the resistance of the nanotube network, V_{BI} is the built in voltage in the semiconductor, C_S is the d.c. capacitance of the semiconductor, C_{IT} is the d.c. capacitance of charge stored in interface traps, C_p and C_n are the differential capacitance of holes/electrons in semiconductor, C_{it} is the differential capacitance of charge stored in interface traps.

5.2.4 Device response comparison

The response of thin and thick SWNT-MOS capacitors to molecular oxygen-adsorption in both bottom-contacted and top-contacted configurations have been presented. The response, $C(V_G)$, of the devices exhibited similar increased capacitance in the depletion regime upon oxygen-adsorption. The relative increase in conductance and capacitance was found to be greater in the thin SWNT network device, see Table 5.9.

As stated in Section 1.7 the gate capacitance, C_G, can be expressed as

$$C_G = \frac{C_o C_S}{(C_o + C_S)} = C_o \qquad ((1.21))$$

where C_S is the capacitance of the semiconductor and C_o is the capacitance of the oxide. The oxide capacitance has two parallel components due to the metal contact and the carbon nanotube network, Figure 5.24. The capacitance of the oxide and SWNT network consist of two capacitances in series - the oxide capacitance with respect to the nanotube network ($C_o{}^{NT}$) which depends on the oxide thickness and density of SWNT, and quantum capacitance (C_Q) which is a function of the SWNT Fermi energy E_F (at $T = 0$ $C_Q = e^2 g(E_F)$ [177]). The total capacitance of the SWNT network and oxide is therefore $C = (1/C_o{}^{NT} + 1C_Q)^{-1}$. $C_Q = 10C_o{}^{NT}$ [176, 178] and the dominant effect arises from that of $C_o{}^{NT}$. Studies on SWNT network capacitor (with no semiconducting silicon present) have shown that as voltage between SWNT network and substrate is increased the total capacitance decreases indicating that C_Q is decreasing and therefore

		Label	Thickness (nm) [a]	R (k Ω)	ΔG % , UV → O_2	$\Delta C(V_{FB_{SWNT}})$ %, $f_{AC} = 10$ kHz, UV → O_2
Thick	Top-contacted	O1A	2200 ± 300	14.21 ± 0.02	4 ± 2	8 ± 2
	Bottom-contacted	U1A	1100 ± 200	44.62 ± 0.08	13 ± 2	11 ± 2
Thin	Top-contacted	O2A	40 ± 30	394 ± 1	10 ± 2	26 ± 3
	Bottom-contacted	U2A	200 ± 40	1274 ± 3	30 ± 3	18 ± 3

[a]Calculated from UV-absorption spectra, Chapter 2.1.3

Table 5.9 Summarised data for device response to oxygen-adsorption from a UV-desorbed state. $\Delta G\%$ is calculated from the steady state values of conductance in each state. The change in capacitance at the flat-band voltage of the SWNT network is compared, $\Delta C(V_{FB_{SWNT}})\%$ at $f_{AC} = 10$ kHz. In the case of the thick network $\Delta C(V_{FB_{SWNT}})$ is calculated from the shift of the $V_{FB_{SWNT}}$ between UV-desorbed and O_2-adsorbed state. In the case of the thin network $\Delta C(V_{FB_{SWNT}})$ is calculated from the difference between $V_{FB_{SWNT}}$ and $V_{FB_{SWNT_{O_2}}}$.

playing a greater role in the total capacitance [122]. Snow *et al.* achieved relative changes in capacitance for non-polar molecules benzene, hexane and heptane ~ 200 for concentrations ~ 600 ppm. [114]. The response of the SWNT-MOS device capacitance presented in this Chapter could be improved through greater effort to ensure de-bundled SWNT, greater control over the thickness and through incorporation of a thinner gate oxide or by using a high dielectric constant insulator such as TiO_2.

The variation in $dC/dV_G(V_G)$ is similar for thin and thick networks in the UV-desorbed state, exposure to molecular oxygen introduces thickness dependent differences in $dC/dV_G(V_G)$. The thick SWNT networks (device O1A and U1A) upon O_2 exposure display a positive shift of the flat-band voltage associated with the SWNT network; possibly explained by an increase in the surface dipole of SWNT due to oxygen-adsorption. This behaviour is observed for both the top-contacted and bottom-contacted device configurations with a similar ΔV_G shift observable in both cases. In the case of the thin devices upon O_2-adsorption the minima in $dC/dV_G(V_G)$ associated with flat-band conditions of the gate materials are still present and at similar gate voltages. However, there is a third minima in $dC/dV_G(V_G)$ upon oxygen exposure at $V_{FB_{Cr/Au}} < V < V_{FB_{SWNT}}$. Oxygen adsorption withdraws electrons from the SWNT network shifting the Fermi level, this change in the DOS would increase C_Q which could explain the origin of the third flat-band voltage. Also the third minima could be attributed to a greater efficiency of adsorption at the SWNT/nitride interface -

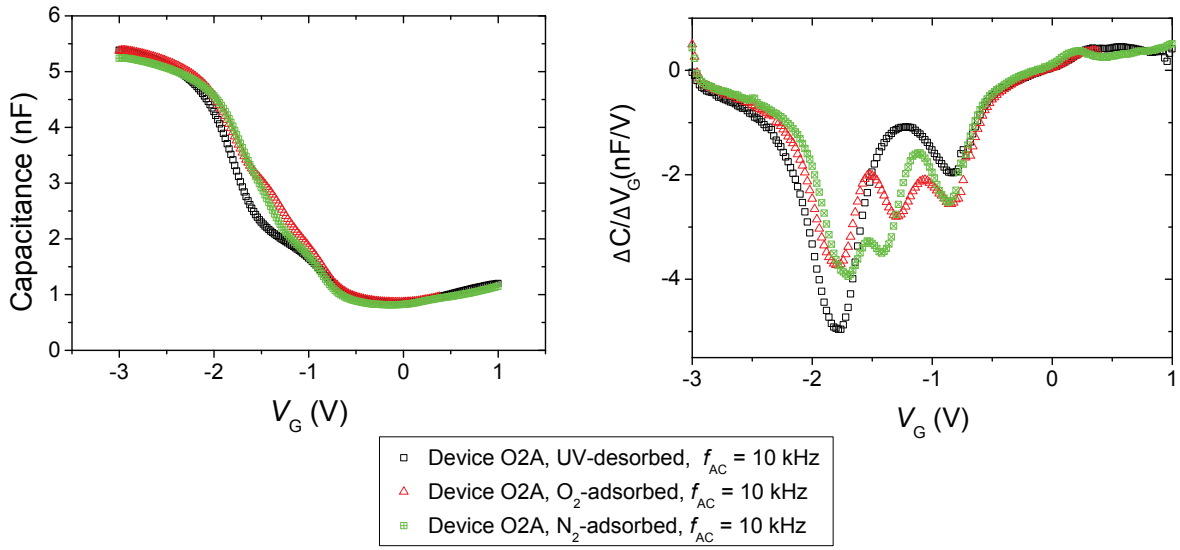

Figure 5.25 $\mathrm{d}C/\mathrm{d}V_\mathrm{G}$ for thin SWNT network device O2A in UV-desorbed, O_2-exposed and N_2-exposed states at $f_\mathrm{AC} = 10$ kHz.

providing a third V_FB as discussed below. The quality of the third flat-band voltage peak in $\mathrm{d}C/\mathrm{d}V_\mathrm{G}(V_\mathrm{G})$ of O2A (top-contacted) is greater than U2A (bottom-contacted) and is likely due to a robust electrical contact as a result of Fermi level pinning.

The transfer characteristics of bottom-contacted devices display a non-zero transconductance. The polarity of gate voltage needed to increase I_D is indicative of p-type transport the cause of which is deeply adsorbed oxygen [15].

The effect of oxygen on the SWNT networks operated as FETs varies with film thickness. The thick device exhibits an increased conductance on oxygen adsorption with no well defined inverse sub-threshold region and small variation in transconductance, indicating minimal field effect on conductance. The thin device exhibits an increased conductance upon oxygen adsorption and an increase in inverse sub-threshold slope, $S = m(A \cdot kT/q)$, where A is constant and $m = 1 + C_\mathrm{IT}/C_\mathrm{ox}$.The increase in S upon oxygen adsorption is attributed to an increase in the capacitance of interface traps through oxygen adsorption. This could also be a basis for explaining the appearance of a third minima in $\mathrm{d}C/\mathrm{d}V_\mathrm{G}(V_\mathrm{G})$ of the thin devices. Oxygen adsorption at the nanotube/nitride interface contributes a new flat-band voltage to the C-V scan. In this case there is effectively a 'new material' at the nitride surface arising from the adsorption of oxygen on the nanotube network with a distinct flat-band voltage. In support of this argument the response of O2A to nitrogen-adsorption is presented and contrasted with oxygen adsorption in Figure 5.25.

There is an appreciable difference in the minima in $\mathrm{d}C/\mathrm{d}V_{\mathrm{G}}$ for device O2A between oxygen and nitrogen exposure, Figure 5.25. The minima previously observed and assigned to the flat-band voltage of the metal contact and SWNT network are still observable at the same voltage irrespective of atmospheric condition. The adsorption of nitrogen/oxygen on the nanotube network provides a distinct flat-band voltage for the adsorption complex. This is not observed in thick films due to the increased metallic component and increased thickness, reducing the amount of adsorption by nanotubes at the nitride surface.

The two thickness groups are sufficiently distinct to draw broad conclusions, however the variation in thickness between samples of the same group reflects a lack of control in the device production and characterisation, this is probably due to the necessity of creating a separate sample for each device (coated under the same conditions of the device) for the purposes of UV-visible spectrophotometry. This technique could be improved markedly by employing reflectance spectroscopy on the same sample, rather than producing a separate sample. This technique could be possible with the existing PerkinElmer Lambda 950 Spectrophotometer with a small modification [2].

The top-contacted samples display lower resistance (factor of $\sim 1/3$) than the bottom-contacted samples, even when the effective thickness is thinner by a factor of four, as is the case for the thin sample set. This is expected as the resistance of the SWNT networks critically depend on the current injection efficiency, comprised primarily of the height and thickness of the metal-nanotube Schottky barrier and the reflectivity of the contact. Top-contacted SWNT are expected to have fewer contaminants at the metal electrode/SWNT interface as a result of metal vapour deposition under vacuum (1×10^{-6} mbar). Bottom-contacted SWNT are expected to have more contaminants at the metal electrode/SWNT interface due to a greater concentration of organic contaminants present during deposition, introducing additional barriers to the current injection in addition to the metal-nanotube Schottky barrier. As discussed in preceding Chapters impurities within the network could affect the electronic properties and response to analyte. The presence of carbonaceous and metallic impurities reduce the base conductance and magnitude and speed of the conductance increase upon oxygen exposure and determine the reversibly on application of vacuum [167]. The reduction of network conductance by the presence of carbonaceous and metallic impurities could reduce the capacitative response of the network by reducing

[2] Universal Reflectance Accessory, PerkinElmer, Inc.

the polarising electric field. The response of the SWNT-MOS sensor may therefore by improved by increasing the purity of SWNT network.

The effect of residual SDS could have affected the current injection efficiency of the devices and may have played a greater role in the thick devices - possibly contributing to the reduced transconductance observed in Figure 5.22. The effect of residual Na ions is unknown and the discussion in Chapter 4 on the possibility of charge transfer occurring through a Na mediated reaction path is still valid.

5.2.5 Reproducibility of results

The general device behaviour described in this Chapter has been observed in a number of SWNT-MOS devices. Gradual improvement of device characteristics and control of processing parameters resulted in the SWNT-MOS devices presented in this Chapter. The most significant improvements in device performance and reproducibility came as a result of:

- improved control of the network thickness through optimisation of the air brush technique.
- Optimisation of silicon wafer processing parameters and the resulting minimisation of leakage current. The optimised silicon wafer processing steps and experimental setup for checking the leakage current are described in Appendix A.

The reproducibility of results occurring on the same sample are good. Care must be taken to apply the same exposure history to achieve similar results, as described in Chapter 4 concerning the reproducibility of resistive SWNT sensor measurements.

Reproducibility in the measurement of $C(V)$ of device O2A is considered in the O_2 adsorbed state. Three $C(V)$ measurements are taken successively. The variation in capacitance, $\mathrm{d}C/\mathrm{d}V(V)$ and V_{FB} is discussed. The standard deviation of capacitance measurements is small, the sd of $\overline{C(V)}$ at $f_{\mathrm{AC}} = 10$ kHz has a value of 0.03% averaged over the range of V. $C(V)$ at 1 MHz, Figure 5.26, 100 Hz and 10 Hz display a large degree of noise. The mathematical derivative of $C(V)$ is calculated and FFT filtration applied at 4 Hz. The noise in $C(V)$ is amplified when the mathematical derivative is taken, Figure 5.27. Extraction of V_{FB} from each of the three sets of $C(V)$ provides a measure of the standard deviation in V_{FB}, Table 5.10. There is zero standard deviation of flat-band voltage of mid-frequency $\mathrm{d}C/\mathrm{d}V(V)$.

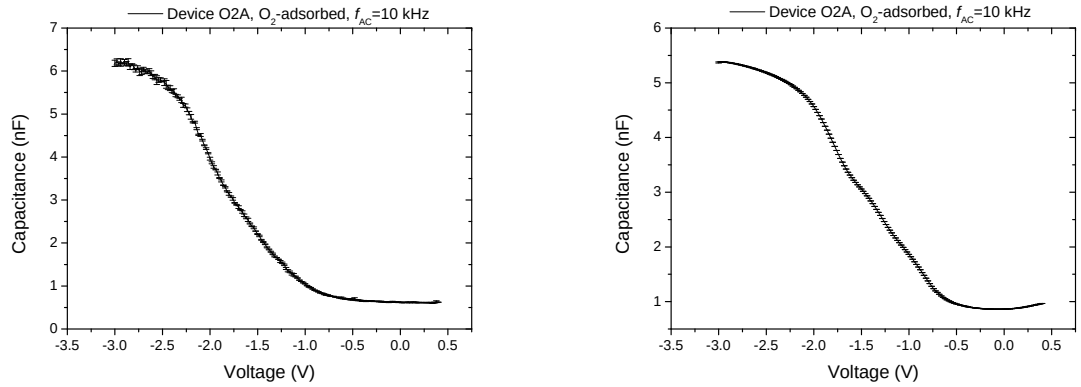

Figure 5.26 $\overline{C(V)}$ for device O2A in the oxygen adsorbed state calculated from three sets of $C(V)$ at $f_{\mathrm{AC}} = 1$ MHz ($f_{\mathrm{AC}} = 10$ kHz) for the LHS (RHS) graph. The standard deviation of $\overline{C(V)}$ is displayed as error bars.

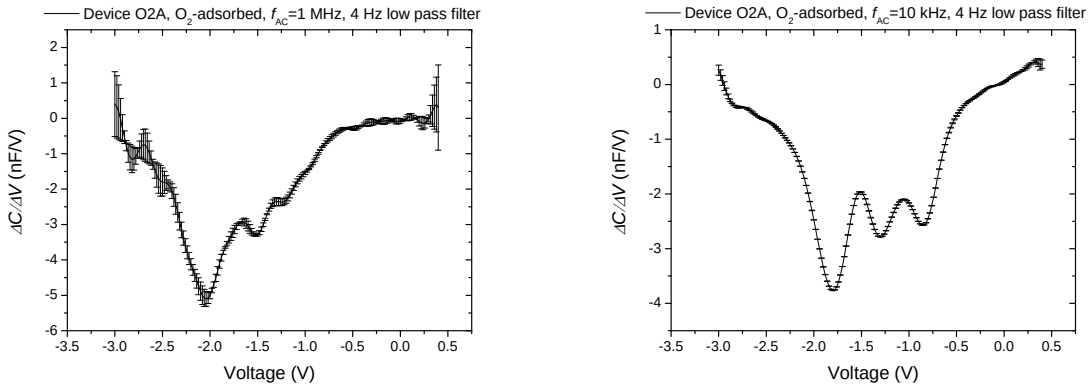

Figure 5.27 $\overline{\mathrm{d}C/\mathrm{d}V(V)}$ for device O2A in the oxygen adsorbed state calculated from three sets of $\mathrm{d}C/\mathrm{d}V(V)$ at $f_{\mathrm{AC}} = 1$ MHz ($f_{\mathrm{AC}} = 10$ kHz) for the LHS (RHS) graph with 4 Hz FFT filtering. The standard deviation of $\overline{\mathrm{d}C/\mathrm{d}V(V)}$ is displayed as error bars.

Freq.	1 MHz	100 kHz	10 kHz	1 kHz	100 Hz	10 Hz
V_{FB}	-2.03	-1.92	-1.80	-1.70	-1.59	-1.71
sd	0.02	0	0	0	0.01	0.03
$\%sd$	1	0	0	0	1	2

Table 5.10 Mean flat-band voltages and associated standard deviation from a sample set of three for SWNT-MOS device O2A.

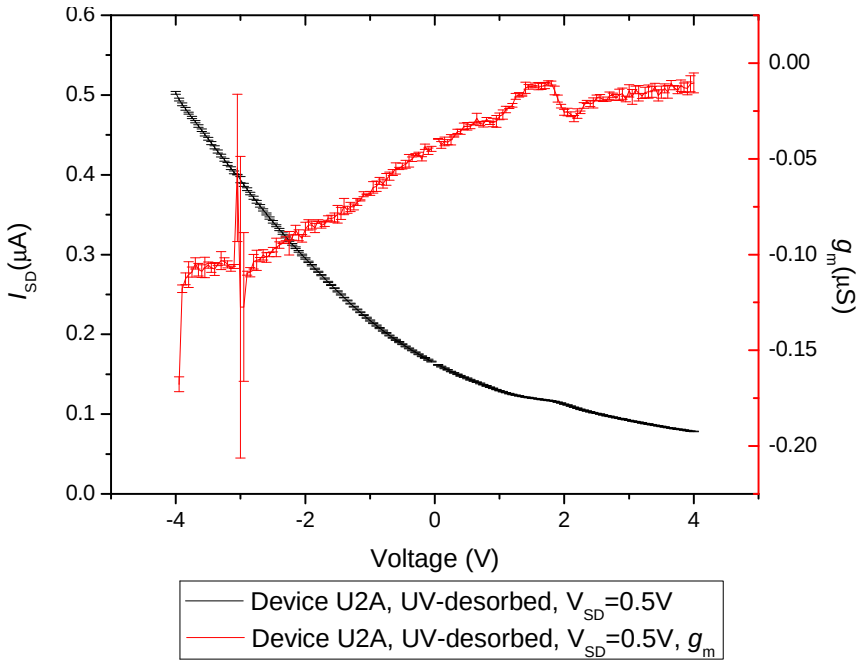

Figure 5.28 Transfer characteristics of device U2A in UV-desorbed state averaged over three cycles. Standard deviation given as error bars.

The repeatability of SWNT-FET characteristics has been investigated. The transfer characteristics of device U2A in the UV-desorbed state were recorded between -4 V $< V_G < 4$ V were repeated three times and the average and standard deviation calculated, Figure 5.28. The average standard deviation of the current is small $\overline{sd} = 0.3\%$. The average standard deviation of the transconductance is large $\overline{sd} = 8\%$ due to instability in the transfer transconductance centered around $V_G = -3$ V, Figure 5.28.

Chapter 6

Conclusion and Further Work

6.1 Conclusion

The adsorption of oxygen onto thin and thick SWNT networks has been investigated. Nanotube networks of controllable thickness were deposited from an aqueous suspension with the airbrush technique. Oxygen-adsorption provided increases in conductance and differential capacitance which are interpreted in terms of the deduced transport characteristics. Oxygen-adsorption on thin SWNT networks provided a detectable change in the sub-threshold slope when operated as a FET.

Temperature dependent transport characteristics of thin and thick networks were investigated in Chapter 3, the room temperature rate limiting process was found to be 3D-VRH. Thin SWNT networks were described by 3D-VRH hopping throughout the entire temperature range 4 K$< T <$ 300 K. Thick SWNT networks were well described by 3D-VRH in the temperature range 60 K$< T <$ 300 K, the conductance of the thick network can be described throughout the entire temperature region 4 K$< T <$ 300 K by a heterogenous model formed through inclusion of a metallic type conductance component. In a thick nanotube network all-metallic pathways are expected to dominate the conduction due to high connectivity and therefore large degree of freedom for the current pathway. The density of states at the Fermi level would be expected to be greater in a network with an increased proportion of metallic pathways and this is indicated through the values of the extracted VRH parameters. The VRH parameter T_0 is inversely proportional to the density of states at the Fermi level, $g(E_{\mathrm{F}})$, and is extremely sensitive to the localisation length, α, as $T_0 \propto g(E_{\mathrm{F}})^{-1}\alpha^{-1/3}$. The VRH parameter G_0 describes the geometry of the nanotube networks, increasing with

number of contributing filamentary branches in the network. Comparison between the fitting parameters for thin and thick nanotube networks in the laboratory-air exposed state reveal $T_0(\text{thin}) \sim 60 \times T_0(\text{thick})$ and $G_0(\text{thick}) \sim 9 \times G_0(\text{thin})$ indicating the increased connectivity and metallic nature of the thick network. Electric field dependent conductance of the thin SWNT network identified an exponential dependence of conductance on applied voltage, indicating a field mediated increase in the hopping or tunnelling probability. UV-desorption of the thin network was shown to reduce G_0 and increase T_0 indicating a reduction in the network connectivity and a decrease in the product $g(E_\text{F}) \cdot \alpha^3$ as a result of oxygen desorption.

The determined transport characteristics were then used as a basis for explaining the observed conductance response of thin and thick SWNT networks to molecular oxygen-adsorption. The conductance of a UV-desorbed SWNT network increases upon oxygen-adsorption. Oxygen doping shifts the Fermi level into a transport band of a percentage of nanotubes increasing the network connectivity which increases the network conductance. Cycling between a vacuum level of 1×10^{-5} mbar and atmospheric pressure oxygen resulted in a decrease in conductivity after each oxygen exposure. The SWNT networks remain oxygen doped in vacuum and due to the experimental set-up the introduction of water-vapour into the network could not be eliminated and could cause the observed decrease in conductance with oxygen/vacuum cycling as a result of the interaction of water molecules with chemisorbed oxygen within the nanotube network. Oxygen is most likely chemisorbed at defect sites in the network. Improvements in the quality of nanotubes is expected to improve the reversibility of the adsorption.

Adsorption kinetics were investigated in Chapter 4. Thin and thick SWNT networks[1] displayed two distinct regions of adsorption dynamics, with characteristic time period dependent on thickness of the network. Initially the adsorption of oxygen onto the network is described by diffusion phenomena. Within the diffusive regime the conductance response dynamics of the network can be further differentiated. A very fast diffusive component is sated after a few minutes, after this point diffusion continues at a lower rate. The transition within the diffusive regime is similar to other diffusive processes which become influenced by trapping of the diffusing particle. This reduction in diffusion rate could be caused by a reduction in doping efficiency as a result of molecular trapping by defects or impurities. The diffusion parameter of the thick nanotube network is significantly less than the thin nanotube network indicating a

[1]These samples are distinct from the thin and thick networks mentioned previously, see Section 4.2.

combination of a greater number of traps, possibly through increased bundle formation or network density and reduction in the doping efficiency as a result of a greater metallic component in the network. The second broad range of adsorption kinetic behaviour is described by an activation limited adsorption process, and so describes the adsorption onto nanotube networks at a high density of adsorbed oxygen. This process continues with an increasing value of required energy for adsorption until the end of the experiment, $t \sim 40$ hours.

In Chapter 5 thin and thick SWNT-MOS devices were exposed to atmospheric pressure oxygen from a UV-desorbed state. The differential capacitance of the devices was measured at various small-signal frequencies whilst scanning the d.c. gate bias V_{G}. Flat-band voltages were extracted for thin and thick networks in top-contacted and bottom-contacted electrode configurations. The SWNT-MOS devices could also be operated as FETs with a conduction channel formed by the nanotube network, the carrier density is modulated by the field from the Ohmic contact at the back-plane of silicon. A large field effect was present in the thin network devices, with a detectable turn-on voltage and sub-threshold slope. The thick network devices displayed little field effect, with no detectable turn-on voltage. These observations support those noted earlier in which the transport characteristics of thicker networks contained a metallic component in the functional form whilst thin networks were more semiconducting. Differences in the differential capacitance response also indicate the metallic and semiconducting nature of the thick and thin networks. Thick networks exhibited a positive shift of the SWNT network flat-band voltage upon oxygen adsorption due to increased surface dipole and charge transfer with the nanotube network. Thin nanotube networks exhibited two detectable flat-band voltages post oxygen-adsorption. One flat-band voltage was unmoved from that attributed to the SWNT network in UV-desorbed state, the other flat-band voltage occurred at a lesser voltage and is attributed to the interaction of oxygen with semiconducting nanotubes at the nanotube-nitride interface. The quality of the third flat-band voltage peak in $\mathrm{d}C/\mathrm{d}V_{\mathrm{G}}(V_{\mathrm{G}})$ was found to be greater in the top-contacted device than in the bottom-contacted device and is indicative of a robust electrical contact as a result of enhanced Fermi level pinning.

Carbon nanotube networks show promising possibilities for use as a gate-electrode on a MOS capacitative sensor. The use of thin top-contacted nanotube networks as a gate electrode in a MOS capacitor results in clear features in $\mathrm{d}C/\mathrm{d}V$ which vary with the

analyte to which the network is exposed. Further more, the UV-desorbed SWNT-MOS device exhibited a response to oxygen adsorption in terms of conductance, flat-band voltage shift and FET characteristics. The SWNT-MOS sensor operated as capacitor, FET and resistor is therefore a potential method of distinguishing analytes through analysis of adsorption characteristics in the above modes. It has been demonstrated that the sensor response signal is dependent on the thickness of SWNT-network, thinner networks exhibiting a greater response to oxygen in each of the modes of operation. The adsorption kinetics of oxygen on thick and thin nanotube networks reveal a greater degree of trapping present in the thick nanotube network. The diffusion and adsorption of oxygen is determined by the degree of surface impurities and defects within the nanotube network. UV-desorption was necessary to desorb dopants from the nanotube network indicating strongly bound species most likely present at defects within the network. The quality of nanotubes and the degree of graphitisation is therefore important in determining the response of the nanotube network to oxygen-adsorption. It is anticipated that through a purification of the network through oxidation of amorphous carbon impurities that the response time and magnitude of signal could be improved. The possibility exits for optimisation of the response signal through optimisation of the network thickness. Control of the quality of nanotubes, including the degree of graphitisation and impurity levels, could lead to improvements in the recovery and adsorption time of the sensor.

6.2 Further work

The work presented in this thesis is of interest from both a fundamental physics and applications perspective. The interaction of molecular species with 1D-systems was investigated and a device was presented with sensitivity to subtle material specific electronic properties such as work-function.

However, many questions remain unanswered. The amount of residual surfactant and associated Na ions present in the nanotube network after the wash technique prescribed in this thesis should be quantified through a suitable spectroscopic technique such as x-ray photoelectron spectroscopy. The effect of residual surfactant and associated Na ions within the nanotube network on the transport characteristics of the networks and conductance/capacitance response to oxygen-adsorption should be investigated. This could be addressed with a sample set differentiated by DIW wash time with some

including organic solvent wash as this has been reported to complectly remove any adsorbed SDS [29]. High temperature annealing $\sim$ 1300 K has been shown through photoemission spectra to completely remove residual Na from SWNT networks [31], comparison of results should also be made with such a sample and the possibility of graphitisation of the nanotube network should be considered.

The sensitivity of the networks to partial pressures of analyte has not been investigated. It would be of great interest to explore the differential capacitative response of thin SWNT-MOS devices to partial pressures of analyte. Intuitively one expects sensitivity to be high due to large surface area and 1D-electronic structure.

The thickness of nanotube network was found to be critical to the differential capacitative response of nanotube networks. Further work should therefore include testing of networks at the cusp of the percolation threshold. Ideally these networks would be directly grown on silicon oxide, minimising contact resistances and defects induced into the nanotubes through processing (ultrasonication).

A study of the response of the SWNT-MOS capacitor sensor to oxygen with differing degrees of quality of SWNT used as the gate material would provide information on the role of defects in the sensing response of SWNT-MOS devices.

Appendix A

Device Fabrication Procedure

1. **Evaporation mask fabrication.**

   - Positive photoresist spincoated and soft baked at 373 K for $\sim$ 1 minute on each side of molybdenum (Mo) sheet.
   - UV mask appropriate for single stripe electrode pattern (see example pattern below) was placed on Mo sheet and exposed in UV light-box.

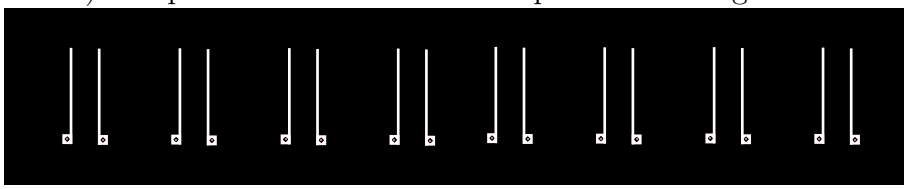

   - The UV exposed photoresist was developed in appropriate developer solution.
   - Mo sheet with single stripe electrode pattern etched in 1 part H_2SO_4 + 1 part HNO_3 + 5 parts H_2O, providing an etch rate of $\sim$ 12 μm/min at 25 °C.
   - Mo sheet rinsed in DIW.

2. **SiO_2/Si_3N_4 layer etched off of one side of silicon wafer.** Both faces of the as supplied wafer[1] comprise a 20 nm SiO_2 thermally grown layer followed by a CVD grown 30 nm Si_3N_4 layer. On one face of the silicon the SiO_2 and Si_3N_4 layer was removed by pipetting 48 wt. % HF in H_2O (Sigma-Aldrich, product number: 380105) onto one face of the wafer, SiO_2/Si_3N_4 is removed when the surface property changes from hydrophillic to hydrophobic. The HF solution is then pipetted off of the Si wafer and Si wafer rinsed in DIW.

[1] Si-Mat, http://www.si-mat.com/

3. **Al Ohmic contact deposited on Si wafer.** 100 nm thick aluminium layer was thermally evaporated onto the exposed silicon face of the wafer. The thickness of deposited Al was determined with a quartz crystal oscillator situated in the same solid angle as the target substrate, the appropriate density of 2.7 g/cm^3 and acoustic impedance of 8.17×10^5 g/cm^{2}s was input into the quartz crystal thickness controller. To improve the Ohmic contact of the Si-Al interface the wafer was annealed at 623 K for 5 minutes in laboratory atmospheric conditions.

4. **Integrity of SiO_2/Si_3N_4 confirmed.** Any holes in the SiO_2/Si_3N_4 layer will introduce significant leakage current upon deposition of the SWNT network. The integrity of the SiO_2/Si_3N_4 layer was confirmed electrochemically through linear sweep voltammetry, using the following procedure:

   - The buffer solution was de-gassed by bubbling nitrogen through the solution for $\geq$ 20 minutes.
   - The silicon wafer is positioned in a suitable electrochemical cell, Figure A.1. A small area of the silicon wafer was exposed to the electrolyte solution through the use of a spring-loaded compression mask and o-ring. The electrolyte comprised a 0.5 M H_2SO_4 solution containing 0.01 M Fe^{3+} and 0.01 M Fe^{2+}, all purchased from Sigma-Aldrich. The cell potential was measured with reference to a Ag/AgCl (3 mol dm^{-3} NaCl) electrode, the counter electrode consisted of platinum foil and the working electrode was in electrical contact with the Al face of the silicon wafer through contact with the brass plate.
   - With the electrodes attached to a suitable potentiometer (Autolab Potentiostat PGSTAT12) linear sweep voltammetry was performed with a scan rate of 100 mV/s.
   - Various areas of the silicon wafer should be tested to confirm homogeneity of SiO_2/Si_3N_4.

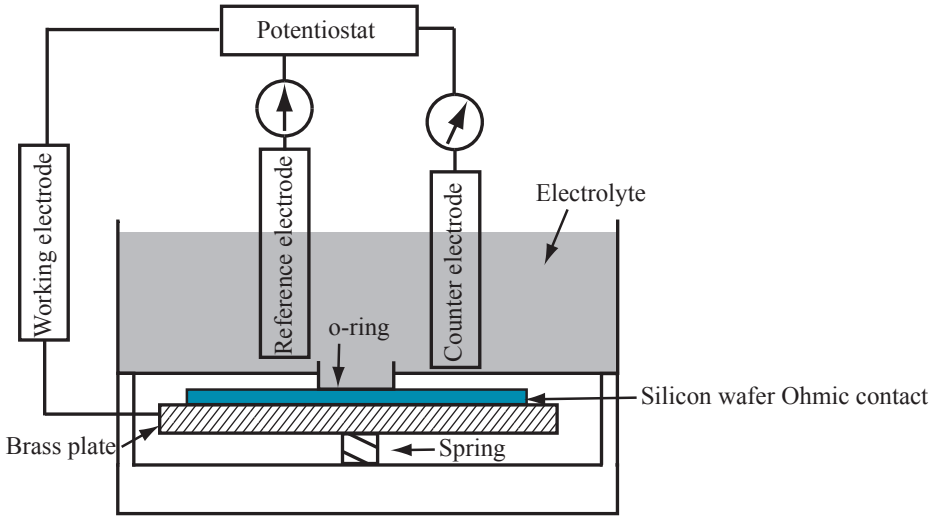

Figure A.1 Experimental setup for leakage current measurements. The reference electrode consisted of a Ag/AgCl electrode the counter electrode consisted of platinum foil and the working electrode was attached to the Ohmically contacted Al face of the Si wafer which was in electrical contact with the brass plate. The potentiostat controlled the potential of the working electrode with respect to the reference electrode while simultaneously measuring the current flowing between the working electrode and the counter electrode.

5. **Si wafer diced.** A diamond tipped scribe and ruler were used to gently scratch a straight line on the Si wafer. The wafer was positioned on a raised edge of the ruler, cotton buds were used to gently press down on either side of the scratched line to cleanly break the wafer.

6. **Silicon wafer cleaned.** The silicon wafer was cleaned through bath sonication in acetone for 5 minutes followed by bath sonication in methanol for 5 minutes. The samples were then rinsed in DIW and blown dry in a nitrogen flow.

7. **Electrodes evaporated.** *Note:* the order of steps 7 and 8 is interchangeable depending on desired top/bottom contacted device configuration.

    - The substrates were aligned with the evaporation mask and placed in thermal deposition chamber.
    - 20 nm Cr (density 7.2 g/cm^3, acoustic impedance 28.95×10^5 g/cm^{2}s) deposited to facilitate adhesion of Au.
    - 80 nm Au deposited (density 19.3 g/cm^3, acoustic impedance 23.18×10^5 g/cm^{2}s).

8. **Nanotube network deposited.**

   - The airbrush [2] was pressurised with filtered compressed air.
   - The SWNT solution was placed in the airbrush well and the airbrush was positioned 5 cm above the device substrate. Single sweep brush strokes were applied.
   - Each deposited brush stroke was allowed to dry before subsequent depositions.
   - Post deposition the SWNT networks were soaked in de-ionised water for 20 minutes to remove excess SDS.

[2] Everythingairbrush, Model AB-135A, http://www.everythingairbrush.com/

Appendix B

Error in Chapter 3 transport measurements

The errors in V and I were treated as originating from the same source (dependent error) and propagated through the calculation of the zero-bias differential conductance, G.

Temperature	G error %	G error	I range	I resolution	I accuracy
300 K	0.39	2×10^{-7}	$1 < I \leq 10$ μA	10 pA	0.05 % + 600 pA
249 K	0.40	2×10^{-7}	$1 < I \leq 10$ μA	10 pA	0.05 % + 600 pA
200 K	0.41	1×10^{-7}	$1 < I \leq 10$ μA	10 pA	0.05 % + 600 pA
160 K	0.42	1×10^{-7}	$1 < I \leq 10$ μA	10 pA	0.05 % + 600 pA
120 K	0.44	7×10^{-8}	$1 < I \leq 10$ μA	10 pA	0.05 % + 600 pA
100 K	0.46	6×10^{-8}	$1 < I \leq 10$ μA	10 pA	0.05 % + 600 pA
90 K	0.47	5×10^{-8}	$1 < I \leq 10$ μA	10 pA	0.05 % + 600 pA
80 K	0.39	4×10^{-8}	100 nA $< I \leq 1$ μA	1 pA	0.05 % + 100 pA
70 K	0.40	3×10^{-8}	100 nA $< I \leq 1$ μA	1 pA	0.05 % + 100 pA
60 K	0.40	2×10^{-8}	100 nA $< I \leq 1$ μA	1 pA	0.05 % + 100 pA
50 K	0.41	2×10^{-8}	100 nA $< I \leq 1$ μA	1 pA	0.05 % + 100 pA
40 K	0.43	1×10^{-8}	100 nA $< I \leq 1$ μA	1 pA	0.05 % + 100 pA
30 K	0.48	9×10^{-9}	100 nA $< I \leq 1$ μA	1 pA	0.05 % + 100 pA
20 K	0.44	4×10^{-9}	$0 < I \leq 100$ nA	100 fA	0.05 % + 30 pA
17 K	0.47	3×10^{-9}	$0 < I \leq 100$ nA	100 fA	0.05 % + 30 pA
15 K	0.50	2×10^{-9}	$0 < I \leq 100$ nA	100 fA	0.05 % + 30 pA
12 K	0.58	2×10^{-9}	$0 < I \leq 100$ nA	100 fA	0.05 % + 30 pA
10K	0.70	1×10^{-9}	$0 < I \leq 100$ nA	100 fA	0.05 % + 30 pA
9 K	0.8	1×10^{-9}	$0 < I \leq 100$ nA	100 fA	0.05 % + 30 pA
8 K	0.96	1×10^{-9}	$0 < I \leq 100$ nA	100 fA	0.05 % + 30 pA
7 K	1.22	9×10^{-10}	$0 < I \leq 100$ nA	100 fA	0.05 % + 30 pA
6 K	1.72	8×10^{-10}	$0 < I \leq 100$ nA	100 fA	0.05 % + 30 pA
5 K	2.70	7×10^{-10}	$0 < I \leq 100$ nA	100 fA	0.05 % + 30 pA
4 K	3.86	7×10^{-10}	$0 < I \leq 100$ nA	100 fA	0.05 % + 30 pA

Table B.1 Error in zero-bias differential conductance, G, of UV-desorbed thin SWNT network in the temperature range 4 K $\leq T \leq$ 300 K.

Appendix C

List of Publications

[P1] D.J. Mowbray, C. Morgan and and K. S. Thygesen. Influence of O_2 and N_2 on the conductivity of carbon nanotube networks. *Physical Review B*, 79:195431, 2009.

[P2] C. Morgan, Z. Alemipour and M. Baxendale. Variable range hopping in oxygen-exposed single-wall carbon nanotube networks. *Physica Status Solidi A*, 205(6):1394:1398, June 2008 [Errata: DOI: 10.1002/pssa.200925122 (awaiting print issue)].

Bibliography

[1] T. Durkop, S. A. Getty, E. Cobas, and M. S. Fuhrer. Extraordinary mobility in semiconducting carbon nanotubes. *Nano Letters*, 4(1):35–39, January 2004.

[2] B. Q. Wei, R. Vajtai, and P. M. Ajayan. Reliability and current carrying capacity of carbon nanotubes. *Applied Physics Letters*, 79(8):1172–1174, August 2001.

[3] J. Hone, M. C. Llaguno, M. J. Biercuk, A. T. Johnson, B. Batlogg, Z. Benes, and J. E. Fischer. Thermal properties of carbon nanotubes and nanotube-based materials. *Applied Physics A-Materials Science & Processing*, 74(3):339–343, March 2002.

[4] B. G. Demczyk, Y. M. Wang, J. Cumings, M. Hetman, W. Han, A. Zettl, and R. O. Ritchie. Direct mechanical measurement of the tensile strength and elastic modulus of multiwalled carbon nanotubes. *Materials Science And Engineering A-Structural Materials Properties Microstructure And Processing*, 334(1-2):173–178, September 2002.

[5] A. Krishnan, E. Dujardin, T. W. Ebbesen, P. N. Yianilos, and M. M. J. Treacy. Young's modulus of single-walled nanotubes. *Physical Review B*, 58(20):14013–14019, November 1998.

[6] H. W Kroto, J. R Heath, S. C O'Brien, R. F Curl, and R. E. Smalley. C_{60}: Buckminsterfullerene. *Nature*, 318:162–163, 1985.

[7] W. Krätschmer, L.D. Lamb, K. Fostiropoulous, and D.R. Huffman. Solid C_{60}: a new form of carbon. *Nature*, 347:354–358, 1990.

[8] S. Iijima. Helical microtubules of graphitic carbon. *Nature*, 354:56, 1991.

[9] R. Saito, G. Dresselhaus, and M. S. Dresselhaus. *Physical Properties of Carbon Nanotubes*. Imperial College Press, 1998.

[10] R. Saito, M. Fujita, G. Dresselhaus, and M.S. Dresselhaus. Electronic structure of chiral graphene tubules. *Applied Physics Letters*, 60:2204, 1992.

[11] M. Reibold, P. Paufler, A. A. Levin, W. Kochmann, N. Patzke, and D. C. Meyer. Materials - carbon nanotubes in an ancient Damascus sabre. *Nature*, 444(7117):286–286, November 2006.

[12] S. Iijima and T. Ichihashi. Single-shell carbon nanotubes of 1-nm diameter. *Nature*, 361:603, 1993.

[13] A. Thess, R. Lee, P. Nikolaev, H. J. Dai, P. Petit, J. Robert, C. H. Xu, Y. H. Lee, S. G. Kim, A. G. Rinzler, D. T. Colbert, G. E. Scuseria, D. Tomanek, J. E. Fischer, and R. E. Smalley. Crystalline ropes of metallic carbon nanotubes. *Science*, 273:483–487, 1996.

[14] W. J. Liang, M. Bockrath, D. Bozovic, J. H. Hafner, M. Tinkham, and H. Park. Fabry-Perot interference in a nanotube electron waveguide. *Nature*, 411(6838):665–669, June 2001.

[15] P. G. Collins, K. Bradley, M. Ishigami, and A. Zettl. Extreme oxygen sensitivity of electronic properties of carbon nanotubes. *Science*, 287:1801, 2000.

[16] J. Kong, N. R. Franklin, C. W. Zhou, M. G. Chapline, S. Peng, K. J. Cho, and H. J. Dai. Nanotube molecular wires as chemical sensors. *Science*, 287(5453):622–625, 2000.

[17] C. Kocabas, S. J. Kang, T. Ozel, M. Shim, and J. A. Rogers. Improved synthesis of aligned arrays of single-walled carbon nanotubes and their implementation in thin film type transistors. *Journal Of Physical Chemistry C*, 111(48):17879–17886, December 2007.

[18] E. S. Snow, J. P. Novak, P. M. Campbell, and D. Park. Random networks of carbon nanotubes as an electronic material. *Applied Physics Letters*, 82:2145, 2003.

[19] P. R. Wallace. The band theory of graphite. *Physical Review*, 71:622–634, 1947.

[20] R. Saito, M Fujita, G. Dresselhaus, and M.S. Dresselhaus. Electronic structure of graphene tubules based on C_{60}. *Physical Review B*, 46:1804, 1992.

[21] P. L. McEuen, M. S. Fuhrer, and H. K. Park. Single-walled carbon nanotube electronics. *Ieee Transactions On Nanotechnology*, 1(1):78–85, March 2002.

[22] M. S. Strano, C. A. Dyke, M. L. Usrey, P. W. Barone, M. J. Allen, H. W. Shan, C. Kittrell, R. H. Hauge, J. M. Tour, and R. E. Smalley. Electronic structure control of single-walled carbon nanotube functionalization. *Science*, 301(5639):1519–1522, 2003.

[23] J. W. G. Wildoer, L. C. Venema, A. G. Rinzler, R. E. Smalley, and C. Dekker. Electronic structure of atomically resolved carbon nanotubes. *Nature*, 391(6662):59–62, January 1998.

[24] A. Jorio, R. Saito, J. H. Hafner, C. M. Lieber, M. Hunter, T. McClure, G. Dresselhaus, and M. S. Dresselhaus. Structural (n, m) determination of isolated single-wall carbon nanotubes by resonant raman scattering. *Physical Review Letters*, 86(6):1118–1121, February 2001.

[25] S.M. Bachilo, M.S. Strano, C. Kittrell, R.H. Hauge, R.E. Smalley, and R.B. Weisman. Structure-assigned optical spectra of single-walled carbon nanotubes. *Science*, 298:2366, 2002.

[26] J. M. Bonard, T. Stora, J. P. Salvetat, F. Maier, T. Stockli, C. Duschl, L. Forro, W. A. deHeer, and A. Chatelain. Purification and size-selection of carbon nanotubes. *Advanced Materials*, 9(10):827–831, 1997.

[27] N. Grossiord, O. Regev, J. Loos, J. Meuldijk, and C. E. Koning. Time-dependent study of the exfoliation process of carbon nanotubes in aqueous dispersions by using UV-visible spectroscopy. *Analytical Chemistry*, 77(16):5135–5139, August 2005.

[28] M. J. O'Connell, S. M. Bachilo, C. B. Huffman, V. C. Moore, M. S. Strano, E. H. Haroz, K. L. Rialon, P. J. Boul, W. H. Noon, C. Kittrell, J. P. Ma, R. H. Hauge, R. B. Weisman, and R. E. Smalley. Band gap fluorescence from individual single-walled carbon nanotubes. *Science*, 297(5581):593–596, July 2002.

[29] Z.-B. Zhang, J. Cardenas, E. E. B. Campbell, and S.-L. Zhang. Reversible surface functionalization of carbon nanotubes for fabrication of field-effect transistors. *Appl. Phys. Lett.*, 87(4):043110–3, July 2005.

[30] P. Poncharal, C. Berger, Y. Yi, Z Wang, and W. de Heer. Room temperature ballistic conduction in carbon nanotubes. *The Journal of Physical Chemistry B*, 106:12104, 2002.

[31] A. Goldoni, R. Larciprete, L. Petaccia, and S. Lizzit. Single-wall carbon nanotube interaction with gases: Sample contaminants and environmental monitoring. *Journal Of The American Chemical Society*, 125(37):11329–11333, 2003.

[32] S. Datta. *Quantum Transport: Atom to Transistor*. Cambridge University Press, 2005.

[33] A. Javey, J. Guo, Q. Wang, M. Lundstrom, and H. J. Dai. Ballistic carbon nanotube field-effect transistors. *Nature*, 424(6949):654–657, 2003.

[34] J. Kong et al. Quantum interference and ballistic transmission in nanotube electron waveguides. *Physical Review Letters*, 87:1068011, 2001.

[35] M. S. Fuhrer, J. Nygard, L. Shih, M. Forero, Y. G. Yoon, M. S. C. Mazzoni, H. J. Choi, J. Ihm, S. G. Louie, A. Zettl, and P. L. McEuen. Crossed nanotube junctions. *Science*, 288(5465):494–497, April 2000.

[36] V. Skakalova, A. B. Kaiser, U. Dettlaff-Weglikowska, K. Hrncarikova, and S. Roth. Effect of chemical treatment on electrical conductivity, infrared absorption, and Raman spectra of single-walled carbon nanotubes. *Journal Of Physical Chemistry B*, 109(15):7174–7181, April 2005.

[37] J. Vavro, J. M. Kikkawa, and J. E. Fischer. Metal-insulator transition in doped single-wall carbon nanotubes. *Physical Review B*, 71(15):155410, April 2005.

[38] Bingbing Liu, T. Wagberg, Eva Olsson, Ruseng Yang, Hongdong Li, Shulin Zhang, Haibin Yang, Guangtian Zou, and B. Sundqvist. Synthesis and characterization of single-walled nanotubes produced with Ce/Ni as catalysts. *Chemical Physics Letters*, 320(3-4):365–372, April 2000.

[39] B. Ruzicka, L. Degiorgi, R. Gaal, L. Thien-Nga, R. Bacsa, J. P. Salvetat, and L. Forro. Optical and dc conductivity study of potassium-doped single-walled carbon nanotube films. *Physical Review B*, 61(4):R2468–R2471, 2000.

[40] D. Hecht, L. B. Hu, and G. Gruner. Conductivity scaling with bundle length and diameter in single walled carbon nanotube networks. *Applied Physics Letters*, 89(13):133112, 2006.

[41] D. Stauffer. *Introduction to Percolation Theory*. Taylor & Francis, 1985.

[42] E. Bekyarova, M. E. Itkis, N. Cabrera, B. Zhao, A. P. Yu, J. B. Gao, and R. C. Haddon. Electronic properties of single-walled carbon nanotube networks. *Journal Of The American Chemical Society*, 127:5990–5995, 2005.

[43] L. Hu, D. S. Hecht, and G. Gruner. Percolation in transparent and conducting carbon nanotube networks. *Nano Letters*, 4(12):2513–2517, December 2004.

[44] J. K. W. Sandler, J. E. Kirk, I. A. Kinloch, M. S. P. Shaffer, and A. H. Windle. Ultra-low electrical percolation threshold in carbon-nanotube-epoxy composites. *Polymer*, 44(19):5893–5899, 2003.

[45] B. Kim, J. Lee, and I. S. Yu. Electrical properties of single-wall carbon nanotube and epoxy composites. *Journal Of Applied Physics*, 94(10):6724–6728, 2003.

[46] V. Skakalova, A. B. Kaiser, Y.-S. Woo, and S. Roth. Electronic transport in carbon nanotubes: From individual nanotubes to thin and thick networks. *Physical Review B (Condensed Matter and Materials Physics)*, 74(8):085403, 2006.

[47] J. E. Fischer, H. Dai, A. Thess, R. Lee, N. M. Hanjani, D. L. Dehaas, and R. E. Smalley. Metallic resistivity in crystalline ropes of single-wall carbon nanotubes. *Physical Review B*, 55(8):R4921–R4924, 1997.

[48] M. Shiraishi and M. Ata. Conduction mechanisms in single-walled carbon nanotubes. *Synthetic Metals*, 128(3):235–239, 2002.

[49] H. Y. Yu, S. H. Jhang, Y. W. Park, A. Bittar, H. J. Trodahl, and A. B. Kaiser. Properties of single-wall carbon nanotubes. *Synthetic Metals*, 121(1-3):1223–1224, 2001.

[50] P. Sheng. Fluctuation-induced tunneling conduction in disordered materials. *Physical Review B*, 21(6):2180–2195, 1980.

[51] l. Pietronero. Ideal conductivity of carbon pi-polymers and intercalation compounds. *Synthetic Metals*, 8(3-4):225–231, 1983.

[52] M. S. Fuhrer, W. Holmes, P. L. Richards, P. Delaney, S. G. Louie, and A. Zettl. Nonlinear transport and localization in single-walled carbon nanotubes. *Synthetic Metals*, 103(1-3):2529–2532, June 1999.

[53] M. Jaiswal, W. Wang, K. A. S. Fernando, Y. P. Sun, and R. Menon. Charge transport in transparent single-wall carbon nanotube networks. *Journal of Physics: Condensed Matter*, 19(44):446006–, 2007.

[54] M. S. Fuhrer, Marvin L. Cohen, A. Zettl, and Vincent Crespi. Localization in single-walled carbon nanotubes. *Solid State Communications*, 109(2):105–109, December 1998.

[55] J. M. Benoit, B. Corraze, and O. Chauvet. Localization, Coulomb interactions, and electrical heating in single-wall carbon nanotubes/polymer composites. *Physical Review B*, 65(24):241405, June 2002.

[56] N. F. Mott and E. A. Davis. *Electronic Processes in Non-crystalline Materials*. Oxford University Press, second edition, 1979.

[57] J.-Y. Park, S. Rosenblatt, Y. Yaish, V. Sazonova, H. Ustunel, S. Braig, T.A. Arias, P.W. Brouwer, and P.L. McEuen. Electron-phonon scattering in metallic single-walled carbon nanotubes. *Nano Lett.*, 4(3):517–520, 2004.

[58] M. S. Purewal, B. H. Hong, A. Ravi, B. Chandra, J. Hone, and P. Kim. Scaling of resistance and electron mean free path of single-walled carbon nanotubes. *Phys. Rev. Lett.*, 98(18):186808–4, May 2007.

[59] A. B. Kaiser, V. Skakalova, and S. Roth. Thin transparent carbon nanotube networks: effects of ion irradiation. *Physica Status Solidi B-Basic Solid State Physics*, 244:4199–4203, 2007.

[60] A. B. Kaiser. Electronic transport properties of conducting polymers and carbon nanotubes. *Rep. Prog. Phys*, 64:1–49, 2001.

[61] F. Leonard and J. Tersoff. Role of Fermi-level pinning in nanotube Schottky diodes. *Physical Review Letters*, 84(20):4693–4696, May 2000.

[62] M. Freitag, J.C. Tsang, A. Bol, D. Yuan, J. Liu, and Ph. Avouris. Imaging of the Schottky barriers and charge depletion in carbon nanotube transistors. *Nano Lett.*, 7(7):2037–2042, 2007.

[63] J. Appenzeller, J. Knoch, V. Derycke, R. Martel, S. Wind, and Ph. Avouris. Field-modulated carrier transport in carbon nanotube transistors. *Phys. Rev. Lett.*, 89(12):126801–, August 2002.

[64] J. Appenzeller, M. Radosavljevic, J. Knoch, and Ph. Avouris. Tunneling versus thermionic emission in one-dimensional semiconductors. *Phys. Rev. Lett.*, 92(4):048301–4, January 2004.

[65] Y. Yaish, J.-Y. Park, S. Rosenblatt, V. Sazonova, M. Brink, and P. L. McEuen. Electrical nanoprobing of semiconducting carbon nanotubes using an atomic force microscope. *Phys. Rev. Lett.*, 92(4):046401–, January 2004.

[66] R. Martel, T. Schmidt, H. R. Shea, T. Hertel, and Ph. Avouris. Single- and multi-wall carbon nanotube field-effect transistors. *Applied Physics Letters*, 73:2447, 1998.

[67] S. J. Tans, A. R. M. Verschueren, and C. Dekker. Room-temperature transistor based on a single carbon nanotube. *Nature*, 393:49, 1998.

[68] S. M. Sze. *Physics of Semiconductor Devices*. Wiley, 1981.

[69] R. Martel, V. Derycke, C. Lavoie, J. Appenzeller, K. K. Chan, J. Tersoff, and Ph. Avouris. Ambipolar electrical transport in semiconducting single-wall carbon nanotubes. *Phys. Rev. Lett.*, 87(25):256805, Dec 2001.

[70] S. Heinze, J. Tersoff, R. Martel, V. Derycke, J. Appenzeller, and Ph. Avouris. Carbon nanotubes as schottky barrier transistors. *Phys. Rev. Lett.*, 89(10):106801, Aug 2002. must read.

[71] Y. M. Lin, J. Appenzeller, J. Knoch, and P. Avouris. High-performance carbon nanotube field-effect transistor with tunable polarities. *Ieee Transactions On Nanotechnology*, 4:481–489, 2005.

[72] A. Javey, J. Guo, D. B. Farmer, Q. Wang, E. Yenilmez, R. G. Gordon, M. Lundstrom, and H. J. Dai. Self-aligned ballistic molecular transistors and electrically parallel nanotube arrays. *Nano Letters*, 4(7):1319–1322, 2004.

[73] S. Kumar, N. Pimparkar, J. Y. Murthy, and M. A. Alam. Theory of transfer characteristics of nanotube network transistors. *Applied Physics Letters*, 88:123505, 2006.

[74] Y. Li, D. Mann, M. Rolandi, W. Kim, A. Ural, S. Hung, A. Javey, J. Cao, D. Wang, E. Yenilmez, Q. Wang, J.F. Gibbons, Y. Nishi, and H. Dai. Preferential growth of semiconducting single-walled carbon nanotubes by a plasma enhanced CVD method. *Nano Lett.*, 4(2):317–321, February 2004.

[75] P. G. Collins, M. S. Arnold, and P. Avouris. Engineering carbon nanotubes and nanotube circuits using electrical breakdown. *Science*, 292:706, 2001.

[76] L. An, Q. Fu, C. Lu, and J. Liu. A simple chemical route to selectively eliminate metallic carbon nanotubes in nanotube network devices. *J. Am. Chem. Soc.*, 126(34):10520–10521, 2004.

[77] E. J. Bae, Y. S. Min, U. J. Kim, and W. J. Park. Thin film transistors of single-walled carbon nanotubes grown directly on glass substrates. *Nanotechnology*, 18(49):495203, December 2007.

[78] J. Kong and H. J. Dai. Full and modulated chemical gating of individual carbon nanotubes by organic amine compounds. *Journal Of Physical Chemistry B*, 105(15):2890–2893, 2001.

[79] K. Bradley, J. C. P. Gabriel, A. Star, and G. Gruner. Short-channel effects in contact-passivated nanotube chemical sensors. *Applied Physics Letters*, 83(18):3821–3823, 2003.

[80] X. L. Liu, Z. C. Luo, S. Han, T. Tang, D. H. Zhang, and C. W. Zhou. Band engineering of carbon nanotube field-effect transistors via selected area chemical gating. *Applied Physics Letters*, 86(24), 2005.

[81] V. Derycke, R. Martel, J. Appenzeller, and Ph. Avouris. Controlling doping and carrier injection in carbon nanotube transistors. *Applied Physics Letters*, 80:2773, 2002.

[82] G. U. Sumanasekera, C. K. W. Adu, S. Fang, and P. C. Eklund. Effects of gas adsorption and collisions on electrical transport in single-walled carbon nanotubes. *Physical Review Letters*, 85(5):1096–1099, 2000.

[83] D. Kang, N. Park, J. Ko, E. Bae, and W. Park. Oxygen-induced p-type doping of a long individual single-walled carbon nanotube. *Nanotechnology*, 16(8):1048, 2005.

[84] S. H. Jhi, S. G. Louie, and M. L. Cohen. Electronic properties of oxidized carbon nanotubes. *Phys. Rev. Lett.*, 85(8):1710–1713, Aug 2000.

[85] J. J. Zhao, A. Buldum, J. Han, and J. P. Lu. Gas molecule adsorption in carbon nanotubes and nanotube bundles. *Nanotechnology*, 13(2):195–200, April 2002.

[86] K. Bradley, S. H. Jhi, P. G. Collins, J. Hone, M. L. Cohen, S. G. Louie, and A. Zettl. Is the intrinsic thermoelectric power of carbon nanotubes positive? *Physical Review Letters*, 85(20):4361–4364, November 2000.

[87] J. P. Small, K. M. Perez, and P. Kim. Modulation of thermoelectric power of individual carbon nanotubes. *Phys. Rev. Lett.*, 91(25):256801–, December 2003.

[88] Seung Mi Lee et al. Defect-induced oxidation of graphite. *Physical Review Letters*, 82:217, 1999.

[89] H. Dai, E. W. Wong, and C. M. Lieber. Probing electrical transport in nanomaterials: Conductivity of individual carbon nanotubes. *Science*, 272:523 – 526, 1996.

[90] X. Feng, S. Irle, H. Witek, K. Morokuma, R. Vidic, and E. Borguet. Sensitivity of ammonia interaction with single-walled carbon nanotube bundles to the presence of defect sites and functionalities. *J. Am. Chem. Soc.*, 127(30):10533–10538, August 2005.

[91] M. Grujicic, G. Cao, and R. Singh. The effect of topological defects and oxygen adsorption on the electronic transport properties of single-walled carbon-nanotubes. *Applied Surface Science*, 211(1-4):166–183, April 2003.

[92] S.-P. Chan, G. Chen, X. G. Gong, and Z.-F. Liu. Oxidation of carbon nanotubes by singlet O_2. *Phys Rev Lett*, 90(8):086403, 2003.

[93] L. Valentini, I. Armentano, L. Lozzi, S. Santucci, and J. M. Kenny. Interaction of methane with carbon nanotube thin films: role of defects and oxygen adsorption. *Materials Science and Engineering: C*, 24(4):527–533, June 2004.

[94] C.-W. Chen, M.-H. Lee, and S. J. Clark. Gas molecule effects on field emission properties of single-walled carbon nanotube. *Diamond and Related Materials*, 13(4-8):1306–1313, 2004.

[95] P. C. P. Watts, N. Mureau, Z. N. Tang, Y. Miyajima, J. D. Carey, and S. R. P. Silva. The importance of oxygen-containing defects on carbon nanotubes for the detection of polar and non-polar vapours through hydrogen bond formation. *Nanotechnology*, 18(17):175701, 2007.

[96] R. Brukh, O. Sae-Khow, and S. Mitra. Stabilizing single-walled carbon nanotubes by removal of residual metal catalysts. *Chemical Physics Letters*, 459(1-6):149–152, June 2008.

[97] I. S. Grigoriev and E. Z. Meilikhov, editors. *Handbook of Physical Quantities*. CRC Press, 1997.

[98] X. Y. Cai, S. Akita, and Y. Nakayama. Current induced light emission from a multiwall carbon nanotube. *Thin Solid Films*, 464:364–367, 2004.

[99] M. Monthioux, B. W. Smith, B. Burteaux, A. Claye, J. E. Fischer, and D. E. Luzzi. Sensitivity of single-wall carbon nanotubes to chemical processing: an electron microscopy investigation. *Carbon*, 39(8):1251–1272, 2001.

[100] A. G. Rinzler, J. Liu, H. Dai, P. Nikolaev, C. B. Huffman, F. J. Rodriguez-Macias, P. J. Boul, A. H. Lu, D. Heymann, D. T. Colbert, R. S. Lee, J. E. Fischer, A. M. Rao, P. C. Eklund, and R. E. Smalley. Large-scale purification of single-wall carbon nanotubes: process, product, and characterization. *Applied Physics A-Materials Science & Processing*, 67(1):29–37, 1998.

[101] O. Suekane, A. Nagataki, and Y. Nakayama. Current-induced curing of defective carbon nanotubes. *Applied Physics Letters*, 89(18):183110, 2006.

[102] P. Giannozzi, R. Car, and G. Scoles. Oxygen adsorption on graphite and nanotubes. *The Journal of Chemical Physics*, 118(3):1003–1006, 2003.

[103] H. Ulbricht, G. Moos, and T. Hertel. Physisorption of molecular oxygen on single-wall carbon nanotube bundles and graphite. *Physical Review B*, 66(7):075404, 2002.

[104] J. A. Robinson, E. S. Snow, S. C. Badescu, T. L. Reinecke, and F. K. Perkins. Role of defects in single-walled carbon nanotube chemical sensors. *Nano Letters*, 6(8):1747–1751, August 2006.

[105] L. Valentini, F. Mercuri, I. Armentano, C. Cantalini, S. Picozzi, L. Lozzi, S. Santucci, A. Sgamellotti, and J. M. Kenny. Role of defects on the gas sensing properties of carbon nanotubes thin films: experiment and theory. *Chemical Physics Letters*, 387(4-6):356–361, 2004.

[106] R. Pati, Y. Zhang, S. K. Nayak, and P. M. Ajayan. Effect of H_2O adsorption on electron transport in a carbon nanotube. *Applied Physics Letters*, 81(14):2638–2640, September 2002.

[107] P. S. Na, H. Kim, H. So, K. J. Kong, H. Chang, B. H. Ryu, Y. Choi, J. Lee, B. K. Kim, J. J. Kim, and J. Kim. Investigation of the humidity effect on the electrical properties of single-walled carbon nanotube transistors. *Appl. Phys. Lett.*, 87(9):093101–3, August 2005.

[108] A. Zahab, L. Spina, P. Poncharal, and C. Marliere. Water-vapor effect on the electrical conductivity of a single-walled carbon nanotube mat. *Physical Review B*, 62(15):10000–10003, 2000.

[109] Y. Maniwa, K. Matsuda, H. Kyakuno, S. Ogasawara, T. Hibi, H. Kadowaki, S. Suzuki, Y. Achiba, and H. Kataura. Water-filled single-wall carbon nanotubes as molecular nanovalves. *Nature Materials*, 6:135–141, 2007.

[110] H. E. Romero, G. U. Sumanasekera, S. Kishore, and P. C. Eklund. Effects of adsorption of alcohol and water on the electrical transport of carbon nanotube bundles. In *Journal of Physics-Condensed Matter* [106], pages 1939–1949.

[111] W. Kim, A. Javey, O. Vermesh, O. Wang, Y. M. Li, and H. J. Dai. Hysteresis caused by water molecules in carbon nanotube field-effect transistors. *Nano Letters*, 3(2):193–198, 2003.

[112] D. Sung, S. Hong, Y. H. Kim, N. Park, S. Kim, S. L. Maeng, and K. C. Kim. Ab initio study of the effect of water adsorption on the carbon nanotube field-effect transistor. *Applied Physics Letters*, 89(24), 2006.

[113] C. Y. Lee and M. S. Strano. Amine basicity (pk(b)) controls the analyte blinding energy on single walled carbon nanotube electronic sensor arrays. *Journal Of The American Chemical Society*, 130(5):1766–1773, February 2008.

[114] E. S. Snow, F. K. Perkins, E. J. Houser, S. C. Badescu, and T. L. Reinecke. Chemical detection with a single-walled carbon nanotube capacitor. *Science*, 307(5717):1942–1945, 2005.

[115] C. Staii and A. T. Johnson. DNA-decorated carbon nanotubes for chemical sensing. *Nano Letters*, 5(9):1774–1778, 2005.

[116] J. P. Novak, E. S. Snow, E. J. Houser, D. Park, J. L. Stepnowski, and R. A. McGill. Nerve agent detection using networks of single-walled carbon nanotubes. *Applied Physics Letters*, 83(19):4026–4028, 2003.

[117] C. Y. Lee, S. Baik, J. Q. Zhang, R. I. Masel, and M. S. Strano. Charge transfer from metallic single-walled carbon nanotube sensor arrays. *Journal Of Physical Chemistry B*, 110(23):11055–11061, 2006.

[118] R. J. Chen, N. R. Franklin, J. Kong, J. Cao, T. W. Tombler, Y. Zhang, and H. Dai. Molecular photodesorption from single-walled carbon nanotubes. *Applied Physics Letters*, 79(14):2258–2260, 2001.

[119] K. Cattanach, R. D. Kulkarni, M. Kozlov, and S. K. Manohar. Flexible carbon nanotube sensors for nerve agent simulants. *Nanotechnology*, 17(16):4123–4128, 2006.

[120] T. Zhang, M. B. Nix, B. Y. Yoo, M. A. Deshusses, and N. V. Myung. Electrochemically functionalized single-walled carbon nanotube gas sensor. *Electroanalysis*, 18(12):1153–1158, 2006.

[121] F. Picaud, R. Langlet, M. Arab, M. Devel, C. Girardet, S. Natarajan, S. Chopra, and A. M. Rao. Gas-induced variation in the dielectric properties of carbon nanotube bundles for selective sensing. *Journal Of Applied Physics*, 97(11):114316, 2005.

[122] E. S. Snow and F. K. Perkins. Capacitance and conductance of single-walled carbon nanotubes in the presence of chemical vapors. *Nano Letters*, 5(12):2414–2417, December 2005.

[123] J. E. Lennard-Jones. Processes of adsorption and diffusion on solid surfaces. *Trans. Faraday Soc.*, 28:333 – 359, 1932.

[124] J.-P. Bouchaud, A. Ott, D. Langevin, and W. Urbach. Anomalous diffusion in elongated micelles and its Levy flight interpretation. *Journal de Physique Ii*, 1(12):1465–1482, December 1991.

[125] J.-P. Bouchaud, A. Georges, J. Koplik, A. Provata, and S. Redner. Superdiffusion in random velocity fields. *Phys. Rev. Lett.*, 64(21):2503–, May 1990.

[126] G. A . Somorjai. *Principles of Surface Chemistry*. Prentice-Hall, Inc., 1972.

[127] C.T. Sah. *Fundamentals of Solid State Electronics*. World Scientific Publishing, 1991.

[128] Y. D. Hong, Y. T. Yeow, W. K. Chim, K. M. Wong, and J. J. Kopanski. Influence of interface traps and surface mobility degradation on scanning capacitance microscopy measurement. *Ieee Transactions On Electron Devices*, 51(9):1496–1503, September 2004.

[129] S. Decossas, J. J. Marchand, and G. Bremond. Electrical characterisation of local electronic properties of self-assembled semiconductor nanostructures using AFM. *Physica E-Low-Dimensional Systems & Nanostructures*, 23(3-4):396–400, 2004.

[130] I. Lundstrom, S. Shivaraman, C. Svensson, and L. Lundkvist. A hydrogen - sensitive MOS field - effect transistor. *Appl. Phys. Lett.*, 26(2):55–57, January 1975.

[131] F. Winquist, A. Spetz, M. Armgarth, C. Nylander, and I. Lundstrom. Modified palladium metal-oxide-semiconductor structures with increased ammonia gas sensitivity. *Applied Physics Letters*, 43(9):839–841, 1983.

[132] C. Nylander, M. Armgrath, and I. Lundström. Ammonia detector based on conducting polymers. *Analytical Chemistry Symposia Series*, 17:203–207, 1983.

[133] P. N. Bartlett, P. B. M. Archer, and S. K. Lingchung. Conducting polymer gas sensors. 1. Fabrication and characterization. *Sensors And Actuators*, 19(2):125–140, 1989.

[134] Q. Fang, D. G. Chetwynd, J. A. Covington, C. S. Toh, and J. W. Gardner. Micro-gas-sensor with conducting polymers. *Sensors And Actuators B-Chemical*, 84(1):66–71, 2002.

[135] J. Fraden. *Handbook of Modern Sensors: Physics, Designs, and Applications*. American Institute of Physics, 2001.

[136] M. Hoummady, A. Campitelli, and W. Wlodarski. Acoustic wave sensors: design, sensing mechanisms and applications. *Smart Materials & Structures*, 6(6):647–657, 1997.

[137] B. D. Maccraith, G. Okeeffe, C. Mcdonagh, and A. K. Mcevoy. LED-based fiber optic oxygen sensor using sol-gel coating. *Electronics Letters*, 30(11):888–889, 1994.

[138] Q. Zhu, K.F. Karlsson, E. Pelucchi, and E. Kapon. Transition from two-dimensional to three-dimensional quantum confinement in semiconductor quantum wires/quantum dots. *Nano Lett.*, 7:2188 – 2195, 2007.

[139] A. M. Rao, E. Richter, S. Bandow, B. Chase, P. C. Eklund, K. A. Williams, S. Fang, K. R. Subbaswamy, M. Menon, A. Thess, R. E. Smalley, G. Dresselhaus, and M. S. Dresselhaus. Diameter-selective Raman scattering from vibrational modes in carbon nanotubes. *Science*, 275(5297):187–191, 1997.

[140] M. S. Dresselhaus and P. C. Eklund. Phonons in carbon nanotubes. *Advances In Physics*, 49(6):705–814, 2000.

[141] S. D. M. Brown, A. Jorio, M. S. Dresselhaus, and G. Dresselhaus. Observations of the D-band feature in the Raman spectra of carbon nanotubes. *Physical Review B*, 64(7):art. no.–073403, 2001.

[142] H. Kataura, Y. Kumazawa, Y. Maniwa, I. Umezu, S. Suzuki, Y. Ohtsuka, and Y. Achiba. Optical properties of single-wall carbon nanotubes. *Synthetic Metals*, 103(1-3):2555–2558, June 1999.

[143] S. D. M. Brown, A. Jorio, P. Corio, M. S. Dresselhaus, G. Dresselhaus, R. Saito, and K. Kneipp. Origin of the Breit-Wigner-Fano lineshape of the tangential g-band feature of metallic carbon nanotubes. *Physical Review B*, 63(15):155414, 2001.

[144] M. S. Strano. Probing chiral selective reactions using a revised kataura plot for the interpretation of single-walled carbon nanotube spectroscopy. *Journal Of The American Chemical Society*, 125(51):16148–16153, 2003.

[145] Dr. Maruyama, The University of Tokyo, http://www.photon.t.u-tokyo.ac.jp/~maruyama/kataura/kataura.html.

[146] R. Engel-Herbert, H. Pforte, and T. Hesjedal. CVD synthesis and purification of single-walled carbon nanotubes using silica-supported metal catalyst. *Materials Letters*, 61(11-12):2589–2593, May 2007.

[147] M. E. Itkis, D.E. Perea, R. Jung, S. Niyogi, and R.C. Haddon. Comparison of analytical techniques for purity evaluation of single-walled carbon nanotubes. *J. Am. Chem. Soc.*, 127(10):3439–3448, 2005.

[148] H. R. Byon, H. Lim, H. J. Song, and H. C. Choi. A synthesis of high purity single-walled carbon nanotubes from small diameters of cobalt nanoparticles by using oxygen-assisted chemical vapor deposition process. *Bulletin Of The Korean Chemical Society*, 28:2056–2060, 2007.

[149] E. Kymakis and G. A. J. Amaratunga. Electrical properties of single-wall carbon nanotube-polymer composite films. *Journal of Applied Physics*, 99(8):084302, 2006.

[150] W. Zhou, Y. H. Ooi, R. Russo, P. Papanek, D. E. Luzzi, J. E. Fischer, M. J. Bronikowski, P. A. Willis, and R. E. Smalley. Structural characterization and diameter-dependent oxidative stability of single wall carbon nanotubes synthesized by the catalytic decomposition of co. *Chemical Physics Letters*, 350(1-2):6–14, 2001.

[151] S. Reich, C. Thomsen, and P. Ordejn. Electronic band structure of isolated and bundled carbon nanotubes. *Phys. Rev. B*, 65(15):155411–, March 2002. lit review.

[152] B. Zhao, M. E. Itkis, S. Niyogi, H. Hu, J. Zhang, and R. C. Haddon. Study of the extinction coefficients of single-walled carbon nanotubes and related carbon materials. *Journal Of Physical Chemistry B*, 108(24):8136–8141, June 2004.

[153] J. L. Bahr, E. T. Mickelson, M. J. Bronikowski, R. E. Smalley, and J. M. Tour. Dissolution of small diameter single-wall carbon nanotubes in organic solvents? *Chemical Communications*, 2(2):193–194, 2001.

[154] B. Zhou, Y. Lin, H. Li, W. Huang, J.W. Connell, L.F. Allard, and Y.-P. Sun. Absorptivity of functionalized single-walled carbon nanotubes in solution. *J. Phys. Chem. B*, 107(49):13588–13592, December 2003.

[155] M. J. OConnell et al. Band gap fluorescence from individual single-walled carbon nanotubes. *Science*, 297:593–596, 2002.

[156] N. Sclar. Resistivity and deep impurity levels in silicon at 300 K. *Ieee Transactions On Electron Devices*, 24(6):709–712, 1977.

[157] G. U. Sumanasekera, C. K. W. Adu, S. Fang, and P. C. Eklund. Effects of gas adsorption and collisions on electrical transport in single-walled carbon nanotubes. *Phys. Rev. Lett.*, 85(5):1096–1099, Jul 2000.

[158] A. B. Kaiser. Systematic conductivity behavior in conducting polymers: Effects of heterogeneous disorder. *Advanced Materials*, 13(12-13):927–941, 2001.

[159] Z. Yao, C. L. Kane, and C. Dekker. High-field electrical transport in single-wall carbon nanotubes. *Physical Review Letters*, 84:2941, 2000.

[160] C. L. Kane, E. J. Mele, R. S. Lee, J. E. Fischer, P. Petit, H. Dai, A. Thess, R. E. Smalley, A. R. M. Verschueren, S. J. Tans, and C. Dekker. Temperature-dependent resistivity of single-wall carbon nanotubes. *Europhysics Letters*, 41(6):683–688, 1998.

[161] A. B. Kaiser, V. Skakalova, and S. Roth. Modelling conduction in carbon nanotube networks with different thickness, chemical treatment and irradiation. *Physica E-Low-Dimensional Systems & Nanostructures*, 40(7):2311–2318, 2008.

[162] V. Skakalova, A. B. Kaiser, Z. Osvath, G. Vertesy, L. P. Biro, and S. Roth. Ion irradiation effects on conduction in single-wall carbon nanotube networks. *Applied Physics A-Materials Science & Processing*, 90:597–602, 2008.

[163] K. Tohji, T. Goto, H. Takahashi, Y. Shinoda, N. Shimizu, B. Jeyadevan, I. Matsuoka, Y. Saito, A. Kasuya, T. Ohsuna, H. Hiraga, and Y. Nishina. Purifying single-walled nanotubes. *Nature*, 383(6602):679–679, 1996.

[164] Y. Yosida and I. Oguro. Variable range hopping conduction in bulk samples composed of single-walled carbon nanotubes. *Journal of Applied Physics*, 86(2):999–1003, 1999.

[165] R. A. Jishi, M. S. Dresselhaus, and G. Dresselhaus. Electron-phonon coupling and the electrical-conductivity of fullerene nanotubules. *Physical Review B*, 48(15):11385–11389, 1993.

[166] A.B. Kaiser and Y.W. Park. Current-voltage characteristics of conducting polymers and carbon nanotubes. *Synthetic Metals*, 152(1-3):181–184, September 2005.

[167] H. F. Kuo, D. H. Lien, W. K. Hsu, N. H. Tai, and S. C. Chang. Gas sensing improvement of carbon nanotubes by NH_4OH-flash treatment: a nondestructive purification technique. *Journal Of Materials Chemistry*, 17(34):3581–3584, 2007.

[168] W. Fa, J. Chen, and J.thermionically Dong. Effects of topological defects in the semiconductor carbon nanotube intramolecular junctions. *The European Physical Journal B - Condensed Matter and Complex Systems*, 37(4):473–478, February 2004.

[169] Hajin Kim, Jhinhwan Lee, Sungjun Lee, Young Kuk, Ji-Yong Park, and Se-Jong Kahng. Local electronic density of states of a semiconducting carbon nanotube interface. *Phys. Rev. B*, 71(23):235402–4, June 2005.

[170] H. B. Michaelson. The work function of the elements and its periodicity. *J. Appl. Phys.*, 48(11):4729–4733, November 1977.

[171] M. Shiraishi and M. Ata. Work function of carbon nanotubes. *Carbon*, 39(12):1913–1917, 2001.

[172] S. Suzuki, C. Bower, Y. Watanabe, and O. Zhou. Work functions and valence band states of pristine and Cs-intercalated single-walled carbon nanotube bundles. *Applied Physics Letters*, 76(26):4007–4009, 2000.

[173] Jijun Zhao, Jie Han, and Jian Ping Lu. Work functions of pristine and alkali-metal intercalated carbon nanotubes and bundles. *Phys. Rev. B*, 65(19):193401–, April 2002.

[174] M. C. Steele, J. W. Hile, and B. A. Maciver. Hydrogen-sensitive palladium gate MOS capacitors. *Journal Of Applied Physics*, 47(6):2537–2538, 1976.

[175] D. Dwivedi, R. Dwivedi, and S. K. Srivastava. Sensing properties of palladium-gate MOS (Pd-MOS) hydrogen sensor-based on plasma grown silicon dioxide. *Sensors And Actuators B-Chemical*, 71(3):161–168, 2000.

[176] E. S. Snow, P. M. Campbell, M. G. Ancona, and J. P. Novak. High-mobility carbon-nanotube thin-film transistors on a polymeric substrate. *Applied Physics Letters*, 86(3):33105, 2005.

[177] S. Rosenblatt, Y. Yaish, J. Park, J. Gore, V. Sazonova, and P. L. McEuen. High performance electrolyte gated carbon nanotube transistors. *Nano Letters*, 2(8):869–872, 2002.

[178] J. Guo, S. Goasguen, M. Lundstrom, and S. Datta. Metal-insulator-semiconductor electrostatics of carbon nanotubes. *Applied Physics Letters*, 81(8):1486–1488, 2002.